

University of Nottingham
UK | CHINA | MALAYSIA

Mathematical Modelling of Brain Tumour Growth and Therapy

Lee Curtin, MMath

Thesis submitted to The University of Nottingham for the degree of Doctor of Philosophy

August 2, 2019

ABSTRACT

Glioblastoma multiforme (GBM) is the most aggressive primary brain tumour with an expected median survival of just 15 months post-diagnosis in spite of treatment. GBMs are highly invasive, such that their cells can be found in low densities far away from the apparent tumour edge indicated by magnetic resonance imaging (MRI). It is this invasiveness that can limit the efficacy of surgery. However, surgery acts as a unique opportunity for further local drug delivery which is currently not exploited as a standard of care.

A local drug delivery polymer is in development at the Children's Brain Tumour Research Centre at the University of Nottingham; this biodegradable polymer can be loaded with chemotherapy drugs and pasted onto the cavity wall immediately following the surgical removal of the tumour bulk, to treat the remaining GBM cells that could not be removed. The drug delivery dynamics through the polymer are not fully understood. We have developed *in vitro* experiments and an analogous mathematical model to characterise the dynamics of diffusion through the polymer. We noticed that the polymer constructs swell during *in vitro* experiments, and our mathematical model fits suggest a temporally decreasing diffusion coefficient of drug travelling through the polymer. Together, these suggest that the polymer swelling inhibits drug diffusion over time.

In further collaboration with the Hounsfield Facility at the University of Nottingham, we have gathered state-of-the-art microCT data of unswollen polymer constructs. We have applied homogenisation of diffusion theory to diffusive drug transport in the mixture of polymer particles and liquid medium. The microCT data has been used for input geometries of the resulting cell problems, whose solutions define the homogenised tensor of diffusion coefficients. We have found these solutions using a finite element method in FEniCS. This theory allows us to quantify the rates of effective diffusion and the effect of the internal geometries on this rate. The homogenised coefficients suggest that both channels of polymer and gaps of liquid medium are present in the polymer constructs, such that the liquid channels are the primary mechanism by which drug would diffuse through the polymer in these constructs. We see a significantly lower average diffusion rate in the direction

that the polymer constructs were packed into their moulds, highlighting the importance of the method of application of this treatment and its subsequent impact on the diffusion rate of chemotherapy drugs.

With the Precision Neurotherapeutics Innovation Program at the Mayo Clinic, we have extended the Proliferation Invasion Hypoxia Necrosis Angiogenesis (PIHNA) model, a PDE model that recapitulates the dynamics between angiogenesis and GBM growth at the tissue level. We show that the original term that denotes the efficiency of the vasculature to provide nutrients to the tumour can produce counter-intuitive behaviour in some cases, and hence include a more realistic term. Unlike previous PIHNA publications, we have allowed for different hypoxic and normoxic cell diffusion rates, as literature suggests the hypoxic cell rate is faster than its normoxic counterpart. We linearised the PIHNA model to find an analytical expression to predict the minimum possible wavespeed, and have shown that this minimal wavespeed is reached if the diffusivity of normoxic cells is greater than or equal to that of their hypoxic counterpart. However, when the hypoxic diffusion rate is markedly faster than the normoxic diffusion rate, we see a faster numerical wavespeed, suggesting that the hypoxic cells can drive the tumour growth. We then apply this model to perioperative ischemia, a reduction in functional blood vessels that can occur as a surgical complication, which has been seen clinically to increase the chance of patients having a distally recurring tumour. A distally recurring tumour returns with a different progression pattern such that it appears far away from the original site (distant recurrence) or more diffuse (diffuse recurrence) on MRI. We see in the PIHNA model that if a tumour becomes hypoxic and necrotic at a fast enough rate due to the decrease in nutrient availability caused by ischemia, and the ischemia is severe enough, the tumour can reappear on simulated MRI far away from the expected local recurrence location if it has a high enough migration rate and low enough proliferation rate - giving a distant recurrence. This work therefore supports the hypothesis that hypoxia can act as a driver for distantly recurring GBM, and suggests conditions by which this can occur.

Ultimately, we plan to bring together the two themes of this thesis with a tumour growth model similar to PIHNA that incorporates the local drug delivery polymer to test the potential efficacy of this treatment for brain tumour patients.

ACKNOWLEDGEMENTS

PhDs are a huge undertaking and take the support of many to be realised. I owe my gratitude to many people that have helped me along the way. First, I would like to acknowledge the time and nurturing guidance given by my supervisors: Professor Markus Owen and Dr Kris Van der Zee throughout the past four years, as well as the University of Nottingham for funding me and providing me with the means to do my research. I would also like to thank my collaborators from three research groups: those at the Children's Brain Tumour Research Centre for being so welcoming to a mathematician in a wet lab, the Hounsfield Facility for allowing us to use their microCT scanners, and the Precision Neurotherapeutics Innovation Program at Mayo Clinic for hiring me as a Research Trainee, Research Collaborator and now Informatics Specialist, and financially enabling my research visits to their lab. I would also like to thank my assessors, Dr Reuben O'Dea and Dr Matthew Hubbard for their critical feedback during my PhD, as well as my external assessor Professor Mark Chaplain for taking the time to read this work and being so friendly during my viva.

I have had personal setbacks during my PhD, during which times I have been extremely grateful for the emotional support of my friends and family. Dr Emma McIvor has been a constant rock to bounce ideas off of, share well-needed work breaks with and is a great calibrator of my work-life balance. Sergio Ibarra has been there for me in ways that I did not even know that I needed, and shown me that there is more to life than education. I would like to personally thank those that I met along the way: Hannah, Alex, Jon, George, Harriet, Ramon, Victoria, Felipe, Acacia, Tove and Jenny, for being there when I needed them and keeping my spirits up. My family have supported me throughout my life and have facilitated the privilege I have had in doing a PhD. My thanks therefore goes to Mark and Jenny Curtin, Natalie and Anthony Newman, and of course the recent addition, Lola Newman.

CONTENTS

1 INTRODUCTION AND LITERATURE REVIEW 8
- 1.1 Statistical Models 10
- 1.2 Tumour Growth Models 13
  - 1.2.1 Avascular Tumour Models 13
  - 1.2.2 Angiogenesis and Vascular Tumour Models 15
  - 1.2.3 Metastasis Models 21
- 1.3 Tumour Growth and the Immune System 22
- 1.4 Glioma Models 25
- 1.5 Modelling Local Drug Delivery to Brain Tumours 32
- 1.6 Homogenisation Theory 34

2 MODELLING DRUG DIFFUSION THROUGH PLGA/PEG POLYMER CONSTRUCTS 36
- 2.1 Background 36
- 2.2 In Vitro Experiments 38
  - 2.2.1 PLGA/PEG Particle Preparation 42
  - 2.2.2 Experiment 1 - Theophylline Release from PLGA/PEG 42
  - 2.2.3 Experiment 2 - Theophylline Diffusion through PLGA/PEG 45
  - 2.2.4 Experiment 3 - Theophylline Entering PLGA/PEG 48
  - 2.2.5 Accounting for Other Effects 49
- 2.3 Two-Domain Mathematical Model for Experiment 1 53
  - 2.3.1 Numerical Scheme for the Two-Domain Model 55
  - 2.3.2 Two-Domain Model Input Values Derived from *In Vitro* Data 61
- 2.4 Two-Domain Model Fitting to Experiment 1 62
- 2.5 Three-Domain Mathematical Model for Experiment 2 65
  - 2.5.1 Numerical Scheme for Three-Domain Model 69
  - 2.5.2 Three-Domain Model Input Values Derived from *in vitro* Data 71
- 2.6 Three-Domain Model Fitting to Experiment 2 71

2.7 Three-Domain Mathematical Model for Experiment 3 75
2.8 Model Validation Through Experiment 3 76
2.9 Results and Discussion 77
2.10 Future Work 79
3 HOMOGENISATION OF DIFFUSION APPLIED TO PLGA/PEG POLYMER CONSTRUCTS 81
3.1 Background 81
3.2 Theory 82
3.2.1 Assumptions 83
3.2.2 Homogenisation in One Spatial Dimension 83
3.2.3 Homogenisation in N Spatial Dimensions 85
3.3 Solving Numerically 87
3.3.1 Numerical Scheme 87
3.3.2 From Periodic Boundary Conditions to Zero Dirichlet and Zero Neumann 92
3.3.3 Solving in Parallel 97
3.4 Data Collection and Preparation 99
3.5 Parameter Values 102
3.6 Statistical Methods 103
3.7 Results 104
3.7.1 Results of Preliminary MicroCT Data 104
3.7.2 Results of MicroCT Replicates 106
3.8 Discussion and Future Work 111
4 A MATHEMATICAL MODEL FOR BRAIN TUMOUR GROWTH APPLIED TO VASCULAR ISCHEMIA 114
4.1 Introduction 114
4.2 Alterations to the PIHNA Model 117
4.2.1 Original Vascular Efficiency 119
4.2.2 Nutrient-Based Vascular Efficiency 120
4.3 The PIHNA Model in One Spatial Dimension 123
4.3.1 Comparing Vascular Efficiencies 125
4.3.2 Travelling Wave Analysis 132
4.3.3 Wavespeed Verification 135
4.4 The PIHNA Model in Two Spatial Dimensions 139
4.4.1 Individual tumour kinetics affect recurrence location following perioperative ischemia 144

4.4.2 Faster Hypoxic Diffusion Rates Promote Distant Recurrence 145
4.5 Discussion and Future Work 147
5 CONCLUSION 150
Appendices 152
A MODELLING DRUG DIFFUSION THROUGH PLGA/PEG POLYMER CONSTRUCTS 153
A.1 PLGA/PEG Swelling Mass Data 153
B HOMOGENISATION OF DIFFUSION APPLIED TO PLGA/PEG POLYMER CONSTRUCTS 155
B.1 Sample Cubes for Replicates 155
B.2 Wilcoxon Signed Rank Test Significance Values 155
B.3 Kolmogorov-Smirnov Test Significance Values 155
C A MATHEMATICAL MODEL FOR BRAIN TUMOUR GROWTH APPLIED TO VASCULAR ISCHEMIA 159
C.1 PIHNA Non-Dimensionalisation 159
C.2 PIHNA 2D Numerical Scheme 160

1

INTRODUCTION AND LITERATURE REVIEW

Cancer is one of the leading causes of death in England and Wales and it is predicted that anyone born after 1960 has a 50% chance of developing cancer in their lifetime [1, 45]. The need for novel therapies and treatment delivery techniques is as great as ever to counter the increasing longevity of the average person. Unfortunately, this is not a simple task; not only are many cancers able to spread throughout the body so are hard to target, they can also be present in clinically undetectable densities. Even when tumours are easy to access, a treatment will sometimes only destroy or remove a subset of cancer cells at its most effective. The term cancer encompasses many diseases of uncontrolled growth of abnormal cells. With all these factors in mind, it is no surprise that cancer is yet to be cured despite many years of high quality research. The research in this thesis focuses on the brain tumour Glioblastoma Multiforme (GBM), a grade IV glioma. The median life expectancy of a GBM patient is only 15 months following diagnosis despite a combination of resection, chemotherapy and radiation therapy as a standard of care for this disease [132, 133]. At the Children's Brain Tumour Research Centre (CBTRC), a novel local drug delivery system is being developed to treat GBM and will be evaluated here through a combination of *in silico* and *in vitro* experiments (Chapters 2 and 3). We then model GBM spread with the Proliferation Invasion Hypoxia Necrosis Angiogenesis model, and apply it to investigate how GBM recurrence patterns are affected by ischemia following resection (Chapter 4).

In this chapter, the history and development of cancer models will be introduced, including statistical, analytical and computational models. We roughly categorise the tumour models into avascular tumour models, vascular tumour models, metastasis models, and tumour interactions with the immune system. We will then focus on some literature pertaining to the research of this thesis, namely mathematical models of brain tumours, examples of local drug delivery modelling and homogenisation of diffusion theory.

A cancer is defined as a disease caused by an uncontrolled division of abnormal cells in a part of the body. As this definition is so broad, it acts as an umbrella term for many diseases and fails to describe the high level of complex interactions that occur within each type of cancer. To eliminate cancer, we must fully understand how it develops and continues to grow while outsmarting the body's natural defences against it. A widely used checklist of characteristics for cancer was defined and subsequently updated by Hanahan and Weinberg [56, 57]. They originally gave six hallmarks of cancer: evading growth suppressors; enabling replicative immortality; activating invasion and metastasis; inducing angiogenesis; resisting cell death; and sustaining proliferative signalling [56]. Since then, they have extended these hallmarks with two more: deregulating cellular energetics and avoiding immune destruction [57]. They have also introduced two enabling characteristics for tumours: genome instability and mutation, and tumour-promoting inflammation. It is often one or more of the hallmarks that are targeted during tumour treatment. For example, the drug bevacizumab inhibits angiogenesis [64], cytotoxic chemotherapy drugs aim to stop replication of tumour cells [112], vaccine therapies aim to facilitate the immune system to kill the tumour cells [34] and migrastatics aim to stop invasion and metastasis [46].

In the majority of cases, a tumour has four broad stages of growth: avascular growth, angiogenesis, vascular growth and metastasis. Often, once a cell has become cancerous, it divides into a small bundle of cancerous cells that have access to ample nutrients through simple molecular diffusion and their population can grow exponentially. As the nutrients move through the bundle of cells, they are metabolised and their concentrations decrease; this means that once the avascular tumour has reached a critical size, the concentration of nutrients in the centre of the tumour is too low to sustain the cells, which can lead to necrosis. In order to keep growing, the tumour enters its angiogenic phase; it releases angiogenic growth factors such as vascular endothelial growth factor. Once such a growth factor is released, it diffuses into the surrounding tissue and can come into contact with endothelial cells (ECs); these surround blood vessels. The ECs respond by degrading the basement membrane surrounding the parent blood vessel, sprouting new blood vessels, proliferating and directionally migrating chemotactically towards the source of the angiogenic growth factor. Once a tumour is vascularised, its growth is no longer limited by nutrient availability and its cells can use the blood stream to transport themselves to a secondary focus in the body where they

can divide into a secondary tumour – a process known as metastasis. For these reasons, angiogenesis is seen as a key therapeutic target. Due to the distinct mechanics of the tumour at different stages of its growth, mathematical models of tumour growth can be roughly categorised into three groups: avascular models (Section 1.2.1), angiogenesis and vascular models (Section 1.2.2) and metastasis models (Section 1.2.3). However, there are also models that only consider established tumours that do not directly model vasculature or access to nutrients. For example, there are models that look into the dynamics between tumours and the immune system; these will be discussed in Section 1.3. Some of the earliest mathematical modelling of cancer was statistical work on cancer death incidence. Such work aims to recreate population-level cancer incidence rates based on previous cancer victim data and carcinogenesis theory; this will be discussed first.

1.1 STATISTICAL MODELS

One of the first statistical models of cancer was created by Armitage and Doll in 1954 [8]. They aimed to fit a function to data regarding the number of cancer incidences across different cancers and age ranges. Following the proposition by Nordling that cancer is the result of seven mutations and that the incidence rate occurs to the sixth power of time [102], Armitage and Doll proposed that if each mutation occurs with probability per unit time p_i, $i = 1 \dots 7$, then the incidence rate r is given by

$$r = k p_1 p_2 p_3 p_4 p_5 p_6 p_7 t^6, \tag{1}$$

where k is a dimensionless constant and t is time (or more specifically, age). Naturally, Equation (1) leads to

$$\log r = 6 \log t + \log k p_1 p_2 p_3 p_4 p_5 p_6 p_7,$$

from which it is clear that, according to this model, the logarithm of the incidence rate of cancer should be directly proportional to the logarithm of the age and should increase six times as quickly. After comparing their model to population data, they found that it was in line with some cancers but not others. The model was reasonably accurate in predicting the incidence rate for cancers of the stomach, oesophagus, pancreas, colon and rectum however, it was not as good at predicting cancers of the lungs, bladder, prostate, ovary or breast. The cause of the second set of cancers is attributed to lifestyle choices

that exposed the cancer patients to carcinogens at unique times; this does not follow the assumption of the model that each mutation was random and equally likely to occur at any one time point, and was used as the reasoning for the unconvincing fit to the data.

Armitage and Doll later showed that similar results could be obtained with a two-step model for cancerous cells [9]. However, this model shows a better fit for the cancers that they previously attributed to lifestyle choices. They followed the suggestion by Platt [113] that exposure to a carcinogen could create a subpopulation with a selective advantage over the normal cells; this new population will grow exponentially with rate k (that has dimensions of 1/time and captures the advantage gained by the subpopulation) and will be proportional to the dose of the carcinogen d_1. This faster growing population could then be subjected to a second discrete dose d_2 that leads to cancer. Under these assumptions, the incidence rate for this model is given by

$$r = \alpha d_1 d_2 e^{kt}$$

where α is a constant of proportionality. However, these two discrete events do not have to be environmental, at least one of them can be a predisposed genetic mutation.

This line of thought was followed in another statistical analysis of cancer patients carried out by Alfred and Knudson in 1971 [4]. They examined 48 cases of retinoblastomas and agreed with Armitage and Doll's view that the cancer, for retinoblastomas at least, was caused by two mutational events. They split the retinoblastoma cases into the inherited, where there is one germinal mutation[1] and one seminal mutation[2], and nonhereditary cases, where both mutations leading to retinoblastomas are seminal. Although someone with an inherited germinal mutation is predisposed to retinoblastomas, they will only be affected if they have a seminal mutation at some stage. If this seminal mutation does not occur, that person is known as an unaffected carrier. Those that have one or more retinoblastoma(s) can be divided into unilateral and bilateral depending on if the retinoblastoma(s) are in one or both eyes, respectively. There are therefore 4 subclasses: unilateral hereditary retinoblastoma, bilateral hereditary retinoblastoma, unilateral non-hereditary retinoblastoma and bilateral non-hereditary retinoblastoma. However, the chance of someone

1 A germinal mutation is an inherited mutation in the DNA that is passed to offspring as well as the progeny of all cells.

2 A seminal mutation occurs in a cell and is inherited by its progeny, but does not pass on to offspring.

having two seminal mutations in both eyes is very small, and consequently bilateral non-inherited retinoblastomas did not appear in their dataset of only 48 patients. After taking into account literature on percentages of each of these subclasses, they postulated and in turn found that the number of hereditary tumours per person could be well described by a Poisson distribution. Moreover, they show that the data for unilateral and bilateral cases is best described by a Poisson distribution with $m = 3$, and that the most commonly occurring number of tumours per patient is also 3. In this paper, they calculate reasonable estimates for both germinal mutation rates and the seminal mutation rate. They therefore provided mathematical evidence that with just two mutational events, retinoblastoma could be caused at the incidence rates seen in the population.

Dewanji *et al.* implemented a mathematical model of incidence and size of colorectal adenomas to influence the screening process of this cancer using similar poisson distribution processes to that of Knudson [39].

In 2015, Tomasetti and Vogelstein linked lifetime cancer risk within each tissue to the normal total divisions of self-renewing cells involved in the maintenance of that tissue's homeostasis [145]. They noted a 0.81 Pearson's correlation coefficient for a linear regression fit between the lifetime risk of each cancer type and the total number of cell divisions of stem cells in the corresponding tissue, alongside a coefficient of determination of 0.646. Their work suggests that DNA replication is the major factor in cancer genesis. Along with this correlation, they defined an Extra Risk Score (ERS) as

$$\text{ERS} = \log_{10}(\text{Incidence Rate}) \times \log_{10}(\text{Total Stem Cell Divisions}). \qquad (2)$$

They then used a k-means clustering algorithm with 2 clusters on the collection of ERS scores, and noted that this clustered the cancers into those known to be caused by environmental factors and/or hereditary mutations, and those caused by random mutations. This was noteworthy as the ERS score, which does not directly take into account whether a tumour is caused by random mutations or not, was the only input into the k-means algorithm.

For a review of mathematical modelling of somatic mutations, including the heterogeneous somatic evolution within individual tumours, see [11].

1.2 TUMOUR GROWTH MODELS

1.2.1 *Avascular Tumour Models*

Some of the earliest models of tumour growth consider only the avascular growth stage. Modelling the complex dynamics of this early growth stage then acted as a foundation to include even more complexity through the tumour interactions with vasculature (Section 1.2.2). These early models for avascular tumour growth tend to model the tumour with radial symmetry and the radial growth of the tumour is assumed to only depend on one nutrient (usually oxygen). As is suggested by Byrne in a review article [22], this type of modelling could have appealed to the pioneering mathematicians due to the tumour's shared characteristics (under the aforementioned assumptions) with other physical systems. One such system is the expansion of metal when heated; models already existed for this and could be transferred to tumour growth.

In 1955, Thomlinson and Gray modelled avascular tumours composed of stratified squamous epithelium as cylinders due to the observation that these tumors tend to grow as rods [144].

Thomlinson and Gray used their model to determine oxygen gradients within human lung cancer tumours; these gradients were important to quantify due to their effect on radiotherapy, anoxic regions were known to be less effected by radiotherapy. Histological slices of tumour tissue revealed necrotic cores of tissue in the centre of the tumour mass, and their sizes were quantified in this study to validate the oxygen consumption rates used in the model.

Early tumour growth models used exponential growth to explain tumour growth rates. However, it was observed by Steel that this did not always fit well to data [130]. Tumours only grow exponentially when they are not limited by a resource.

In 1964, Laird used experimental data on mice, rat and rabbit tumour cell populations to show that tumour growth limited by nutrient supply would follow a Gompertzian growth function more closely than an exponential function [76]. These functions follow the form

$$W(t) = W_0 e^{\frac{A}{\alpha}(1-e^{-\alpha t})}, \tag{3}$$

which for small times reduce to an exponential expression at first order. For large times, this expression has an asymptote at

$$W(t) = W_0 e^{\frac{A}{\alpha}}, \tag{4}$$

which can be considered a carrying capacity of the model and does not occur for the exponential growth case.

Greenspan (1972) modelled the diffusion-limited growth of spherical tumours [52]. Greenspan expanded on the work of Thomlinson and Gray by including a concentration of chemical produced by the tumour that inhibits proliferation of tumour cells. This paper looked at the varying model dynamics that would occur if this chemical was produced as a waste product of living cells or through necrosis and described simple experimental data that could provide evidence to support either case.

Greenspan also extended his work to look at the effect of asymmetric perturbations on the spherical shape of the tumour [53]. This model analytically considered a proliferating layer of cells on the surface of the tumour with a necrotic core where the birth and death of the cells caused a pressure gradient; this gradient led to the movement of the cellular material. In this work, Greenspan modelled surface tension and showed that the tumor could change shape or even pinch off into multiple tumors, depending on the tumour growth and necrotic debris elimination rates. Even though the assumption of radial symmetry was still present, this paper shows that thought was being put towards the stability of the tumour's shape. Many treatments used Greenspan's model as a base to include more dynamics in-line with experimental data [35, 93, 94].

In 1985, Krug and Taubert applied the logistic growth model to experimental mouse model tumour population values and shown to provide a good fit over time [71]. The logistic growth solution is given by

$$W(t) = \frac{K}{1 + \frac{K - W_0}{W_0} e^{-rKt}}, \tag{5}$$

where now K is the carrying capacity of the model. This has been widely used since in tumour growth models.

Another avascular tumour model worth noting is that of Ward and King [150, 151], they modelled both living and dead cells of a spherically symmetric tumour with a background of generic nutrient, and tracked the radial growth over time. They showed that for later times, the tumour growth rate was constant and they found this travelling wave speed analytically under certain

conditions; they then showed that this had good agreement with numerical simulations.

Cristini *et al.*'s nonlinear boundary-integral model of avascular carcinoma growth suggested that a tumour would exhibit invasive fingering if it had limited access to nutrients, but would always stay compact if it had an ample supply through sufficient vasculature [31]. This was further backed up by Gerlee and Anderson in a different mathematical setting [47]. They used neural networks alongside a cellular automaton to describe the tumour evolution during the avascular stage of growth. Each individual cell behaviour was modelled as a response to environmental variables of glucose, oxygen and hydrogen ion concentrations as well as the number of neighbours the cell has. They found that the simulated background oxygen concentration was a key factor in the growth dynamics of the simulated tumours as a whole. Low oxygen led to a fingering growth pattern, with high oxygen leading to a homogeneous leading edge. This model simulated the avascular tumour growth stage. As oxygen is depleted by the outer cells, the central tumour cells become hypoxic and necrotic as they do not have access to sufficient nutrients. This work was extended upon by Jeon *et al.*, who modelled cellular invasion on an off-lattice model [65].

1.2.2 *Angiogenesis and Vascular Tumour Models*

Vascular tumours are more difficult to study biologically than avascular tumours. Even *in vitro*, a vasculature network that is comparable to *in vivo* dynamics is hard to create. As well as complying with the ethics associated with tumour initiation and sacrificing of animals for *in vivo* experiments, the tumours are less accessible and the growth dynamics are less reproducible than the simpler avascular tumours. Due to these difficulties in data collection and the lack of early transferable research in other mathematical fields, vascular tumour modelling did not begin until much later.

In 1985 the seminal paper by Balding and McElwain laid the foundations for work on tumour-induced angiogenesis [10]. They modelled the diffusion of an angiogenic growth factor as well as the formation and movement of sprouts from existing vessels as a chemotactic response to the presence of angiogenic growth factor. Interestingly, they noted that the process of angiogenesis is analogous to fungal growth, and made use of a model by Edelstein on the subject [40]. Balding and McElwain created this model to describe

experiments within which tumour cells were implanted into mouse and rabbit corneas *in vivo*. These cells then encouraged new blood vessels to grow from the limbus to the tumour. This model was based on experimental *in vivo* mouse data from Muthukkaruppan *et al*, that implanted tumour fragments into mice cornea and imaged the vasculature that grew towards them [97].

Balding and McElwain assumed the capillary density $\rho(x,t)$ (with units of capillary length per unit area) can only increase by the movement of capillary tips, so that

$$\frac{\partial \rho}{\partial t} = -nv - d,$$

where $n(x,t)$ is the tip density, $v(x,t) < 0$ is the tip velocity and $d(\rho) = \gamma\rho$ is the death rate of capillaries. Following Edelstein [40], they assumed that

$$\frac{\partial n}{\partial t} = -\frac{\partial (nv)}{\partial x} + \sigma, \tag{6}$$

where σ is the net rate of tip creation. They also used a chemotaxis term in the equation for the flux of the cells.

After adding terms for tip creation and tip to branch anastomosis to Equation (6), they were left with the following:

$$\frac{\partial \rho}{\partial t} = -nv - \gamma\rho \tag{7}$$

$$\frac{\partial n}{\partial t} = -\frac{\partial (nv)}{\partial x} + \alpha c\rho - \beta n\rho \tag{8}$$

$$c(x,t) = \frac{2}{\sqrt{\pi}} \int_{x/\sqrt{t}}^{\infty} e^{-s^2}\, ds \tag{9}$$

$$v(x,t) = -\frac{\chi}{\sqrt{\pi t}} e^{-x^2/t}, \tag{10}$$

where the expression for chemoattractant (c) is found by solving the diffusion equation on a semi-infinite domain assuming that initially there is no angiogenic growth factor outside the tumour and there is a fixed concentration at the tumour's edge. Balding and McElwain chose parameters that led to similar model behaviour to that observed experimentally. The model can produce a wave front of vascular activity that was described by experimentalists, be altered for varying response strengths and adjusted to reproduce experimentally observed vessel lengths and tip speeds.

Of course, this angiogenic model has its limitations. As this model is continuous, there is no scope to give a detailed description at a microscopic level. Furthermore, there is no distinction between the different types of blood vessels and their morphology is ignored, only the concentration differences are

modelled. Therefore, with this system, the difference between one large vessel and many smaller vessels is indistinguishable.

Later research has avoided some of the limitations of the work by Balding and McElwain by using reaction-diffusion equations for nutrients coupled with a cellular automaton that better captures the morphology; these are known as hybrid models. For example, Stokes and Lauffenburger coupled a probabilistic equation for endothelial cell movement with a deterministic equation for the diffusion of angiogenic growth factor [131]. They produced various two-dimensional predictions of sprouting from a parent vessel in response to differing chemotactic response levels. Their model predicted a positive correlation between chemotactic response levels and the level of directional growth; this agreed with *in vivo* experiments. They also predicted that a relatively large amount of random motion is necessary for vessel loops and anastamosis to occur[3].

Anderson and Chaplain proposed a model for angiogenesis [7], their work added a haptotaxis term that allowed modelling of the interaction between ECs and extracellular matrix (ECM) macromolecules. In this work, Anderson and Chaplain proposed both a continuous and a discrete model for angiogenesis, and stressed the different benefits of each. The continuum model was good at capturing large-scale features and the discrete model, which was based on the continuum model, was better at recreating smaller-scale features such as capillary sprout branching. The results gained in this model agreed with the results of Stokes and Lauffenburger [131], as well as an earlier model proposed by Chaplain and Stuart [26], that a sufficient chemotactic response was necessary to initiate the capillary network to deform and grow towards the source of angiogenic growth factor. However, rather than only having growth towards the source of the angiogenic growth factor, the haptotaxis term in the continuous model gave rise to local growth factor gradients around the areas of high endothelial cell density that led to lateral growth in the model.

Hahnfeldt *et al*. modelled the effects of the angiogenic inhibitors endostatin, angiostatin and TNP-470 on tumour growth [55]. This work was carried out both *in vivo* and *in silico*. Mice were given Lewis lung carcinoma cells and the tumour dimensions were measured. After a period of growth, two groups of mice were injected with either angiostatin or endostatin daily and a third

3 Vessel loops and anastamosis are important during angiogenesis, as they enable flow through the new vasculature.

group with TNP-470 every other day. The effects of these drugs on tumour growth were then recorded.

The mathematical model proposed by Hahnfeldt *et al.* adds a time-dependent carrying capacity for the tumour as a reflection of the maximum tumour size that the vasculature can support. The carrying capacity is controlled by the balance of pro-angiogenic and anti-angiogenic factors that come from the tumour and administered inhibitors from the drug. Unlike other models, the treatment is not added explicitly into the equation. For tumour mass $V(t)$ with carrying capacity $K(t)$ and tumour growth rate λ_1, the growth rate is given by a Gompertzian form

$$\frac{dV}{dt} = -\lambda_1 V \log\left(\frac{V}{K}\right). \tag{11}$$

The carrying capacity is given by

$$\frac{dK}{dt} = -\lambda_2 K + bV - dKV^{2/3} - eKg(t), \tag{12}$$

where the first term is the spontaneous loss of functional vasculature, the second and third terms correspond to the tumour's capacity to promote and inhibit vasculature respectively and the last is the inhibition of vasculature due to treatment. The terms corresponding to the tumour's influence on its own vasculature were derived from the following clinical observation. Sometimes primary tumours were seen to release enough inhibiting agents that they would cause tumours at a secondary focus to die (if they were nearby), but the primary tumour would continue to grow [114]. It was later found that the inhibiting agents were released and spread throughout the whole tumour whereas promoting agents could only be found near their source – suggesting they had a much shorter half-life [104]. To ascertain the effect of this difference and the appropriate orders of magnitude for the second and third terms in Equation (12), Hahnfeldt *et al.* solved a diffusion-consumption partial differential equation.

A quick analysis of the system (V, K) given by (11) and (12) leads to the trivial fixed point $(0, 0)$ and the non-trivial fixed point that still depends on time through the term $g(t)$

$$\left(\left(\frac{b - \lambda_2 - eg(t)}{d}\right)^{3/2}, \left(\frac{b - \lambda_2 - eg(t)}{d}\right)^{3/2}\right).$$

Once their model was parametrised, Hahnfeldt *et al.* noted that it drew attention to a principle of tumour growth; the tendency of a tumour in some

cases to reach a plateau in its growth. Under enough treatment, the vascularised tumour could reach a balance between the anti-angiogenic agents and the angiogenic agents. This limits the vascular support available to the tumour and would in turn create a limiting factor to tumour growth. The aim of the anti-angiogenic treatment would be to reduce the asymptotic plateau point of tumour growth to a clinically manageable level. Both TNP-470 and Angiostatin treatments showed evidence of this plateau, which importantly was irrespective of the initial size of the tumour.

McDougall, Anderson, Chaplain and Sherratt extended the previous work of Anderson and Chaplain [7] to study the fluid flow through the pre-existing vasculature [91]. They adapted modelling tools from the field of petroleum engineering to study the rate of flow through the network, the amount of fluid in the network at a given time and the amount of fluid that reaches the tumour. This model was then applied to see how much of a chemotherapy drug would reach a tumour. Their results emphasised the important role that the tumour's morphology plays in the delivery of both anti-angiogenic and chemotherapeutic drugs. Following this work, there have been a variety of extensions in this field [152, 86, 92]. A model, named the Dynamic Adaptive Tumour-Induced Angiogenesis (DATIA) model, was developed; rather than studying effects through a pre-existing vasculature, this model incorporated fluid flow during the growth of new vasculature, and included shear-induced capillary branching [92]. Another paper compared *in silico* and *in vivo* results of retinal vasculature development in mice, to gain a mechanistic understanding of this process [152]. This paper found the pruning of capillaries was an important mechanism that allowed vasculature to provide oxygen more efficiently throughout the network. Capillary pruning led to an increase in blood flow through vessels that would otherwise be poorly supplied; these vessels were then more likely to expand and receive a better bloody supply, to in turn provide more oxygen.

Multi-scale models are used to model dynamics of many factors in spatio-temporal tumour growth on differing scales of time and length. For a good summary of such multi-scale models, see [36]. An example of such work was carried out by Owen *et al*. [105], (based on a multi-scale model framework also used in [2, 3]). They modelled four different layers, each representing a different scale:

- The subcellular level: as the name suggests, this is where the activity within both normal and cancerous cells occurs. Such as the proteins that regulate the cell's cycle and VEGF production.
- The cellular level: this is the layer where the cell-cell dynamics are captured for both normal and cancerous cells.
- Diffusible species: this is the layer where extracellular oxygen and VEGF are modelled.
- Vascular layer: the layer within which angiogenesis is modelled as well as other key processes such as blood flow, nutrient source terms, drug delivery and the loss of vessels (vessel pruning).

These four layers are coupled with each other in a variety of ways. Due to the higher level of detail captured in these models when compared with previous hybrid models of angiogenesis, they are much more computationally intensive. These models tend to have a lot of parameters which cannot easily be calibrated and a lattice assumption is not geometrically realistic. To avoid this, there are also off-lattice models that can give rise to more geometrically-realistic vascular networks [111].

Shirinifard *et al.* used the open-source cellular automata CompuCell3D ([142]) to compute the process of angiogenesis and its effect on tumour growth [123]. The timescale of such simulations allowed for various morphologies to form throughout the avascular growth phases. Unlike many of the models considered in Section 1.2.1, they included pre-existing vasculature in the early growth phase of the tumours. Once the tumour is too large to be supported through the nutrients available from the pre-existing vasculature, the tumour encourages vessels to grow towards it through angiogenesis. As expected, the Shirinifard *et al.*'s simulations showed that angiogenesis provides more nutrients to the tumour and allow for further tumour growth.

A multi-scale model proposed by Macklin *et al.* included ECM degradation by matrix degrading proteolytic enzymes in a tumour invasion model along with the DATIA model of tumour-induced angiogenesis [85]. By breaking down the ECM, these enzymes provide room for further tumour growth and aid in the attachment of cancerous cells to ECM macromolecules. Macklin *et al.* showed *in silico* that if there is enough ECM degradation, the tumour is protected by a halo of growth space that inhibits efficient angiogenic growth. Instead of penetrating the tumour, the vasculature will instead encompass it.

1.2.3 *Metastasis Models*

Metastasis is the process of secondary tumours developing away from the primary cancer site. This often occurs through the transport of tumour cells from the primary tumour mass to other sites in the body via blood or lymph vessels. One of the earliest mathematical models of metastasis is from Saidel *et al*. This group created an ODE birth-death model consisting of the following: tumour cell count in the tumour, tumour surface area, invading tumour cells on the inner vessel surface, arrested tumour cells in the pulmonary vessels, and pulmonary metastatic foci [118]. Each of these quantities represents a different stage of metastasis. This model was calibrated with experimental data on fibrosarcoma metastasis and then used to look at the effects of trauma, amputation, lung damage, inhibition of vascularisation, and inhibition of tumour cell penetration of vessels on the metastatic dynamics, which had good agreement against experimental data.

Shortly following this work was a stochastic model of metastasis from the same research group [80]. Through a two-dimensional Markov process[4], they introduced a probabilistic element into the modelling of metastasis. They model the temporal probability of having no metastatic foci as well as the probability of metastasis occurring, which depends on the clump size of the cells that have entered pulmonary vessels. The experimental data used is from a fibrosarcoma mouse model within which mice are given a tumour in a femoral muscle region. Metastatic foci are classed as the number of macroscopically visible foci in the excised lungs of the mice. However, it is estimated that it takes six days for a metastasis to become visible macroscopically, so the true number of metastases could be higher than seen visually. To make sure all metastases were macroscopically visible at the time of sacrifice, the tumour-bearing limbs of the mice were amputated twelve days beforehand.

Markov modelling of metastases has since continued to be used. More recently, a paper by Newton *et al*. has used Markov chain modelling to simulate disease progression pathways and their corresponding timescales when starting in the lung [100]. They include 50 potential metastatic sites of the body in their model and autopsy data from nearly 4000 patients to train the

4 Markov processes are random processes in which the future is independent of the past. Each state has a probability distribution of moving to other states (including itself). The collection of these probabilities across all states in the model is stored in a matrix known as the transition matrix.

transition matrix of the model. The probability of moving between each two states in the transition matrix was not predefined, instead they let the model fit the autopsy data. The probabilities that came from this fitting suggested which metastatic sites have a higher probability of being a zero-order site (that seeds to itself), a first-order site (that is directly reached by a metastasis) or a second-order site (a site that is reached through multiple metastatic steps).

Scott *et al.* created a model to determine the likely mechanism of self-seeding, a process where a tumour sheds cells into the vasculature which later return and promote further growth in the primary tumour [122]. Their model consisted of logistically growing tumours at primary and secondary sites that stochastically shed tumour cells into the vasculature. Two mechanisms of self-seeding were tested: the tumour cells shed from the primary tumour, enter the vasculature, and return to the primary site; or the tumour cells leave the vasculature to a secondary site, where they populate, shed, and some return to the primary site. The authors found regions in parameter space that promoted primary tumour growth (through the creation of more loci), and compared these with estimated return probabilities for the two mechanisms along with Fermi estimates[5]. The model suggested that the only possible mechanism for self-seeding that promoted growth in the primary site is through the intermediary second site, rather than directly through circulating tumour cells in the vasculature.

1.3 TUMOUR GROWTH AND THE IMMUNE SYSTEM

For a cancer to grow successfully, it needs to evade or overcome the immune system. However, as the cancer cells are mutated host cells, sometimes the immune system does not recognise the cancer as foreign. The immune system does have the potential to stop a cancer from spreading and there are various mechanisms to prevent, repair or eliminate cells with mutations, as well as immunotherapies that aim to encourage the immune system to attack cancerous cells.

Early immune-tumour mathematical models used ODE approaches to model cancer and the immune system [38, 73, 72]. A seminal paper by

5 Named after Enrico Fermi, who estimated the energy of a nuclear blast within an order of magnitude after dropping pieces of paper during the shockwave. This refers to estimating something through best guesses of its constituent components multiplied together and tracking the overall error.

Kirschner and Panetta modelled the immune-tumour interactions alongside immunotherapy [69]. They found a stable limit cycle between the antigenicity[6] of a tumour and the tumour itself. The authors suggested this stable limit cycle could be an explanation for tumour recurrence, which occurred on long timescales for tumours with low antigenicity. When including immunotherapy, they found a tumour-free state could be achieved if the therapy was applied early enough and in a sufficient dose.

Owen and Sherratt spatially modelled the dynamics between macrophages and an avascular tumour [107]. They showed spatial inhomogeneities were produced by the macrophage's ability to selectively kill tumour cells. However, the macrophages were not able to stop the tumour progression. Owen *et al.* modelled macrophages that could deliver drugs to hypoxic cell regions [106] through an extension of the aforementioned model from Ward and King [150, 151]. Owen *et al.* found that the presence of engineered macrophages, that chemotactically moved to hypoxic regions through a chemoattractant produced by cells experiencing hypoxia, could displace the tumour cells from hypoxia towards the outside of the spheroid, and in turn make them more vulnerable to other therapies that target highly proliferative cells, such as chemotherapy.

Work by Matzavinos, Chaplain and Kuznetsov modelled the dynamics between tumour-infiltrating cytotoxic lymphocytes and small tumours that are yet to become vascularised [90]. Such tumours were considered to be in an equilibrium with the immune system, and it is the dynamics of this equilibrium that the authors sought to understand. Four quantities were modelled spatially: tumour-infiltrating cytotoxic lymphocytes, tumour cells, complexes and chemokines, and a linear stability analysis was undertaken which showed a stable limit cycle exists between tumour-lymphocyte complexes, tumour cells, and tumour-infiltrating cytotoxic lymphocytes. The authors suggest that the model could suggest observed heterogeneities of cytotoxic lymphocytes in solid tumours and that understanding these dynamics could lead to more effective anti-cancer vaccinations.

It is proposed that there are certain abilities that a cell must express before it can evade the immune system; these are known as the immune hallmarks of cancer [24], and follow a similar idea to the landmark paper on the hallmarks of cancer by Hanahan and Weinberg [56]. There have been a number

6 Antigenicity in this context is the extent to which tumour cells present antigens that can be recognised by the immune system.

of papers that have modelled a tumour's interaction with the immune system with kinetic theory [12, 13, 14]. The models found in these papers do not explicitly model the vascularisation of the tumour or even its access to nutrients, but instead focus on how the tumour cells acquire their abilities that hinder the immune system and the competition with the immune system that the cancerous cells undergo.

One application of kinetic theory towards cancer and the immune system was carried out by Belloquid *et al.* [14]. The cells were split into eight different groups known as functional subsystems, each group corresponded to a type of cell or a cell showing a specific ability. Each functional subsystem has m different states. For state u_i,

$$0 = u_1 < u_2 < \ldots < u_{m-1} < u_m = 1.$$

It is assumed that as u_i increases for the cells in each functional subsystem, so does the expression of that cell's ability. The ability is captured by the discrete probability distribution function

$$f_{ij}(t), \quad i = 1, \ldots, 8, \quad j = 1, \ldots, m,$$

where the subscript ij corresponds to the functional subsystem i and particles in state u_j. The distribution function follows the ODE

$$\frac{df_{ij}(t)}{dt} = J_{ij}[f](t) = C_{ij}[f](t) + P_{ij}[f](t) - D_{ij}[f](t) - L_{ij}[f](t). \tag{13}$$

The net flux $J_{ij}[f](t)$ is split into

- $C_{ij}[f](t)$ – the net flux due to conservative interactions (also called local interactions) that only modify the microscopic activity of interacting cells, not the population size directly
- $P_{ij}[f](t)$ – the gain of particles from proliferation
- $D_{ij}[f](t)$ – the loss of particles due to destructive events
- $L_{ij}[f](t)$ – the relaxation of the immune system back to a healthy state, once it can no longer detect the cancer (as the cancer is not there, or it has become undetectable by the immune system).

Depending on the chosen parameter values in this model, for large times the cancer will either die out, reach a plateau in its growth, or continue to grow with no signs of slowing.

The kinetic theory approach is reasonably well-suited to model cancer's accumulation of characteristics to overcome the immune system. It seems like a similar approach could be undertaken to model the eight hallmarks of cancer given in the extension of Hanahan and Weinberg's hallmarks of cancer [57]. Although the kinetic theory model by Belloquid has a lot of parameters, identifying qualitative trends in such a model could be beneficial in highlighting important interactions or pathways for therapeutic targeting.

Clinical interest in immunotherapy has continued to grow as have mathematical models of such treatments. A comprehensive review of mathematical models of immune therapies, as well as in combination with chemotherapy, can be found by de Pillis, Eladdadi and Radunskaya [41].

1.4 GLIOMA MODELS

Gliomas derives its name from glial cells[7], that were originally thought to be the origin of this disease. Recent research has suggested that they could originate from glial progenitor cells or even neural stem cells [23]. Although they can metastasise, gliomas are less likely to do so when compared to other cancers; this is due to the blood brain barrier (BBB) which only small molecules can pass through [108, 109]. The most aggressive form of glioma is glioblastoma multiforme (GBM), that has a short median survival time when compared with many other types of cancer of only 15 months [132]. GBMs usually kill a patient from a combination of factors, including but not limited to: herniation in the brain caused by high pressure, systemic decline caused by the progressive degeneration of brain function, brain-stem tumour invasion, or radiation damage [127]. GBMs typically contain highly migratory cells, that spread out across the brain; this high level of cell motility limits the efficacy of surgical resection as not all of the tumour can be removed or even seen. Murray [96] proposed the following spatiotemporal model for tumour cell density:

$$\frac{\partial c}{\partial t} = \nabla \cdot (D \nabla c) + \rho c, \tag{14}$$

where $c(\mathbf{x}, t)$ is the tumour cell density at position $\mathbf{x}$ and time t, ρ is the net growth rate of cells and D is the net diffusion coefficient which models the random tumour cell movement over the whole population.

7 Glial cells are found in the peripheral nervous system, they provide support to neuronal cells, maintain homeostasis and create myelin.

Radial growth models similar to the avascular growth models discussed in Section 1.2.1 made use of Murray's proposal with diffusion and proliferation coefficients estimated from clinical data and observations [20, 146, 154]. Burgess *et al*. compared different combinations of proliferation and diffusion coefficients on the density and spread of gliomas [20]. Two proliferation coefficients were estimated from observed doubling times of tumour volumes; a rapidly proliferating tumour, $\rho = 0.012$/day and a slowly proliferating tumour, $\rho = 0.0012$/day. Burgess tracked the detectable tumour margin to find an average growth velocity, v (cm/day). Fisher's approximation for the minimum wavespeed of outward growth for large times for Equation (14),

$$D = \frac{v^2}{4\rho}, \tag{15}$$

was then used with the previously estimated proliferation coefficients to give $D = 0.0013\text{cm}^2/\text{day}$ for the high migration rate and $D = 0.00013\text{cm}^2/\text{day}$ for the slow migration rate. This approximation is only valid for large times where the assumed radial growth of the tumour is dominated by its linear approximation. Burgess *et al*. also tested Murray's reaction-diffusion equation (14) for tumours with all combinations of high and low D and ρ. Using only these two parameters, it was shown by Woodward that the model supports: that gliomas cannot be cured through resection alone due to their diffuse nature; maximal surgical resections are most beneficial to the patient's survival (under an assumptions that patient death occurs at a set tumour size); and that patient-specific measurement of diffusion and proliferation rates might better predict survival rates than histological analysis [154].

Murray's governing equation (Equation (14)) was extended by Swanson *et al*. [136] to take into account the different diffusivity between white and grey matter. They proposed a diffusion coefficient

$$D(\mathbf{x}) = \begin{cases} D_g & \text{if there is grey matter at position } \mathbf{x} \\ D_w & \text{if there is white matter at position } \mathbf{x}. \end{cases}$$

This, along with detailed 3D brain scans from the Brainweb database [28, 29, 74, 75], allowed Swanson *et al*. to create detailed simulations of tumour growth which could then be compared to MRI scans. The goal of such a model is to look past the MRI resolution and predict where the rest of the tumour might be; armed with this prediction, clinicians could be better informed when choosing future treatment plans. Swanson has coined this model the

Proliferation Invasion (PI) Model. Later, Swanson *et al.* added an extra term to account for chemotherapy [138]

$$\frac{\partial c}{\partial t} = \nabla \cdot (D(\mathbf{x})\nabla c) + \rho c - G(t)c.$$

Swanson's group also modelled surgical resection by setting the tumour density at the resection bed to zero at the time point of resection. From a modelling point of view, a tumour resection does not stop the tumour growth, only delays it. If there is already substantial growth in the model beyond the resection cavity at the time point of resection, the resection does not affect the growth dynamics at this leading edge. The benefit of resection to an *in silico* patient's survival is simply that the tumour takes time to re-establish itself to the assumed radial tumour size that causes death in that patient. It is widely accepted by neurosurgeons and mathematical oncologists alike that a maximal extent of resection is most beneficial for a patient's survival. The decrease in pressure due to tumour resection leads to a relaxation of the brain that partially reduces the size of the cavity and can decreases symptoms (see Figure 1), it is also important that neurological function is not lost as a result of surgery; the affect of treatment on quality of life is not taken into account in these models, but naturally is a serious consideration for clinicians.

By assuming the tumour densities that appear on different standard-of-care MR modalities, T1-weighted with Gadolinium contrast (T1Gd) and T2, Swanson can calibrate D and ρ in the PI model using two pre-treatment time points to determine the predicted growth of a patient-specific brain tumour. Neal and Swanson have looked at 3D anatomical and 1D spherical growth simulations [98]. To compute patient-specific D and ρ rates, linear radial growth is assumed for the volumetric spherical equivalent of an anatomical tumour. At each time point, the T1Gd and T2 volumes are computed through manual segmentation of the MRI slices and are then reduced to spheres, of which a radius is computed. The tumour velocity is calculated as the difference in these radii over time and used in Equation (15). The (T1Gd$-$T2) radial value from one time point is used against stored PI simulations to give a value for D/ρ. Together, these calculate the individual D and ρ for the patient. These radii are also computed from MRI slices during treatment. A metric used to evaluate treatment efficacy is known as the "Days Gained" metric. With the assumed linear radial growth, the simulated radius $r(t)$ is given by

$$r(t) = mt + r(t_{pre}) \tag{16}$$

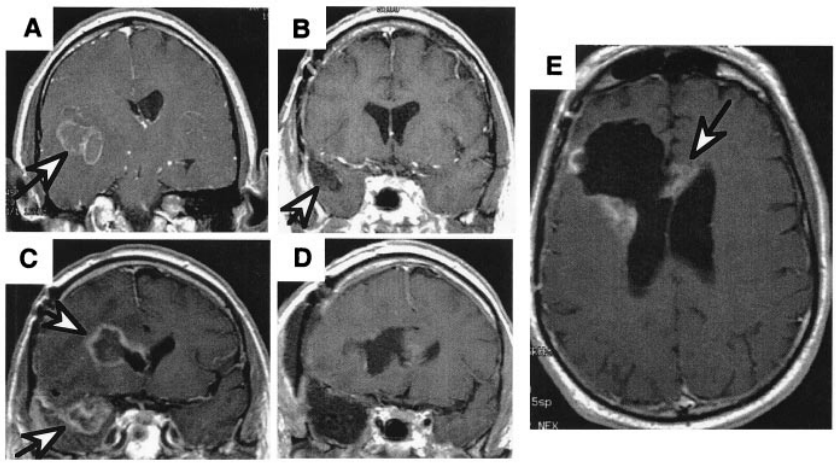


Figure 1: T1-weighted MRI scans with Gadolinium contrast to illustrate the spread of a GBM. (A) Presurgical scan with the GBM (arrow) surrounded by fluid. (B) Postsurgical scan showing resection, notice the change between the original tumour site and the resection site (arrow). (C) Six months later with tumour reoccurrence (arrows). (D) Another resection at the primary and secondary sites. (E) 3 months later showing re-occurence of the tumour at the edge of the second resection site. This figure is adapted from [62].

where $r(t_{pre})$ is the radial size of the tumour at the second pre-treatment scan, t is the time in days from the first pre-treatment scan and m is the gradient computed from the two different simulated radii at each of the pre-treatment scans. A simple rearrangement of Equation (16) at time t_0 gives

$$t_0 = \frac{r(t_0) - r(t_{pre})}{m}.$$

Now assume that t_0 is the time in Equation (16) at which $r(t_0) = r_{post}$, where r_{post} is the tumour radius after treatment. We can use this to find the time along the extrapolated linear growth line at which the radius was the same as it is after treatment (see Figure 2). This along with the fact that Days Gained is equivalent to $t_{post} - t_0$, gives

$$\text{Days Gained} = t_{post} - \frac{r_{post} - r(t_{pre})}{m}.$$

If used literally, this metric assumes that if the equivalent radius, calculated from the mass conservation of the anatomical tumour, is the same post-treatment as it was sometime before treatment then the tumour itself is equivalent – effectively resetting the tumour to a previous state. This would be a

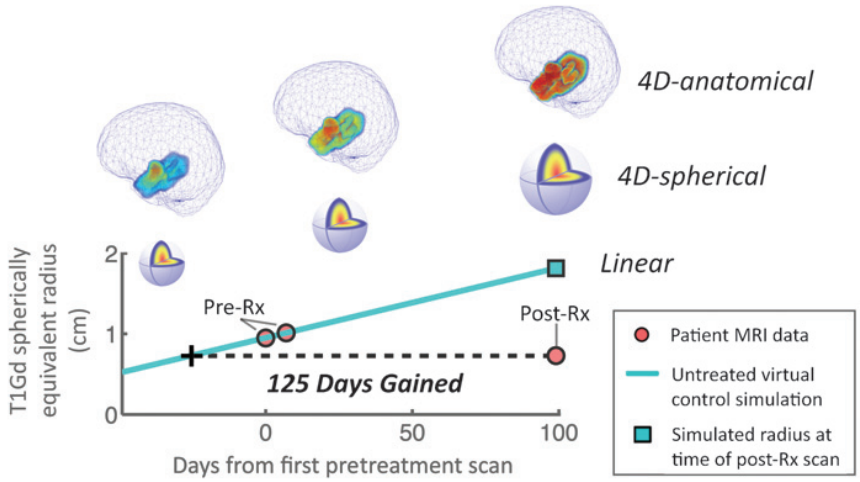


Figure 2: The assumed linear radial tumour growth is extrapolated as the untreated virtual control from the two imaging time points, and compared to the actual radial value with treatment from patient MRI data. The difference in time between the time of the patient MRI with treatment and the corresponding time point along the untreated virtual control line with the same radius is the "Days Gained" value. This figure is taken from [98].

dangerous assumption as the tumour could in fact be more aggressive, more resistant to therapy or have migrated further around the brain; these properties would make the tumour much harder to treat. In reality, this metric is used as a measure of treatment response, and not to say that a specific patient will survive for that number of days more than they would have without treatment. For this metric to be calculated, there needs to be at least two pretreatment scans for the patient, which does not always occur.

The Days Gained metric was also used to determine whether a tumour was undergoing pseudoprogression[8]. This process was carried out using Kaplan-Meier analyses to find a statistically significant Days Gained value that would retroactively discriminate between patients who had progressed or pseudoprogressed for both progression-free survival and overall survival times [98].

The PI model was specifically designed to be simple, with only two parameters that can be calibrated on a patient basis. A byproduct of this simplicity is that the model overlooks other mechanisms of the growth of a tumour.

8 Pseudoprogression occurs when a tumour appears larger or denser in post-treatment scans and can be misinterpreted as progression, which can diminish the apparent efficacy of the treatment regime. This can be due to tumour inflammation or an hypoxic microenvironment caused by treatment.

Extensions of the PI model have been created to capture other phenomena: the Proliferation Invasion Hypoxia Necrosis Angiogenesis (PIHNA) model [140] incorporates angiogenesis and its effects on tumour growth, PIHNA with Oedema (PIHNA-E) [59] goes one step further to include the oedema created by the presence of the tumour and the Proliferation Invasion Recruitment (PIR) model [89] ties in the ability of tumour cells to recruit otherwise healthy cells, through an increase in platelet derived growth factor.

PIHNA models five quantities of interest: normoxic cell density (c), hypoxic cell density (h), necrotic cell density (n), vascular cell density (v) and angiogenic factor concentration (a). The governing equations for the PIHNA model are given by the following five PDEs:

$$\overbrace{\frac{\partial c}{\partial t}}^{\substack{\text{Rate of change}\\ \text{of normoxic}\\ \text{cell density}}} = \overbrace{\nabla\cdot(D(1-T)\nabla c)}^{\substack{\text{Net diffusion of}\\ \text{normoxic}\\ \text{glioma cells}}} + \overbrace{\rho c(1-T)}^{\substack{\text{Net proliferation}\\ \text{of normoxic}\\ \text{glioma cells}}} + \overbrace{\gamma h V}^{\substack{\text{Conversion}\\ \text{of hypoxic}\\ \text{to normoxic}}} - \overbrace{\beta c(1-V)}^{\substack{\text{Conversion}\\ \text{of normoxic}\\ \text{to hypoxic}}} - \overbrace{\alpha_n \frac{nc}{K}}^{\substack{\text{Conversion}\\ \text{of normoxic}\\ \text{to necrotic}}}$$

$$\overbrace{\frac{\partial h}{\partial t}}^{\substack{\text{Rate of change}\\ \text{of hypoxic}\\ \text{cell density}}} = \overbrace{\nabla\cdot(D(1-T)\nabla h)}^{\substack{\text{Net diffusion of}\\ \text{hypoxic}\\ \text{glioma cells}}} - \overbrace{\gamma h V}^{\substack{\text{Conversion}\\ \text{of hypoxic}\\ \text{to normoxic}}} + \overbrace{\beta c(1-V)}^{\substack{\text{Conversion}\\ \text{of normoxic}\\ \text{to hypoxic}}} - \overbrace{\left(\alpha_h h(1-V) + \alpha_n \frac{nh}{K}\right)}^{\substack{\text{Conversion}\\ \text{of normoxic}\\ \text{to necrotic}}}$$

$$\overbrace{\frac{\partial n}{\partial t}}^{\substack{\text{Rate of change}\\ \text{of necrotic}\\ \text{cell density}}} = \overbrace{\alpha_h h(1-V)}^{\substack{\text{Conversion}\\ \text{of hypoxic}\\ \text{to necrotic}}} + \overbrace{\alpha_n \frac{n(c+h+v)}{K}}^{\substack{\text{Contact necrosis}\\ \text{of all}\\ \text{living cells}}} \tag{17}$$

$$\overbrace{\frac{\partial v}{\partial t}}^{\substack{\text{Rate of change}\\ \text{of vessel}\\ \text{cell density}}} = \overbrace{\nabla\cdot(D(1-T)\nabla v)}^{\substack{\text{Net diffusion of}\\ \text{vasculature}}} - \overbrace{\mu \frac{a}{K_m + a} v(1-T)}^{\substack{\text{Net proliferation}\\ \text{of vasculature}}} + \overbrace{\alpha_n \frac{nv}{K}}^{\substack{\text{Conversion}\\ \text{of vasculature}\\ \text{to necrotic}}}$$

$$\overbrace{\frac{\partial a}{\partial t}}^{\substack{\text{Rate of change}\\ \text{of angiogenic}\\ \text{factor}\\ \text{concentration}}} = \overbrace{\nabla\cdot(D\nabla a)}^{\substack{\text{Net diffusion of}\\ \text{angiogenic factor}}} + \overbrace{\delta_c c + \delta_h h}^{\substack{\text{Net production}\\ \text{of angiogenic factor}}} - \overbrace{q\mu \frac{a}{K_m + a} v(1-T) - \omega a v - \lambda a}^{\substack{\text{Net consumption and}\\ \text{decay of angiogenic factor}}}$$

where $V = v/(v+c+h)$, $T = (c+h+n+v)/K$ and K is the carrying capacity of the model. The PIHNA model has been repeatedly used in suggesting possible mechanisms for clinically observed phenomena [140, 54, 139]. An example of this is PIHNA suggests that observed clinical tumour grade progression can be caused simply by an increase in tumour size or a function

of time, rather than a phenotypic change in the kinetics of the tumour cells themselves [140]. Although PIHNA can describe more phenomena than the PI model, it does so at the cost of many more parameters. Such a model with many parameters can be hard to calibrate due to lack of data that is either available or even possible to produce.

Work by Engwer, Hillen *et al*. is furthering Swanson and Murray's approach in another direction to PIHNA, they have created a fully anisotropic model of the brain [42]. Their work makes use of Diffusion Tensor Imaging (DTI); this is an MR modality that creates a complex tensor image of the movement of water molecules in the brain. DTI has been used by Engwer and Hillen to inform the diffusion tensors in the model instead of fixing the diffusion coefficient within different tissues, the tensor's direction and magnitude are used. An uncommon diffusion tensor is also derived from first principles

$$\nabla \cdot (\nabla(D(\mathbf{x})c)) = \nabla \cdot (D(\mathbf{x})\nabla c) + \nabla \cdot (\nabla(D(\mathbf{x}))c).$$

This operator can be split up into the Fickian term for diffusion, and a haptotactic term that depends on the gradient of the diffusion tensor rather than a velocity field. Together, the diffusion tensor and the haptotactic term describe where the cancer cells are likely to move to. Engwer, Hillen *et al.* use logistic growth to give the governing equation

$$\frac{\partial c}{\partial t} = \nabla \cdot (\nabla(D(\mathbf{x})c)) + \rho c \left(1 - \frac{c}{K}\right). \tag{18}$$

The validation of this model is carried out by Swan against the PI model with exponential growth. Swan shows that the fully anisotropic diffusion operator with DTI-guided diffusion tensors can more accurately simulate patient-specific tumour geometries for nine of ten patients in an *in silico* study in both two and three spatial dimensions, where accuracy is defined using the Jaccard Index [134]. Underlying structures can be obscured or destroyed by the tumour in DTI imaging. To mitigate this, Swan showed that using a reflection of the DTI data from the opposite hemisphere to the tumour hemisphere increased the accuracy of the tumour growth predictions.

Other research has also included DTI in models of brain tumour growth, as well as the mass effect caused by the growth of the tumour displacing the brain [27, 60, 95]. These models often make use of finite element theory to model the complex geometries of both the tumour and the brain throughout the growth of the tumours.

PDE models certainly are the most widely used when it comes to predicting *in vivo* growth of GBMs post diagnosis. However, there have been cellular

automata and agent based models exploring the early stages of the tumour's growth, which sometimes follow this growth to the tissue level stage [66]. In *in vitro* conditions, an establishing GBM population forms branches as it invades into surrounding regions. Sander *et al*. modelled this branching process seen in GBM growth with a lattice based model [121]. By using chemotactic movement as well as homotypic attraction between cells, they showed that qualitatively similar branching to that seen in *in vitro* experiments could be recreated *in silico*.

1.5 MODELLING LOCAL DRUG DELIVERY TO BRAIN TUMOURS

Unfortunately, conventional systemic drug delivery is inadequate for brain tumours due to the BBB; only small lipid-soluble molecules are likely to pass through it. To account for this, clinicians have to administer a relatively high drug concentration to the rest of the body. With systemic chemotherapy comes the well known symptoms of hair loss and the inhibition of nail growth as well as any other highly proliferative cell phenotypes such as immune and stem cells. These symptoms are due to the indiscriminate nature of such chemotherapy drugs, leading any susceptible proliferating cell that it encounters towards an apoptotic pathway.

With local drug delivery to the brain, the simplest administration opportunity is during resection when the brain is exposed. This opportunity has been capitalised on by a local drug delivery implant called Gliadel. Gliadel wafers are a polymeric biodegradable delivery system that are loaded with a lipophilic drug called carmustine, which has been shown to increase the median survival time of GBM patients in a phase III clinical trial by 2 months, which is notable due to the 15 months median survival for the disease [153]. Six to eight Gliadel wafers are applied immediately post resection around the cavity wall. The Gliadel treatment relies on passive diffusion out of the wafer and is currently in clinical use but is not a standard-of-care treatment. When Gliadel is applied, it is usually during sub-total resection, when the visible tumour could not completely be removed.

Gliadel wafers, and other potential polymeric matrices such as PLGA constructs have been mathematically modelled both *in vitro* and *in vivo* [19, 44]. Polymeric matrices can hold drugs in a variety of ways: simply mixed in with the polymer as is the case with Gliadel, through encapsulation within microspheres [147], or through conjugation between the polymer and drug. The

release of the drug also depends on the properties of the polymer and can occur through: diffusion (which is the case with Gliadel), surface erosion, bulk erosion or be controlled by swelling; it could even be a combination of these.

Siepmann *et al.* have modelled drug release from PLGA microparticles, that depends on the microparticle degradation [125], using a combination of partial differential equations and Monte-Carlo simulations. They validated their work with experimental data of PLGA microparticles releasing Fluorouracil into phosphate buffer solution. This *in vitro* release data showed three phases of drug release: an initial burst release, followed by a sustained release and then a final burst release due to the degradation of the PLGA microparticles. Due to the complexity of the PLGA degradation process, in that it is hard to predict which bonds in the microparticles break and in which order, a Monte-Carlo technique was applied over time to randomise the degradation within microparticles, which themselves were discretised into independent PLGA units. This mathematical model was able to accurately recreate the full release profile of the Fluorouracil over time, which was particularly notable due to the three different release phases in the data.

Shortly before Siepmann *et al.* published their work, Wang *et al.* carried out an investigation into PLGA microparticle drug release and continuously measured the release rate of octreotide acetate into an acetate buffer using high powered liquid chromatography [149]. They complemented this with scanning electron microscopy to study the surface of PLGA microparticles at different time points of release. They noted that, after 24 hours, the surface pores had almost entirely closed on the microparticles. The release rate of the drug varied throughout time and decreased as the PLGA permeability decreased. There was also evidence of swelling in the particles and a skin that covered the surfaces of the particles, limiting the release of the drug.

Drug diffusion has been modelled analytically by Siepmann *et al*. from autocatalysing PLGA/PEG microspheres based on empirical data [124]. They showed that the diffusion rate of drug from within microparticles increased with the particles' radii and suggested this relationship was due to the autocatalysing effects within the microparticles. Saltzman has characterised the diffusion of drugs through various polymers as well as their diffusion and elimination in brain tissue [119, 120].

As well as polymeric matrices, convection-enhanced delivery has been proposed to treat GBM with phase I/II clinical trials [78, 148] and *in vivo* simulations based on *in vitro* observations have been carried out [79]. This treatment

involves infusion of chemotherapy drugs through a catheter inserted into the brain. This delivery technique is theoretically more beneficial than polymeric matrices for larger treatment regions; making use of convection from the extracellular space can move drug much farther from the location that the drug is administered than passive diffusion alone. Convection enhanced delivery is yet to be realised clinically for the treatment of GBM as has yet to produce a convincing phase III clinical trial.

1.6 HOMOGENISATION THEORY

Homogenisation is a process by which an assumed small scale building block of a material is analysed and generalised across the material as a whole. In the case of diffusion, this process smoothly combines diffusion coefficients of inherent composite materials within this building block to give a predicted effective diffusion tensor across the material as a whole. This theory relies on the assumption that the assumed building block is sufficiently small that it can become an independent scale of interest to that of the whole material.

Asymptotic expansions are taken of terms within a governing PDE and only the first two scales of interest are considered: the scale of the whole material, and the small scale of the assumed building block. Homogenisation theory has been used for both diffusion and fluid flow and applied to various imageable materials such as bone, soil and concrete [33, 63, 101]. This theory has also been applied to poroelastic media [21, 30] as well as cells in a tissue [99, 61]. More specifically, homogenisation has been applied to both the propogation of action potentials through cardiac cells [67], as well as calcium dynamics within the cytoplasm of a cell, where Goal *et al.* coupled a homogenised domain with a nonhomogenised domain [49]. This theory has also been used to study the diffusive transport of ligands into the extracellular space and their subsequent binding to the receptors on the surface of cells [87]. Using this theory, the extent to which different periodic structures affect the overall diffusion of a material can be quantified, even when the proportions of the composite materials are equal between the assumed building blocks [16].

One clear benefit of this theory is the vast reduction in computational expense that it allows for. By assuming the periodic building block on a small epsilon scale, simulations only run on this small geometry to compute the macro-scale quantity of interest; this quantity is then applied on simulations of the macro-scale. This theory also reduces computational

expense in simulating rapidly changing values across a material as a whole, as numerical mesh sizes do not necessarily have to be as small to capture the dynamics of the microscale. The asymptotic analysis that this theory requires can also shed light on the dominating terms within model equations. This theory can also be used to predict how future formulations of the material of interest would behave were its microstructure adapted somehow into different shapes, patterns or sizes [16].

The following three chapters in this thesis consist of the creation, adaptation, and application of mathematical models to GBM growth and treatment. The next chapter in this thesis (Chapter 2) focuses on the novel local drug delivery system, a biodegradable polymer, in development at the Children's Brain Tumour Research Centre through the combination of *in vitro* experiments and analogous mathematical models on the polymer macroscale. We find that the polymer swells throughout its delivery lifespan, and that after including this swelling in a mathematical model, the best fit to the data from our mathematical model gives a diffusion coefficient within the polymer that slows down over time; suggesting that the observed polymer swelling can slow down macroscale diffusion of drug from the polymer delivery system.

In the third chapter (Chapter 3), we apply homogenisation of diffusion theory to microCT geometries of the novel polymer to look at the microscale of the polymer drug delivery system and analyse how its internal structure can play a role in drug diffusion dynamics. We see that different regions of the polymer express different diffusion dynamics, and that fluid channels present in unswollen polymers are important for the release of drugs.

In the final research chapter of this thesis (Chapter 4), we explore adaptations to the Proliferation Invasion Hypoxia Necrosis Angiogenesis (PIHNA) model, a previously published mathematical model that aims to reproduce the angiogenic dynamics of GBM growth. We will apply our adapted PIHNA model to vascular ischemia, which was observed to correlate with different recurrence patterns in brain tumours when it occurred following surgery [143]. The PIHNA model suggests that the ischemia leads to a local decrease in cell density such that the tumour can first appear on imaging outside of this ischemic region. We provide conditions on the simulated tumour populations that facilitate this behaviour.

2

MODELLING DRUG DIFFUSION THROUGH PLGA/PEG POLYMER CONSTRUCTS

In this chapter, we describe experiments and a mathematical model to characterise the diffusion of drugs from a construct of poly(lactic-co-glycolic acid) (PLGA) incorporated with poly(ethylene-glycol) (PEG). PLGA/PEG is a proposed local chemotherapy drug delivery system for the treatment of glioblastoma multiforme (GBM), an aggressive brain tumour. The mathematical model is calibrated alongside *in vitro* experiments in collaboration with the Children's Brain Tumour Research Centre (CBTRC). The author of this work carried out the experimental design, data collection and data analysis of these experiments at the CBTRC. From our experiments, we found that the PLGA/PEG polymer swells throughout its treatment timescale and our calibrated mathematical model suggests that this swelling slows down the drug diffusion rate through PLGA/PEG over time; this is an important consideration for using this polymer as a chemotherapy treatment for GBM going forward.

2.1 BACKGROUND

Although there are a wide variety of clinically approved chemotherapy drugs for cancer treatment, the vast majority act by altering the structure of DNA, so that when the cell tries to proliferate during the mitotic phase of the cell cycle, it instead follows an apoptotic pathway and dies; drugs that act in this way are known as cytotoxic. A standard of care cytotoxic chemotherapy drug used for GBM is Temozolomide (TMZ). TMZ is an example of an alkylating agent that alters the DNA's structure through the addition of an alkyl group so that when the cell enters its mitotic phase and tries to proliferate, it instead follows an apoptotic pathway. Although TMZ indiscriminately alkylates cells,

it only has a major impact on cells with a proliferative phenotype, as they enter the mitotic phase more often.

Drug delivery is an important consideration for all drugs; TMZ is usually ingested orally [103]. Due to its aforementioned effects on rapidly dividing cells, a chemotherapy drug will impact the growth of tumours as well as hair and nail follicles, and the skin. However, for brain tumours such as GBM, the orally ingested drugs have to be given in larger doses so that a therapeutic quantity will reach the tumour through the blood-brain barrier (BBB)[1]. This larger dose of chemotherapy drug has to be finely tuned so that it does not become too toxic in other parts of the body. The necessity for a large dose can be bypassed by using a molecularly smaller chemotherapeutic drug that could move through the BBB with ease, or by direct application to the brain; the CBTRC has proposed that the latter could be achieved through the use of a drug-loaded PLGA/PEG construct applied immediately following surgical removal of the bulk of the tumour, known as resection [115, 129].

PLGA/PEG is a biodegradable polymer that can deliver chemotherapy drugs through a variety of mechanisms such as: simple bulk diffusion of drug through the polymer; conjugation, where a covalent bond is created between the drug and the polymer, which has to be broken before the drug can start diffusing; and degradable microspheres of polymer, in which the drug is encapsulated inside the spheres, which have to degrade before the drug can diffuse out of the polymer [147]. The experiments and subsequent model considered here use PLGA/PEG constructs that consist of particles sintered together, where bulk diffusion is the only mechanism of drug release present. There are three different scales of interest for the polymer: the microscale, mesoscale and macroscale. The microscale is where a drug can be conjugated in some way to the polymer. At the mesoscale, the polymer clumps into irregular structures with gaps between them (see Chapter 3); this is the scale on which degradable microspheres can be created. The macroscale is concerned with drug release from PLGA/PEG into an external material such as fluid or brain tissue, and is the scale that we will focus on in this chapter. Due to the invasive nature of resection, the application of PLGA/PEG can usually only happen at one time point and it is therefore vital that the release dynamics from PLGA/PEG are well understood both *in vitro* and *in vivo*.

1 The BBB is a natural barrier that inhibits the free movement of larger molecules both to and from the brain and is useful in stopping pathogens from reaching the brain

Inserting drug-releasing polymers into the cavity left post resection is not a new concept. There are currently Gliadel wafers in clinical use that release a cytotoxic chemotherapy drug called carmustine into the brain. Gliadel wafers were approved following a successful phase III clinical trial [153]; the trial showed a two month average increase in survival time with Gliadel. These wafers do not stick to the cavity wall, and are manufactured in a set shape that cannot be easily altered. In contrast, PLGA/PEG adheres well to brain tissue [115] and can be formed into any irregular shape at the time of application, as it has been designed to sinter at body temperature.

To examine the diffusion dynamics of drug moving through PLGA/PEG, we carried out *in vitro* experiments using a variety of set ups, of drug moving through or from within the PLGA/PEG constructs. Following the experimental outline and results, we present an analogous one dimensional spatial-temporal mathematical model to represent these experiments. This model uses partial differential equations to simulate the dynamic movement of drug through a system containing various materials.

2.2 IN VITRO EXPERIMENTS

The first experiment considered is the diffusion of theophylline from inside a PLGA/PEG construct into water, where we have tracked the theophylline concentration in the water over time. In the second experiment, a theophylline concentration is added on top of an initially theophylline-free PLGA/PEG construct with distilled water underneath; we track theophylline as it diffuses through the PLGA/PEG construct and into the distilled water below. In the third experiment, we place theophylline concentrations above and below an initially theophylline-free PLGA/PEG construct and track the theophylline concentrations above and below over time. These experiments will be referred to as Experiment 1, Experiment 2 and Experiment 3, respectively. Theophylline was chosen for these experiments due to its molecular similarities to TMZ.

For all of our experiments, samples of medium are analysed for their theophylline concentration using ultraviolet-visible (UV-vis) spectrophotometry. UV-vis spectrophotometry records the intensity of wavelengths in the ultraviolet spectral range that travel through a sample. The spectrophotometer is calibrated to zero with a sample of distilled water and subsequently returns

values based on the UV light intensity of the impurities (in our case theophylline) in the subsequent samples.

The intensity of the pure water, I_0, and the intensity of the sample I are used to calculate the absorption A using the relationship

$$A = log_{10}\left(\frac{I_0}{I}\right). \tag{19}$$

The more impurities that are present in a sample, the lower I will be. The intensity I can also be no larger than I_0. Therefore, $A \geq 0$ and A increases as the concentration of interest, I_0, increases. In fact, the Beer-Lambert Law states that

$$A = a(\lambda)bC \tag{20}$$

where $a(\lambda)$ is the wavelength-dependent absorptivity coefficient, b is the path length taken by the lightwaves and C is the concentration. Therefore, we can find a linear relationship between absorption values and known concentrations; this is known as a calibration curve (despite it being a straight line). Using a range of known theophylline concentrations, we can create a calibration that we then use to convert the sample absorptions to the true concentrations of the samples. Figures 3 and 4 show calibration curves for theophylline across our experiments. The curves are all calculated using least squares regression and we consistently see $R^2 > 0.99$ for each repeat across all samples, from which it is clear that a linear relationship gives a good fit to each calibration curve.

To ensure independence between replicates within each experiment, each replicate has its own theophylline solution with its own calibration curve. In total we created six theophylline solutions with their respective calibration curves; this is because Experiment 1 was carried out at a different time to Experiments 2 and 3. Figures 3 and 4 show these curves with their respective equations and R^2 values. The spectrophotometer outputs the absorption values across a range of wavelengths and we chose to store the absorption values and calibration curves at 242nm, as this wavelength gave a consistently clear signal on the spectrophotometer across the range of concentrations of interest in the experiments. We also ran calibration samples of Experiment 1 through the UV-Vis spectrophotometer three times to ascertain the consistency of the machine. We present the results of these in Table 1, where we see very consistent absorption values output by the spectrophotometer.

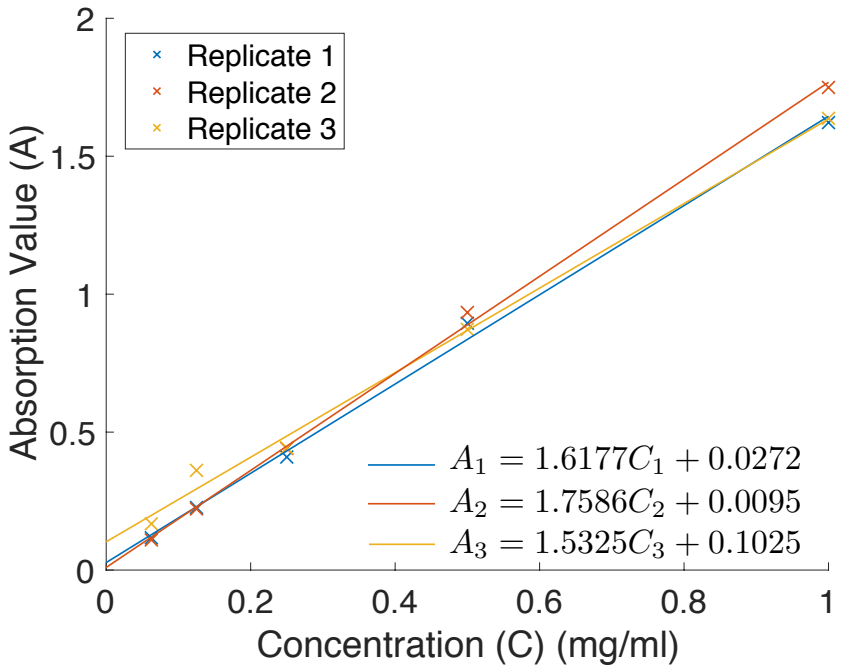


Figure 3: Three calibration curves for theophylline for solutions used in Experiment 1. Known concentrations (C) of 1, 0.5, 0.25, 0.125 and 0.0625 (mg/mL) were each run once through the UV-vis Nanodrop machine and gave the corresponding absorptions (A). The linear equations for the least squares error are shown, each has an $R^2 > 0.99$. This is clearly a linear relationship.

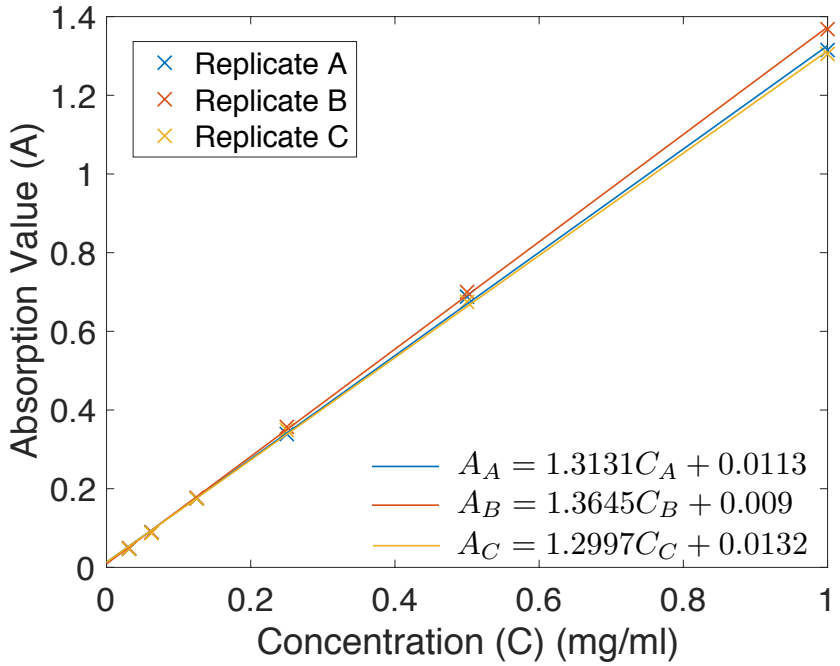


Figure 4: Calibration curves for the three repeats in Experiments 2 and 3. Known concentrations (C) of 1, 0.5, 0.25, 0.125, 0.0625 and 0.03125 (mg/mL) were each run once through the UV-vis Nanodrop machine and gave the corresponding absorptions (A). The equation of each calibration curve is given, each has $R^2 > 0.999$.

2.2.1 *PLGA/PEG Particle Preparation*

The PLGA/PEG was prepared in a ratio of 93.5:6.5, PLGA:PEG, by weight using PLGA 85:15, lactide:glycolide and PEG 400. The PLGA is mixed with the PEG on a hot plate at 80-90°C; this was carried out by hand with a polytetrafluoroethylene (PTFE)-coated spatula. The mixture was then allowed to cool until it hardened and sheets of the polymer were blended into particles using a coffee grinder. The particles were then sieved to select for particle diameters between 100-200μm.

These particles were later mixed with a theophylline solution of 2mg/ml (see Experiment 1) or distilled water (see Experiments 2 and 3). In all of the following experiments, 0.25g of PLGA/PEG was mixed with 0.2ml of solution, for each replicate. This creates a paste that can be moulded into any shape and sintered at 37 degrees Celsius.

2.2.2 *Experiment 1 - Theophylline Release from PLGA/PEG*

This experiment was designed to track the theophylline concentration released over time from PLGA/PEG constructs into water. We only track the concentration of theophylline in the water compartment as we are unable with our techniques to track the theophylline concentration within the PLGA/PEG without destroying the integrity of the experiment.

In each of the three replicates of this experiment, a PLGA/PEG paste was created by mixing 0.2ml of a 2mg/ml theophylline solution with 0.25g of PLGA/PEG particles, prepared as described in Section 2.2.1. The three pastes were then filled into the bottom of three wells and left in a humidified closed container at 37°C for 2 hours to sinter. Once sintered, a 1ml volume of distilled water was added to each well, which was then sealed with an adhesive film, and the concentration was recorded over time through intermittent sampling. Between sampling time points, the well plate was kept in humidified conditions at 37 degrees Celsius on a rocker, which we assume creates well-mixed fluid volumes. A schematic of the experiment can be seen in Figure 5.

A calibration curve was determined for each theophylline solution as previously described, see Figure 3. Each curve has an $R^2 > 0.99$ and we quantified the consistency of the spectrophotometer in Table 1.

	Concentration	Mean Reading			Range			σ		
Replicate		1	2	3	1	2	3	1	2	3
	1	1.6220	1.7493	1.6373	0.021	0.005	0.037	0.010536	0.002517	0.02108
	0.5	0.8947	0.9337	0.8727	0.011	0.006	0.013	0.005859	0.003215	0.006807
	0.25	0.4097	0.4407	0.4430	0.004	0.002	0.011	0.002082	0.001155	0.006083
	0.125	0.2267	0.2217	0.3613	0.003	0.001	0.003	0.001528	0.0005774	0.001528
	0.0625	0.1170	0.1093	0.1677	0.004	0.006	0.007	0.002000	0.003215	0.003512

Table 1: Each calibration sample for Experiment 1 was ran through the spectrophotometer three times to see the consistency of the UV-vis spectrophotometer. Known concentration is given in mg/ml and both the mean and standard deviation (σ) are given to 4 significant figures, with the range given exactly. The range in absorption values calculated by the UV-Vis spectrophotometer is extremely low for each sample.

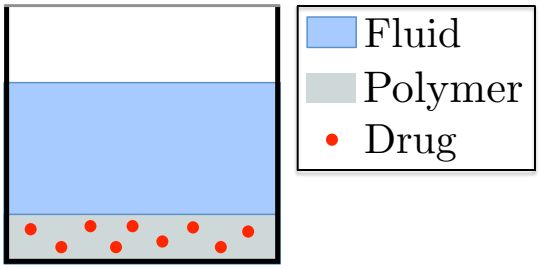


Figure 5: A schematic of the initial experimental setup for Experiment 1 - theophylline concentration is within the PLGA/PEG construct. This concentration is subsequently released from the polymer into the fluid compartment. We track the concentration within the fluid compartment over time.

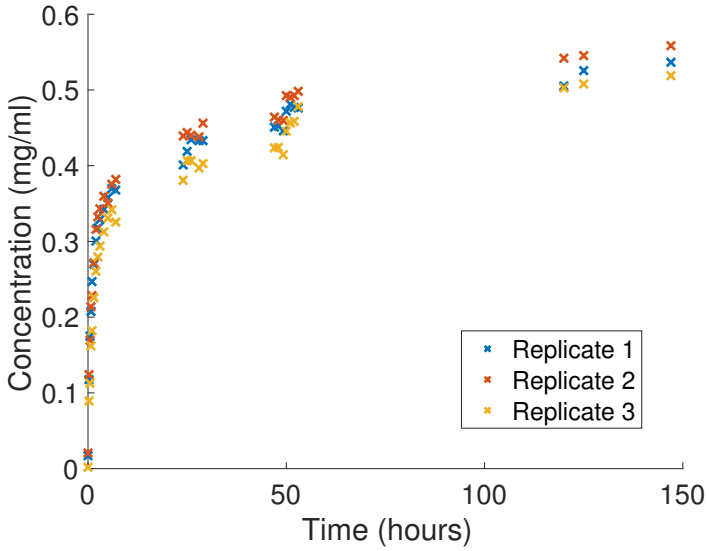


Figure 6: Release data for theophylline from the PLGA/PEG polymer over time. The release from all three replicates shows a higher concentration than expected, suggesting again that solvent is being lost. A schematic of the experimental setup is shown in Figure 5.

We label the three replicates 1, 2 and 3. The concentrations of the samples taken from the fluid compartment of the three replicates over time can be seen in Figure 6. Samples from each replicate were taken over a period of 147 hours, with a total of 28 time points, denoted $T_1(\alpha)$ for $\alpha = 1, \ldots, 28$, with corresponding mean concentrations $C_{data}(T_1^\alpha)$ across the three replicates. Only 2μl was taken as a sample from each replicate at each time point to minimise the volume reduction in the fluid compartment over the course of the experiment. The theophylline concentrations show a fast initial release from the PLGA/PEG constructs, followed by a slowly increasing concentration that starts to level off.

Due to there being an initial 0.2ml of a 2mg/ml concentration within the PLGA/PEG that has had 1ml of fluid added to it, we would expect an equilibrium concentration of around 0.33mg/ml if there were no water or drug lost from the system during sintering or throughout the experiment. However, all three repeats significantly surpassed this concentration and continued to increase throughout the experiment, with the largest concentrations of 0.537mg/ml, 0.558mg/ml and 0.519mg/ml seen at the end time point in Replicates 1, 2 and 3, respectively. This larger-than-expected concentration is not due to an increase in theophylline in the system, rather a decrease in the solvent available to dilute it. We became aware in earlier preliminary experiments that this was occurring, and took steps to minimise the decrease in solvent as well as to account for it. We measured evaporation of water from the well plate during the experiment as well as swelling of the polymer in a separate experiment. We will explain these further in Section 2.2.5.

2.2.3 *Experiment 2 - Theophylline Diffusion through PLGA/PEG*

The second experiment was designed to determine how quickly theophylline would travel through a cylinder of PLGA/PEG. A theophylline concentration was added on top of a PLGA/PEG disc with water below, see Figure 7. The concentration of theophylline was then measured over time in both the top and bottom water compartments.

Netwell Inserts

To keep our PLGA/PEG scaffolds fixed in place during this experiment, we used Netwell well plate inserts. These are polystyrene inserts with a mesh of polyester on the bottom to allow for filtration, among other purposes.

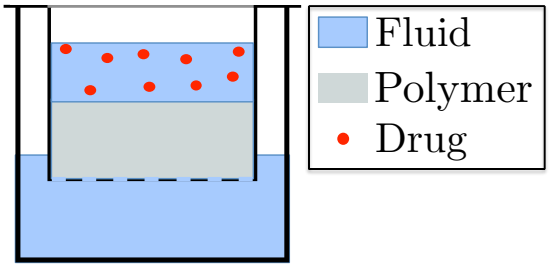


Figure 7: A schematic for the initial setup for Experiment 2 - theophylline concentration is initially in the top fluid compartment above a PLGA/PEG construct suspended over water. Diffusing theophylline travels through the polymer into the lower fluid compartment, concentrations in both fluid compartments are tracked over time.

We used Netwells with a 15.6mm diameter and a mesh size of 74μm; this size was chosen to allow free movement of drug without allowing our PLGA/PEG particles of diameter 100-200μm through.

A 1.3ml volume of distilled water was added to well plates of radius 22.4mm. Three Netwell inserts each containing a PLGA/PEG disc (prepared *in situ* according to Section 2.2.1) were added to the well plates. Concurrently, a 0.7ml solution of theophylline with concentration 1mg/ml was added on top of each PLGA/PEG disc. These fluid volumes were chosen to mitigate effects of initial fluid movement between the Netwell and well plate, caused by a combination of capillary effects and gravity. An adhesive film was stuck over the top of each Netwell. The well plates were then kept in humidified conditions within an airtight container at 37°C. The experimental setup was placed on a rocker that we used throughout the experiment, which we assume well-mixes the fluid volumes.

A total of 23 time points were taken for each repeat over a 51 hour period and run through a UV-Vis spectrophotometer (Nanodrop) in one session. Time points will be denoted $T_2(\beta)$ for $\beta = 1, \ldots, 23$, with corresponding mean concentrations $C_{data}(T_2^\beta)$. A calibration curve was also created for each replicate, A, B and C, using the corresponding theophylline solution used in each replicate (Figure 4).

This experiment showed a clear decrease in the concentration in the top compartment and a clear increase in the concentration in the bottom compartment for all three repeats. However, we would expect the concentrations to level out to the same concentration as the system reached equilibrium. We did

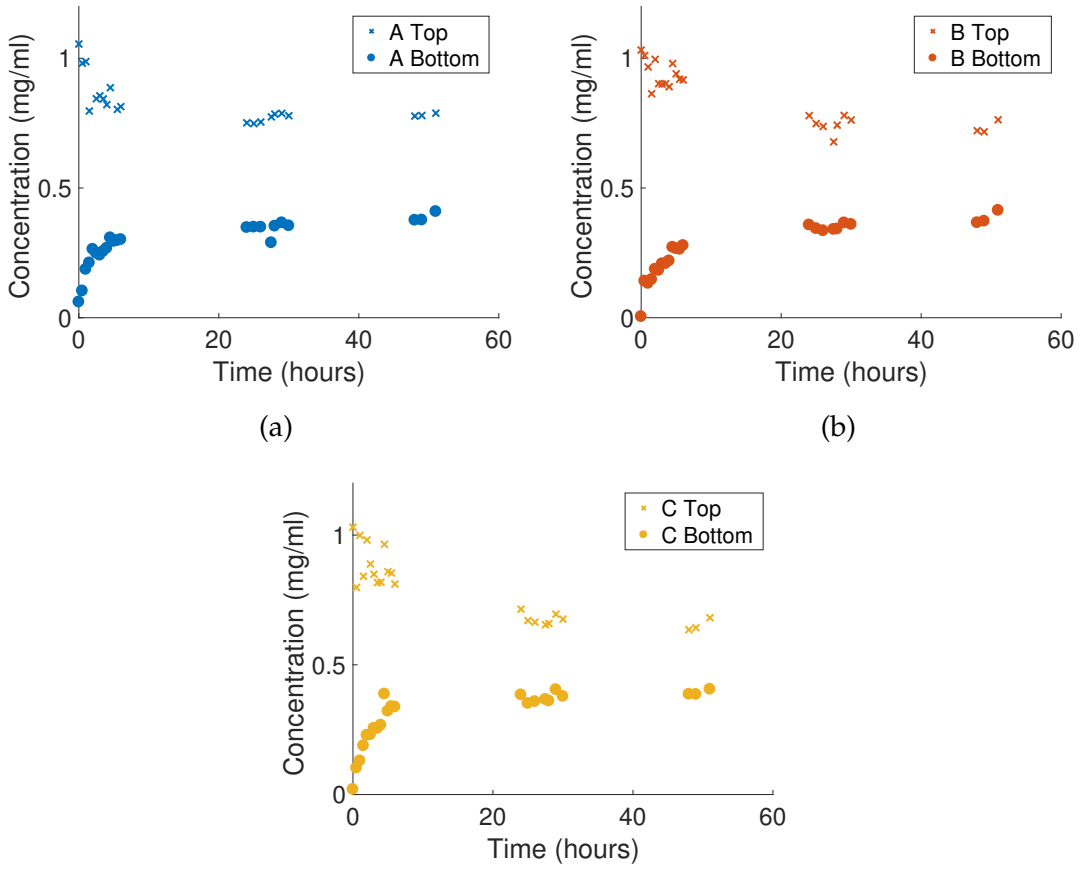


Figure 8: Concentrations of theophylline in each repeat of Experiment 2. Similar behaviour occurs in each replicate, the concentration in the top compartment decreases over time, whereas the bottom increases. Both concentrations level off in all repeats, but to different values.

not observe this in our data. The observed concentrations approach different values at large times, see Figure 8.

As in Experiment 1, we observe higher concentrations than expected, which would either suggest that theophylline is being created or solvent is being lost. As there are no mechanisms by which theophylline is created, we looked for other effects in the experiment that could remove solvent from the system, see Section 2.2.5.

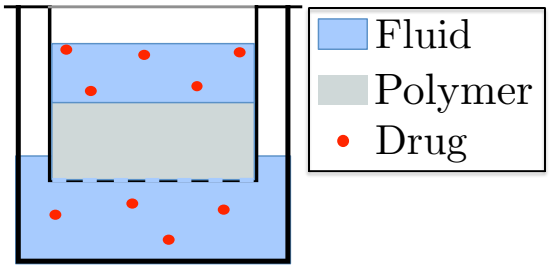
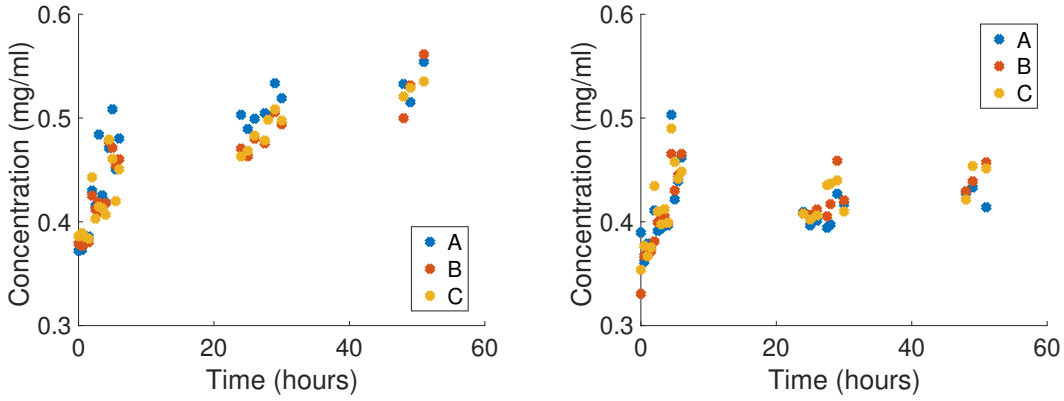


Figure 9: A schematic of the setup for Experiment 3, where theophylline concentration starts in both the top and bottom compartments.



(a) (b)

Figure 10: Subfigure 10a shows the concentration over time of the top compartments for this experiment. Subfigure 10b shows the bottom compartments. Although all concentrations increased over time, the top compartments consistently increased more than the bottom, suggesting that more solvent was lost from the top compartment relative to its volume.

2.2.4 *Experiment 3 - Theophylline Entering PLGA/PEG*

As a final experiment, to observe penetration of theophylline into the PLGA/PEG polymer, we added 0.35mg/ml concentrations of theophylline to the top and bottom fluid compartments with the same experimental setup as Experiment 2. We then tracked these concentrations over time at the same time points as Experiment 2, and denote the average concentration as $C_{data}(T_3^\beta)$.

Although we would expect to see a decrease in measured concentrations over time, the trends in our data do not show an overall decrease. Intuitively, drug should be entering the initially drug-free PLGA/PEG polymer

constructs. We have evidence that it passed through to some degree in Experiment 2. Any decrease in drug concentration due to drug entering the polymer construct is eclipsed by other effects. The data shows that the top compartments consistently had a larger increase in concentration than the bottom, suggesting that they lost a larger proportion of their fluid volume compared with the bottom compartment. Again, as in Experiments 1 and 2, it is clearly important that we track these other effects in this experiment, we will discuss this in the next section.

2.2.5 *Accounting for Other Effects*

We looked for effects that the Netwell could have on the movement of theophylline; these were important to minimise for the validity of the experiment and subsequent mathematical model fitting. Although no inhibition of theophylline through the Netwell was observed, there was capillary action as well as gravitational effects that would quickly balance the volumes within the top and bottom fluid compartments. Our experiments that used Netwell inserts therefore started with these balanced volumes of 0.7ml in the top fluid compartment and 1.3ml in the bottom. These volumes minimise drug concentration being dragged through PLGA/PEG constructs through fluid flow.

Following preliminary experiments, concentrations were observed that were much higher than would be expected if water was conserved in the system. We visually noticed that the PLGA/PEG constructs swell over time, and assumed that there would be some evaporation of the water over time. We wanted to account for the evaporation through loss of mass from our well plate. We did this by taking the initial mass of the experimental setup and measuring it throughout the experiment. There was a loss of mass from the system with each time point taken, more than the amount taken through sampling. Interestingly, the loss of mass that we attribute to evaporation of water correlates much more strongly with the number of time points taken than it does with the length of time that the experiment has been running (Figure 11). In this figure, we present the mass lost after accounting for the known loss due to sampling.

We ran an experiment to test the stability of the theophylline concentration over time and saw no change in the values of three independent repeats at the wavelength that we use for UV-Vis (242nm); this allowed us to store samples and run them through the UV-Vis spectrophotometer in one session. We also

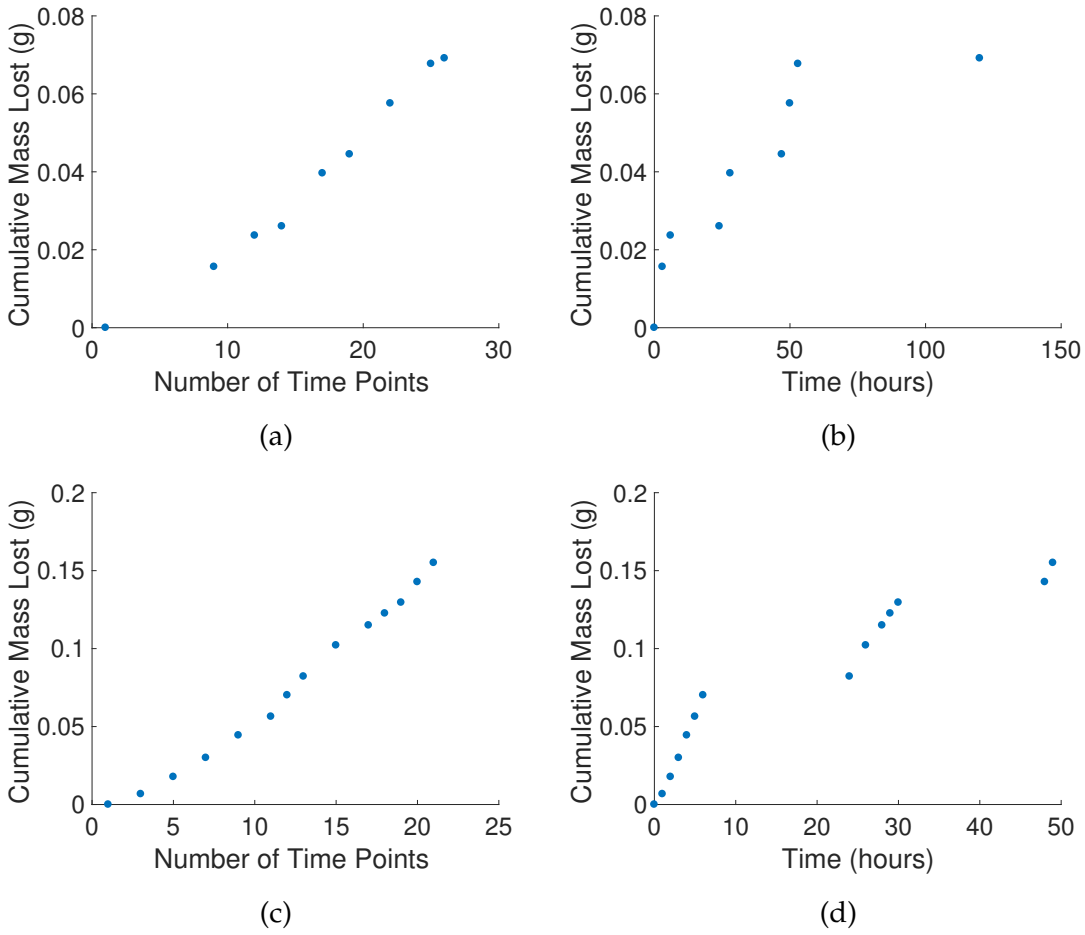


Figure 11: These four subfigures show mass lost from each well plate in Experiments 1 ((a) and (b)) and 2 and 3 ((c) and (d)) after accounting for known loss due to sampling; this correlates much better with the number of time points taken ((a) and (c)) than with the time course of the experiments ((b) and (d)). This shows that it is the measuring of the system itself that causes the loss of weight from the system.

ran samples of PLGA/PEG in water over time, to check for any other signals that might be produced. We observed none.

We also noticed that the polymer was swelling *in vitro*, as at the end of preliminary experiments the constructs were larger; this led to a further experiment to gather data on the rate at which this swelling would occur. The mechanism for PLGA/PEG swelling is hydrolysis. As the name suggests, hydrolysis is the breaking of compounds by water. The polymer swelling is important to consider since it removes water from the system that would otherwise be available as solvent for the drug, increases the concentration of drug in the system, and alters the domain sizes. Three separate PLGA/PEG

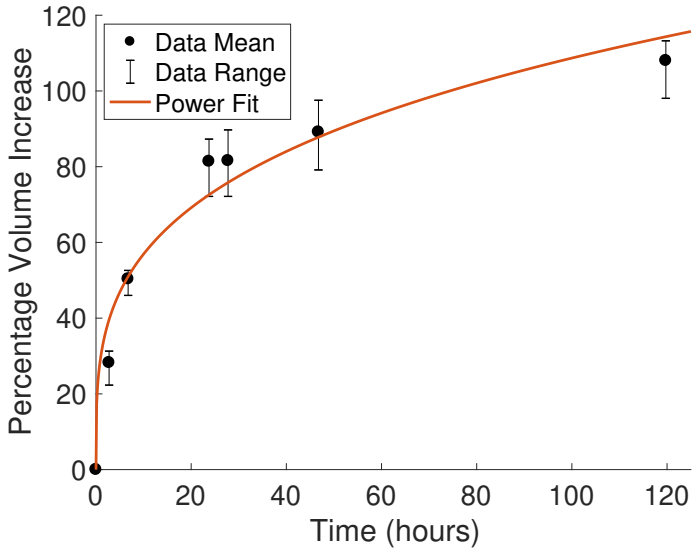


Figure 12: The mean and range of the PLGA/PEG swelling data is shown against the power fit swelling equation used in the model, $29.82t^{0.2808}$.

cylindrical constructs of 6mm diameter and 12mm length were placed in excess distilled water. We tracked the increase in the mass of these PLGA/PEG replicates, and their increase in diameter and length over time. The polymer constructs were placed on tissue paper for 10 seconds before being measured, to allow for the release of excess water. We present the volume increase along with a power fit in Figure 12. We see the best fit to the percentage volume increase of the PLGA/PEG constructs of $29.82t^{0.2808}$, with an R^2 value of 0.9677. A power fit was chosen as it gave a good fit to the data, goes through the origin, and previous work has done the same for the mass of swelling polymers [17].

The data allows us to estimate the PLGA/PEG volume fraction over time, which along with the volume fraction that fills with water makes up the total construct. We do this using the measured volume and weight of PLGA/PEG constructs, a PLGA density from the literature of 1.2825g/ml [128][2] and a PEG density value from the literature of 1.1118g/ml [116][3]. We first compute the density of PLGA/PEG from the initial mass of PLGA and PEG that we used

2 The temperature associated with this density is not given. However as PLGA is a solid, the change in density with temperature is often considered negligible.

3 PEG is a liquid and its density value was calculated using linear interpolation of the published density values for various temperatures to find the density at 37 degrees Celcius.

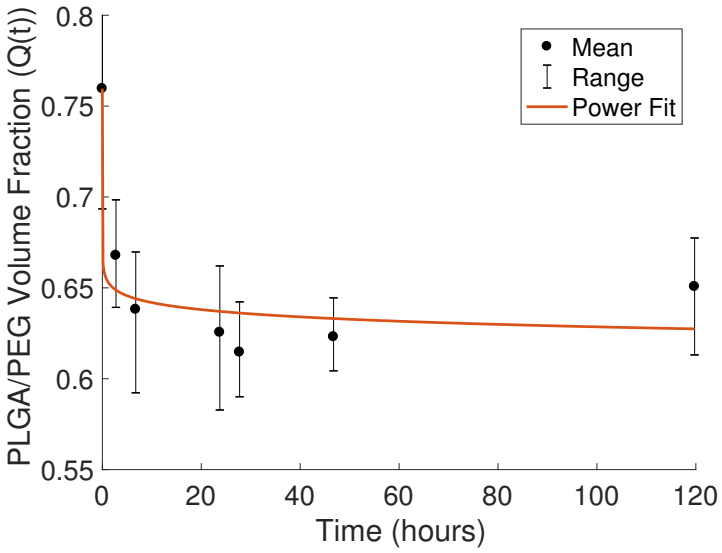


Figure 13: The mean and range of the PLGA/PEG volume fraction data is shown against the power fit swelling equation, $Q(t) = Q(0) - 0.1057t^{0.04668}$ with $R^2 = 0.89$.

to make the constructs along with the aforementioned densities for PLGA and PEG, we have

$$\rho_{PLGA/PEG} = \frac{m_{PLGA/PEG}(0)}{V_{PLGA/PEG}(0)} = \frac{m_{PLGA/PEG}(0)}{\frac{m_{PLGA}(0)}{\rho_{PLGA}} + \frac{m_{PEG}(0)}{\rho_{PEG}}} = 1.2698\text{g/ml}\,, \tag{21}$$

where ρ is density, m is mass and V is volume. We then divide the measured PLGA/PEG mass values from the data by this density to find the PLGA/PEG volume over time during swelling. This value is then divided by the volume of the construct at the respected times to find the dynamic PLGA/PEG volume fraction, $Q(t)$

$$Q(t) = \frac{m_{PLGA/PEG}(t)/\rho_{PLGA/PEG}}{V_{construct}(t)}. \tag{22}$$

This calculation relies on the assumptions that the construct does not contain excess water when weighed. We present our estimated PLGA/PEG volume fraction in Figure 13, where we found a power fit of $Q(t) = Q(0) - 0.1057t^{0.04668}$ to fit the data with $R^2 = 0.89$.

We now present the two-domain mathematical model that is analogous to Experiment 1.

2.3 TWO-DOMAIN MATHEMATICAL MODEL FOR EXPERIMENT 1

Consider the domain $x(t) \in \left[0, x_{end}(T_1^\alpha)\right]$ that consists of subdomains $[0, x_{PLGA/PEG}(t)]$ and $\left[x_{PLGA/PEG}(t), x_{PLGA/PEG}(t) + x_{fluid}(t)\right]$, where $x_{end}(T_1^\alpha) = x_{PLGA/PEG}(t) + x_{fluid}(t)$ and T_1^α represents data time points. Let the drug concentration $C(x,t)$ be a solution of the governing equation

$$\frac{\partial C}{\partial t} = \frac{\partial}{\partial x}\left(D(x,t)\frac{\partial C}{\partial x}\right), \tag{23}$$

where

$$D(x,t) = \begin{cases} D_{PLGA/PEG}(t) & \text{if } x \in [0, x_{PLGA/PEG}(t)] \\ D_{fluid} & \text{otherwise.} \end{cases} \tag{24}$$

We have $x_{PLGA/PEG}(t)$ and $x_{fluid}(t)$ depend on simulated time as these subdomain lengths change due to swelling, which is a continuous process. We assume that swelling acts as a moving internal boundary, increasing $x_{PLGA/PEG}(t)$ and decreasing $x_{fluid}(t)$ at the same rate. On the other hand, $x_{end}(T_1^\alpha)$ only depends on the data time points, as this point only moves due to sampling and evaporation, which we model as discrete events following our observed correlation between evaporation and data time points in Figure 11. Therefore, $x_{end}(T_1^\alpha)$ is constant between data time points.

As we assume no theophylline or solvent leaves the system between data time points, zero flux boundary conditions are employed on the ends of the domain

$$D_{PLGA/PEG}(t)\frac{\partial C(0,t)}{\partial x} = D_{fluid}\frac{\partial C(x_{end},t)}{\partial x} = 0.$$

We also add the interface condition

$$C(x^-_{PLGA/PEG}(t), t) = (1 - Q(t))C(x^+_{PLGA/PEG}(t), t), \tag{25}$$

where $1 - Q(t)$ is the water volume fraction within the PLGA/PEG constructs ($Q(t)$ defined as in Equation (22)) and the subscripts $-$ and $+$ denote the point on the domain as approaching from the left and right, respectively. This is included to ensure that the theophylline concentrations in water are equal between the PLGA/PEG and fluid subdomains. We also assume continuity of flux across this internal interface.

The initial condition is given by

$$C(x(0), 0) = H(x_{PLGA/PEG}(0) - x(0))C_0, \tag{26}$$

where H is a Heaviside function and C_0 is the initial drug concentration in the PLGA/PEG, the only concentration initially in the system. See Figure 14

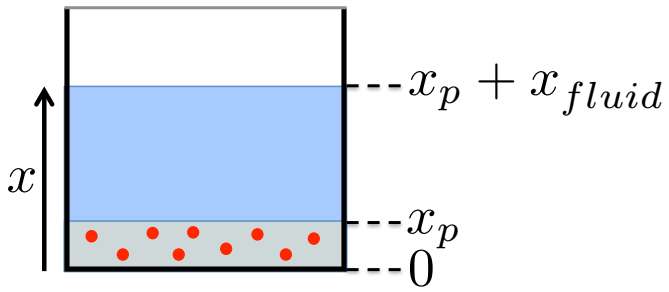


Figure 14: A schematic of the setup for Experiment 1, where theophylline concentration starts in the PLGA/PEG, marked with the model domain.

for a schematic of the initial condition of the model marked with subdomain labels.

Sampling removes fluid volume and drug concentration from the system at each data time point T_1^α, and evaporation removes fluid solvent that we have assumed also occurs at each data time point due to our supporting data shown in Figure 11. These are therefore included in the model as discrete events occurring at the times when $t = T_1^\alpha$ for some α. During this time, we remove some of the fluid subdomain to represent sampling, denoted x_s, and some to represent evaporation, denoted x_e; this transforms $x_{end}(T_1^\alpha)$ into $x_{end}(T_1^{\alpha+1})$, such that

$$x_{end}(T_1^{\alpha+1}) = x_{end}(T_1^\alpha) - x_e - x_s, \tag{27}$$

which updates the domain from $x(T_1^{\alpha+1}) \in [0, x_{end}(T_1^\alpha)]$ to $\hat{x}(T_1^{\alpha+1}) \in [0, x_{end}(T_1^{\alpha+1})]$. Sampling also removes concentration from the system, whereas evaporation only removes water, which increases the theophylline concentration at each data time point. In terms of the model this leads to an update to the concentration at each time point T_1^α. We have

$$\begin{aligned}\int_0^{x_{end}(T_1^{\alpha+1})} \hat{C}(\hat{x}(T_1^{\alpha+1}), T_1^{\alpha+1})\, d\hat{x} = &\int_0^{x_{end}(T_1^\alpha)} C(x(T_1^{\alpha+1}), T_1^{\alpha+1})\, dx \\ &- \int_{x_{end}(T_1^{\alpha+1})}^{x_{end}(T_1^{\alpha+1})+x_s} C(x(T_1^{\alpha+1}), T_1^{\alpha+1})\, dx,\end{aligned} \tag{28}$$

where we use $\hat{C}$ and $\hat{x}$ to denote the updated concentration and domain, respectively.

The now smaller fluid subdomain contains a higher concentration of drug which is equal throughout, as this subdomain is assumed to be well-mixed due to the rocker used in the experiment. The simulated concentration in

the PLGA/PEG subdomain is unaffected by the data time point, and alongside the increased concentration in the fluid subdomain becomes the initial condition for the model until the next data time point where this process is repeated. The concentration that is added to the new smaller fluid subdomain is given by

$$I_e = \frac{1}{x_{fluid}(T_1^{\alpha+1})} \int_{x_{end}(T_1^{\alpha+1})}^{x_{end}(T_1^{\alpha+1})+x_e} C(x(T_1^{\alpha+1}), T_1^{\alpha+1})\, dx. \tag{29}$$

So we have

$$\hat{C}(\hat{x}(T_1^{\alpha+1}), T_1^{\alpha+1}) = \begin{cases} C(x(T_1^{\alpha+1}), T_1^{\alpha+1})) & \text{if } \hat{x} \in [0, x^-_{PLGA/PEG}(T_1^{\alpha+1})] \\ C(x(T_1^{\alpha+1}), T_1^{\alpha+1})) + I_e & \text{if } \hat{x} \notin [0, x^-_{PLGA/PEG}(T_1^{\alpha+1})]. \end{cases} \tag{30}$$

We assume that the movement of the internal boundary at $x_{PLGA/PEG}(t)$ can be described by the power fit to the PLGA/PEG volume time series data during swelling described in Section 2.2.5. Due to the fixed radius provided by the sides of the well that Experiment 1 was contained within, the measured percentage volume change is equivalent to the percentage height change in the model. We also assume that $Q(t)$ follows the power fit to the PLGA/PEG volume fraction derived from the data also described in Section 2.2.5, which is only possible with our assumption that the volume changes are equivalent between experiments.

2.3.1 *Numerical Scheme for the Two-Domain Model*

The numerical scheme for this model makes use of finite element theory[4] in space and finite difference theory in time and is implemented in Matlab 2017a. In the interest of equation readability, in this section $PLGA/PEG$ subscripts will be denoted P.

At each simulated time point, the one-dimensional space $x(t)$ is partitioned into two sets of points, one set for each subdomain with each point denoted $x_i(t)$ for $i = 1, 2, \ldots, m$. The PLGA/PEG subdomain, $[0, x_P^-(t)]$, is discretised to the set of points $0 = x_0, x_1, \ldots, x_l = x_P^-(t)$ and the fluid subdomain $[x_P^+(t), x_{end}]$ is discretised to $x_P^+(t) = x_{l+1}, x_{l+2}, \ldots, x_m = x_{end}(T_1^\alpha)$. Time is also discretised, so that t is partitioned into $t = t^0, t^1, \ldots, t^N$, where $t^n = n\tau$ for fixed τ and $n = 1, \ldots, N$. The constant time step, τ, is chosen in such

4 For an accessible introductory book on these methods, see Larson and Bengzon [77]

a way that there exists a $t^n = T_1^\alpha$ for some n and all $\alpha = 1, \ldots, 28$. As a reminder, 28 is used in this case as it is the total number of data time points in this experiment. To solve Equation (23), a suitable weak form needs to be derived. To do this, the basis functions for the discretised space, known as hat functions, take the following form:

$$N_i(t^n) = \begin{cases} \frac{x(t^n) - x_{i-1}(t^n)}{x_i(t^n) - x_{i-1}(t^n)} & \text{if } x(t^n) \in [x_{i-1}(t^n), x_i(t^n)] \\ \frac{x_i(t^n) - x(t^n)}{x_{i+1}(t^n) - x_i(t^n)} & \text{if } x(t^n) \in [x_i(t^n), x_{i+1}(t^n)] \\ 0 & \text{otherwise.} \end{cases} \tag{31}$$

The basis of hat functions is convenient as each one is only non-zero on one point along the discretisation of x, so each hat function can be linearly scaled to represent a point within a function. Therefore, a linear combination of hat functions can be used to describe a function, in our case C. Multiplying each side of Equation (23) by a continuous test function V_h and integrating over the domain with respect to x gives

$$\int_o^{x_{end}} \frac{\partial C}{\partial t} V_h \, dx = \int_0^{x_{end}} \frac{\partial}{\partial x} \left(D(x(t)) \frac{\partial C}{\partial x} \right) V_h \, dx$$

As V_h is arbitrary, we can choose it to be an arbitrary basis function, N_h. The integral of the diffusion term can then be split across the subdomains to give

$$\begin{aligned} \int_0^{x_{end}} \frac{\partial}{\partial x} \left(D(x) \frac{\partial C}{\partial x} \right) N_h \, dx = D_P \int_0^{x_P} \frac{\partial^2 C}{\partial x^2} N_h \, dx \\ + D_{fluid} \int_{x_P}^{x_P + x_{fluid}} \frac{\partial^2 C}{\partial x^2} N_h \, dx \end{aligned}$$

The right hand side terms can be integrated by parts to give

$$\begin{aligned} \int_0^{x_{end}} \frac{\partial}{\partial x} \left(D(x) \frac{\partial C}{\partial x} \right) N_h \, dx = D_P \left[\frac{\partial C}{\partial x} N_h \right]_0^{x_P} - D_P \int_0^{x_P} \frac{\partial C}{\partial x} \frac{\partial N_h}{dx} \, dx \\ + D_{fluid} \left[\frac{\partial C}{\partial x} N_h \right]_{x_P}^{x_P + x_{fluid}} - D_{fluid} \int_{x_P}^{x_P + x_{fluid}} \frac{\partial C}{\partial x} \frac{\partial N_h}{dx} \, dx \end{aligned}$$

The continuity of flux, continuous test function space and Neumann boundary conditions lead to cancellation of the non-integral terms. In order to make full use of the test function space we are working in, we can re-express C as a linear combination of hat functions N_j (of which there are m) and coefficients C_j, i.e.

$$C = \sum_{j=1}^{m} C_j N_j.$$

Using this, Equation (23) becomes

$$\sum_{j=1}^{m} \frac{\partial C_j}{\partial t} \int_0^{x_{end}} N_j N_h \, dx = \sum_{j=1}^{m} C_j \Bigg(- D_P \int_0^{x_P} \frac{\partial N_j}{\partial x} \frac{\partial N_h}{dx} \, dx - D_{fluid} \int_{x_P}^{x_P + x_{fluid}} \frac{\partial N_j}{\partial x} \frac{\partial N_h}{dx} \, dx \Bigg)$$

Discretising the time derivative with a backwards Euler approach gives the approximation for the first term of Equation (23) at the nth time step (for time interval τ)

$$\sum_{j=1}^{m} \frac{\partial C_j}{\partial t}^n \int_0^{x_{end}} N_j N_h \, dx \approx \sum_{j=1}^{m} \left(\frac{C^n - C^{n-1}}{\tau} \right)_j \int N_j N_h \, dx.$$

Re-expressing this problem in condensed matrix notation across all test basis functions gives

$$\left(\frac{M^{n+1}}{\tau} + D(x(t^{n+1}))A^{n+1} \right) \mathbf{C}^{n+1} = \frac{M^n}{\tau} \mathbf{C}^n,$$

where M will be referred to as the mass matrix and A is the stiffness matrix. The entries of these matrices are given by

$$M_{ij} = \int_{x_0}^{x_{end}} N_i N_j \, dx \quad \text{and} \quad A_{ij} = \int_{x_0}^{x_{end}} N_i' N_j' \, dx, \tag{32}$$

where subscript $i = 1 \dots m$ refers to each test basis function, subscript $j = 1 \dots m$ refers to each basis function in the decomposition of C and N' represents the spatial derivative of N. These two integrals are computed for each interval $[x_{i-1}, x_{i+1}]$ using Gaussian quadrature; this uses the roots of the Legendre polynomial, y_k, to find points $X_{i,k}$ that are then used in a weighted sum to accurately evaluate the integrals. The points $X_{i,k}$ are computed for each interval $[x_i, x_{i+1}]$. As the hat functions are linear, only two Legendre roots need to be computed. So to find the integrals within $[x_i, x_{i+1}]$, we compute two $X_{i,k}$ values and combine these with the Legendre roots. We find each $X_{i,k}$ using

$$X_{i,k} = \frac{x_i(1 - y_k) + x_{i+1}(1 + y_k))}{2} \text{ for } x \in [x_i, x_{i+1}], k = 1, 2. \tag{33}$$

Using a Chebyshev-Gauss weighting function, the weights w_k can also be found for each node[5]. As our basis functions are linear, the two roots are

5 The Legendre roots and weights can be found on a normalised interval and then scaled up to each interval at every instance. In this way the roots only need to be found once (or just taken from a reference table such as [84]). Although in the case for this numerical scheme, the integrals can easily be computed by hand, it is a good platform to expand upon if we were to ever decide to introduce more complex basis functions.

$y_k = \pm\sqrt{3}/3$ and the weights are equal at $w_k = 1$ for $k = 1, 2$ [84]. However, we have left them as w_k to show the theory in a more general form.

As each hat function N_i is only non-zero across an interval $[x_{i-1}, x_{i+1}]$, the matrices given in Equation (32) are sparse. The non-zero terms in the mass matrix are given by

$$\begin{aligned} M_{i,i} &= \int_{x_0}^{x_{end}} N_i N_i \, dx = \int_{x_{i-1}}^{x_i} N_i N_i \, dx + \int_{x_i}^{x_{i+1}} N_i N_i \, dx \\ &= \sum_{k=1}^{2} \frac{w_k (X_{i-1,k} - x_{i-1})^2}{x_i - x_{i-1}} + \sum_{k=1}^{2} \frac{w_k (x_{i+1} - X_{i,k})^2}{x_{i+1} - x_i}, \\ M_{i,i+1} &= M_{i+1,i} = \int_{x_0}^{x_{end}} N_{i+1} N_i \, dx = \int_{x_{i-1}}^{x_i} N_{i+1} N_i \, dx + \int_{x_i}^{x_{i+1}} N_{i+1} N_i \, dx \\ &= 0 + \sum_{k=1}^{2} \frac{w_k (x_{i+1} - X_{i,k})(X_{i-1,k} - x_i)}{x_{i+1} - x_i}. \end{aligned}$$

The non-zero terms in the stiffness matrix are given by

$$\begin{aligned} A_{i,i} &= \int_{x_0}^{x_{end}} N_i' N_i' \, dx = \int_{x_{i-1}}^{x_i} N_i' N_i' \, dx + \int_{x_i}^{x_{i+1}} N_i' N_i' \, dx \\ &= \sum_{k=1}^{2} \frac{w_k (1)^2}{x_i - x_{i-1}} + \sum_{k=1}^{2} \frac{w_k (-1)^2}{x_{i+1} - x_i}, \\ A_{i,i+1} &= A_{i+1,i} = \int_{x_0}^{x_{end}} N_{i+1}' N_i' \, dx = \int_{x_{i-1}}^{x_i} N_{i+1}' N_i' \, dx + \int_{x_i}^{x_{i+1}} N_{i+1}' N_i' \, dx \\ &= 0 + \sum_{k=1}^{2} \frac{w_k (1)(-1)}{x_{i+1} - x_i}. \end{aligned}$$

In our simulations, the difference between adjacent points in the discretised space is known as the step size, $h(t)$. When computing the mass matrix and stiffness matrix on the whole domain, it is convenient to find each of these matrices on each subdomain and couple them all together; this is strongly enforced (directly imposed on the matrices) and allows us to add the interface condition (Equation (25)) into the model.

To create the mass matrix for the whole domain, the mass matrices corresponding to each subdomain, M_P of size $l \times l$ and M_{fluid} of size $(m-l) \times (m-l)$ are collated into a block diagonal matrix, M. They must be coupled together within this block diagonal matrix to properly define our problem. This is done through a translation of the non-zero entries in the top row of M_{fluid} to the bottom row of M_P and the top row of M_{fluid} is replaced with zeros. This row of zeros can then be filled with a new equation to couple the domains. We input $-1/h(t)$ and $1/h(t)$ at positions $M_{l+1,l}$ and $M_{l+1,l+1}$ in the block diagonal matrix; this couples the time scales of each subdomain together and sets them equal. The stiffness matrix, A, is created in a similar way

to M but instead of coupling together the subdomains so that they are equal, we add $-1/h(t)$ at $A_{l+1,l}$ and $(1-Q(t))/h(t)$ at $A_{l+1,l+1}$ so that Equation (25) is included in the model.

To include evaporation and sampling, which occurs when $t^n = T_1^\alpha$ for $\alpha = 1,\ldots,28$, we reduce the domain lengths and update the concentration according to Equations (27), (28) and (30), and continue the numerical scheme until the next data time point. We use the inbuilt trapezium rule *trapz.m* function in Matlab 2017a to calculate the mass of drug in the fluid subdomain which we then use to find I_e. This process is repeated until the desired end point of the simulation.

Conservation of Mass for Deforming Continuum Bodies

An immediate concern for the numerical scheme with a moving time-dependent mesh is whether or not it conserves mass between simulated time points; in this small aside, we will use a more generalised example to show that it does.

Consider an arbitrary shape moving through $\mathbb{R}^N$ space with velocity field v. Throughout time, we track a small element of the shape, which we will denote $P(t)$. Conservation of mass with flux $\mathbf{j}$ and normal $\mathbf{n}$, along with a source term s, gives the equation

$$\frac{d}{dt}\int_{P(t)} u\,dt = \int_{\partial P(t)} -\mathbf{j}\cdot\mathbf{n}\,dt + \int_{P(t)} s\,dt. \tag{34}$$

Using a combination of Reynold's Transport Theorem and the Divergence Theorem we can re-express the previous equation as

$$\int_{P(t)} \dot{u} + u\nabla\cdot v\,dt = \int_{P(t)} -\nabla\cdot\mathbf{j}\,dt + \int_{P(t)} s\,dt, \tag{35}$$

where in this instance $\dot{u}$ represents the material derivative of u. The material derivative of u is given by (for $N=1$)

$$\dot{u} = \lim_{\delta t\to 0}\frac{u(x(t+\delta t),t+\delta t) - u(x(t),t)}{\delta t}. \tag{36}$$

As we have chosen an arbitrary element, we can generalise Equation (35) to hold across the whole domain to give

$$\dot{u} + u\nabla\cdot v = -\nabla\mathbf{j} + s. \tag{37}$$

The question now is, can we discretise this equation using a finite element method to conserve mass regardless of the moving mesh? First, we re-express u as a sum of coefficients u_j and basis functions N_j

$$u = \sum_{j=1}^{n} u_j N_j, \tag{38}$$

and then integrate Equation (37) over the whole domain; this gives

$$\int_{\omega(t)} \sum_{j=1}^{n} (u_j \dot{N}_j) + u_j N_j \nabla v \, dt = \int_{\omega(t)} -\nabla \mathbf{j} \, dt + \int_{\omega(t)} s \, dt. \tag{39}$$

The chain rule now gives

$$\sum_{j=1}^{n} \int_{\omega(t)} \dot{u_j} N_j + u_j \dot{N}_j + u_j N_j \nabla v \, dt = \int_{\omega(t)} -\nabla \mathbf{j} \, dt + \int_{\omega(t)} s \, dt. \tag{40}$$

Although basis functions N_j move spatially, their value does not change. Consider an arbitrary basis function N_j from time t^* to time $t^* + \delta t$, we can see that it has a zero material derivative. We define

$$N_j(x(t), t) = \begin{cases} \frac{x(t) - x_{j-1}(t)}{x_j(t) - x_{j-1}(t)} & \text{if } x \in [x_{j-1}, x_j] \\ \frac{x_j(t) - x(t)}{x_{j+1}(t) - x_j(t)} & \text{if } x \in [x_j, x_{j+1}] \\ 0 & \text{otherwise.} \end{cases}$$

Now consider a linear mapping from $x(t^*)$ to $x(t^* + \delta t)$, such that each point $x_j(t)$ maps to each point $x_j(t + \delta t)$. Each point in $x(t^*)$ is mapped to a unique point in $x(t^* + \delta t)$, which by extension holds true for $N_j(x(t^*), t^*)$ and $N_j(x(t^* + \delta t), t^* + \delta t)$. Clearly, outside of the interval $[x_{j-1}(t^*), x_{j+1}(t^*)]$, which maps to $[x_{j-1}(t^* + \delta t), x_{j+1}(t^* + \delta t)]$, the material derivative of the basis function is zero as the basis functions are zero. Inside the interval, the mapping ensures that at each point in x, $N_j(x(t^*), t^*) = N_j(x(t^* + \delta t), t^* + \delta t)$ and so the material derivative is zero here, too. The material derivative of the basis functions then vanishes, which gives the following:

$$\sum_{j=1}^{n} \int_{\omega(t)} \dot{u_j} N_j + u_j N_j \nabla v \, dt = \int_{\omega(t)} -\nabla \mathbf{j} \, dt + \int_{\omega(t)} s \, dt \tag{41}$$

and we can use the Divergence Theorem and Reynold's Transport Theorem in the other direction to give

$$\frac{d}{dt} \int_{\omega(t)} \sum_{j=1}^{n} u_j N_j \, dt = \int_{\omega(t)} -\nabla \mathbf{j} \, dt + \int_{\omega(t)} s \, dt, \tag{42}$$

which is the original conservation of mass equation,

$$\frac{d}{dt}\int_{\omega(t)} u\,dt = \int_{\omega(t)} -\nabla \mathbf{j}\,dt + \int_{\omega(t)} s\,dt, \tag{43}$$

where we have used Equation (38). So we have shown that it is indeed possible to discretise the equation with a moving mesh and still conserve mass, as long as there is a sufficient mapping within the domain.

We ran three simulations of the two-domain model with various effects and found the total mass of drug over time. The first simulation only had swelling, the second with swelling and evaporation, and the third with swelling, evaporation and sampling. We present the mass of drug in the system at time t, divided by the initial mass of drug in the system in Figure 15. More precisely, we have

$$\Phi(t) = \frac{\int_0^{x_{end}(t)} C(x,t)dx}{\int_0^{x_{end}(0)} C(x,0)dx}, \tag{44}$$

which we would expect to remain as 1 as long as we do not intentionally take drug out of the system. As expected, we see that drug mass is lost only once sampling is included in the model, as the simulated sampling method removes mass from the system at each data time point. We see that this result persists across all constant and time-dependent diffusion coefficients. We have also calculated $\Phi(t)$ for the three-domain model (see Section 2.5 for the model definition) and see the same results persist.

2.3.2 *Two-Domain Model Input Values Derived from* In Vitro *Data*

To initiate the model, we need to find values for the initial concentration (C_0), the initial widths of the subdomains ($x_{fluid}(0)$ and $x_{PLGA/PEG}(0)$), and the subdomain widths lost due to sampling (x_s) and evaporation (x_e).

We know the initial volumes of the fluid volume (1ml = 1000mm^3), as well as the radius of the well-plate (11.2mm). Using these, a simple volume equation for a cylinder yields the estimated domain length that we use.

$$x_{fluid}(0) = \frac{1000}{11.2^2\pi} = 2.5375\text{mm}. \tag{45}$$

To calculate the initial length of the PLGA/PEG construct, we use the initial total mass of the PLGA/PEG powder and fluid, alongside the PLGA/PEG density calculated in Section 2.2.5 and the initial fluid volume fraction, $Q(0)$. This gives

$$x_{PLGA/PEG}(0) = \frac{450(1 - Q(0) + Q(0)/1.2698)}{11.2^2\pi} = 0.9599\text{mm} \tag{46}$$

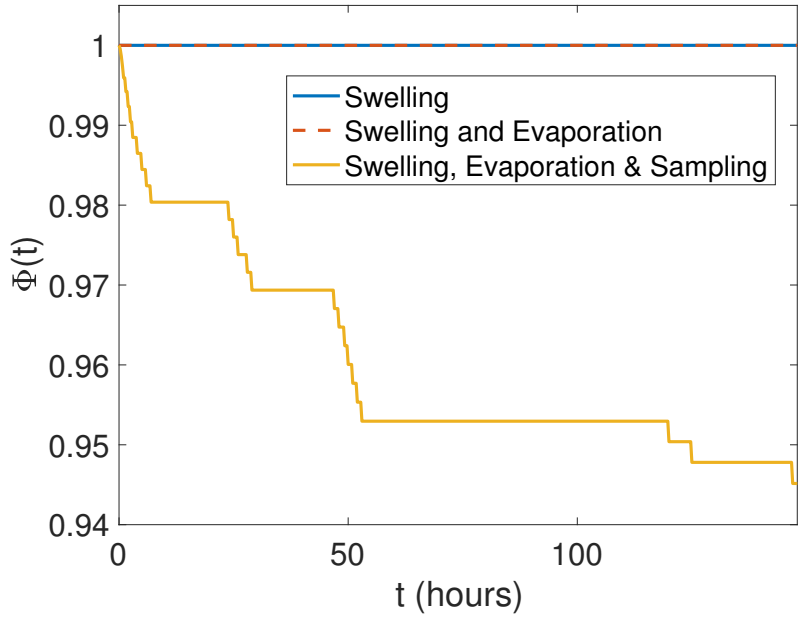


Figure 15: We present $\Phi(t)$ as defined in Equation (44) for three simulations with various effects included in the two-domain model (see Figure legend). Swelling and evaporation do not contribute to loss of drug, whereas sampling does only at each data time point.

Each sample takes away 2μl of fluid, a similar calculation then yields

$$x_s = \frac{2}{11.2^2\pi} = 0.00508\text{mm}. \tag{47}$$

We use the gradient of the best fit to the evaporation data to find the fluid lost per time point, in this case we have

$$x_e = \frac{2.998}{11.2^2\pi} = 0.00761\text{mm}. \tag{48}$$

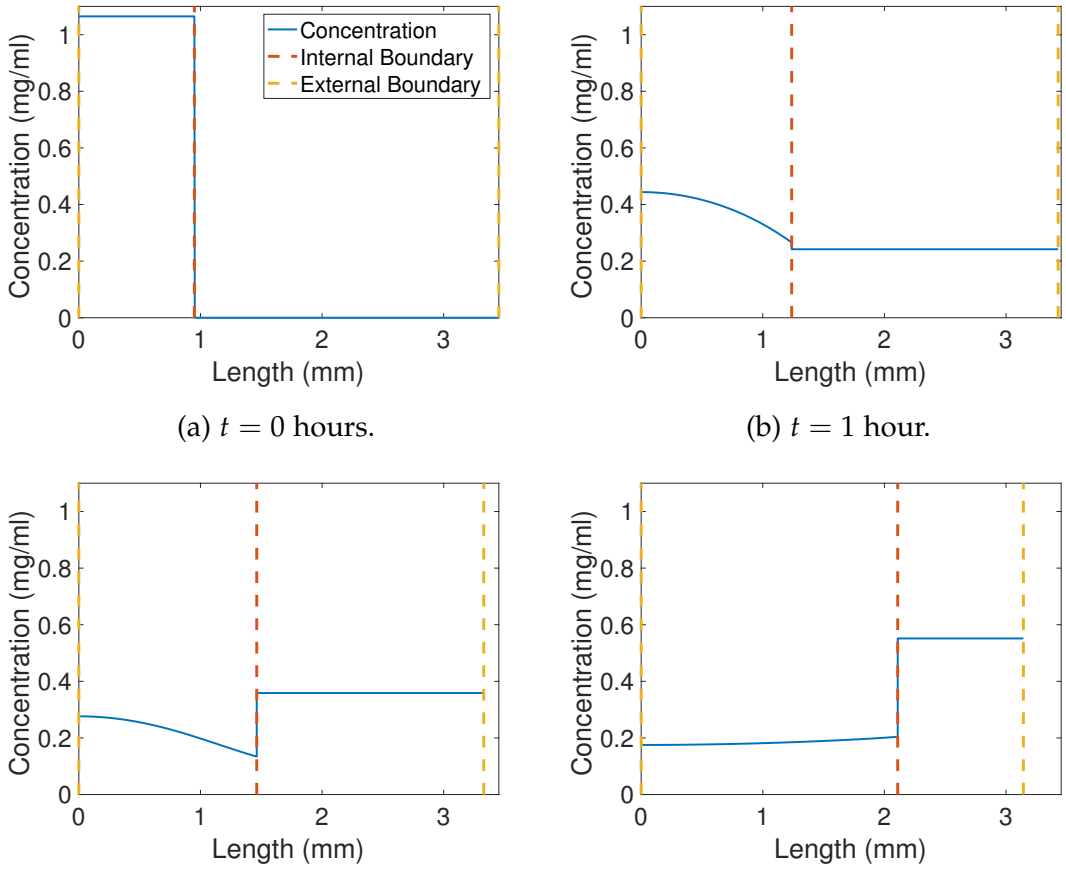
The initial concentration is given by the total drug in the construct, divided by the total volume of the PLGA/PEG construct at the initial time point

$$C_0 = \frac{2 \times 2000}{450(1 - Q(0)) + 450Q(0)/1.2698} = 1.0574\text{mg/ml} \tag{49}$$

We use the power fit in Section 2.2.5 for the swelling, which extends the PLGA/PEG subdomain, as well as the power fit for $Q(t)$. We present snapshots of an example simulation with these input values in Figure 16.

2.4 TWO-DOMAIN MODEL FITTING TO EXPERIMENT 1

We have used three different functional forms of diffusion within the PLGA/PEG construct to see which gives the best fit to the *in vitro* data. Con-



(a) $t = 0$ hours.

(b) $t = 1$ hour.

(c) $t = 8$ hours.

(d) $t = 148$ hours.

Figure 16: Snapshots of a two-domain simulation for Experiment 1. $D_0 = 10\text{mm}^2/\text{hour}$, $\alpha = 10^{0.375}/\text{hour}$, $\beta = 10^{-1.5}\text{mm}^2/\text{hour}$. Notice that the internal boundary (red) moves to the right as the PLGA/PEG swells. The right hand side external boundary moves inwards as evaporation, swelling, and sampling reduces the level of fluid in this subdomain. Domain lengths and initial conditions were taken from Section 2.3.2.

stant diffusion $D_{PLGA/PEG}(t) = D_1(t) = D_0$, exponentially decreasing diffusion $D_{PLGA/PEG}(t) = D_2(t) = D_0 e^{-\alpha t}$, and exponentially decreasing to a lower limit $D_{PLGA/PEG}(t) = D_3(t) = (D_0 - \beta)e^{-\alpha t} + \beta$. To incorporate the assumed well-mixed fluid compartment, we set $D_{fluid} = 1\text{mm}^2/\text{s}$, which is notably faster than the diffusion rates we see as best fits in the PLGA/PEG construct. In total, we have a maximum of three parameters to fit, D_0, α and β. We ran a variety of simulations across D_0, α and β and used a Euclidean-norm regression between the simulated data points, which are the average

concentrations within the fluid subdomain at each $t = T_1^\alpha$ and the actual data points, $C_{data}(T_1^\alpha)$, as our error measurement. We have

$$L^2 = \sqrt{\sum_{\alpha=1}^{28} \left(\frac{\int_{x_{PLGA/PEG}(T_1^\alpha)}^{x_{end}(T_1^\alpha)} C(x, T_1^\alpha)\, dx}{x_{fluid}(T_1^\alpha)} - C_{data}(T_1^\alpha) \right)^2}. \tag{50}$$

The broad parameter scan was carried out on a log scale for D_0, α and β, we used $D_0 \in [10^{-1}, 10^3]$mm^2/hour, $\alpha \in [10^{-1}, 10^2]$/hour, and $\beta \in [10^{-4}, 10^1]$mm^2/hour all with increments of $10^{0.125}$ in their intervals. These ranges were chosen to be large so that we could isolate the global error minimum in the parameter space. For $D_1(t)$, we only fit D_0, for the exponentially decreasing diffusion $D_2(t)$, we fit D_0 and α, and for $D_3(t)$, we fit all three parameters.

We show an example simulation in Figure 16, with the input values from Section 2.3.2. In this figure we see the three boundaries: two external boundaries and one internal boundary. The internal boundary moves to the right due to swelling of the PLGA/PEG construct, and the right-most external boundary moves left due to evaporation and sampling at each T_1^α. Initially, the concentration is all contained in the PLGA/PEG construct. Over time, the concentration moves out towards the fluid domain, and is discontinuous across the internal boundary due to the interface condition, Equation 25. Due to the fast diffusion rate for the fluid subdomain in the model, the concentration is close to constant at each time point.

We find a best fit from all three functional forms of the time-dependent diffusion coefficient, and compare their errors (Equation 50) to see which functional form performs the best. The best fits are given by

$$D_1 = D_0 = 0.56\text{mm}^2/\text{hour}, \; L^2 = 0.17\text{mg/ml} \tag{51}$$

$$D_2(t) = D_0 e^{-\alpha t} = 5.6 e^{-1.78t}\text{mm}^2/\text{hour}, \; L^2 = 0.13\text{mg/ml} \tag{52}$$

$$D_3(t) = (D_0 - \beta)e^{-\alpha t} + \beta = (4.2 - 0.032)e^{-1.78t} + 0.032 \text{ mm}^2/\text{hour}, \quad L^2 = 0.078\text{mg/ml}. \tag{53}$$

We therefore see that the best fit across all three functional forms is given by $D_3(t)$, which suggests that the diffusion is time-dependent and goes to a lower limit for Experiment 1. We have presented the best fits of the simulated data points against the mean data points with their ranges in Figure 17; the time is presented on a $\log_{10}$ scale for visual clarity.

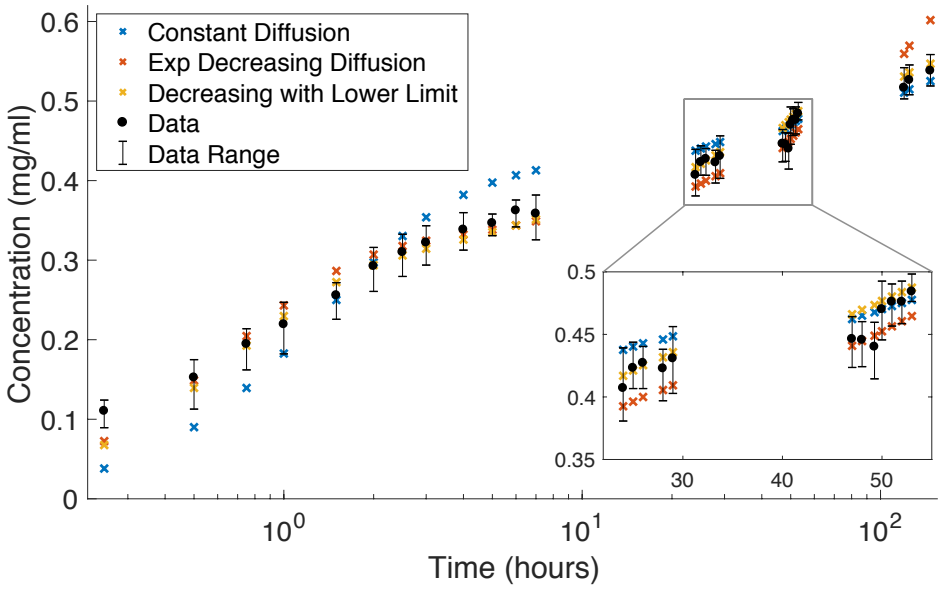


Figure 17: The best fits of the constant diffusion, D_1 (blue), exponentially decreasing diffusion, $D_2(t)$ (red) and exponentially decreasing diffusion with a lower limit, $D_3(t)$ (yellow) are shown against the average data (black) with the error bars as the range of all three experimental replicates. The exponentially decreasing diffusion with a lower limit gives the best fit to the data. Inset used as a visual aid to see the model fits more clearly.

2.5 THREE-DOMAIN MATHEMATICAL MODEL FOR EXPERIMENT 2

Consider the domain $\left[-x^b_{fluid}(t), x_{end}(t)\right]$ that comprises subdomains of fluid and PLGA/PEG. These subdomains are given by

- $\left[-x^b_{fluid}(t), 0\right]$,
- $[0, x_{PLGA/PEG}(t)]$ and
- $\left[x_{PLGA/PEG}(t), x_{PLGA/PEG}(t) + x^a_{fluid}(t)\right]$,

where $x_{end}(t) = x_{PLGA/PEG}(t) + x^a_{fluid}(t)$. We distinguish the two fluid subdomains as fluid subdomain a and fluid subdomain b, with corresponding superscripts on their subdomain lengths. As in the two-domain setup, let the

drug concentration C be a solution of the governing equation, Equation (23), where now

$$D(x,t) = \begin{cases} D_{fluid} & \text{if } x \in \left[-x^b_{fluid}(t), 0\right] \\ D_{PLGA/PEG}(t) & \text{if } x \in [0, x_{PLGA/PEG}(t)] \\ D_{fluid} & \text{if } x \in [x_{PLGA/PEG}(t), x_{end}(t)]. \end{cases} \tag{54}$$

We assume that nothing can leave the system between data time points, so zero flux boundary conditions are employed on the ends of the domain

$$D_{fluid}\frac{\partial C(-x^b_{fluid}, t)}{\partial x} = D_{fluid}\frac{\partial C(x_{end}(t), t)}{\partial x} = 0.$$

We also add the interface condition between the PLGA/PEG polymer and the fluid subdomains, so that

$$(1 - Q(t))C(0^-, t) = C(0^+, t), \tag{55}$$

and also, as in Experiment 1,

$$C(x^-_{PLGA/PEG}(t), t) = (1 - Q(t))C(x^+_{PLGA/PEG}(t), t), \tag{56}$$

where $1 - Q(t)$ is the water volume fraction within the PLGA/PEG constructs and $Q(t)$ is defined in Equation (22).

The initial condition for Experiment 2 is given by

$$C(x(0), 0) = \begin{cases} C_0 & \text{if } x(t) \in [x_{PLGA/PEG}(t), x_{end}(t)] \\ 0 & \text{otherwise.} \end{cases} \tag{57}$$

where C_0 is the initial drug concentration. See Figure 18 for a schematic of the model with the subdomain labels marked. We assume a cylindrical domain so that we can apply our one-dimensional model to the experiment. As in the two-domain model, we have to simulate sampling, evaporation and swelling. We do this using the same method as the two-domain model except we also have to remove fluid from subdomain b and consider the swelling dynamics.

We assume that swelling is a bulk process, which removes the same amount of fluid from subdomains a and b throughout time. This is complicated by the fixed internal boundary where the PLGA/PEG construct is attached to the Netwell insert, which does not allow swelling towards subdomain b. Under these assumptions, the external boundary at subdomain a moves away from the PLGA/PEG construct at a constant rate of $\dot{x}_{PLGA/PEG}/2$ and the external boundary at subdomain b moves towards the PLGA/PEG construct at the

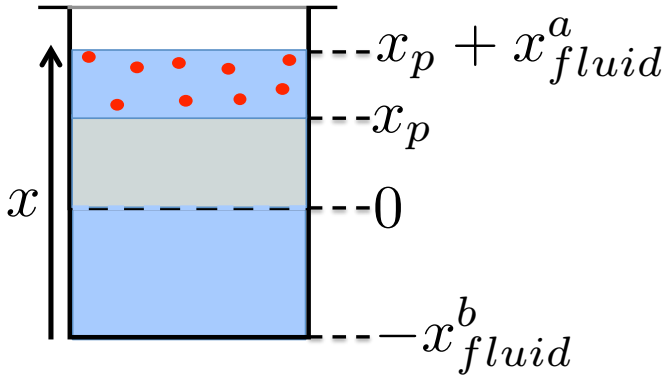


Figure 18: A schematic of the setup for Experiment 2, where theophylline concentration starts in the top fluid subdomain a, marked with the subdomain labels. We assume this cylindrical domain to apply our one-dimensional three-domain model.

same rate. To remedy this in the model, and in the subsequent numerical method to solve the model, we transform $x(t)$ to a moving frame of reference, $\bar{x}(t)$. We have

$$\bar{x}(t) = x(t) - x_{PLGA/PEG}(t)/2, \tag{58}$$

which gives

$$\dot{\bar{x}}(t) = \dot{x}(t) - \dot{x}_{PLGA/PEG}(t)/2. \tag{59}$$

In $\bar{x}$, the ends of the domain are fixed in space between data time points. The origin in the transformed domain is in the centre of the PLGA/PEG construct, such that the previously fixed internal boundary at the Netwell now moves towards subdomain b at rate $-\dot{x}_{PLGA/PEG}/2$. From now on, we only consider the transformed frame of reference and drop the $\bar{x}$ notation. To clarify, the subdomains are now given by

$$[-x^b_{fluid}(T_2^\beta), -x_{PLGA/PEG}(t)/2], \tag{60}$$

$$[-x_{PLGA/PEG}(t)/2, x_{PLGA/PEG}(t)/2] \text{ and} \tag{61}$$

$$[x_{PLGA/PEG}(t)/2, x_{PLGA/PEG}(t)/2 + x^a_{fluid}(T_2^\beta)]. \tag{62}$$

In this new frame of reference, the inclusion of evaporation and sampling is much like the two-domain model. At time point $t = T_2^{\beta+1}$ for some β, we update the domain from x to $\hat{x}$ such that the end points become

$$\hat{x}^a_{end}(T_2^{\beta+1}) = x^a_{end}(T_2^\beta) - Ex_e - x_s, \tag{63}$$

$$\hat{x}^b_{fluid}(T_2^{\beta+1}) = x^b_{fluid}(T_2^\beta) - (1-E)x_e - x_s, \tag{64}$$

where x_s and x_e are the domain lengths lost to sampling and total evaporation per data time point, respectively. We say that this transforms the domain as a whole, whose internal subdomains are continuously changing due to swelling, from $x(T_2^{\beta+1})$ to $\hat{x}(T_2^{\beta+1})$. We include a new parameter, $E \in [0,1]$, into these relationships as we do not know the proportion of evaporation that occurred in each fluid compartment. As before, sampling also removes concentration from the system, whereas evaporation does not, which in the model leads to

$$\begin{aligned}\int_{-x^b_{fluid}(T_2^{\beta+1})}^{x_{end}(T_2^{\beta+1})} \hat{C}(\hat{x}(T_2^{\beta+1}), T_2^{\beta+1})\, d\hat{x} = &\int_{-x^b_{fluid}(T_2^{\beta})}^{x_{end}(T_2^{\beta})} C(x(T_2^{\beta+1}), T_2^{\beta+1})\, dx \\ &- \int_{x_{end}(T_2^{\beta+1})}^{x_{end}(T_2^{\beta+1})+x_s} C(x(T_2^{\beta+1}), T_2^{\beta+1})\, dx, \\ &- \int_{-x^b_{fluid}(T_2^{\beta+1})-x_s}^{-x^b_{fluid}(T_2^{\beta+1})} C(x(T_2^{\beta+1}), T_2^{\beta+1})\, dx,\end{aligned} \tag{65}$$

where $\hat{C}$ and $\hat{x}$ are the updated concentration and updated domain, respectively.

The updated fluid subdomains are shorter, and the concentrations within them are higher as evaporation removes fluid but not drug. The simulated concentration in the PLGA/PEG subdomain is unaffected at the data time point, and alongside the new concentrations in the fluid compartments become the initial condition for the model until the next data time point where this process is repeated. The concentrations that are added to each fluid subdomain are given by

$$I_e^a = \frac{1}{\hat{x}^a_{fluid}(T_1^{\beta+1})} \int_{x_{end}(T_2^{\beta+1})}^{x_{end}(T_2^{\beta+1})+Ex_e} C(x(T_2^{\beta+1}), T_2^{\beta+1})\, dx \tag{66}$$

and

$$I_e^b = \frac{1}{\hat{x}^b_{fluid}(T_1^{\beta+1})} \int_{-x^b_{fluid}(T_2^{\beta+1})-(1-E)x_e}^{-x^b_{fluid}(T_2^{\beta+1})} C(x(T_2^{\beta+1}), T_2^{\beta+1})\, dx, \tag{67}$$

for fluid domain a and fluid domain b, respectively. So we have

$$\hat{C}(\hat{x}(T_2^{\beta+1}), T_2^{\beta+1}) = \begin{cases} C(x(T_2^{\beta+1}), T_2^{\beta+1})) + I_e^b & \text{if } x \in \text{fluid } b, \\ C(x(T_2^{\beta+1}), T_2^{\beta+1})) & \text{if } x \in \text{PLGA/PEG}, \\ C(x(T_2^{\beta+1}), T_2^{\beta+1})) + I_e^a & \text{if } x \in \text{fluid } a, \end{cases} \tag{68}$$

which acts as the condition to continue the model to the next data time point.

We assume that the swelling rate is the same as the power fit to the swelling data described in Section 2.2.5 and $Q(t)$ follows the power fit to the

PLGA/PEG volume fraction derived from the data also described in Section 2.2.5.

2.5.1 *Numerical Scheme for Three-Domain Model*

There are many similarities between the two-domain and three-domain numerical schemes. As in Section 2.3.1, we denote $PLGA/PEG$ subscripts as P in this section.

For each time, the one-dimensional space $x(t)$ is partitioned into three sets of points, one set for each subdomain. We use the same basis functions as described by Equation (31). Multiplying each side of Equation (23) by a test function V_h, a continuous function, and integrating over the domain with respect to x gives

$$\int_{-x^b_{fluid}}^{x_{end}} \frac{\partial C}{\partial t} V_h \, dx = \int_{-x^b_{fluid}}^{x_{end}} \frac{\partial}{\partial x} \left(D(x(t)) \frac{\partial C}{\partial x} \right) V_h \, dx$$

As V_h is arbitrary, we can choose it to be an arbitrary basis function, N_h. The integral of the diffusion term can then be split across the subdomains to give

$$\begin{aligned} \int_{-x^b_{fluid}}^{x_{end}} \frac{\partial}{\partial x} \left(D(x) \frac{\partial C}{\partial x} \right) N_h \, dx = D_{fluid} \int_{-x^b_{fluid}}^{-x_P/2} \frac{\partial^2 C}{\partial x^2} N_h \, dx + D_P \int_{-x_P/2}^{x_P/2} \frac{\partial^2 C}{\partial x^2} N_h \, dx \\ + D_{fluid} \int_{x_P/2}^{x_P/2 + x^a_{fluid}} \frac{\partial^2 C}{\partial x^2} N_h \, dx \end{aligned}$$

Each of these terms can now be integrated by parts which leads to the following across the whole domain:

$$\begin{aligned} \int_{-x^b_{fluid}}^{x_{end}} \frac{\partial}{\partial x} \left(D(x) \frac{\partial C}{\partial x} \right) N_h \, dx =& D_{fluid} \left[\frac{\partial C}{\partial x} N_h \right]_{-x^b_{fluid}}^{-x_P/2} - D_{fluid} \int_{-x^b_{fluid}}^{-x_P/2} \frac{\partial C}{\partial x} \frac{\partial N_h}{dx} \, dx \\ &+ D_P \left[\frac{\partial C}{\partial x} N_h \right]_{-x_P/2}^{x_P/2} - D_P \int_{-x_P/2}^{x_P/2} \frac{\partial C}{\partial x} \frac{\partial N_h}{dx} \, dx \\ &+ D_{fluid} \left[\frac{\partial C}{\partial x} N_h \right]_{x_P/2}^{x_P/2 + x^a_{fluid}} \\ &- D_{fluid} \int_{x_P/2}^{x_{P/2} + x^a_{fluid}} \frac{\partial C}{\partial x} \frac{\partial N_h}{dx} \, dx \end{aligned}$$

The continuity of flux, continuous test function space and Neumann boundary conditions lead to cancellation of the non-integral terms. In order to make full use of the test function space we are working in, we can re-express C as a

linear combination of hat functions N_j (of which there are m) and coefficients C_j, i.e.

$$C = \sum_{j=1}^{m} C_j N_j.$$

Using this, Equation (23) becomes

$$\begin{aligned}\sum_{j=1}^{m} \frac{\partial C_j}{\partial t} \int_{-x^b_{fluid}}^{x_{end}} N_j N_h \, dx = \sum_{j=1}^{m} C_j \Bigg(& - D_{fluid} \int_{-x^b_{fluid}}^{-x_P/2} \frac{\partial C}{\partial x} \frac{\partial N_h}{dx} \, dx \\ & - D_P \int_{-x_P/2}^{x_P/2} \frac{\partial N_j}{\partial x} \frac{\partial N_h}{dx} \, dx \\ & - D_{fluid} \int_{x_P/2}^{x_P/2 + x^a_{fluid}} \frac{\partial N_j}{\partial x} \frac{\partial N_h}{dx} \, dx \Bigg)\end{aligned}$$

Discretising the time derivative with a backwards Euler approach gives the approximation for the first term of Equation (23) at the nth time step (for time interval τ)

$$\sum_{j=1}^{m} \frac{\partial C_j}{\partial t}^n \int N_j N_h \, dx \approx \sum_{j=1}^{m} \left(\frac{C^n - C^{n-1}}{\tau} \right)_j \int N_j N_h \, dx.$$

Re-expressing this problem in condensed matrix notation across all test basis functions gives

$$\left(\frac{M^{n+1}}{\tau} + D(x(t)) A^{n+1} \right) \mathbf{C}^{n+1} = \frac{M^n}{\tau} \mathbf{C}^n,$$

where M will be referred to as the mass matrix and A is the stiffness matrix, and $\mathbf{C}^0$ is the initial condition of the model (Equation (57) for Experiment 2 and (83) for Experiment 3). The entries for these matrices are calculated in the same way as previously described in Section 2.3.1. However, as we now have three subdomains with a total of two interface conditions, the coupling of the mass matrices for each subdomain is slightly more involved. We use the same basic method of coupling together matrices as outlined for the two-domain model. This technique ensures that the three properly defined problems on each subdomain are coupled together appropriately.

At each data time point, we implement Equations (63)-(65) and (68) to remove the sampling and evaporation volumes, and set the concentration in the fluid domains for the scheme to continue to the next data time point. The scheme continues in this fashion until the desired end time point is reached.

2.5.2 *Three-Domain Model Input Values Derived from* in vitro *Data*

As we did for the two-domain model, we need to find the initial widths of the subdomains ($x^a_{fluid}(0)$ and $x^b_{fluid}(0)$) and ($x_{PLGA/PEG}(0)$), and the subdomain widths lost due to sampling (x_s) and evaporation (x_e).

We know the initial volumes of the fluid subdomains (0.7ml in x^a_{fluid} and 1.3ml in x^b_{fluid}), as well as the radius of the well-plate (7.8mm). Using these, a simple volume equation for a cylinder yields the initial domain lengths that we need:

$$x^a_{fluid}(0) = \frac{700}{7.8^2\pi} = 3.6623\text{mm}, \tag{69}$$

and

$$x^b_{fluid}(0) = \frac{1300}{7.8^2\pi} = 6.8015\text{mm}. \tag{70}$$

To calculate the initial length of the PLGA/PEG construct, we use the initial total weight of the PLGA/PEG powder (0.25g) and fluid (0.2g), alongside the calculated PLGA/PEG density from Section 2.2.5 and the initial fluid volume fraction, $Q(0)$. This gives

$$x_{PLGA/PEG}(0) = \frac{450((1-Q(0)) + Q(0)/1.2698)}{7.8^2\pi} = 1.9744\text{mm} \tag{71}$$

Each sample takes away 2μl of fluid, a similar calculation then yields

$$x_s = \frac{2}{7.8^2\pi} = 0.0105\text{mm}. \tag{72}$$

We use the gradient of the best fit to the evaporation data to find the fluid lost per time point, in this case we have

$$x_e = \frac{8.08}{7.8^2\pi} = 0.0423\text{mm}. \tag{73}$$

We use the power fit in Section 2.2.5 for the swelling, which extends the PLGA/PEG subdomain, as well as the power fit for $Q(t)$.

2.6 THREE-DOMAIN MODEL FITTING TO EXPERIMENT 2

We use the same functional forms of diffusion as we did for the two-domain model fit, $D_1(t) = D_0$, $D_2(t) = D_0 e^{-\alpha t}$, and $D_3(t) = (D_0 - \beta)e^{-\alpha t} + \beta$. We also have to fit the proportion of evaporation within each fluid subdomain, E. We slightly decreased the parameter range of D_0, α and β compared with Section 2.4 to limit the computational expense of our parameter search. We used $D_0 \in [10^{-1}, 10^2]\text{mm}^2/\text{hour}$, $\alpha \in [10^{-1}, 10^1]/\text{hour}$, and $\beta \in [10^{-3}, 10^1]\text{mm}^2/\text{hour}$ all

with increments of $10^{0.125}$. For E, we use 11 values, $0, 0.1, 0.2, \ldots, 1$. For the error, we use an analogous term to that presented for the fitting to the two-domain model (Section 2.4). We find the average across each simulated fluid subdomain at each simulated time point, $t = T_2^\beta$ for all $\beta = 1, \ldots, 23$, which are given by

$$\mu^a = \frac{\int_{x_{PLGA/PEG}(T_2^\beta)/2}^{x_{end}(T_2^\beta)} C(x, T_2^\beta)\, dx}{x^a_{fluid}(T_2^\beta)} \tag{74}$$

and

$$\mu^b = \frac{\int_{-x^b_{fluid}(T_2^\beta)}^{-x_{PLGA/PEG}/2} C(x, T_2^\beta)\, dx}{x^b_{fluid}(T_2^\beta)}. \tag{75}$$

We express the error as

$$L^2 = \sqrt{\sum_{\beta=1}^{23} \left(\mu^a - C^a_{data}(T_2^\beta)\right)^2 + \left(\mu^b - C^b_{data}(T_2^\beta)\right)^2}, \tag{76}$$

and minimise this expression to find the optimal parameter set for each functional form of diffusion, where C^a_{data} and C^b_{data} are the mean data point concentrations across the three replicates for subdomain a and subdomain b, respectively.

We find that the best fits of the model to our *in vitro* data for Experiment 2 are achieved for

$$D_1(t) = D_0 = 0.75\text{mm}^2/\text{hour}\ , E = 0, L^2 = 1.02\text{mg/ml}, \tag{77}$$

$$D_2(t) = D_0 e^{-\alpha t} = 5.6e^{-0.18t}\text{mm}^2/\text{hour}\ , E = 1, L^2 = 0.74\text{mg/ml and} \tag{78}$$

$$D_3(t) = (D_0 - \beta)e^{-\alpha t} + \beta = 7.5e^{-0.42t} + 0.32\text{mm}^2/\text{hour}, E = 1,$$
$$L^2 = 0.71\text{mg/ml}. \tag{79}$$

As in Experiment 1 with the two-domain model, we see that the minimum error is achieved across all three functional forms of diffusion for $D_3(t)$. However, compared to Experiment 1 these errors are much larger and there is less relative difference in the error between the best fit for $D_2(t)$ and $D_3(t)$.

We present the simulation concentration data points against the actual data points in Figure 19. As can be seen in this figure, the simulated concentration in the fluid subdomain b is consistently less than the data across all functional forms of diffusion.

The fit of the model to the data for Experiment 2 suggests that there is more solvent lost than we measured. As we measured the weight of the

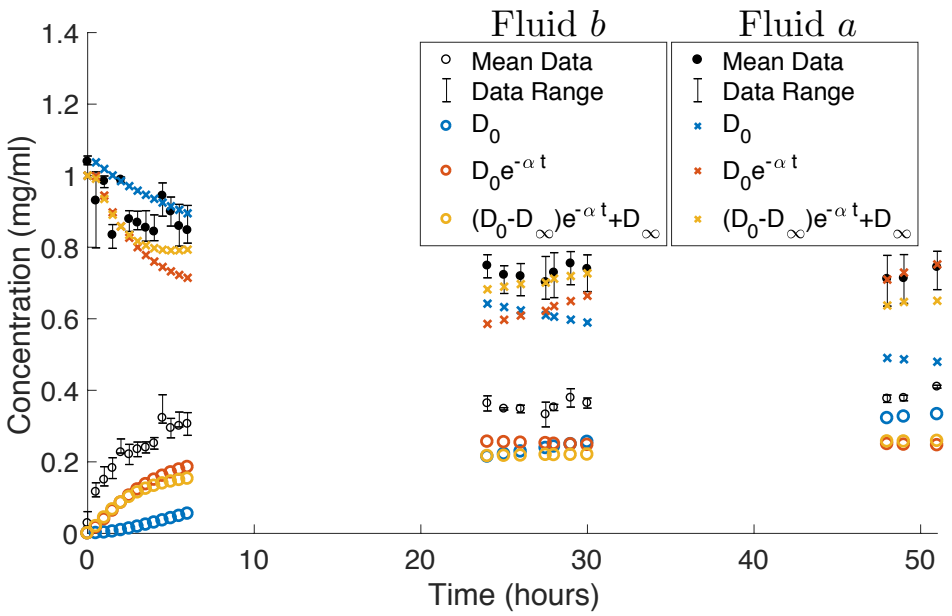


Figure 19: The best fits of the constant diffusion (blue), exponentially decreasing diffusion (red) and exponentially decreasing diffusion with a lower limit (yellow) are shown against the average data (black) with the error bars as the range of all three experimental repeats. The exponential diffusion with a lower limit gives the best fit to the data, followed closely by the exponential diffusion. Constant diffusion gives the worst model fit to the data.

well-plate during the experiment, we know that more water did not leave the system as a whole. It must be the case that water left the experimental setup or was used elsewhere. Water that evaporated but condensed onto the well plate or onto the sides of the Netwell was not measured, and could be a possible cause for this discrepancy. We include an extra parameter in the model to consider this extra water loss, denoted as x_{WL} and assume it occurs at each data time point with the measured evaporation, x_e. We ran another parameter scan with parameters as described in Section 2.5.2 and included values of $x_{WL} \in [0.05, 0.20]$mm with an increment of 0.01mm. Following the

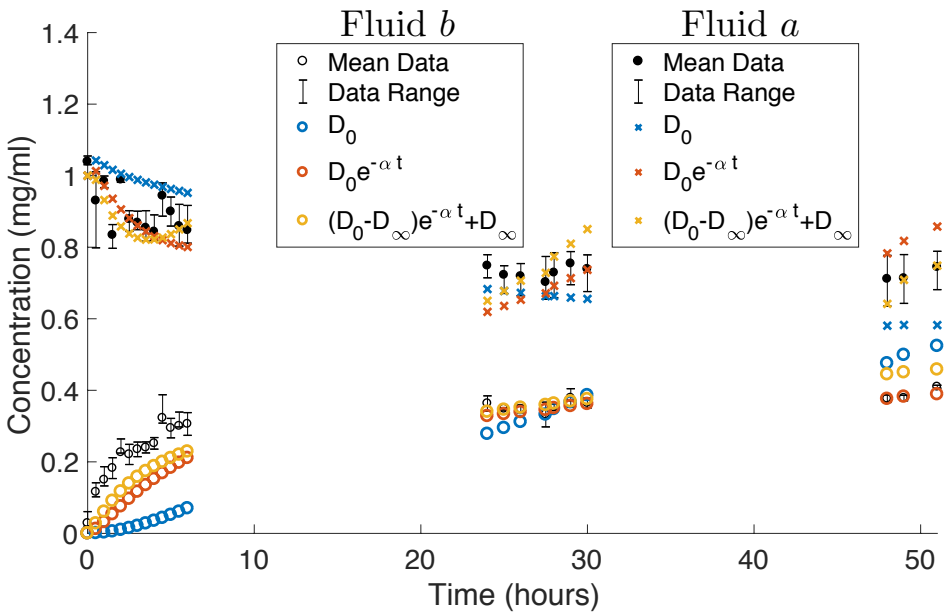


Figure 20: The best fits of the constant diffusion (blue), exponentially decreasing diffusion (red) and exponentially decreasing diffusion with a lower limit (yellow) are shown against the average data (black) with the error bars as the range of all three experimental repeats. With the extra water loss fitting, the exponentially diffusing coefficient with a lower limit gives the best fit. Constant diffusion still gives the worst model fit to the data.

parameter scan, we find the best fits to the data for Experiment 2 with the extra water loss, x_{WL}, are given by

$$D_1 = 0.75\text{mm}^2/\text{hour}\ , E = 0.1, x_{WL} = 0.14\text{mm}, L^2 = 0.91\text{mg/ml}, \tag{80}$$

$$D_2(t) = 4.2e^{-0.13t}\text{mm}^2/\text{hour}\ , E = 0.3, x_{WL} = 0.15\text{mm}, \quad L^2 = 0.54\text{mg/ml}, \tag{81}$$

$$D_3(t) = (10 - 0.56)e^{-0.42t} + 0.56\text{mm}^2/\text{hour}, E = 0.4, x_{WL} = 0.19\text{mm}, \quad L^2 = 0.42\text{mg/ml}. \tag{82}$$

Again, we see that $D_3(t)$ gives the best fit to the data. We present the simulated data points for the best fits for all functional forms of diffusion against the actual mean data points in Figure 20. The model fit suggests that x_{WL} is larger than domain length lost for measured evaporation in this experiment across all time-dependent functional forms of diffusion, suggesting that in future experiments it is important to measure this extra loss.

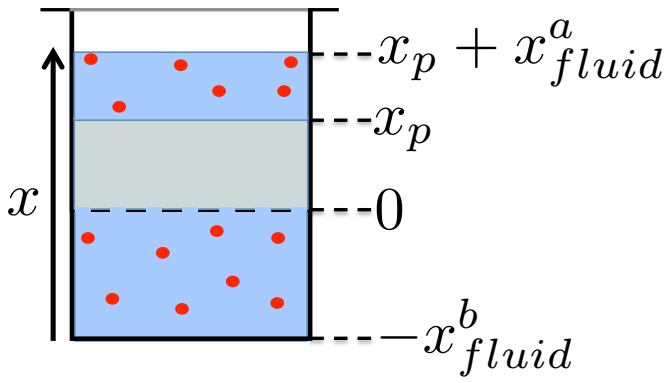


Figure 21: A schematic of the setup for Experiment 3, where theophylline concentration starts in both the top and bottom compartments, marked with the subdomain end points. We assume that the domain can be modelled as a cylinder so that we can apply our one-dimensional three-domain model.

2.7 THREE-DOMAIN MATHEMATICAL MODEL FOR EXPERIMENT 3

The three-domain model setup for Experiment 3 is almost identical to the model setup for Experiment 2 (Section 2.5). The only difference is the initial condition, $C(x(0), 0)$. As in this experiment the drug concentration began in both fluid subdomain a and fluid subdomain b, we have

$$C(x(0), 0) = \begin{cases} C_0 & \text{if } x \text{ is in a fluid subdomain,} \\ 0 & \text{otherwise.} \end{cases} \tag{83}$$

where C_0 is the initial drug concentration of 0.35mg/ml. See Figure 21 for the initial assumed model domain. As in the model to describe Experiment 2, we transform the domain so that we have fixed external boundaries.

The numerical scheme for this model is exactly the same as the model setup for Experiment 2 and is found in Section 2.5.1.

	Experiment 1	Experiment 2	Experiment 3	Units
$x_{PLGA/PEG}(0)$	0.95	1.97	1.97	mm
$x^A_{fluid}(0)$	2.54	3.66	3.66	mm
$x^B_{fluid}(0)$	-	6.80	6.80	mm
$C(x_{PLGA/PEG}(0)\,,0)$	0	1	0.35	mg/ml
$C(x^A_{fluid}(0)\,,0)$	1.06	0	0.35	mg/ml
$C(x^B_{fluid}(0)\,,0)$	-	0	0	mg/ml
x_e	7.35×10^{-3}	4.23×10^{-2}	4.23×10^{-2}	mm
x_s	5.08×10^{-3}	1.05×10^{-2}	1.05×10^{-2}	mm

Table 2: Initial conditions for the lengths and concentrations of the domains in the model, as well as the reduction in domain length per time point due to evaporation.

2.8 MODEL VALIDATION THROUGH EXPERIMENT 3

The experimental setup and subsequent model setup for Experiment 3 are extremely similar to those for Experiment 2. The only difference is the initial placement of the drug, which in Experiment 3 is in a lower concentration across both fluid subdomains, whereas in Experiment 2 it is only initially in fluid subdomain a. We therefore decided to use the diffusion and water loss parameter fits of Experiment 2 against the data of Experiment 3 to see if the time-dependent exponentially decreasing diffusion coefficient with a lower limit, $D_3(t)$, has the best fit.

As can be seen in Table 3, the best fit to the data for Experiment 3 was given by $D_2(t)$ for the case with extra water loss. This further suggests that there is some slowing of the diffusion dynamics over time in the PLGA/PEG constructs, as well as extra water loss. However, due to the initial condition, the dynamics for Experiment 3 are dominated much more by the water lost through evaporation, swelling and any other water-loss mechanisms. We have shown the best-fit simulated data points against the mean data points for Experiment 3 and their range in Figure 22. We see that the extra water loss in subdomain a leads to a quickly increasing simulated concentration. We also do not see a good fit for subdomain b towards the start of the experiment. It is also curious that the best fit to this Experiment is given by $D_2(t)$ and not $D_3(t)$, this could be due to the differences in extra water loss between these

	Parameter Set						Units
D_0	0.75	0.75	5.6	4.2	7.5	10	$mm^2/hour$
α	-	-	0.18	0.13	0.42	0.42	1/hour
D_∞	-	-	-	-	0.32	0.56	$mm^2/hour$
E	0	0.1	1	0.3	1	0.4	1
x_{WL}	-	0.14	-	0.15	-	0.19	mm
L^2	0.56	0.46	0.53	0.28	0.54	0.37	mg/ml

Table 3: The optimal parameter sets from calibration to Experiments 2 were used to validate against Experiment 3. We see that the minimal L^2 error occurs in the cases of extra water loss for time-dependent diffusion, certainly not constant diffusion; suggesting that diffusion is time dependent in these experiments. Unlike the model fitting for Experiments 1 and 2 (both with and without the extra water loss), we see that $D_2(t)$ fits best in these cases.

experimental fits. We would need to conduct more experiments to extensively validate our parameter sets.

2.9 RESULTS AND DISCUSSION

From our *in vitro* experiments, it is clear that PLGA/PEG swells in water. Our mathematical model suggests that drug diffusion through the PLGA/PEG is time dependent and decreases throughout its treatment lifespan. We have observed no clear differences in the diffusion dynamics between the release of drug that was present during the polymer sintering process and diffusion of drug through the pre-sintered polymer but we do see varying rates in our best model fits. Although the optimal diffusion parameters do differ between the experiments, it is unclear as to whether or not this is significant due to the higher than expected concentrations in Experiments 2 and 3, despite accounting for variables such as evaporation and swelling in the model, as well as fitting for extra water lost in Experiment 2.

We have found that the PLGA/PEG polymer swells and the drug dynamics slow down over time. These effects, which appear related, are important considerations in drug diffusion dynamics for the PLGA/PEG construct in clinical use. Over the proposed timescale of treatment of 2-3 weeks, the time-dependent diffusion of the PLGA/PEG makes it somewhat harder to give a

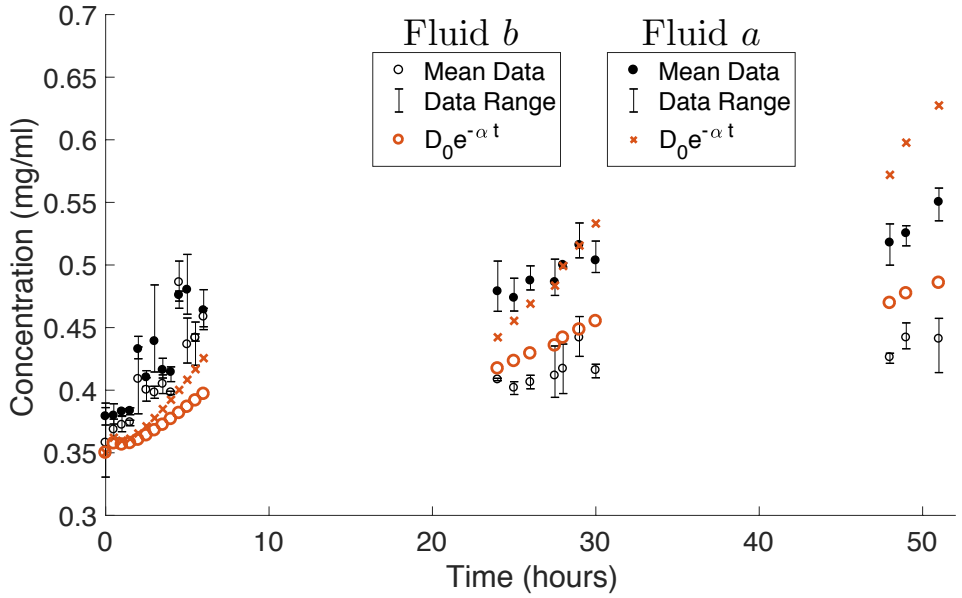


Figure 22: The best fit of the exponentially decreasing diffusion (red) is shown against the average data from Experiment 3 (black) with the error bars as the range of all three experimental repeats. This was the best fit to the data from the previous calibrations, as can be seen from Table 3.

sustained constant dose to a cancerous tissue region. With this treatment, we want to be able to treat as many cancerous cells as possible. We need to get a therapeutic dose to the cancerous region for the whole treatment window, which is hard to achieve if the release slows down over time.

We also note that our initial values for our drug diffusion, D_0, are high relative to reported theophylline diffusion values through water [51]. Faster dynamics than expected could be due to the rocking of the experiment having an impact on the movement of the drug. This is why we have refrained from making quantitative judgements of our computed diffusion rates and instead focused on qualitative results of the drug diffusion slowing down over time. To get a more accurate handle on the quantitative rates, we would have to create another iteration of our experimental design. Even though the rocker would have increased the rate at which diffusion occurred, this effect was constant between data time points throughout all experiments.

2.10 FUTURE WORK

There are many assumptions in our model that we used to simulate our *in vitro* experiments. Some of our assumptions could be explored further to allow for a more accurate mathematical model or an experimental setup that is more aligned with *in vivo* conditions. We have assumed, for example, that the volume increase observed in our swelling data will be the same as in Experiments 1, 2 and 3. However, the radial swelling observed in the swelling data cannot occur in our other experiments due to the radial boundary of the well plate, and PLGA/PEG constructs adhere to other surfaces. In the future, we could measure swelling of PLGA/PEG constructs that are inhibited by a radial boundary to test the validity of our assumption as well as provide a water volume fraction in the PLGA/PEG under these circumstances ($Q(t)$ in the model). It might be that the inhibition of radial swelling instead creates a denser PLGA/PEG construct, which decreases $Q(t)$ more than we observed in the swelling data, and could further explain the time-dependent diffusion observed in our model fitting.

Our model could easily be adapted to include a one dimensional layer of brain. In the future, we could create more *in vitro* experiments to include a layer of mouse brain and see how quickly theophylline diffuses into the brain. If we were to include some fluid flow, we could test the importance of adherence of the PLGA/PEG constructs to the brain and the effects of a fluid gap between them.

It is not yet clear whether the retardation of drug diffusion over time is an important consideration in the efficacy of the treatment when compared with a constant diffusion coefficient. Although we have not observed this directly in our experiments, the swelling of a thicker PLGA/PEG paste might inhibit drug diffusion before it can be fully released. In which case, the drug would be held in the polymer construct until it degraded sufficiently. In the future, we would like to include our PLGA/PEG model within a tumour growth model. We could use such a model to test various PLGA/PEG geometries, thicknesses and formulations to study treatment efficacy *in silico*.

The faster-than-expected rate that our calibrated one-dimensional model has given for the initial diffusion through the PLGA/PEG polymer has hindered our ability to make quantitative assessments of the diffusion dynamics. In future work, we would redesign our *in vitro* experiments so that the rocker was not included, to see for certain whether it was the increasing factor in the

diffusion rates. Such a design would ideally incorporate UV-vis spectrophotometry to directly measure the concentrations within the set up throughout time.

3

HOMOGENISATION OF DIFFUSION APPLIED TO PLGA/PEG POLYMER CONSTRUCTS

In this chapter, we will introduce homogenisation of diffusion theory in one spatial dimension, before describing it in N dimensions. The one-dimensional theory leads to an analytical homogenised diffusion coefficient, whereas N-dimensional theory ($N > 1$) needs to be solved numerically.

We apply the theory in three dimensions to a novel chemotherapy drug delivery polymer under development at the Children's Brain Tumour Research Centre as a brain tumour treatment with finite element simulations. The internal structure and drug diffusion dynamics through this polymer are not fully understood. We use microCT scans of the polymer, which on this small scale consists of polymer clumps and gaps between them, as domains in these finite element simulations. The simulated homogenised diffusion values are then used to test variability within and between polymer replicates, as well as to analyse the structure of these polymers.

Results show that the homogenised diffusion coefficients correlates strongly with polymer density, with fluctuations caused by polymer's structure. Asymptotic analysis of the homogenised diffusion coefficients suggest that both polymer channels and gap channels exist throughout the polymer structure. It is important that the density and structure of the polymer is considered in future patient applications to keep the treatment consistent.

3.1 BACKGROUND

Homogenisation of diffusion is a process that finds an equation for the large scale diffusion behaviour of a composite material. Once derived, this equation leads to an effective diffusion tensor for diffusion through the composite material, that is computed using the diffusion coefficients of substances diffusing through the constituent materials and the constituent materials' small-scale

structures. A comprehensive book by Pavliotis and Stuart gives the theory of homogenisation for a variety of mathematical equations [110]. In this chapter, we focus only on homogenisation of diffusion for partial differential equations.

As we have already discussed in Chapter 2, the drug delivery system is a polymer called poly(lactic-co-glycolic acid)/poly(ethylene glycol) (PLGA/PEG) that can be loaded with chemotherapy drugs and applied directly to a cavity wall created after a tumour has been surgically removed. Diffusion dynamics of chemotherapy drugs through PLGA/PEG have not been quantified on a small scale. The brain tumour that this treatment is being developed for is called glioblastoma multiforme (GBM), it is the most aggressive primary brain tumour with only a 15 month expected survival post diagnosis despite treatment [132, 133]. Surgical removal of the tumour, known as a resection, is part of the standard of care for these tumours but does not act as a cure [132, 133]. This is because GBMs typically have a very diffuse leading edge, so that the tumour cells disperse within the healthy tissue as the tumour grows. These cells are often hard to remove as doing so would remove too much healthy tissue and could limit brain function. It is these tumour cells, on the leading edge of the tumour, that chemotherapy drugs released from PLGA/PEG would treat [115].

For the PLGA/PEG treatment, consistency both between and within patients is important. To be most effective, this treatment should give a dose to the remaining tumour cells in the brain that is consistent and predictable. So ideally a small region of the polymer should have the same drug delivery dynamics as the rest. This could also allow for the tailoring of the polymer thickness to optimise the spatial delivery of the chemotherapy drug dose within patients. For example, an area with high tumour cell density post resection might have a thicker application of the PLGA/PEG paste than an area with only a few tumour cells remaining.

3.2 THEORY

In this section we look at the assumptions of homogenisation of diffusion theory, before stating the theory in 1 and then N dimensions.

3.2.1 *Assumptions*

To begin with, periodic assumptions are made on the PLGA/PEG so that the material can be split into small equivalent blocks. Note that this forces the diffusion to be periodic also. Although not strictly necessary for the theory, we shall assume that our periodic structures are symmetric about all centre axes; this assumption ensures the preservation of any channels through the composite material.

We also assume that the periodic structures in the PLGA/PEG are on a sufficiently small scale, such that submaterials of the PLGA/PEG constructs and subsequently their corresponding drug diffusion coefficients change rapidly on the scale of the PLGA/PEG construct as a whole. More precisely, the solution is assumed to have some average behaviour with small zero-average fluctuations on a sufficiently small scale.

The final assumption is that the small scale and large scales can be considered independent.

3.2.2 *Homogenisation in One Spatial Dimension*

Start with a simple Fickian diffusion equation in one spatial dimension

$$\frac{\partial C}{\partial t} = \frac{\partial}{\partial x}\left(D\left(\frac{x}{\epsilon}\right)\frac{\partial C}{\partial x}\right), \tag{84}$$

where the assumption of the diffusion depending on the small scale behaviour has been used for some sufficiently small ϵ. For homogenisation to apply, C has to have some average behaviour with small fluctuations of order ϵ.

Consider two variables on different length scales that are assumed independent: $z = x$ and $\xi = x/\epsilon$. We then have that

$$C(x,t) = C(z(x), \xi(x), t). \tag{85}$$

With the use of the chain rule

$$\frac{\partial}{\partial x} = \frac{\partial}{\partial z} + \frac{1}{\epsilon}\frac{\partial}{\partial \xi}, \tag{86}$$

Equation (84) becomes

$$\frac{\partial C}{\partial t} = \frac{\partial}{\partial z}\left(D(\xi)\left(\frac{\partial C}{\partial z} + \frac{1}{\epsilon}\frac{\partial C}{\partial \xi}\right)\right) + \frac{1}{\epsilon}\frac{\partial}{\partial \xi}\left(D(\xi)\left(\frac{\partial C}{\partial z} + \frac{1}{\epsilon}\frac{\partial C}{\partial \xi}\right)\right). \tag{87}$$

Now make use of the assumption that C has some average behaviour with small zero average fluctuations within each periodic subdomain. Set

$$C(z,\xi,t) = \bar{C}(z,t) + \epsilon w(z,\xi,t), \tag{88}$$

where $w(\xi)$ and its ξ derivative are periodic, with $\int_0^1 w\, d\xi = 0$ (zero average). Also note that the average behaviour, $\bar{C}(z,t)$, has no dependence on the small scale, ξ. Expanding $\bar{C}$ and w into their power series solutions gives

$$\bar{C} = C_0 + \epsilon C_1 + \mathcal{O}(\epsilon^2), \tag{89}$$

$$w = w_0 + \epsilon w_1 + \mathcal{O}(\epsilon^2). \tag{90}$$

We can substitute the power series solutions and Equation (88) into our latest governing equation, Equation (87); this leads to an equation of the form

$$A\epsilon^{-1} + B\epsilon^0 + \mathcal{O}(\epsilon) = 0. \tag{91}$$

Equating coefficients of ϵ shows that both $A = 0$ and $B = 0$. We ignore higher order epsilon terms as we assume they are negligible. The $A = 0$ equation is given by

$$\frac{\partial}{\partial \xi}\left(D(\xi)\left(\frac{\partial w_0}{\partial \xi} + \frac{\partial C_0}{\partial z}\right)\right) = 0. \tag{92}$$

Collecting terms of order ϵ^0 gives our $B = 0$ equation:

$$\frac{\partial C_0}{\partial t} = \frac{\partial}{\partial \xi}\left(D(\xi)\left(\frac{\partial w_1}{\partial \xi} + \frac{\partial w_0}{\partial z} + \frac{\partial C_1}{\partial z}\right)\right) + \frac{\partial}{\partial z}\left(D(\xi)\left(\frac{\partial C_0}{\partial z} + \frac{\partial w_0}{\partial \xi}\right)\right). \tag{93}$$

The zero average assumption on w and independence of $\bar{C}$ with respect to ξ also hold on each of the terms in their respective power series expansions. To make use of this, integrate Equation (93) across the periodic microdomain with respect to ξ. The periodicity of both w_1 and its derivative with respect to ξ cause the $\partial w_1/\partial \xi$ term of Equation (93) to vanish. The periodicity of both $D(\xi)$ and w_0 with respect to ξ along with the independence of C to ξ cause the $\partial w_0/\partial z$ and $\partial C_1/\partial z$ terms to vanish, too. We are then left with

$$\frac{\partial C_0}{\partial t} = \int_0^1 \frac{\partial}{\partial z}\left(D(\xi)\left(\frac{\partial C_0}{\partial z} + \frac{\partial w_0}{\partial \xi}\right)\right) d\xi. \tag{94}$$

This equation will become our new homogenised equation and is completely in terms of C_0 except for the $\partial w_0/\partial \xi$ term. Fortunately, we can derive an expression for $\partial w_0/\partial \xi$ in terms of C_0 by solving the ϵ^{-1} equation, Equation (92). We start by integrating Equation (92) with respect to ξ; this gives

$$D(\xi)\left(\frac{\partial w_0}{\partial \xi} + \frac{\partial C_0}{\partial z}\right) = \alpha(z), \tag{95}$$

which rearranges to

$$\frac{\partial w_0}{\partial \xi} = \frac{\alpha(z)}{D(\xi)} - \frac{\partial C_0}{\partial z}, \tag{96}$$

for an unknown, $\alpha(z)$. We can fix our unknown $\alpha(z)$ using the periodicity condition on w_0,

$$\int_0^1 \frac{\partial w_0}{\partial \xi} d\xi = w(1) - w(0) = 0. \tag{97}$$

Using the above equation with our expression for $\partial w_0/\partial \xi$ gives

$$0 = \int_0^1 \left(\frac{\alpha(z)}{D(\xi)} - \frac{\partial C_0}{\partial z} \right) d\xi. \tag{98}$$

So

$$\alpha(z) = \frac{\partial C_0}{\partial z} \left(\int_0^1 \frac{1}{D}\, d\xi \right)^{-1}, \tag{99}$$

where we have used the independence of the variables to move those that do not depend on ξ outside the integral. We are then left with our expression for $\partial w_0/\partial \xi$ in terms of C_0

$$\frac{\partial w_0}{\partial \xi} = \left(\frac{1}{D} \left(\int_0^1 \frac{1}{D}\, d\xi \right)^{-1} - 1 \right) \frac{\partial C_0}{\partial z}, \tag{100}$$

Equation (100) now simplifies Equation (94) to give the homogenised version of Equation (84)

$$\frac{\partial C_0}{\partial t} = D^{eff} \frac{\partial^2 C_0}{\partial z^2}, \tag{101}$$

where

$$D^{eff} = \left(\int_0^1 \frac{1}{D(\xi)}\, d\xi \right)^{-1} = \epsilon \left(\int_0^\epsilon \frac{1}{D\left(\frac{x}{\epsilon}\right)}\, dx \right)^{-1}. \tag{102}$$

This effective diffusion is the harmonic average of the spatially-dependent diffusion coefficients. If all diffusion coefficients, D, are equal across the domain, the effective diffusion reduces to D.

A species diffusing in one spatial dimension has to travel through every subdomain of constituent material in order to reach the other side. Most real-world problems would not have this simple structure and must be modelled in higher spatial dimensions.

3.2.3 *Homogenisation in N Spatial Dimensions*

It is not possible for a homogenised diffusion tensor to be found analytically on domains of dimension higher than one (that are not reducible to one dimension). Therefore, the diffusion tensor must be found numerically.

The theory for higher dimensions is otherwise a generalisation of the one-dimensional case. Start with the equation

$$\frac{\partial C}{\partial t} = \nabla \cdot (D(\boldsymbol{\xi}) \nabla C) \,. \tag{103}$$

Assuming again that there are two independent variables $\boldsymbol{z} = \boldsymbol{x}$ and $\boldsymbol{\xi} = \boldsymbol{x}/\epsilon$. We will note our small ϵ-scale subdomain S, that exists in an N-dimensional space. Expand C into its mean field approximation and a smaller variable on the ϵ scale

$$C = \bar{C} + \epsilon w, \tag{104}$$

with $\bar{C}$ independent of $\boldsymbol{\xi}$, w is a periodic function of $\boldsymbol{\xi}$ with zero average. Expand $\bar{C}$ and w into their power series solutions and equate orders of ϵ. Collecting and equating terms of ϵ^{-1} gives

$$\nabla_{\xi} \cdot \left(D(\boldsymbol{\xi}) [\nabla_{\xi} w_0 + \nabla_z C_0] \right) = 0. \tag{105}$$

The terms of ϵ^0 give

$$\frac{\partial C_0}{\partial t} = \nabla_{\xi} (D(\boldsymbol{\xi}) [\nabla_{\xi} w_1 + \nabla_z (C_1 + w_0)]) + D(\boldsymbol{\xi}) \nabla_z [\nabla_{\xi} w_0 + \nabla_z C_0]. \tag{106}$$

Terms of higher order of epsilon are considered negligible and ignored from the model. We can solve Equation (105) using the ansatz

$$w_0 = W(\boldsymbol{\xi}) \cdot \nabla_z C_0, \tag{107}$$

where

$$W(\boldsymbol{\xi}) = (W_1, W_2, \ldots, W_N)^T \,,$$

with N the dimension of the space. Using this ansatz simplifies Equation (105) to the point where it can be solved numerically as a set of cell problems, the process for which can be seen clearly using the summation convention. Ansatz (107) becomes

$$w_0 = W_i \frac{\partial C_0}{\partial z_i}; \tag{108}$$

which when substituted into Equation (105) gives

$$\nabla_{\xi} \cdot \left(D(\boldsymbol{\xi}) \left[\nabla_{\xi} \left(W_i \frac{\partial C_0}{\partial z_i} \right) + \nabla_z C_0 \right] \right) = 0.$$

Noting that C_0 is independent of the small $\boldsymbol{\xi}$ scale and the definition of the gradient operator leads to the following:

$$\nabla_{\xi} \cdot \left(D(\boldsymbol{\xi}) \left[\frac{\partial W_i}{\partial \xi_j} \frac{\partial C_0}{\partial z_i} + \frac{\partial C_0}{\partial z_j} \right] \right) = 0,$$

where $j = 1, \ldots, N$. Again using the assumption that C_0 is independent of $\boldsymbol{\xi}$ leads to

$$\nabla_{\boldsymbol{\xi}} \cdot \left(D(\boldsymbol{\xi}) \left[\frac{\partial W_i}{\partial \xi_j} + \delta_{ij} \right] \right) \frac{\partial C_0}{\partial z_i} = 0.$$

Equating coefficients of $\partial C_0 / \partial z_i$ leads to the set of cell problems given by

$$\nabla_{\boldsymbol{\xi}} \cdot (D(\boldsymbol{\xi})[\nabla_{\boldsymbol{\xi}} W_i(\boldsymbol{\xi}) + e_i]) = 0, \tag{109}$$

subject to periodic boundary conditions on each $W_j(\boldsymbol{\xi})$, inherited from those assumed on w. We have denoted e_i as the unit vector in the direction of i.

Now assuming that $W(\boldsymbol{\xi})$ is known (see Section 3.3 for how this is found). Integrating Equation (106) across a whole periodic domain, S, causes the first two terms to vanish due to the periodic assumptions on D and w; this gives

$$\frac{\partial C_0}{\partial t} = \int_S D(\boldsymbol{\xi}) \nabla_z [\nabla_{\boldsymbol{\xi}} w_0 + \nabla_z C_0] \, d\boldsymbol{\xi}.$$

Now substitute Ansatz (108) for w_0 into the above; this leads to

$$\frac{\partial C_0}{\partial t} = D^{eff} \nabla_z^2 C_0, \tag{110}$$

where

$$D_{ij}^{eff} = \int_S D(\boldsymbol{\xi})(e_i + \nabla_{\boldsymbol{\xi}} W_i) \cdot e_j \, d\boldsymbol{\xi}. \tag{111}$$

This is often presented in the equivalent form

$$D_{ij}^{eff} = \int_S D(\boldsymbol{\xi})(e_i + \nabla_{\boldsymbol{\xi}} W_i) \cdot (e_j + \nabla_{\boldsymbol{\xi}} W_j) \, d\boldsymbol{\xi}, \tag{112}$$

the extra term does not contribute to the integral by construction, assuming that the structure has reflectional symmetry across all axes going through the centre of the structure; see for example [5, 16].

The effective diffusion tensor, D^{eff}, is an NxN matrix. If the assumed periodic structure is invariant to any $\pi/2$ rotation, D^{eff} is a scalar multiple of the identity matrix. If there is reflectional symmetry across all axes going through the centre of the structure, then D^{eff} is a diagonal matrix with possibly different entries. The periodic blocks of PLGA/PEG that we use have reflectional symmetry and will therefore give diagonal matrices for their effective diffusion tensors.

3.3 SOLVING NUMERICALLY

3.3.1 *Numerical Scheme*

To compute the effective diffusion, the cell problem given by Equation (109) needs to be solved numerically. We have done this with a continuous galerkin

finite element method using periodic shape functions. Multiply Equation (109) by a continuous and periodic linear finite element test function V and integrate with respect to $\boldsymbol{\xi}$ over one periodic domain

$$\int_S \nabla_{\boldsymbol{\xi}}(D(\boldsymbol{\xi})[\nabla_{\boldsymbol{\xi}} W_j(\boldsymbol{\xi}) + e_j])V \, d\boldsymbol{\xi} = 0, \tag{113}$$

which gives

$$[D(\nabla_{\boldsymbol{\xi}} W_j + e_j)V]_S - \int_S D(\nabla_{\boldsymbol{\xi}} W_j + e_j)\nabla_{\boldsymbol{\xi}} V \, d\boldsymbol{\xi} = 0. \tag{114}$$

Subsequently, due to the periodic assumptions on D, W and V,the boundary terms vanish to give

$$\int_S D\nabla_{\boldsymbol{\xi}} W_j \cdot \nabla_{\boldsymbol{\xi}} V \, d\boldsymbol{\xi} = -\int_S De_j \cdot \nabla_{\boldsymbol{\xi}} V \, d\boldsymbol{\xi}. \tag{115}$$

Although it does not change the effective diffusion values, solutions W_j presented here will be normalised so that they have 0 integral over the domain. This allows for uniqueness in the solution and is consistent with our previous assumptions. For all of our numerical solutions we used the open source finite element software FEniCS, making use of the DOLFIN library [6, 81, 82].

Homogenisation Examples

In this section we show some homogenisation examples. These are used to illustrate the differences between homogenisation theory and intuitive averages that one might expect should be used to find effective diffusion coefficients. Figures 23 and 24 compare some intuitive averaging ideas against the homogenised coefficient for specific test cases. In these 2D cases, effective diffusion simulations are run on a square of a composite material with area 1, containing a centralised square of a submaterial with area 1/4. The diffusion coefficient through the material presented in red is varied, with the other (blue) submaterial's diffusion coefficient fixed at 1. As you can see, the effective diffusion does not follow the harmonic average (as it would in 1D) or the volume weighted average in either test case. The geometry of the periodic composite material is extremely important for the effective diffusion dynamics. We see in Figure 23 that there is little sensitivity to a change in the relative diffusion (D_{rel}) between the inner material (red) and the outer material (blue), as the outer material connects the outside of the periodic domain. Conversely, in Figure 24, varying D_{rel} makes a large difference to the effective diffusion, as

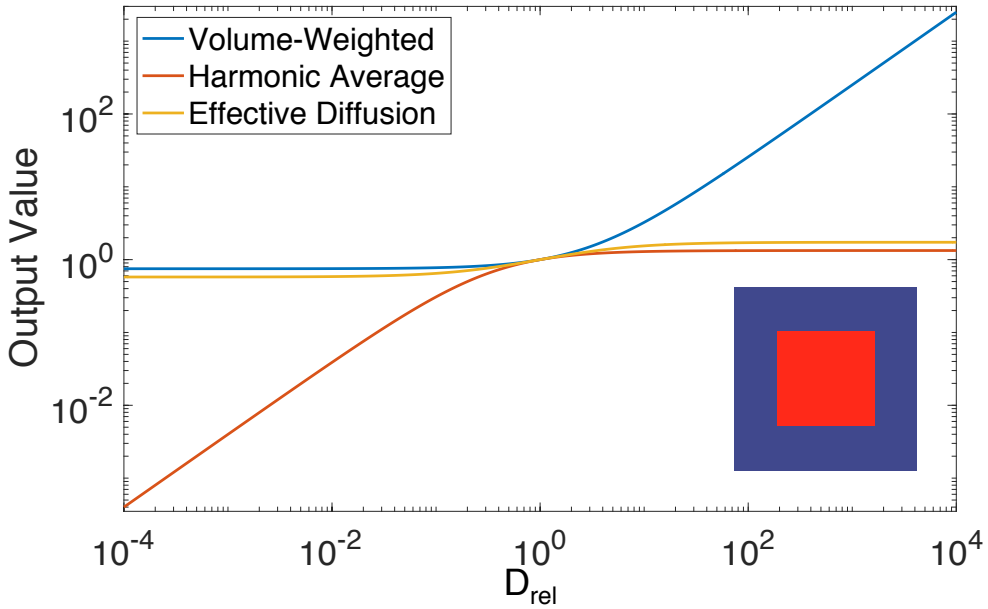


Figure 23: Some intuitive options for diffusion as the diffusion coefficient in the inner square with 1/4 area of the whole square (red in inset) is varied with the outer geometry diffusion coefficient fixed at 1. The volume-weighted average (blue), the harmonic average (red) and the actual effective diffusion (yellow) are shown. As the internal submaterial (red) is surrounded by the external submaterial (blue), it cannot have a large effect on the effective diffusion.

in this case the submaterial that we vary the diffusion coefficient of connects the periodic microstructure.

In general, with two submaterials A and B within a composite material, if we see continuing sensitivity in the effective diffusion to a decrease in $D_A/D_B = D_{rel} < 1$, then channels of submaterial B do not exist throughout the periodic domain; if we do not see continuing sensitivity, there do exist channels of submaterial B. If we see continuing sensitivity of the effective diffusion to an increase of $D_{rel} > 1$, this implies there are channels of submaterial A throughout the periodic domain; if we do not see this sensitivity, then there are not channels of submaterial A throughout.

The shape used in Figure 23 is one used in Bourgat's paper [16], where various different internal two-dimensional geometries were tested and it was shown that a change in this geometry, while keeping relative areas the same, can change the effective diffusion coefficient. Simulations for various diffu-

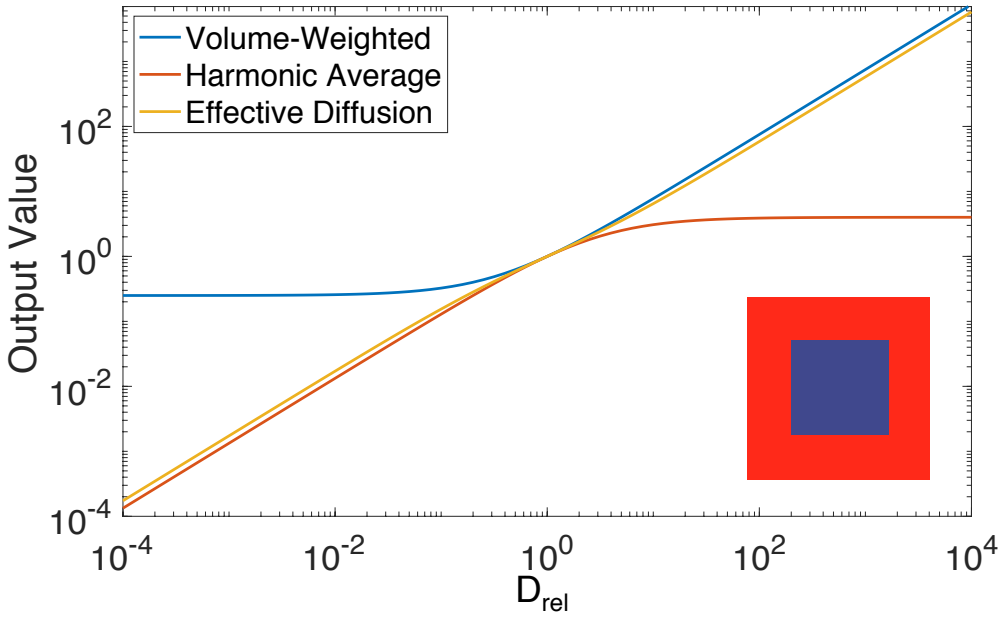


Figure 24: Some intuitive options for diffusion as the diffusion coefficient in the outer square with 3/4 area of the whole square (red in inset) is varied with the inner geometry diffusion coefficient fixed at 1. The volume-weighted average (blue), the harmonic average (red) and the actual effective diffusion (yellow) are shown. As the external submaterial (red) connects the sides of the assumed periodic shape, changing its associated diffusion coefficient has a large effect on the effective diffusion value.

sion coefficients and microstructure geometries of D^{eff} can be seen in Figure 25.

The choice of the assumed periodic domain within the PLGA/PEG is important and must be carried out in a systematic way. This is reinforced in Figure 26. A circle and square are chosen as two-dimensional internal geometries and their areas are increased from 0 to 1, at which point they consume the assumed periodic square. As the areas are increased, the internal circle touches the periodic boundary and creates channels of its material through the structure. Whereas the internal square will not touch the boundary until its area is 1. This difference in behaviour results in different D^{eff} values between the two periodic microstructures. In Figure 26, we set the diffusion of the internal shape (the circle or square) to a tenth and ten times that of the external material, respectively.

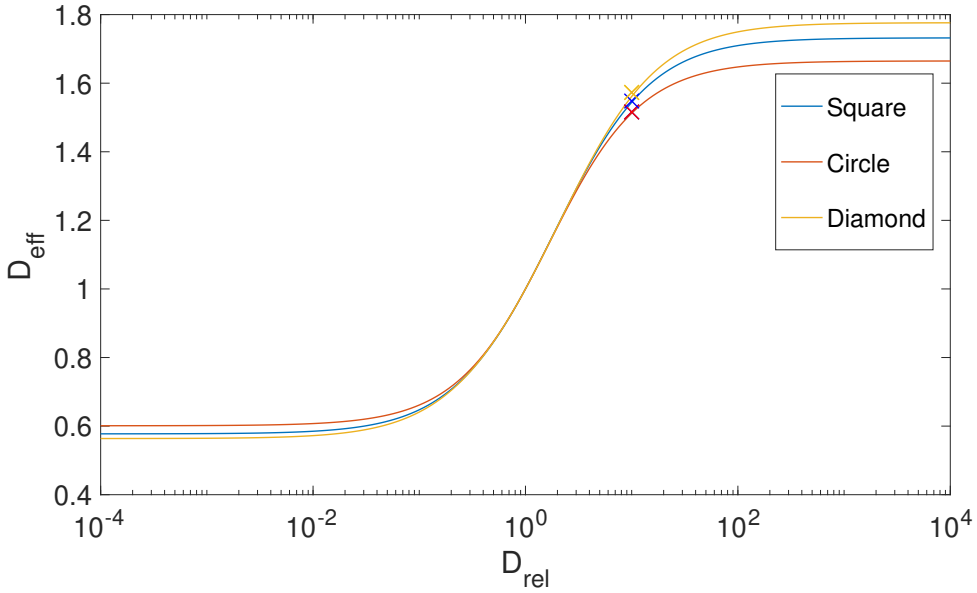


Figure 25: Simulations run in 2D of a unit square of diffusion 1 with centred internal geometries (square, circle and diamond) of relative area 1/4. The internal diffusion was varied and an upper asymptotic limit is clearly visible in the results; this is because there are no channels of the internal submaterial through the unit square. The crosses on the diagram show Bourgat's results, which our results agree with.

Homogenisation in Practice

Using imaging techniques such as microCT, it is possible to isolate cubes of the PLGA/PEG microstructure and choose them as the periodic domain of the construct as a whole. However, choosing an appropriate epsilon scale and volume of the microstructure that will accurately represent the construct is not a trivial task. We want to include the maximum data that our computational power will allow, so that we are using representative blocks of the PLGA/PEG constructs in each simulation.

To create our periodic microstructure, we initially reflected each of our chosen data samples in the x, y and z directions to preserve any underlying structure, such as channels of a submaterial. However, this leads to an eight times increase in computational expense as compared with a simulation on a data sample. As we want to maximise the amount of data we can use for each simulation and we have an upper limit on the amount of computational power we can use, we have chosen instead to reduce our periodic cell problem

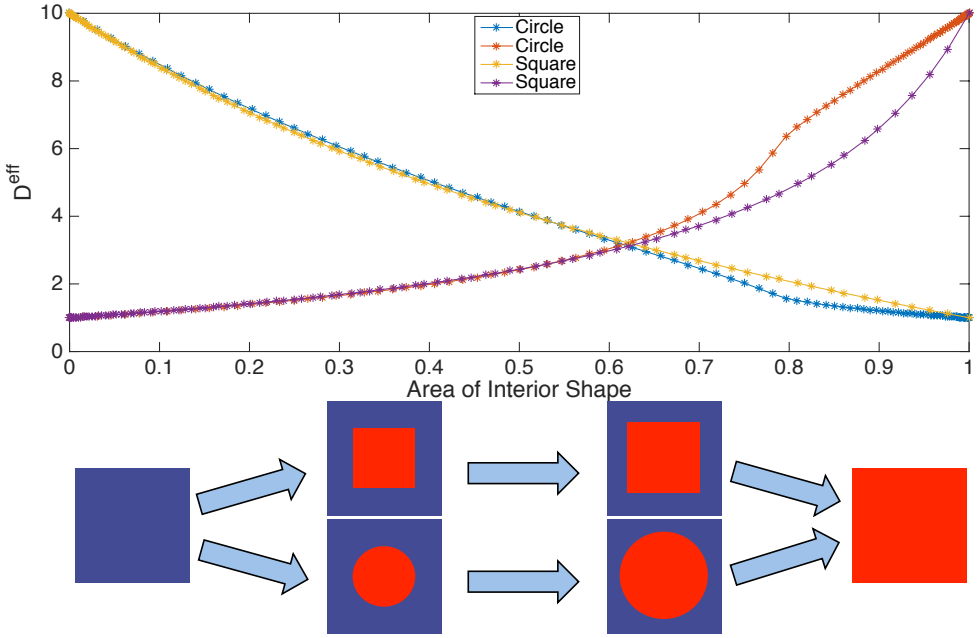


Figure 26: Results of simulations of a unit square with internal geometries of a circle and a square whose area are increased with each simulation until it becomes the whole unit square. The differences in the effective diffusion values seen here are due to the creation of channels through the composite material that occur earlier with the circle than they do the square. We have simulated cases where the internal geometry is 10 and the external geometry 1 and vice versa.

to a smaller problem with zero Dirichlet and zero Neumann boundary conditions that does not require the data samples to be reflected into a periodic geometry. I will now show that the solution to the reflected cube of data can be reconstructed by this Dirichlet-Neumann problem.

3.3.2 *From Periodic Boundary Conditions to Zero Dirichlet and Zero Neumann*

Let us first remind ourselves of the cell problems that we are solving

$$\nabla_{\boldsymbol{\xi}} \cdot (D(\boldsymbol{\xi})[\nabla_{\boldsymbol{\xi}} W_i(\boldsymbol{\xi}) + e_i]) = 0, \tag{116}$$

such that each W_i is periodic in every dimension, $i = x, y, z$. In the reflected cubes, we have reflected symmetry in our materials and subsequently their diffusion values, $D(\boldsymbol{\xi})$. If $W_i(\boldsymbol{\xi})$ is a solution to Equation (116) for $\boldsymbol{\xi} = \mathbf{x}/\epsilon$, we can show that $-W_i(-x_i/\epsilon, x_j/\epsilon)$ and $W_i(x_i/\epsilon, -x_j/\epsilon)$ $(j \neq i)$ are also

solutions to Equation (116). Showing that the solution to Equation (116) is odd in the dimension of i and even for the other dimensions.

Let us show this with an example case. Breaking down Equation (116) for $i = x$, we have

$$\frac{\partial}{\partial \xi_x}\left(D(\boldsymbol{\xi})\left(\frac{\partial W_1}{\partial \xi_x}+1\right)\right)+\frac{\partial}{\partial \xi_y}\left(D(\boldsymbol{\xi})\frac{\partial W_1}{\partial \xi_y}\right)+\frac{\partial}{\partial \xi_z}\left(D(\boldsymbol{\xi})\frac{\partial W_1}{\partial \xi_z}\right)=0. \quad (117)$$

Now if we set the ansatz $W_1(\xi_x, \xi_y, \xi_z) = -W_1(-\xi_x, \xi_y, \xi_z)$, we have

$$-\frac{\partial}{\partial \xi_x}\left(D(\boldsymbol{\xi})\left(\frac{\partial W_1(-\xi_x, \xi_y, \xi_z)}{\partial \xi_x}+1\right)\right)-\frac{\partial}{\partial \xi_y}\left(D(\boldsymbol{\xi})\frac{\partial W_1(-\xi_x, \xi_y, \xi_z)}{\partial \xi_y}\right) - \frac{\partial}{\partial \xi_z}\left(D(\boldsymbol{\xi})\frac{\partial W_1(-\xi_x, \xi_y, \xi_z)}{\partial \xi_z}\right)=0,$$

from which it is clear that $W_1(-\xi_x, \xi_y, \xi_z)$ is also a solution.

In a similar fashion, setting $W_1(\xi_x, \xi_y, \xi_z) = W_1(\xi_x, -\xi_y, \xi_z)$ in Equation (116) leads to

$$\frac{\partial}{\partial \xi_x}\left(D(\boldsymbol{\xi})\left(\frac{\partial W_1(\xi_x, -\xi_y, \xi_z)}{\partial \xi_x}+1\right)\right)+\frac{\partial}{\partial \xi_y}\left(D(\boldsymbol{\xi})\frac{\partial W_1(\xi_x, -\xi_y, \xi_z)}{\partial \xi_y}\right) + \frac{\partial}{\partial \xi_z}\left(D(\boldsymbol{\xi})\frac{\partial W_1(\xi_x, -\xi_y, \xi_z)}{\partial \xi_z}\right)=0,$$

and $W_1(\xi_x, -\xi_y, \xi_z)$ is a solution. Clearly the same holds for $W_1(\xi_x, \xi_y, \xi_z) = W_1(\xi_x, \xi_y, -\xi_z)$ due to the symmetry of the problem. So we see that the solution is odd in ξ_x, and even in ξ_y and ξ_z. This extends to the other values of i such that the solution is odd in the direction of i and even in the other directions.

As the solution to cell problem i is odd and sums to zero in the direction of ξ_i, it must be 0 on the plane $\xi_i = 0.5$, where we have let 1 be the domain length. Also, as the solutions in ξ_j and ξ_k are even and sum to zero, there must be zero flux on the planes $\xi_j = 0.5$ and $\xi_k = 0.5$. We can use these conditions as boundary conditions on the original domain of data. As we are still implicitly encapsulating the periodic boundary conditions in the problem, any channels of a submaterial through the composite material are still preserved in the solutions to the new Dirichlet-Neumann setup. Formally, the problem is reduced to the following cell problems:

$$\nabla_{\boldsymbol{\xi}} \cdot (D(\boldsymbol{\xi})[\nabla_{\boldsymbol{\xi}} W_i(\boldsymbol{\xi}) + e_i]) = 0, \quad (118)$$

where $\xi_x \in [0, 0.5]$, $\xi_y \in [0, 0.5]$ and $\xi_z \in [0, 0.5]$. Subject to the boundary conditions

$$W_i(\xi_i = 0) = W_i(\xi_i = 0.5) = 0, \tag{119}$$

$$\frac{\partial W_i(\xi_j = 0)}{\partial \xi_j} = \frac{\partial W_i(\xi_j = 0.5)}{\partial \xi_j} = 0 \text{ and} \tag{120}$$

$$\frac{\partial W_i(\xi_k = 0)}{\partial \xi_k} = \frac{\partial W_i(\xi_k = 0.5)}{\partial \xi_k} = 0. \tag{121}$$

Of course, after we have computed the solution on this smaller domain, we need to find the effective diffusion tensor on the whole reflected domain. As the smaller domain is an eighth of the reflected domain, we have eight cubes to consider and convert each of their integrals into an expression of the cube at $[0, 1/2] \times [0, 1/2] \times [0, 1/2]$.

Numerical Scheme for the Dirichlet Neumann Cell Problem

As in the periodic case, we have used a continuous galerkin finite element method to solve our cell problem. Multiply Equation (118) by a continuous linear finite element test function V that satisfies our required boundary conditions (Equation (119) – (121)) and integrate with respect to $\boldsymbol{\xi}$ over the domain of size $[0, 0.5] \times [0, 0.5] \times [0, 0.5]$

$$\int_S \nabla_{\boldsymbol{\xi}}(D(\boldsymbol{\xi})[\nabla_{\boldsymbol{\xi}} W_j(\boldsymbol{\xi}) + e_j])V \, d\boldsymbol{\xi} = 0, \tag{122}$$

which gives

$$[D(\nabla_{\boldsymbol{\xi}} W_j + e_j)V]_S - \int_S D(\nabla_{\boldsymbol{\xi}} W_j + e_j)\nabla_{\boldsymbol{\xi}} V \, d\boldsymbol{\xi} = 0. \tag{123}$$

The boundary terms still vanish as they did in the periodic case, but it is not so trivial as to why. As the test function satisfies the boundary conditions, it is zero along the zero-Dirichlet boundary, leading to that boundary term being zero. The zero-Neumann boundaries are handled by the zero-Neumann properties of W_j along the respective boundaries. We then have

$$\int_S D\nabla_{\boldsymbol{\xi}} W_j \cdot \nabla_{\boldsymbol{\xi}} V \, d\boldsymbol{\xi} = -\int_S De_j \cdot \nabla_{\boldsymbol{\xi}} V \, d\boldsymbol{\xi}, \tag{124}$$

so the numerical scheme is relatively unchanged. As before, we define this problem in FEniCS, which gives our numerical solution.

Verification of the Dirichlet Neumann Cell Problem

We need to show that the solution to the cell problem for the zero Dirichlet and zero Neumann cell problem leads to the same solution as the periodic case.

We want to be able to recreate the periodic solution by only using the solution to the Dirichlet Neumann cell problem. To do this, we need to find expressions for all parts of a cube with dimensions $[0,1] \times [0,1] \times [0,1]$ in terms of the integral for the cube at $[0,0.5] \times [0,0.5] \times [0,0.5]$, for all nine entries in the effective diffusion tensor, where now the off-diagonal entries are non-zero. In other words, we have to construct the integral from the reflected cube

$$D_{ij}^{eff} = \int_0^1 \int_0^1 \int_0^1 D(\boldsymbol{\xi})(e_i + \nabla_{\boldsymbol{\xi}} W_i) \cdot e_j \, d\xi_z d\xi_y d\xi_x; \tag{125}$$

this can be split into the eight smaller domains

$$\begin{aligned}
D_{ij}^{eff} = &\int_0^{0.5} \int_0^{0.5} \int_0^{0.5} D(\boldsymbol{\xi})(e_i + \nabla_{\boldsymbol{\xi}} W_i) \cdot e_j \, d\xi_z d\xi_y d\xi_x \\
&+ \int_0^{0.5} \int_0^{0.5} \int_{0.5}^{1} D(\boldsymbol{\xi})(e_i + \nabla_{\boldsymbol{\xi}} W_i) \cdot e_j \, d\xi_z d\xi_y d\xi_x \\
&+ \int_0^{0.5} \int_{0.5}^{1} \int_0^{0.5} D(\boldsymbol{\xi})(e_i + \nabla_{\boldsymbol{\xi}} W_i) \cdot e_j \, d\xi_z d\xi_y d\xi_x \\
&+ \int_0^{0.5} \int_{0.5}^{1} \int_{0.5}^{1} D(\boldsymbol{\xi})(e_i + \nabla_{\boldsymbol{\xi}} W_i) \cdot e_j \, d\xi_z d\xi_y d\xi_x \\
&+ \int_{0.5}^{1} \int_0^{0.5} \int_0^{0.5} D(\boldsymbol{\xi})(e_i + \nabla_{\boldsymbol{\xi}} W_i) \cdot e_j \, d\xi_z d\xi_y d\xi_x \\
&+ \int_{0.5}^{1} \int_0^{0.5} \int_{0.5}^{1} D(\boldsymbol{\xi})(e_i + \nabla_{\boldsymbol{\xi}} W_i) \cdot e_j \, d\xi_z d\xi_y d\xi_x \\
&+ \int_{0.5}^{1} \int_{0.5}^{1} \int_0^{0.5} D(\boldsymbol{\xi})(e_i + \nabla_{\boldsymbol{\xi}} W_i) \cdot e_j \, d\xi_z d\xi_y d\xi_x \\
&+ \int_{0.5}^{1} \int_{0.5}^{1} \int_{0.5}^{1} D(\boldsymbol{\xi})(e_i + \nabla_{\boldsymbol{\xi}} W_i) \cdot e_j \, d\xi_z d\xi_y d\xi_x.
\end{aligned}$$

Let us name these domains $V_{111}, V_{112} \ldots V_{222}$ to correspond to the regions $[0,0.5]$x$[0,0.5]$x$[0,0.5]$, $[0,0.5]$x$[0,0.5]$x$[0.5,1]$, $\ldots$, $[0.5,1]$x$[0.5,1]$x$[0.5,1]$. We also define $I_{111}, I_{112} \ldots I_{222}$ for the corresponding integrals. So that a subscript 1 corresponds to the region $[0,0.5]$ and subscript 2 corresponds to the region $[0.5,1]$ of the corresponding direction.

We have to convert each of the latter seven integrals in terms of the first, so that we can use our solution that we have computed for the Dirichlet Neumann problem on each of the eight subdomains.

We have shown in Section 3.3.2 that if we are solving the ith cell problem, the solution W_i is odd in the direction of ξ_i and even in the other directions.

Therefore we also know that our solution to the Dirichlet Neumann cell problem, which we call $\hat{W}_i$, has the following properties for each $i = 1, 2, 3$:

$$W_i(\xi_x, \xi_y, \xi_z) = \begin{cases} \hat{W}_i(\xi_x, \xi_y, \xi_z) & \text{in } V_{111}, \\ \hat{W}_i(\xi_x, \xi_y, 1-\xi_z)(-1)^{\delta_{i3}} & \text{in } V_{112}, \\ \hat{W}_i(\xi_x, 1-\xi_y, \xi_z)(-1)^{\delta_{i2}} & \text{in } V_{121}, \\ \hat{W}_i(\xi_x, 1-\xi_y, 1-\xi_z)(-1)^{\delta_{i2}}(-1)^{\delta_{i3}} & \text{in } V_{122}, \\ \hat{W}_i(1-\xi_x, \xi_y, \xi_z)(-1)^{\delta_{i1}} & \text{in } V_{211}, \\ \hat{W}_i(1-\xi_x, \xi_y, 1-\xi_z)(-1)^{\delta_{i1}}(-1)^{\delta_{i3}} & \text{in } V_{212}, \\ \hat{W}_i(1-\xi_x, 1-\xi_y, \xi_z)(-1)^{\delta_{i1}}(-1)^{\delta_{i2}} & \text{in } V_{221}, \\ -\hat{W}_i(1-\xi_x, 1-\xi_y, 1-\xi_z) & \text{in } V_{222}. \end{cases} \tag{126}$$

Using these equalities in the different regions in question leads to a variety of results. Without loss of generality, let us focus on the e_1 cell problem. So we are now only looking at D^{eff}_{xj} where $j = [x, y, z]$. We have

$$I_{III} = \int_{V_{111}} D(\boldsymbol{\xi})(e_x + \nabla_{\boldsymbol{\xi}} \hat{W}_x(\xi_x, \xi_y, \xi_z)) \cdot e_j \, d\xi_z d\xi_y d\xi_x. \tag{127}$$

Expanding the dot product leads to

$$I_{III} = \begin{cases} \int_{V_{111}} D(\boldsymbol{\xi}) \left(1 + \frac{\partial}{\partial \xi_x} \hat{W}_x(\xi_x, \xi_y, \xi_z)\right) d\xi_z d\xi_y d\xi_x, & \text{if } j = x, \\ \int_{V_{111}} D(\boldsymbol{\xi}) \left(\frac{\partial}{\partial \xi_y} \hat{W}_x(\xi_x, \xi_y, \xi_z)\right) d\xi_z d\xi_y d\xi_x, & \text{if } j = y, \\ \int_{V_{111}} D(\boldsymbol{\xi}) \left(\frac{\partial}{\partial \xi_z} \hat{W}_x(\xi_x, \xi_y, \xi_z)\right) d\xi_z d\xi_y d\xi_x, & \text{if } j = z. \end{cases} \tag{128}$$

We need to convert all the other integrals into I_{111}. We have, from the expression for I_{112} along with Equation 126,

$$I_{II2} = \begin{cases} \int_{V_{112}} D(\boldsymbol{\xi}) \left(1 + \frac{\partial}{\partial \xi_x} \hat{W}_x(\xi_x, \xi_y, 1-\xi_z)\right) d\xi_z d\xi_y d\xi_x, & \text{if } j = x, \\ \int_{V_{112}} D(\boldsymbol{\xi}) \left(\frac{\partial}{\partial \xi_y} \hat{W}_x(\xi_x, \xi_y, 1-\xi_z)\right) d\xi_z d\xi_y d\xi_x, & \text{if } j = y, \\ -\int_{V_{112}} D(\boldsymbol{\xi}) \left(\frac{\partial}{\partial \xi_z} \hat{W}_x(\xi_x, \xi_y, 1-\xi_z)\right) d\xi_z d\xi_y d\xi_x, & \text{if } j = z. \end{cases} \tag{129}$$

If we introduce a change of variables $\xi'_z = 1 - \xi_z$, we see that $d\xi'_z = -d\xi_z$. Under this transformation, the z domain $[0.5, 1]$ transforms to $[0.5, 0]$. Noting that also the integral from 0.5 to 0, is the negative of the integral from 0 to 0.5, gives us a transformation from V_{112} to V_{111}, and we have

$$I_{II2} = \begin{cases} \int_{V_{111}} D(\boldsymbol{\xi}) \left(1 + \frac{\partial}{\partial \xi_x} \hat{W}_x(\xi_x, \xi_y, \xi'_z)\right) d\xi'_z d\xi_y d\xi_x, & \text{if } j = x, \\ \int_{V_{111}} D(\boldsymbol{\xi}) \left(\frac{\partial}{\partial \xi_y} \hat{W}_x(\xi_x, \xi_y, \xi'_z)\right) d\xi'_z d\xi_y d\xi_x, & \text{if } j = y, \\ -\int_{V_{111}} D(\boldsymbol{\xi}) \left(\frac{\partial}{\partial \xi'_z} \hat{W}_x(\xi_x, \xi_y, \xi'_z)\right) d\xi'_z d\xi_y d\xi_x, & \text{if } j = z. \end{cases} \tag{130}$$

This is equal to I_{111} in the $j = x$ and $j = y$ cases, but the negative of I_{111} in the $j = z$ case.

Expanding this reasoning to all of the integrals, we see that for $j = x$, the integrals are always equal to I_{111}. For the $j = y$ and $j = z$ cases, they are equal to I_{111} half of the time (including I_{111} itself) and are equal to $-I_{111}$ for the other half. Therefore, as expected the off-diagonal entries to the effective diffusion tensor vanish to 0 in the whole unit cube. The diagonal effective diffusion values in the tensor for the periodic cube are equal to 8 times their counterpart in the Dirichlet Neumann cell problem in each respective direction.

To check the validity of this further, a number of simulations have been run on reflected unit length cubes with periodic boundary conditions to compute their effective diffusion tensors. We have also computed the effective diffusion tensors on each respective original cube of voxel data using our Dirichlet-Neumann approach. When we compared the solutions we did indeed note a factor of 8 between them. We used DOLFIN within FEniCS with the DOLFIN python library to compute these solutions [6, 81, 82].

3.3.3 *Solving in Parallel*

Even with the reduction in domain size through the Dirichlet-Neumann cell problems (Equations (118) – (121)), running simulations on our whole microCT domains is not possible for the computational power that we have. However, we could further increase the size of our simulation domains by running our FEniCS code in parallel instead of serial.

To run homogenisation of diffusion simulations in parallel, the input mesh needs to be partitioned into smaller meshes. Each unique process is assigned a subdomain to create a mesh and subsequently compute the homogenisation solution on. Once computed, the solutions on the partitioned meshes can be reconstructed to create the solution for the original input mesh.

Although FEniCS has inbuilt parallel solvers such as PETSc and inbuilt mesh partitioning for solving in parallel, we ran into complications in applying the microCT geometries to each partitioned mesh. A tetrahedral unit cube mesh of $N \times N \times N$ smaller cubes has 6 degrees of freedom per small cube, such that the unit cube will have $6N^3$ degrees of freedom in total. In FEniCS, the global index numbering of each degree of freedom in the mesh partitions is not necessarily the same as the global indices as they would have been if the mesh was created whole. We therefore needed to find a map between the

local degrees of freedom indices for each partitioned mesh, l for $l = 1 \dots M$, and the global degrees of freedom indices as they would have been if the mesh was created whole, g for $g = 1 \dots 6N^3$.

We created a matrix of global coordinates (x_g, y_g, z_g) for $g = 1 \dots 6N^3$ corresponding to each degree of freedom. Each (x_g, y_g, z_g) coordinate was coupled with its corresponding global degree of freedom index, g, to give a list of (x_g, y_g, z_g, g) vectors. We then imported this matrix into FEniCS and compared each local coordinate (x_l, y_l, z_l) within each mesh partition with coordinates from the list of (x_g, y_g, z_g, g). Once a match is identified between l and g, the corresponding g value is stored.

As mentioned previously, the number of degrees of freedom for the whole mesh can become quite large. For example, if we take an 100x100x100 sample of microCT data, we will have $6,000,000$ degrees of freedom in our solver. It was therefore important to optimise our FEniCS code so that the map creation did not take an unreasonable amount of time. There are two main steps taken that reduce this computational time. The first of these is a simple deletion of (x_g, y_g, z_g, g) from the global coordinate matrix once the corresponding local coordinate has been found, so that in the next iteration of the loop there is one less coordinate to check for a match against. The second is to put a bounding box around each mesh partition so that we only need to check coordinates within said box. This is carried out simply by looking for the local maxima and minima in each direction within each local process and isolating the coordinate list to that box.

To give an example of the run times that these mappings have, running an 100x100x100 cube to find this map takes around 10 hours across 16 CPUs (with 16 processes[1]). The mapping is then stored, along with the mesh and its partitions, and takes less than a second to reapply. So once we have found the map, we are no longer limited by it in future simulations.

As long as the size of the data sample and the number of processes used are fixed, we can use the same stored map for different data samples. This works as the map does not rely on the diffusion coefficients themselves, which are applied alongside the map.

Once the unforeseen issues with the map had been solved, we still needed to solve the cell problems. Direct solvers create massive inversion problems

1 We have checked that our solutions do not depend on the number of processes used. We have run simulations with 50 processes and seen that the solutions are produced slower than with 16 processes (simulation speeds were slower by around 20%) but give the same effective diffusion results.

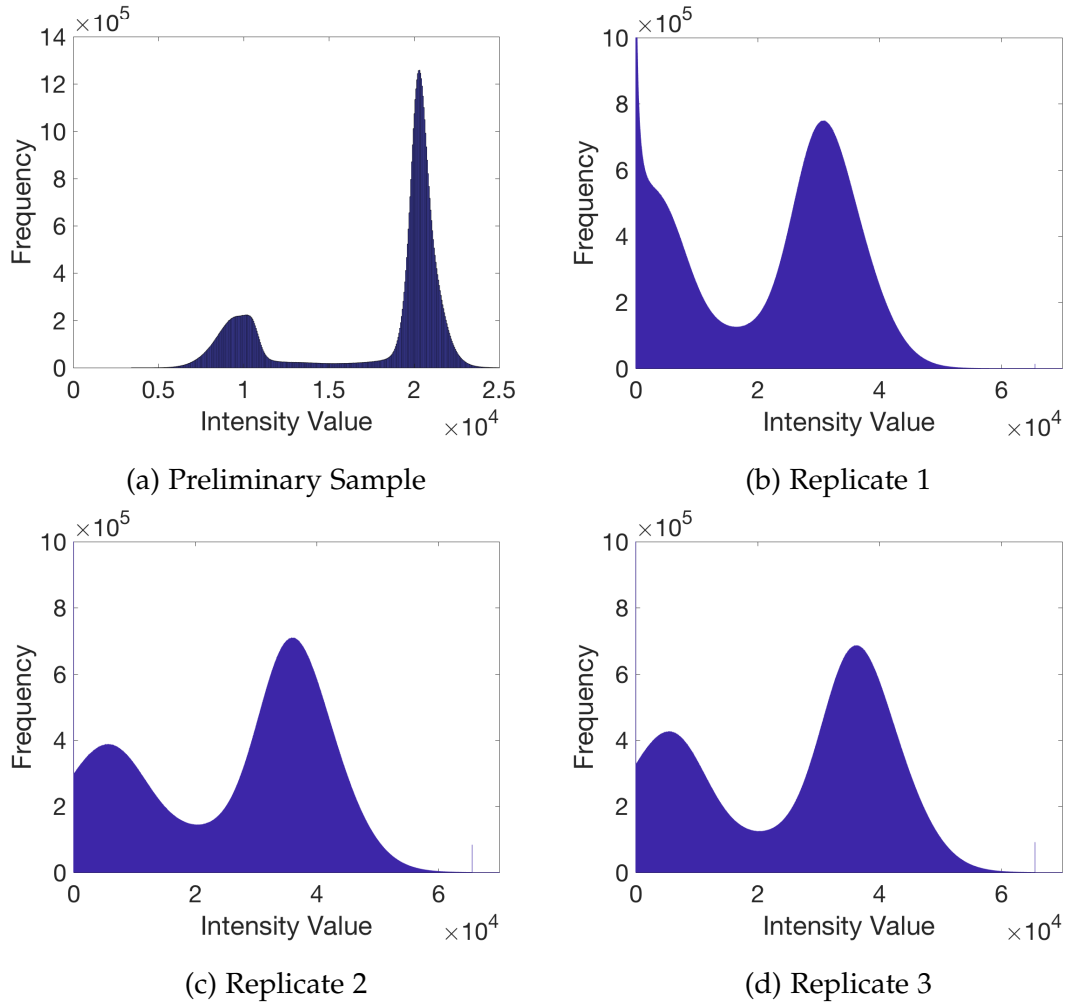
that the server we were using did not have enough memory to solve. Fortunately, iterative solvers and preconditioners can be used to circumvent the memory issues associated with direct solvers. Our stiffness matrices in the finite element scheme are positive semi-definite and symmetric, and it is therefore appropriate to use a conjugate gradient solver with an algebraic multigrid (AMG) preconditioner (we used Hypre BOOMERAMG). Although now with an iterative solver there is some error in the solution, by reducing the relative residual norm to a satisfactory value, this error can be minimised. We found the standard relative tolerance in FEniCS of $e-5$ to be satisfactory for our solutions. We also found good convergence once we set the Hypre BOOMERAMG strength threshold to 0.8 and the maximum number of iterations to 8, and set these parameters as such for our simulations. We checked that iterative solvers converged to solutions of direct solvers for small domains.

3.4 DATA COLLECTION AND PREPARATION

In collaboration with the Hounsfield Facility at Sutton Bonington Campus at The University of Nottingham, we created a proof-of-concept PLGA/PEG polymer following the preparation outline given in Section 2.2.1, with 200mg of polymer powder and 160mg of distilled water. This sample was prepared within a cylindrical mould of 6mm diameter and 12mm depth. Once the scan was created, we received a 16-bit .raw data file with the intensities of a cube of data of 3.75 micron resolution. For this proof-of-concept, we focused on a cube of data with 385x385x376 data points in the x, y and z directions and therefore lengths of 1.44375mm by 1.44375mm by 1.41mm, respectively.

Once we confirmed that we could get a high quality microCT scan of our data that was feasible to use as a domain within simulations, we created three more PLGA/PEG constructs under the same conditions, with 600mg of polymer powder and 480mg of distilled water. For these scans, we collected larger cubes of 1251x1251x1252 data points and a higher resolution of 2.75 microns in all dimensions. Therefore these cubes are 3.44025mm by 3.44025mm by 3.443mm in total. However, as described in the previous section, we do not have the computational power to compute effective diffusion tensors over these whole cubes of data.

By plotting the intensities into histograms for each scan, we see that they are a double peak. We use the local minimum value between these peaks for each polymer sample to binarise the data into data points of polymer and



(a) Preliminary Sample

(b) Replicate 1

(c) Replicate 2

(d) Replicate 3

Figure 27: Histograms of microCT intensities of each individual voxel in the preliminary sample of $385 \times 385 \times 376$ and the three replicate samples of $1251 \times 1251 \times 1252$. There is a clear double peak in the intensity values. The minimum between these peaks was used as a cutoff to binarise the data.

gaps; these gaps will be filled with fluid in a treatment setting. The minimum for the preliminary data is 1.5325×10^4 and for repeats 1, 2 and 3 the minima are 1.6335×10^4, 2.0295×10^4 and 2.0375×10^4, respectively. We present the histograms of intensity values in Figure 27.

Once we have the binarised data, we wanted to choose 100x100x100 cubes to compute homogenised diffusion tensors on, as this is one of the largest sizes that we could simulate. We also wanted these cubes to cover the microCT data as a whole. Choosing the cubes to cover the data is not trivial, since the dimensions of our cubes of data are not divisible by 100. Therefore, we chose cubes on which to run our simulations such that they would cover the

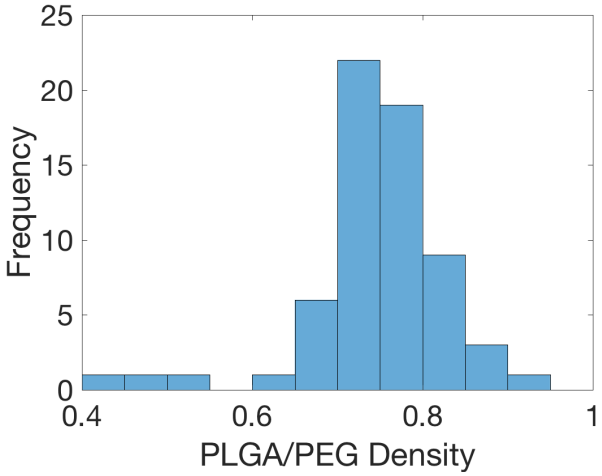


Figure 28: Here we see the density histogram for the preliminary data once it has been binarised and split into $100 \times 100 \times 100$ cubes.

data with minimal overlap between them. For our preliminary data sample of 385x385x376, we have used 64 cubes with overlap of 5 data points in the x and y directions, and 8 in the z direction. For the three repeats of $1251 \times 1251 \times 1252$, we have 13^3 cubes of size $100 \times 100 \times 100$. With these repeats, there are 12 overlapping regions between cubes in each dimension which does not divide equally in the x or y direction. An overlap of 5 data points is slightly too large, with 4 being too small. As we wanted to represent all of our data, we created the overlaps such that the cubes would still cover the data, and in this case have 11 overlapping regions of 5 data points, with the last being only 4. In the z direction the overlapping region is consistently 5 data points.

Once we have chosen these cubes, we calculated their density distributions for both the preliminary sample (Figure 28) and the three replicates (Figure 29). We see a spread of density values across these histograms and reasonable agreement between the density distributions for the three replicates The first replicate has the lowest density values and is slightly more spread out, whereas the other two are slightly more compact with the second replicate having the highest density values overall.

We also wanted to run detailed scans on a variety of cubes, to see the asymptotic behaviour of their effective diffusion values. Due to the large number of cubes in our replicates, we did not have the timescale required to do this on every cube. However, we wanted to create a subset of cubes that would highlight the range of density values of each polymer, as well as its distribution. We found a subsample of our $100 \times 100 \times 100$ cubes by plotting the histogram of density values of these cubes against each bin's

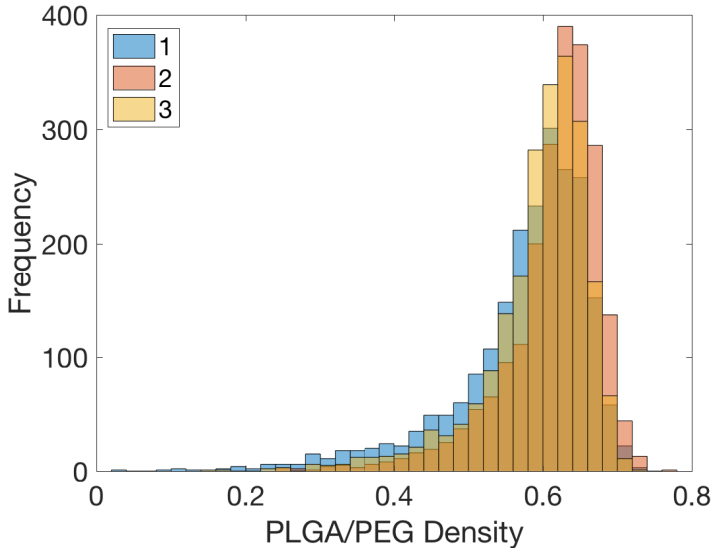


Figure 29: Here we see the density histograms for all three replicate samples once they have been binarised and divided into $100 \times 100 \times 100$ cubes.

probability. After creating a cumulative density function of the bins for each histogram, we took a random sample of 300 values in the interval $[0, 1]$ and found the first bin each value belonged to. With this method, we created a random sample of 300 cubes that follows the density distribution of each polymer sample. Once these cubes have been found, we ran 6 simulations across the relative diffusion coefficients $D_{rel} = 10^i$ for $i = -3, -2, -1, 1, 2, 3$, where $D_{rel} = D_{PLGA/PEG}/D_{fluid}$.

3.5 PARAMETER VALUES

The relative value between the gap diffusion coefficient and the PLGA/PEG diffusion coefficient, D_{rel}, is really the important quantity in question, as multiplying both diffusion coefficients by the same constant multiplies the resulting effective diffusion by the same constant. In most cases, we wanted to keep the results as general as possible, so we have not included any explicit parameter values in our results. If we were to apply this to a specific drug, with a known diffusion coefficient through water (or another fluid), we could set D_{fluid} to that value.

3.6 STATISTICAL METHODS

To test whether there are any statistically significant differences between the effective diffusion values in different directions for each $100 \times 100 \times 100$ cube, we have employed two statistical tests; the first is the Wilcoxon Signed Rank (WSR) Test, and the second is the Kolmogorov-Smirnov (KS) Test.

The WSR Test looks for significance in the median value of two sets of paired data. In our case we have pairs of the effective diffusion coefficients in each dimension within each cube of data. For each $100 \times 100 \times 100$ sample cube, we pair the (D_{xx}, D_{yy}), (D_{yy}, D_{zz}) and (D_{xx}, D_{zz}) effective diffusion values. We will denote D_{xx} as x, D_{yy} as y and D_{zz} as z. We then run a Wilcoxon Signed Rank Test on these paired distributions to test whether the medians of the distributions are significantly different or not.

The WSR Test takes two sets of paired values, say (x_i, y_i) for $i = 1, \ldots, n$, and calculates their absolute differences $|x_i - y_i|$. The test then ranks these differences in order of increasing magnitude, each pair given rank $R_i = 1, \ldots, n$. The sign of the difference is also recorded, which we denote $\text{sgn}(x_i - y_i)$. The test then calculates what is known as the test statistic, defined as

$$W = \sum_{i=1}^{n-1} (sgn(x_i - y_i) R_i). \tag{131}$$

Under the null hypothesis, the distribution of $x - y$ has a zero expected value and variance given by

$$V = \frac{n(n-1)(2n-1)}{6}, \tag{132}$$

which for large enough n converges to a normal distribution. In such a case, the null hypothesis is rejected if

$$|z| > z_0 \text{ where } z = W/\sqrt{V}, \tag{133}$$

for some critical value z_0. To explain further, a positive value of W would mean that there is a preference towards values of x being higher. Conversely, a negative value for W would mean that there is a preference for y. The WSR test calculates whether the value of W that we find is significantly non-zero.

We have three pairs for each of the six values of D_{rel} that we use in our asymptotic analysis for each repeat. Therefore, we carry out a total of 18 WSR Tests to look for significance between median effective diffusion values of directions for the preliminary data and for each replicate.

The KS test is used to test significance between two cumulative distributions. For our application, this test has the null hypothesis that the distributions of paired effective diffusion values are taken from a single distribution. We want to see if the distributions of effective diffusion values are distinct enough that they can be considered significantly likely to be from separate distributions. For two cumulative distributions, $C_{1,n}(w)$ and $C_{2,n}(w)$, where w takes the range of data values of the sample distributions and n is the size of the sample, the KS test calculates

$$K_n = \sup_w |C_{1,n}(w) - C_{2,n}(w)|. \tag{134}$$

The null hypothesis, that the paired distributions of effective diffusion values are taken from the same distribution, is rejected at level α if

$$K_n > c(\alpha)\sqrt{\frac{2n}{n^2}}, \text{ where } c(\alpha) = \sqrt{-0.5 \ln \alpha}. \tag{135}$$

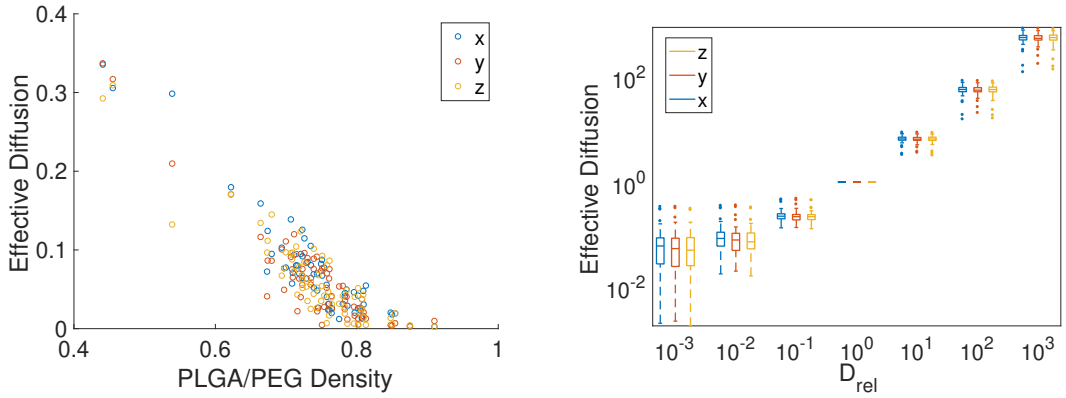
3.7 RESULTS

3.7.1 *Results of Preliminary MicroCT Data*

Running simulations on the 64 cubes of $100 \times 100 \times 100$ data points from the preliminary scan for the effective diffusion with the water diffusion coefficient set to 1 and the PLGA/PEG diffusion coefficient set to 0.001 led to the results in Figure 30a. Here we can see the effective diffusion values for each direction within each of the 64 samples against its density value.

It is clear to see that there is a relationship between the effective diffusion values and the density that holds across all dimensions, with fluctuations off of this line due to the geometry of the submaterials within each of the 64 cubes. Although the data appears to follow a linear relationship, we know that the diffusion values cannot become negative for high density values and that it will become equal to the PLGA/PEG diffusion coefficient when the density reaches 1. Therefore, with this constraint, a linear relationship is not suitable.

For the preliminary PLGA/PEG construct, we ran an asymptotic analysis on all 64 chosen cubes of data. For each of these cubes of data, we ran 6 simulations, and set $D_{rel} = D_{PLGA/PEG}/D_{Fluid} = 10^i$ for $i = -3, -2, -1, 1, 2, 3$. We did not run this analysis for $D_{rel} = 1$ as in this case the effective diffusion is 1 for every cube; this value has been subsequently added into our Figures



(a) Effective diffusion against density for the preliminary sample cubes with $D_{rel} = 0.001$. There is a clear correlation between the PLGA/PEG density and effective diffusion coefficients, with variations seen due to the individual geometry of the sample cubes.

(b) Effective diffusion calculated for various D_{rel} values. Box plots are shown with the median, upper and lower quartiles, and the range. Results are considered outliers if they are further than 1.5 times the interquartile range from the median and shown as a dot. The results suggest that channels of both PLGA/PEG and fluid commonly exist in the data samples.

Figure 30

for reference[2]. The results of these simulations are presented in Figure 30b as box plots.

We observed evidence of a lower limit in the median effective diffusion values of our sample cubes across all three spatial dimensions as D_{rel} becomes small. As we see a lower limit in this region, it suggests that there are fluid channels readily available for drug concentrations to diffuse through in the average case. There are some cubes however that continue to decrease log linearly as D_{rel} becomes small, suggesting that there are not always fluid channels available as the diffusion through the composite material is still limited by the slow PLGA/PEG diffusion.

On the other hand, for the larger values where the diffusion through the PLGA/PEG is faster than the fluid, we see continued sensitivity for increasing D_{rel} in the median effective diffusion values for all spatial dimensions. This sensitivity suggests that the diffusing species can travel through the fast polymer and is not inhibited by the relatively slower fluid, suggesting that

2 We have checked that $D_{rel} = 1$ yields an effective diffusion value of 1 for some sample cubes to verify our code is working as expected.

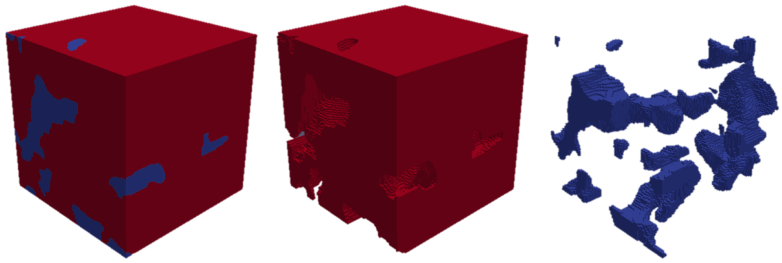


Figure 31: The cube of microCT data with the lowest effective diffusion value for $D_{rel} = 0.001$ in the x and z direction from the preliminary data set. Fluid is shown in blue with polymer in red. Clearly there are no fluid channels available so the concentration is forced to travel through the PLGA/PEG, and the low effective diffusion value reflects this.

channels of PLGA/PEG are also prevelant. Therefore, we see evidence of fluid channels and PLGA/PEG channels throughout our preliminary sample construct.

Looking into this further, we found the sample cube from our preliminary dataset with the lowest effective diffusion for $D_{rel} = 0.001$, that did not follow the trend of the other cubes for low values of D_{rel}, we see that it does indeed lack fluid channels that cross the cube completely; this means that the diffusing species is forced to travel through the slower polymer channels and this is reflected in the effective diffusion value. See Figure 31 for the geometry of this preliminary data cube that we use to solve our Dirichlet-Neumann equation on.

We also ran WSR and KS statistical tests on this preliminary data. We ran each combination of pairs of each x, y and z effective diffusion coefficients within each value of D_{rel}. We see some significance in the x median being lower than the other two directions, given by the WSR test for $p < 0.05$ (Figure 32). However, the KS test did not lead to any significance in the differences between any two distributions. We present these p values in the Appendix (Sections B.2 and B.3).

3.7.2 *Results of MicroCT Replicates*

We ran simulations on the samples of 300 cubes of the 2197 cubes of $100 \times 100 \times 100$ from the three replicates of microCT data (chosen according

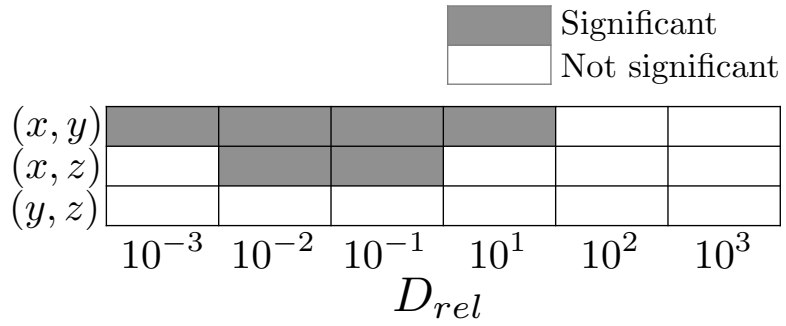


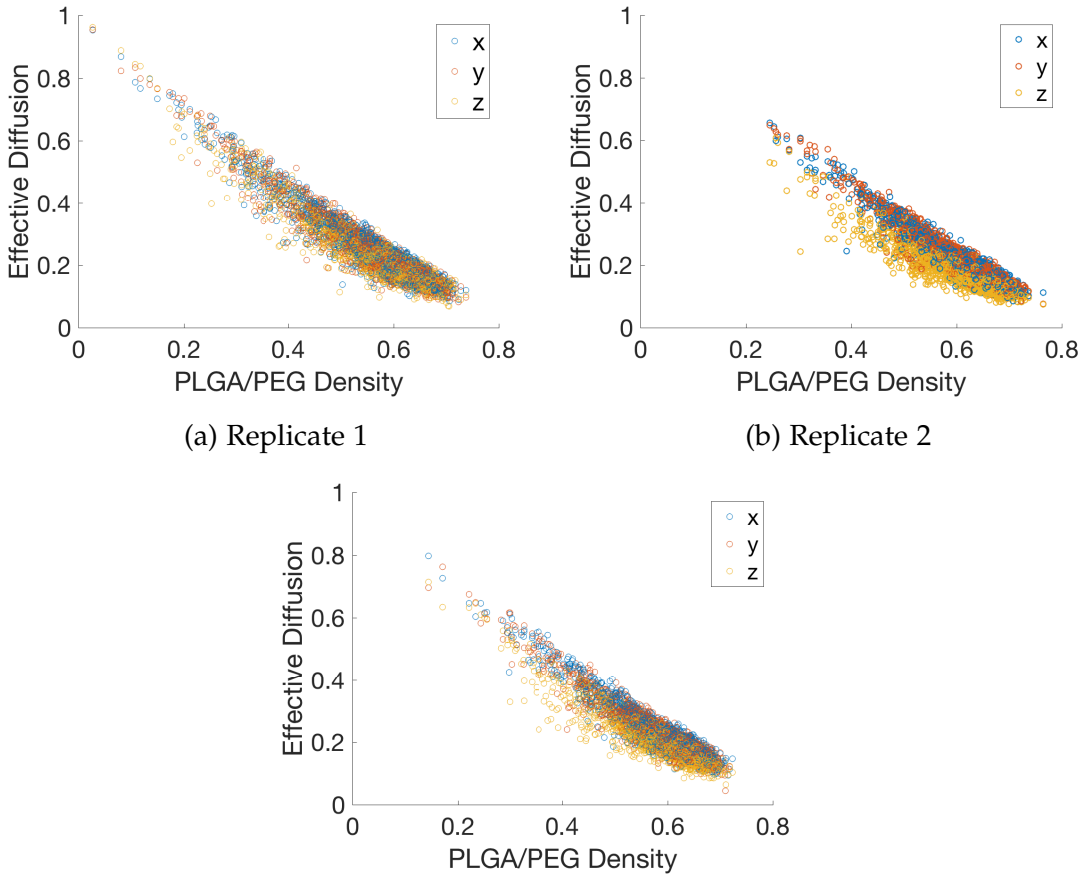
Figure 32: Results of the WSR Test on the significance between the differences in medians of pairs of effective diffusion values for various values of D_{rel}. The medians can be seen in Figure 34. We see some significance emerging between medians of both (x, y) and (x, z), but not (y, z).

to Section 3.4). We set the water diffusion coefficient to 1 and the PLGA/PEG diffusion coefficient to 0.001, such that $D_{rel} = 0.001$. We can see from Figure 33 that the density of these cubes correlates with the computed effective diffusion values. However, there is not a perfect correlation due to fluctuations caused by the geometry of the cubes as was observed in the preliminary data sample.

Let us take a look at the cube with the most discrepancy within its effective diffusion values, we see that this occurs in Replicate 2. We present this cube in Figure 35 and we see that it has a PLGA/PEG density of 0.304. The effective diffusion values in the x, y and z directions are given by 0.607, 0.604 and 0.244, respectively (to 3 significant figures) for $D_{rel} = 0.001$. Looking at the geometry of the cube, it is clear to see why the diffusion would be considerably slower in the z direction than the x and y; it is due to the bunching of PLGA/PEG towards the top of the cube that slows the diffusion rate in the vertical direction, z. However, in the x and y directions there is a lot of available fluid which is relatively faster to travel through, leading to a higher effective diffusion rate in these directions.

We have also run simulations on a sample of 300 cubes from our 2197 cubes within each replicate. These cubes were chosen without replacement following the distribution of the density values, using the inbuilt Matlab 2017a function *datasample.m* [3]. For each cube we have run 6 simulations, each with a

3 We chose to sample 300 cubes for this analysis as is it was impractical to run the same analysis on all 2197 of them. This was due to the computational expense created by the combination of the number of simulations necessary and the access to computational power.



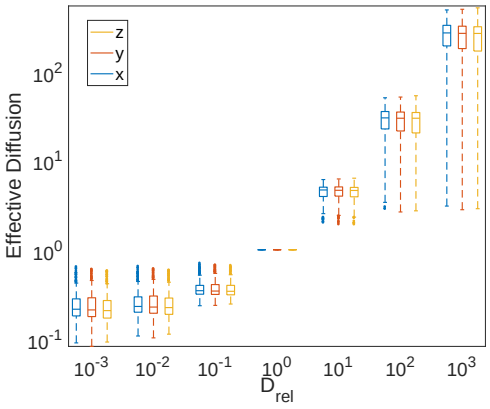
(a) Replicate 1

(b) Replicate 2

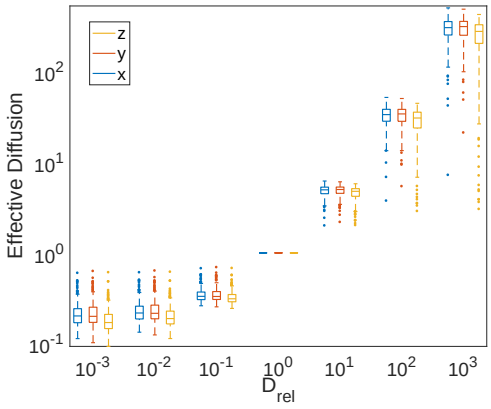
(c) Replicate 3

Figure 33: Effective diffusion results of each sample cube within each repeat plotted with its density. The diffusion of the PLGA/PEG is set to 0.001 and water diffusion set to 1. There is a clear relationship between density and the effective diffusion, with variation due to the geometry of the polymer.

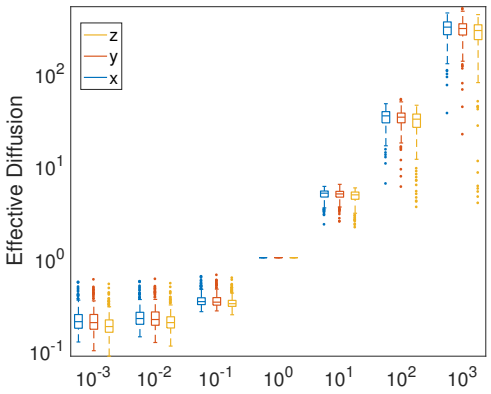
different value of $D_{rel} = 0.001, 0.01, 0.1, 10, 100, 1000$ (as before we did not run simulations with $D_{rel} = 1$ as we know that the effective diffusion is 1 in this case). We present the results in boxplots in Figure 34, showing the median value across all samples within each replicate and the interquartile range. We see no evidence of an upper limit in the median effective diffusion values for high values of D_{rel}, showing that for relatively high PLGA/PEG diffusion values the diffusion is not inhibited by the lower diffusion through the fluid; therefore, there exist PLGA/PEG channels through the composite material as expected. We also see that there is evidence of a lower effective diffusion limit in the median effective diffusion values, showing that for low PLGA/PEG values, the diffusing species is not forced to go through this slow material and in turn suggesting that there are also channels of fluid that are avail-



(a) Replicate 1



(b) Replicate 2



(c) Replicate 3

Figure 34: An asymptotic analysis of the three repeats, looking at the x, y and z-directional effective diffusion behaviour. The results are presented as box plots. The average behaviour is similar across all directions and between repeats. Sensitivity in the effective diffusion is seen for high values of D_{rel}, but not for low.

able to diffuse through. So we see that there are both PLGA/PEG and fluid channels present within our samples and the median behaviour suggests that these both occur commonly. Another point worth noting is that the median qualitative behaviour is similar across the different directions.

Although there exist channels of both PLGA/PEG and fluid on average, we do see evidence in the z direction of an asymptotic upper limit in some cases across all three repeats, which suggests that some cubes do not have PLGA/PEG channels in every direction. We see evidence of this also in the x and y directions for the first sample. This can be seen by looking at the lowest values in Figure 34 for high values of D_{rel}.



Figure 35: Here we see a sample cube of PLGA/PEG (red) and fluid (blue) on which we run effective diffusion simulations. This specific cube gave the largest discrepancy between directional effective diffusion values, for $D_{rel} = 0.001$ across the three replicates. The effective diffusion in the z direction is slower due to the dense volume of PLGA/PEG at the top of the cube, which the concentration diffuses through slowly. Note that this cube does not have a channel of PLGA/PEG in the z direction.

We used the WSR Test to find whether the difference between the medians of our effective diffusion values are significant between pairs (x, y), (x, z) and (y, z). We see significance ($p < 0.05$) across all three replicates in the pairs (x, z) and (y, z) for all values of D_{rel}, except (y, z) in Replicate 1 (which had $p = 0.0505$). We do not see significance in general for the pair (x, y). We do however see significance for high D_{rel} values in (x, y) for Replicate 1. We present the significant and non-significant combinations in Figure 36 with their associated p values in the Appendix (see B.2). These results show that there is in general a significant difference between the median z value and the medians for x and y across all calculated D_{rel} values. As can be seen in Figure 34, the median for the z groups is lower compared to x and y, which we see is a significant result. We attribute this to the packing of the PLGA/PEG polymers into their moulds, that occurred in the z direction.

Using the KS Test to look for significance between pairs of distributions of our directional effective diffusion values, we see that there is significance in Replicates 2 and 3 for the distribution of pairs (x, z) and (y, z) but not for (x, y), across all values of D_{rel}. We use $p < 0.05$ as a threshold for significance and present the p values in the Appendix (see B.3). Replicate 1 did not show significance for any combination of pairs across all D_{rel} values. However, the significant values were found only in pairs (x, z) and (y, z), which agree with the significance found in the WSR test for the difference in the medians of these pairs.

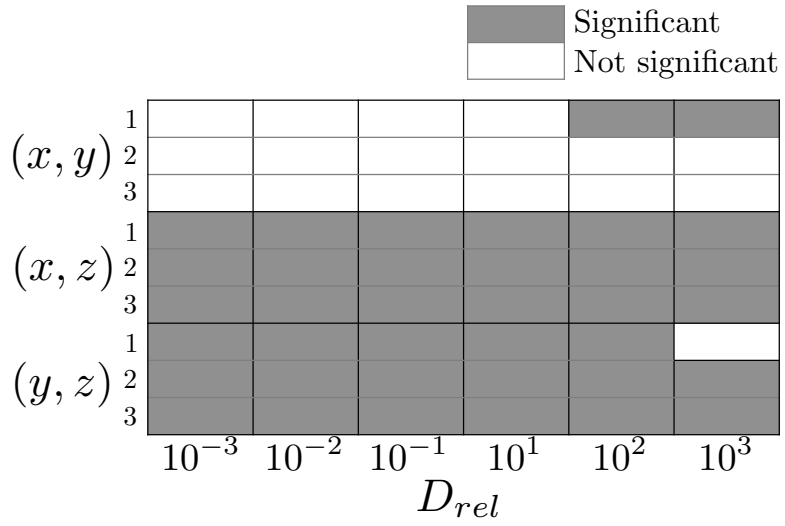


Figure 36: Results of the WSR Test on the significance between the differences in medians of pairs of effective diffusion values for various values of D_{rel}. The medians can be seen in Figure 34. We see significant trends between medians of both (x,z) and (y,z), but not (x,y). Replicates marked as row headings 1, 2 and 3.

Together, the two statistical tests applied to the three replicates suggest that there are significant differences between the effective diffusion values in the z direction and the other two directions.

3.8 DISCUSSION AND FUTURE WORK

We have shown that the geometry of the periodic microstructure of a material can affect its effective diffusion. In both our 2D and 3D examples, we saw that if a channel of a submaterial with a high relative diffusion rate exists across a particular direction, it gives sensitivity of the effective diffusion to the composite material in that direction. However, this does not hold in 1D as the presence of a submaterial immediately means the concentration has to travel through it; it is for this reason that the effective diffusion in one spatial dimension can be reduced to the harmonic average, as we have shown.

Using the microCT data of the PLGA/PEG microstructures as input geometries in our homogenisation simulations led to variation of the effective diffusion within $100 \times 100 \times 100$ data samples. However, the various effective diffusion values found correlate well with the PLGA/PEG density within each sample, with the geometry leading to fluctuations between the effective diffusion values in each direction.

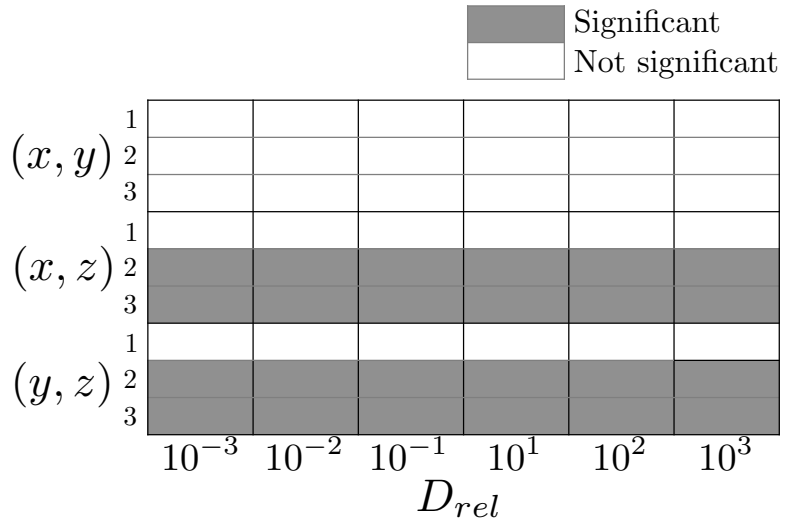


Figure 37: KS Test results, showing significantly different distributions within Replicate 2 and Replicate 3 for pairs of distributions (x, z) and (y, z) across all values of D_{rel}. We do not see significance in any other combination of replicate and paired distribution. Replicates marked as row headings 1, 2 and 3.

As the density of the polymer affects the diffusion of drugs through it, it will be of vital importance in any *in vivo* setting that the density of the polymer is known for the sake of treatment consistency and predictability. It is important that the density is not only known for the PLGA/PEG construct as a whole, but that it is known and consistent within each PLGA/PEG construct. The large effective diffusion and polymer density variation is worth considering further. Due to toxicity concerns for high chemotherapy drug concentrations and sub-optimal treatment for concentrations that are too low, it will be important for this therapy that there is a consistent and predictable drug concentration reaching the cavity wall. In the case that there is a low density polymer area hitting part of the wall, this area would have a higher effective diffusion and therefore could release more drug to the corresponding area of the brain than a PLGA/PEG dense region would.

We have seen that the z direction effective diffusion values have a statistically significant lower median than the y and x counterparts across three replicates (using WSR Tests), and had a statistically significant distribution difference in two of our three replicates (using KS Tests). We attribute these differences to the packing of the PLGA/PEG polymer into their moulds, and suggest further studies are needed to find the effects of packing into brain cavities. If the diffusion rate in the direction of packing is significantly lower

than the other directions, the drug movement towards the tumour cells could be inhibited and limit the efficacy of treatment.

Now that we have simulated the effective diffusion from these three replicates, and seen that channels of fluid and PLGA/PEG exist throughout each polymer, we would like to run some more microCT scans of the polymer once it has been kept in water over time. In Chapter 2, we have shown experimental data of PLGA/PEG swelling over time and our results suggest that this process inhibits the diffusion of theophylline. Running homogenisation of diffusion simulations on swollen PLGA/PEG constructs could show us the dynamics of this inhibition over time. We would expect, in a swollen PLGA/PEG construct, to see sensitivity in the effective diffusion for low D_{rel} values, as the fluid channels are cut off by the swelling process.

Once the swelling dynamics are fully understood, we would include *in silico* PLGA/PEG treatment in a mechanistic cancer growth model such as the model presented in Chapter 4. We could then gain insight into the efficacy of a homogeneous PLGA/PEG construct, such that it has the same density and structure throughout, against an inhomogeneous PLGA/PEG construct, that has varying density and structure. We could then deduce whether or not the homogeneity of the polymer is an important factor in the drug delivery and subsequent treatment, or if there is another factor that dominates.

4

A MATHEMATICAL MODEL FOR BRAIN TUMOUR GROWTH APPLIED TO VASCULAR ISCHEMIA

4.1 INTRODUCTION

Glioblastoma multiforme (GBM) is the highest grade glioma from the World Health Organisation and is the most aggressive type of primary brain tumour [83]. It is uniformly fatal with an average survival time from diagnosis of only 15 months with standard of care treatment [132]. The standard therapy regime for this disease is a combination of resection, radiation and chemotherapy [132, 133]. Magnetic Resonance Imaging (MRI) is the standard imaging modality for GBMs and is used routinely to monitor tumour growth and development throughout the progression of the disease. Different MRI sequences such as gadolinium-enhanced T1-weighted (T1Gd) and T2-weighted (T2) are used to identify the gross tumour volume. Neither sequence directly shows the tumour, rather they show abnormalities in the brain that are caused by the presence of a tumour. T1Gd shows gadolinium that has leaked into brain tissue, and T2 shows water that has done the same, which is known as edema. Gadolinium does not permeate through an intact blood brain barrier (BBB), so in a healthy brain one would only expect to see gadolinium on a T1Gd MRI in large blood vessels or other blood rich regions such as the sagittal sinus. A dense mass of GBM cells causes the breakdown of the BBB through the creation of immature and improperly-formed blood vessels, which can then allow gadolinium through. There are also areas of edema that show on a T2 MRI where the BBB allows excess water through but has not broken down enough to allow gadolinium through; it has been shown that infiltrating tumor cells also exist in lower densities in these regions [32]. However, these MRI sequences together do not show a complete picture. Infiltrating tumour cells also exist beyond the resolution of these MRI sequences. In fact, malignant glioma cells have been cultured from histologically normal

healthy tissue at a distance of 4cm from the gross tumour volume identified by MRI scans [126].

A maximal surgical resection removes the tumor bulk but cannot remove all of the tumor cells due to their infiltrative nature. An unfortunate clinical expectation following surgery is tumor recurrence, which usually presents on the edge of the resection cavity [25]; this is known as a local recurrence. Occasionally, the tumour will recur on T1Gd MRI in a different region of the brain, away from the primary site, or the growth will become much more spread out on T2 MRI relative to T1Gd MRI, these cases are known as distant and diffuse recurrences respectively [25]. In a retrospective study by Thiepold *et al.* it was shown that, following resection in a group of GBM patients, those who had also suffered from perioperative ischemia, defined as an inadequate blood supply to a part of the brain following resection, were more likely to have a distantly and/or diffusely recurring GBM [143]. A disruption in normal vasculature can occur following resection in GBM patients leading to an ischemic event; this affects a patient's tumour in much the same way it affects the healthy tissue. By reducing available nutrients to the tumour, the tumour is forced towards a hypoxic phenotype and becomes necrotic if the reduction is sustained. Thiepold attributed the observed difference in recurrence patterns to the hypoxic conditions caused by the reduction in vasculature [143]. These conditions could have affected the glioma cells in some way

Hypoxia has been shown to induce more migration in gliomas [68, 156]. There is also evidence that glioma cells follow a dichotomy of migration and proliferation [48] and evidence of a lower proliferation marker for cells that exist in hypoxic regions of GBMs [18]. Tumours in hypoxic conditions release angiogenesis-promoting factors to encourage vessels to grow towards them that can then provide nutrients [50, 70, 157]. This process also occurs in normoxic conditions at a lower level [157]. Necrosis occurs in the vast majority of GBMs and presents in the core of the tumour [83].

Reaction-diffusion equations have been used extensively to describe the tissue-level growth of GBMs; a simple reaction-diffusion equation, termed the Proliferation Invasion model, can be calibrated with patient-specific T1Gd and T2 MRI sequences and subsequently used to look past the MRI resolution to where the remaining tumour cells might be [136, 141, 137]. We present this model and its applications in more detail in Section 1.4.

Due to the unstructured nature of vasculature around the bulk of the tumor, and the breakdown of the BBB in this region, predicting the distribution of

drugs aimed at treating the tumor is a nontrivial problem. Fairly recent work has coupled rodent vasculature quantified through optical imaging with a computational model of blood flow, drug diffusion and vessel permeability to understand which parameters drive the drug extravasation into surrounding tissue [15]. The model suggests that all parameters play a role and interact nonlinearly to produce the observed drug concentrations. This work acts as a proof of principle for a similar approach for patient data, in the case that highly detailed structural data of vasculature is available

The Proliferation Invasion Hypoxia Necrosis Angiogenesis (PIHNA) model, which we will present a variation of in this chapter (and is also presented in its original form in Section 1.4), has been used to study different mechanisms of tumour development. The PIHNA model shows similar growth and progression patterns to those seen in patient tumours [140]. However, a change in the vasculature in the published formulation of the model has little effect on the dynamics of the tumour growth; in reality, a high level of nutrients provided by a high vascular density would lead to more normoxic cells within the tumour than a low nutrient case. We will introduce our formulation of the PIHNA model in this chapter that will contain a new term based on nutrient provided by the vasculature and consumed by the tumour. We also allow for different ratios of hypoxic cell diffusion rates to normoxic cell diffusion rates, which have previously been the same.

We carry out a travelling wave analysis on the PIHNA model to determine which parameters drive the outward growth of the tumour as a whole, and compare these analytical results with numerical simulations. We then apply the new formulation of PIHNA to vascular ischemia, and propose a mechanism by which a tumour can recur distantly post-resection using 2D simulations on a realistic brain geometry, which could further explain the results seen by Thiepold *et al.* [143].

4.2 ALTERATIONS TO THE PIHNA MODEL

To simulate glioblastoma growth and spread, we have adapted a previously established tumour growth model – the PIHNA model [140] (see Section 1.4). This model simulates five different species and their interactions:

c – the density of normoxic tumour cells,

h – the density of hypoxic tumour cells,

n – the density of necrotic cells,

v – the density of vascular endothelial cells,

a – the concentration of angiogenic factors.

The dimensions of c, h, v and n are cells/mm^3 of tissue. The angiogenic factor, a, is a diffusing concentration with dimensions μmol/mm^3 tissue.

Previous PIHNA publications have set the migration rate of the hypoxic cell density, denoted D_h, to be the same as the migration rate of the normoxic cell density, denoted D_c. However, hypoxia has been shown to promote migration, so we have allowed for this to be varied in the model [68, 156]. Normoxic cells proliferate with rate ρ and migrate with rate D_c, whereas hypoxic cells do not proliferate and migrate with rate D_h. Cells convert between normoxic and hypoxic phenotypes depending on the ability of the local vascular density to provide nutrients at their location; hypoxic cells in the model become necrotic if they remain in such a region. When any other cell type meets a necrotic cell, they become necrotic with rate α_n.

Angiogenic factors are created by the presence of normoxic and hypoxic cells, decay naturally and are consumed through the creation and presence of vascular cells (v). Angiogenic factors are only consumed by vasculature and not tumour or necrotic cells. Unlike vascular cells, tumour cells are assumed to not have the appropriate receptors to consume angiogenic factors. Necrotic cells are dead and despite some of them being dead vascular cells, it is assumed that the vascular cell receptors become inactive once the vasculature is dead so the necrotic tumour and necrotic vascular cells are treated as the same cell type. The degradation of necrotic cells over time is not considered in the model. The PIHNA model could easily become more complex with the addition of more of these mechanisms, but in the spirit of creating a minimal model that can recreate observed phenomena, we have not extended the PIHNA model in these directions.

The governing equations for the PIHNA model are

$$\overbrace{\frac{\partial c}{\partial t}}^{\substack{\text{Change}\\ \text{of normoxic}\\ \text{cell density}}} = \overbrace{\nabla\cdot(D_c(1-T)\nabla c)}^{\substack{\text{Net diffusion of}\\ \text{normoxic}\\ \text{glioma cells}}} + \overbrace{\rho c(1-T)}^{\substack{\text{Net}\\ \text{proliferation}\\ \text{of normoxic}\\ \text{glioma cells}}} + \overbrace{\gamma h V}^{\substack{\text{Conversion}\\ \text{of hypoxic}\\ \text{to normoxic}}} - \overbrace{\beta c(1-V)}^{\substack{\text{Conversion}\\ \text{of normoxic}\\ \text{to hypoxic}}} - \overbrace{\alpha_n \frac{nc}{K}}^{\substack{\text{Conversion}\\ \text{of normoxic}\\ \text{to necrotic}}} \tag{136}$$

$$\overbrace{\frac{\partial h}{\partial t}}^{\substack{\text{Change}\\ \text{of hypoxic}\\ \text{cell density}}} = \overbrace{\nabla\cdot(D_h(1-T)\nabla h)}^{\substack{\text{Net diffusion of}\\ \text{hypoxic}\\ \text{glioma cells}}} - \overbrace{\gamma h V}^{\substack{\text{Conversion}\\ \text{of hypoxic}\\ \text{to normoxic}}} + \overbrace{\beta c(1-V)}^{\substack{\text{Conversion}\\ \text{of normoxic}\\ \text{to hypoxic}}} - \overbrace{\left(\alpha_h h(1-V) + \alpha_n \frac{nh}{K}\right)}^{\substack{\text{Conversion}\\ \text{of hypoxic}\\ \text{to necrotic}}} \tag{137}$$

$$\overbrace{\frac{\partial n}{\partial t}}^{\substack{\text{Change}\\ \text{of necrotic}\\ \text{cell density}}} = \overbrace{\alpha_h h(1-V)}^{\substack{\text{Conversion}\\ \text{of hypoxic}\\ \text{to necrotic}}} + \overbrace{\alpha_n \frac{n(c+h+v)}{K}}^{\substack{\text{Contact necrosis}\\ \text{of all}\\ \text{living cells}}} \tag{138}$$

$$\overbrace{\frac{\partial v}{\partial t}}^{\substack{\text{Change}\\ \text{of vascular}\\ \text{cell density}}} = \overbrace{\nabla\cdot(D_v(1-T)\nabla v)}^{\substack{\text{Net diffusion of}\\ \text{vasculature}}} + \overbrace{\mu \frac{a}{K_m+a} v(1-T)}^{\substack{\text{Net proliferation}\\ \text{of vasculature}}} - \overbrace{\alpha_n \frac{nv}{K}}^{\substack{\text{Conversion}\\ \text{of vasculature}\\ \text{to necrotic}}} \tag{139}$$

$$\overbrace{\frac{\partial a}{\partial t}}^{\substack{\text{Change}\\ \text{of angiogenic}\\ \text{factor}\\ \text{concentration}}} = \overbrace{\nabla\cdot(D_a\nabla a)}^{\substack{\text{Net diffusion of}\\ \text{angiogenic factor}}} + \overbrace{\delta_c c + \delta_h h}^{\substack{\text{Net production}\\ \text{of angiogenic factor}}} - \overbrace{q\mu \frac{a}{K_m+a} v(1-T) - \omega a v}^{\substack{\text{Net consumption of}\\ \text{angiogenic factor}}} - \overbrace{\lambda a}^{\text{Decay}} \tag{140}$$

where

$$V = V(c,h,v), \tag{141}$$

and

$$T = (c+h+n+v)/K. \tag{142}$$

The term V is called the vascular efficiency and it models the relationship between the vasculature and its effect on the tumour. We let V take values in $[0,1]$ such that it affects the switching rates between the populations c, h and n. A value of $V(c,h,v) \approx 0$ corresponds to a very inefficient vasculature that cannot provide sufficient nutrients to the local tumour population; this would increase the conversion of normoxic cells to hypoxic cells and in turn necrotic cells. A high $V(c,h,v) \approx 1$ should lead to a tumour of predominantly normoxic cells (c). It is appropriate to have an expression for $V(c,h,v)$ that is sensitive to a change in vasculature (v), as a low or high vascular density would lead to a limited or ample nutrient supply to the tumour, respectively. It is worth noting that, regardless of the efficiency of the vasculature, necrosis eventually takes hold due to the contact necrosis in the model.

The expression for T defined in Equation 142 is a spatiotemporal measure of the relative density of the cells in a region. It is used to limit growth and migration and used as a threshold to determine which densities would appear on different MRI sequences. The equation for T is given by

$$K\frac{\partial T}{\partial t}=\nabla\cdot((1-T)(D_c\nabla c+D_h\nabla h+D_n\nabla n+D_v\nabla v))+(1-T)\left(\rho c+\frac{\mu a}{K_m+a}v\right),$$

from which it is clear that at $T=1$, the reaction and diffusion terms vanish, which implies T is restricted by the upper bound of 1 (as long as $T(x,0)<1$). Since T is a sum of non-negative densities and $K>0$, $T\geq 0$. We therefore have that $T\in[0,1]$.

Following the literature [135], we have assumed that a total relative cell density of at least 80% is visible on a T1Gd MRI, and a total relative density of at least 16% is visible on a T2 MRI. In the PIHNA model, this translates to $T\geq 0.8$ being visible on a T1Gd and $T\geq 0.16$ being visible on a T2.

Different D_c and ρ values lead to different density profiles on the leading edge of the tumour. A high D_c and a low ρ will lead to a very diffuse tumour that has a more infiltrative leading edge; diffuse tumours will have a much higher T2 radius than the T1Gd radius. Whereas a low D_c and a high ρ gives a very nodular tumour that grows with a sharper leading edge; nodular tumours have comparatively similar T1Gd and T2 radii. By construction the T1Gd radius is always less than or equal to the T2 radius, which agrees with patient data [58].

4.2.1 *Original Vascular Efficiency*

The expression for $V(c,h,v)$ in the original formulation of PIHNA [140] is

$$V=\frac{v}{v+c+h}. \tag{143}$$

This version of V is contained in the range $[0,1]$ as is appropriate. Clearly as v increases, so does V. However, as c and h increase, V becomes insensitive to a change in v. For high levels of $c+h$ relative to v, the tumour population dominates the function, so that an increase or reduction in v does not have much of an effect on the function V, see Figure 38. We wanted to improve this term with a founding in biological mechanisms.

We propose a new vascular efficiency function based on nutrient consumption of a tumour that has the ability to cover a wider range of V values for large $c+h$ values than the original vascular efficiency term in Equation (143).

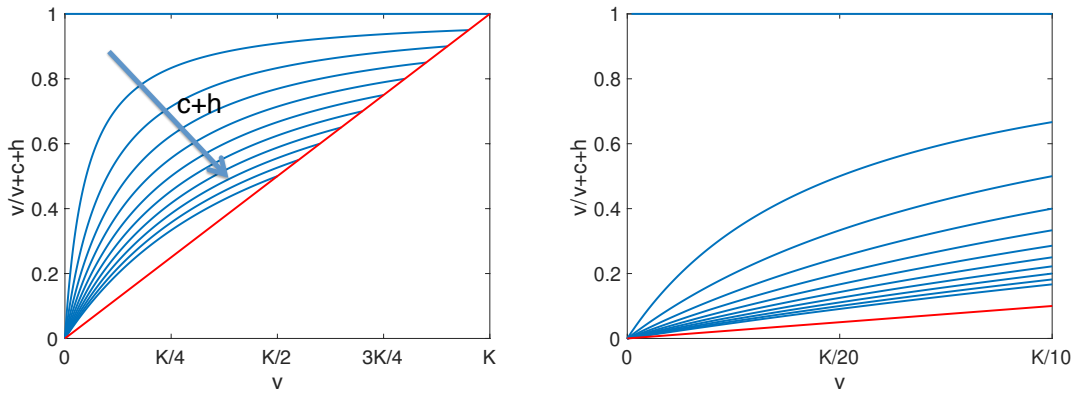


Figure 38: The original vascular efficiency function (Equation (143)) in blue as $c + h$ increases, with the constraint of $v + c + h + n = K$ shown in red (with $n = 0$). Each line is for a fixed value of $c + h$. (a) As $c + h$ increases from 0 to K, the sensitivity to a change in vasculature decreases in the lower regions of v. (b) Focuses on the region of v that we see in the vast majority of simulations throughout time.

This new term is based on a transport equation for nutrient extravasation from vessels and consumption by tumour cells and calibrated through published imaging data of glucose consumption ratios of tumour to healthy tissue.

4.2.2 *Nutrient-Based Vascular Efficiency*

The new vascular efficiency term uses a reaction-transport equation to model the nutrient consumption by the cells. However, we do not include a nutrient explicitly in the model, as we assume a quasi-steady state and limited diffusion. Using this reaction-transport equation for the movement and consumption of nutrient, f[1], the derivation of the vascular efficiency term goes as follows:

$$\frac{\partial f}{\partial t} = \nabla \cdot (D_f \nabla f) + psv(f_{blood} - f) - \eta_c(D_c, \rho)cf - \eta_h(D_h)hf, \tag{144}$$

where p is the permeability of the blood brain barrier to nutrient, s is the surface area of a vascular endothelial cell divided by its volume, f_{blood} is the

1 We denote this as f to represent fuel for the cells, to avoid reusing n which is already assigned to necrotic cells.

concentration of nutrient in the blood which is assumed fixed[2], η_c is the rate of nutrient consumption by normoxic cells and η_h is the nutrient consumption rate by hypoxic cells. We have let η_c depend on the diffusion (D_c) and proliferation (ρ) rates of normoxic cells, as these processes require energy. A larger D_c and ρ will require more energy as the tumour cells migrate and proliferate relatively quickly. Similarly, we have set η_h to depend on the value of D_h, as faster migrating tumour cells require more energy and in turn more nutrient.

Now if we assume that in the timescale of interest, the nutrient concentration rapidly reaches steady state, and that the nutrient is consumed much faster than it diffuses, we can eliminate those terms to be left with

$$0 = 0 + psv(f_{blood} - f) - \eta_c(D_c, \rho)cf - \eta_h(D_h)hf \tag{145}$$

and rearrange to get

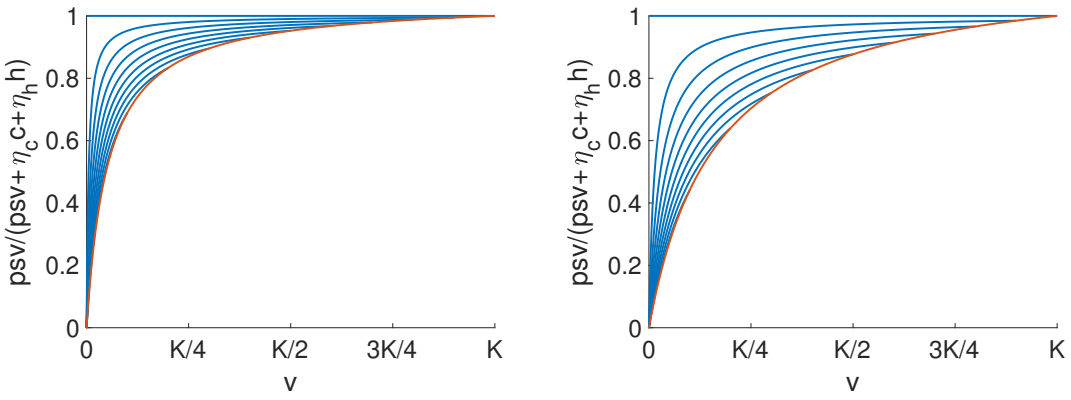
$$\frac{f}{f_{blood}} = \frac{v}{v + \frac{\eta_c(D_c,\rho)c + \eta_h(D_h)h}{ps}}. \tag{146}$$

We assign this expression as the new vascular efficiency, V, as it corresponds to the ability of the vasculature to provide nutrients to the tumour. This term is similar to that seen in the original formulation of PIHNA (Equation (143)). The key difference is the parameters in front of the hypoxic and normoxic cell densities; these parameters can increase the sensitivity of the term to a change in $c + h$, see Figure 39. Although nutrient is consumed by the vasculature, we assume this occurs from the blood inside the vessels and does not change f_{blood}. The nutrient-based vascular efficiency term can be thought of as an extension of the original, where in the original V the rate of uptake of normoxic and hypoxic cells was always equal to the rate at which nutrient extravasates from the vessels.

Calibrating the Nutrient-Based Vascular Efficiency

To estimate the parameters η_c, η_h and ps, we used Fludeoxyglucose (FDG) Positron Emission Tomography (PET) data from a paper by Delbeke *et al.* [37]. FDG is analogous to glucose and can be picked up on PET scans. Although hypoxia is by definition a lack of oxygen, we have chosen glucose as an estimate for our generic nutrient, due to the availability of imaging data that we could use to parametrise our vascular efficiency term.

2 It is well known that nutrient concentrations in blood (such as glucose concentration) fluctuates throughout a single day, however we are interested in modelling tumour growth over many days and months, so only consider the average nutrient concentration across these daily fluctuations.



(a) (b)

Figure 39: Nutrient-based vascular efficiency (Equation 146) term for lowest (a) and highest (b) simulated ρ and D_c (and in turn D_h). There is a larger range of V to low levels of v than in the original term Equation 143. Subfigure (b) shows a vasculature that is less able to support the tumour than subfigure (a), which corresponds with the tumour in subfigure (b) requiring more nutrients.

We note that to parametrise our nutrient-based vascular efficiency term, we only need to consider the ratio between $\eta_c : ps$ and $\eta_h : ps$. As both of these expressions are in the same units of $\text{mm}^3/\text{cell}/\text{year}$, their ratio is dimensionless. Delbeke presents the uptake ratios between tumour and healthy tissue within both white and grey matter. To make use of these values, we assume that in a homeostatic healthy brain, the rate of glucose being used by healthy tissue that is not vasculature is equal to the rate of glucose entering from the vasculature. We do not, however, model healthy tissue in the current formulation of the PIHNA model. For the benefit of this section, let us introduce unaffected healthy tissue u_0, with glucose uptake rate η_u, we assume

$$psv_0 = \eta_u(u_0 - v_0), \tag{147}$$

where v_0 is the initial background vascular cell density in the PIHNA model, and u_0 is the healthy tissue density. We then have $ps = \eta_u(u_0/v_0 - 1)$, which will always be positive in PIHNA simulations as vasculature takes up a small percentage of brain volume compared to other tissue. We assume that in healthy white matter tissue there is 3% vasculature and in grey there is 5%, so we let $v_0/u_0 = 0.03$ in white matter and $v_0/u_0 = 0.05$ in grey matter; these values fall within realistic values for cerebral blood volume [155]. Now the ratios of glucose uptake rates by tumour to the glucose uptake rates by healthy

tissue given by Delbeke can be considered as various values of $P_c = \eta_c/\eta_u$ and $P_h = \eta_h/\eta_u$ in the model. So Equation 146 is now expressed as

$$V = \frac{v}{v + \frac{P_c\eta_u c + P_h\eta_u h}{\eta_u(u_0/v_0 - 1)}}, \tag{148}$$

and the η_u terms cancel to give

$$V = \frac{v}{v + \frac{P_c c + P_h h}{u_0/v_0 - 1}}. \tag{149}$$

We noted that in the work by Delbeke et al.[37] there was a spread of relative tumour uptake values for high grade gliomas within cortical and white matter tissue across 20 patients. As an approximation, we attributed these differences to the nutritional demands of the individual high grade gliomas. We assign normoxic cells with high (low) D_c and high (low) ρ in the PIHNA model with the higher (lower) glucose uptake rates from the literature, which also vary between white and grey matter. We assign hypoxic cells with high (low) D_h high (low) glucose uptake rates in the same manner as the normoxic cells. The values in between the extremes are assigned using a log linear scale, due to the large range of D_c, D_h and ρ values used in PIHNA simulations. The ratios P_c^w, P_c^g, P_h^w and P_h^g are then given by

$$P_c^{w,g}(D_c, \rho) = G_{max}^{w,g} - (G_{max}^{w,g} - G_{min}^{w,g})\frac{\log_{10}\left(\frac{D_{c_{max}}}{D_c}\right) + \log_{10}\left(\frac{\rho_{max}}{\rho}\right)}{\log_{10}\left(\frac{D_{c_{max}}}{D_{c_{min}}}\right) + \log_{10}\left(\frac{\rho_{max}}{\rho_{min}}\right)} \tag{150}$$

and

$$P_h^{w,g}(D_h) = G_{max}^{w,g} - (G_{max}^{w,g} - G_{min}^{w,g})\frac{\log_{10}(D_{h_{max}}/D_h)}{\log_{10}(D_{h_{max}}/D_{h_{min}})}, \tag{151}$$

where we use the extremes of tumour to normal tissue uptake ratios in white matter (taken as $G_{min}^w = 1.66$ and $G_{max}^w = 4.5$) and the extremes of observed uptake ratio in grey matter (taken as $G_{min}^g = 0.5$ and $G_{max}^g = 2$) as the minimum to maximum glucose uptake ratios G_{min} and G_{max}. Note that in the 1D PIHNA model we only model white matter and the 2D PIHNA model includes both white and grey. The maximum and minimum D_c, D_h and ρ values are equal to the maximal and minimal rates that we run in our simulations, see Table 4. This along with the values of v_0/u_0 give the parametrisation of the nutrient-based vascular efficiency term.

4.3 THE PIHNA MODEL IN ONE SPATIAL DIMENSION

Assuming radially symmetric tumour growth, the PIHNA model can be solved in just one spatial dimension. This does not take into account the

	Definition	Value/Range	Units	Source
D_c	Diffusion rate of normoxic cells	$1-1000$	$\frac{\text{mm}^2}{\text{year}}$	[58]
D_h	Diffusion rate of hypoxic cells	$(0.1-100)D_c$	$\frac{\text{mm}^2}{\text{year}}$	[58, 88]*
ρ	Proliferation rate of normoxic cells	$10-100$	$1/\text{year}$	[58]
β	Switching rate from normoxia to hypoxia	$0.1\rho-0.5\rho$	$1/\text{year}$	[140]*
γ	Switching rate from hypoxia to normoxia	0.05	$1/\text{day}$	[140]
α_h	Switching rate from hypoxia to necrosis	0.1β	$1/\text{year}$	[140]
α_n	Rate of contact necrosis	$\log(2)/50$	$1/\text{day}$	[117]
D_v	Diffusion rate of endothelial cells	0.18	$\frac{\text{mm}^2}{\text{year}}$	[140]
D_a	Diffusion rate of angiogenic factors	3.15	$\frac{\text{mm}^2}{\text{year}}$	[140]
δ_c	Normoxic cell production rate of angiogenic factors	2.77×10^{-13}	$\frac{\mu\text{mol}}{\text{cell}\times\text{year}}$	[140]
δ_h	Hypoxic cell production rate of angiogenic factors	5.22×10^{-10}	$\frac{\mu\text{mol}}{\text{cell}\times\text{year}}$	[140]
μ	Angiogenesis vasculature production rate	$\log(2)/15$	$1/\text{day}$	[140]
q	Consumption of angiogenic factors per cell	1.66	$\mu\text{mol/cell}$	[140]
λ	Natural decay rate of angiogenic factors	15.6	$1/\text{day}$	[140]
ω	Rate of removal of angiogenic factors by vasculature	λ/v_0	$\frac{1}{\text{cell}\times\text{day}}$	[140]
K	Maximal cell density	2.4×10^8	cells	[140]
P_c^w	Glucose consumption ratio for normoxic cells in white matter	$1.66-4.5$	-	[37]*
P_h^w	Glucose consumption ratio for hypoxic cells in white matter	$1.66-4.5$	-	[37]*
P_c^g	Glucose consumption ratio for normoxic cells in grey matter	$0.5-2$	-	[37]*
P_h^g	Glucose consumption ratio for hypoxic cells in grey matter	$0.5-2$	-	[37]*

Table 4: Parameter definitions and values for the PIHNA model. *Parameters that we have added/altered in this formulation of PIHNA.

full anatomy of the brain, but it is useful to run simulations in order to gain insight into the model behaviour. In all PIHNA simulations (including in two spatial dimensions), the tumour and necrotic cell densities spread outwards. A peak in normoxic cell density leads and is followed by a peak in hypoxic cell density and then a zone of necrosis, as can be seen in Figure 40. We will show with these simulations how a change in vasculature can have little effect on the behaviour of the tumour when we use the original vascular efficiency term (Equation (143)) and compare it to our nutrient-based vascular efficiency term (Equation (146)).

The PIHNA model is simulated with radial symmetry such that we solve for the radius r of a sphere, with zero-flux boundary conditions at the end points, $r = 0$ and $r = r_{end}$. The initial condition is the same as previous publications of the PIHNA model and is given by

$$c(r, 0) = 1000e^{-100r^2}, \tag{152}$$

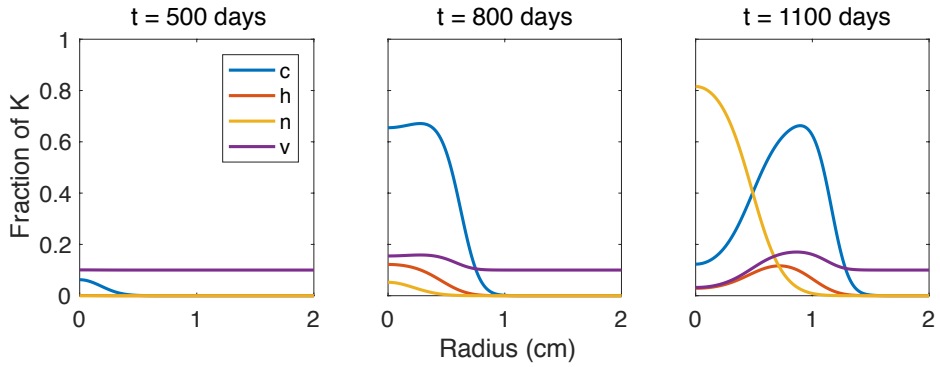
to simulate a small initiating population of normoxic tumour cells decreasing away from the core of the tumour. We also have $h(r, 0) = 0$, $n(r, 0) = 0$, $v(r, 0) = v_0$ and $a(r, 0) = 0$. We run the PIHNA simulations with the parameters found in Table 4.

As previously described, a high D_c/ρ will lead to a diffuse tumour, and a low D_c/ρ will lead to a nodular tumour. As the necrotic cell density is always increasing in the model and encourages all other cell types to become necrotic when they meet (with rate α_n), there is a steady state in the model behind the wave of $(c, h, v, n, a) = (0, 0, 0, N, 0)$. The vasculature increases slightly at the leading edge of the tumour, but dies towards the necrotic core. As previous variations of the PIHNA model have shown, this patterning is similar to that seen clinically [140].

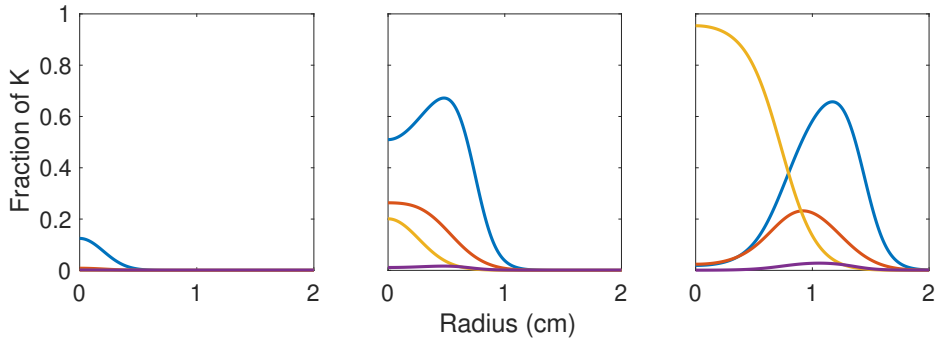
4.3.1 *Comparing Vascular Efficiencies*

To show the effect of a change in vasculature in the model for the original and nutrient-based vascular efficiency terms, we compare simulations with a very small initial vascular density of 0.1% of the carrying capacity ($v_0 = 0.001K$) and a relatively large 10% of the carrying capacity ($v_0 = 0.1K$).

We present snapshots of full simulations of the model with the original vascular efficiency and with the nutrient-based vascular efficiency for these extreme initial vasculature cases in Figures 40 and 41, respectively. In these



(a) $v_0 = 0.1K$



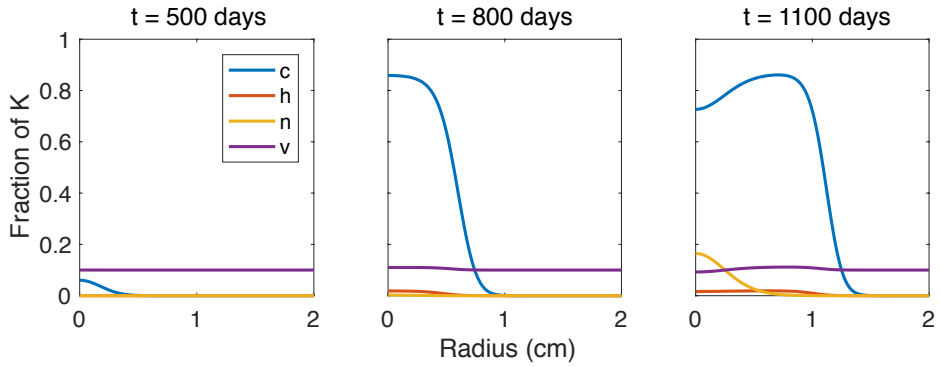
(b) $v_0 = 0.001K$

Figure 40: Snapshots of two simulations with the original vascular efficiency. $D_c = 1\text{mm/year}$, $\rho = 10/\text{year}$ and $D_h = 10D_c$. Notice the simulation with the lower vasculature grows outward faster.

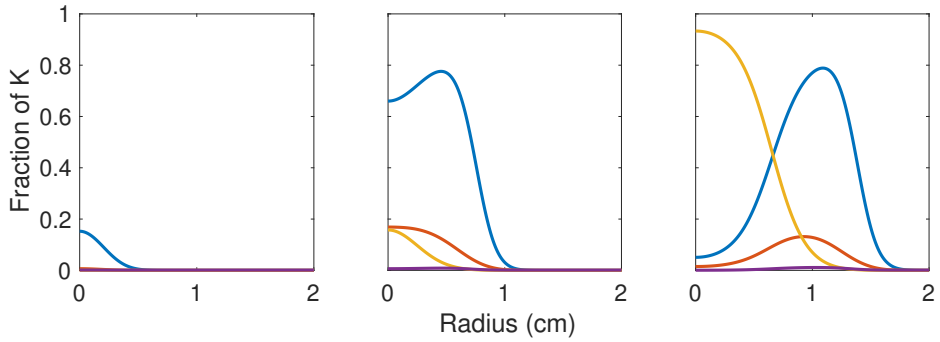
simulations, we have $D_c = 1\text{mm/year}$, $\rho = 10/\text{year}$, $D_h = 10D_c$ and $\beta = 0.1\rho$, which are the lowest values of D_c and ρ that we have simulated. The change in the vascular efficiency term does not appear to affect the rate of outward growth of the presented simulations, but does affect the proportion of the cell density that is normoxic, hypoxic, and necrotic.

In Figure 40 and Figure 41, we noted that the extremely low vasculature ($v_0 = 0.001K$) leads to a faster growing tumour than the higher level ($v_0 = 0.1K$). We wanted to understand the mechanism behind this, which led to a wavespeed analysis in Section 4.3.2.

To look further at the sensitivity in the model to the nutrient vascular efficiency term compared with the original, we have computed the total normoxic, hypoxic and necrotic cell populations and divided them by the sum of these populations. We computed the populations using an integral of the cell densities over the whole sphere (with the inbuilt *trapz.m* function in Matlab



(a) $v_0 = 0.1K$



(b) $v_0 = 0.001K$

Figure 41: Snapshots of two simulations with the nutrient-based vascular efficiency. $D_c = 1\text{mm/year}$, $\rho = 10/\text{year}$ and $D_h = 10D_c$. Notice the simulation with the lower vasculature grows outward faster.

2017a) for all combinations of our minimum and maximum ρ and D_c values. Let us introduce the proportion of tumour that is normoxic c_{prop}, as

$$c_{prop} = \frac{4\pi \int_0^{r_{end}} cr^2\,dr}{4\pi \int_0^{r_{end}} (c+h+n)r^2\,dr}, \tag{153}$$

the hypoxic proportion

$$h_{prop} = \frac{4\pi \int_0^{r_{end}} hr^2\,dr}{4\pi \int_0^{r_{end}} (c+h+n)r^2\,dr} \tag{154}$$

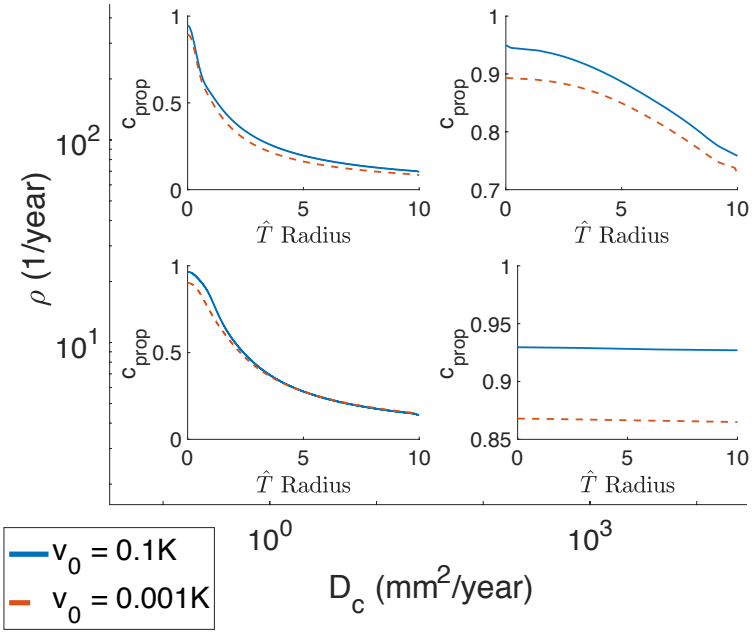
and the necrotic proportion

$$n_{prop} = \frac{4\pi \int_0^{r_{end}} nr^2\,dr}{4\pi \int_0^{r_{end}} (c+h+n)r^2\,dr}. \tag{155}$$

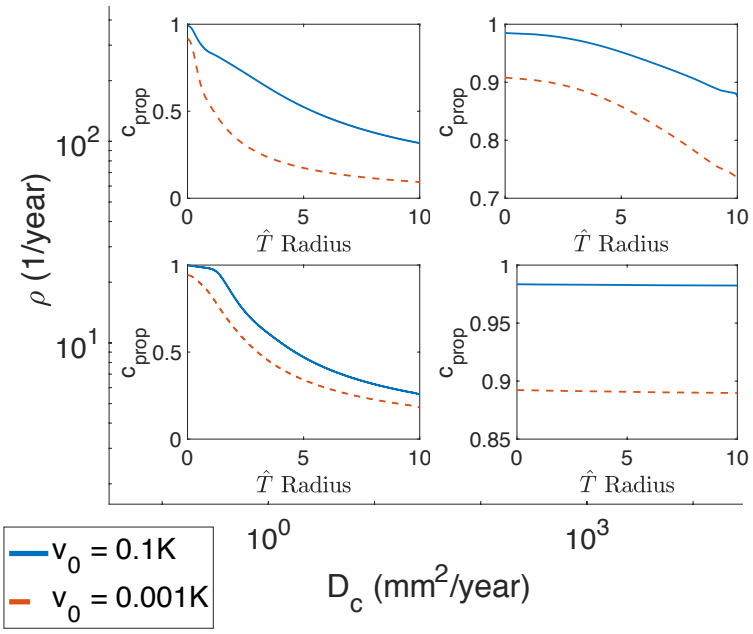
We present c_{prop} in Figure 42 for the original vascular efficiency term (Equation (143)) and for the nutrient-based vascular efficiency term (Equation (146)). We also present the analogous analyses for h_{prop} in Figure 43 and n_{prop} in Figure 44. We wanted to show these proportions against the radial size of the

tumour, rather than time, due to the noticeable differences in the tumour wavespeed for various values of v_0 (which we look into further in Section 4.3.2). We were also aware that if we choose a T1Gd or T2 threshold, that the difference in initial vasculature would affect our results. So for the benefit of this analysis, we instead use $\hat{T} = (c + h + n)/K = 0.5$ as the threshold to compare these different simulations.

We would expect that for a higher initial vasculature, the vasculature would provide more nutrients to the tumour such that c_{prop} would be higher, h_{prop} would be lower and n_{prop} would be higher. However, there is also the consideration that these populations are competing for space in the PIHNA model, and that the high initial background vasculature is taking up 10% of the available space that the tumour can grow into. For the original vascular efficiency term, there is little difference between the low and high initial vasculatures for some cell density proportions and D and ρ values. In most simulations, the nutrient-based vascular efficiency term leads to a larger difference in c_{prop}, h_{prop} and n_{prop} between the two initial vasculatures.

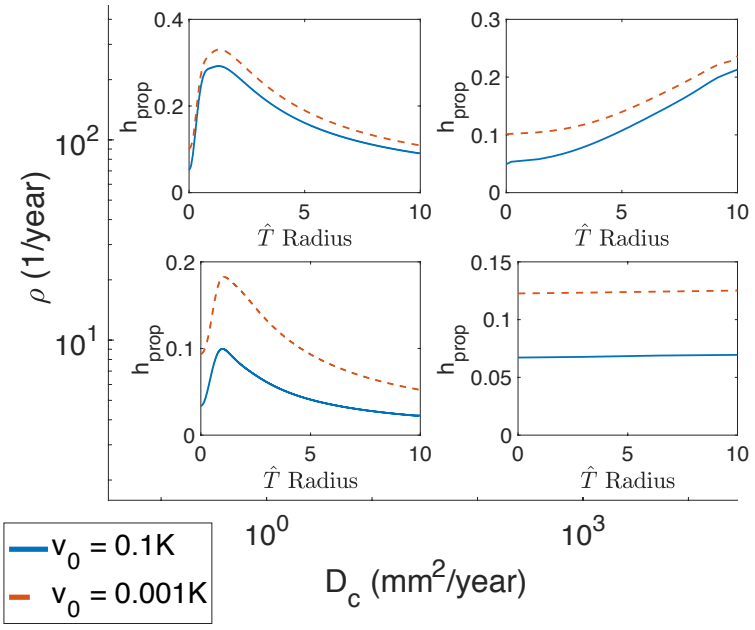


(a) Original Vascular Efficiency

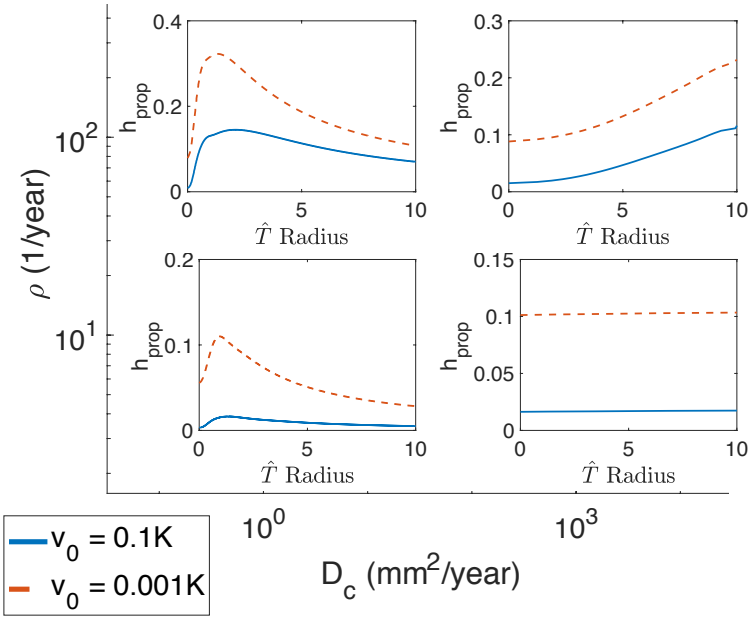


(b) Nutrient-Based Vascular Efficiency

Figure 42: Here we present c_{prop} for simulations with the extreme values of D_c and ρ with $D_h = 10D_c$ and $\beta = 0.1\rho$ with a low initial vascular density ($v_0 = 0.001K$) and high initial vascular density ($v_0 = 0.1K$). We see that (b) the nutrient-based vascular efficiency gives rise to a larger difference in c_{prop} than the original term (a), suggesting that the change in vasculature has a larger impact than for the original vascular efficiency term.

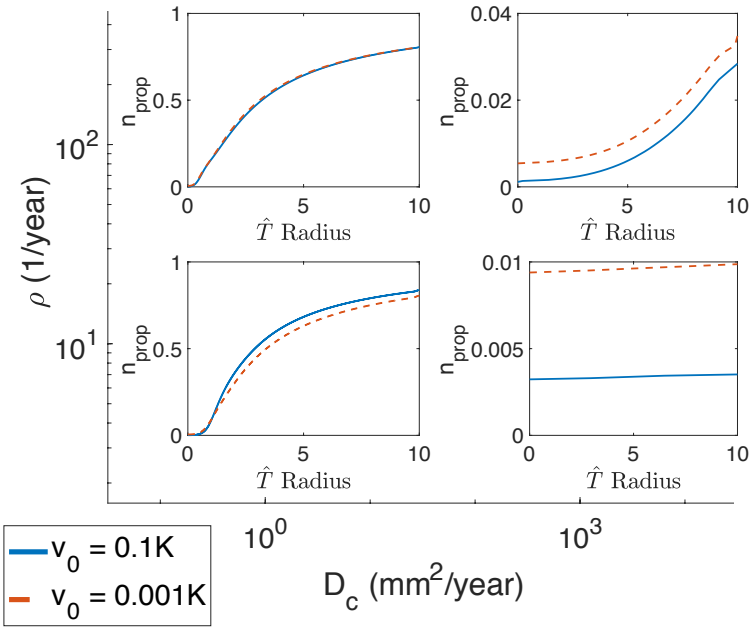


(a) Original Vascular Efficiency

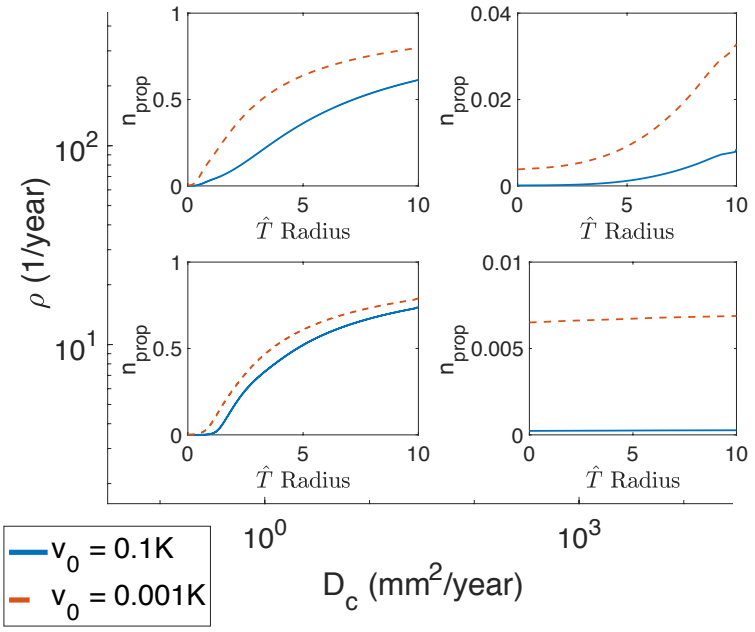


(b) Nutrient-Based Vascular Efficiency

Figure 43: Here we present h_{prop} for simulations with the extreme values of D_c and ρ with $D_h = 10D_c$ and $\beta = 0.1\rho$ with a low initial vascular density ($v_0 = 0.001K$) and high initial vascular density ($v_0 = 0.1K$). We see that the nutrient-based vascular efficiency gives rise to a larger difference in h_{prop} than the original term, suggesting that the change in vasculature has a larger impact than for the original vascular efficiency term.



(a) Original Vascular Efficiency



(b) Nutrient-Based Vascular Efficiency

Figure 44: Here we present n_{prop} for simulations with the extreme values of D_c and ρ with $D_h = 10D_c$ and $\beta = 0.1\rho$ with a low initial vascular density ($v_0 = 0.001K$) and high initial vascular density ($v_0 = 0.1K$). We see that the nutrient-based vascular efficiency gives rise to a larger difference in n_{prop} than the original term, suggesting that the change in vasculature has a larger impact than for the original vascular efficiency term.

In conclusion, the nutrient-based vascular efficiency is a product of a reaction-transport equation with some realistic uptake ratios found in the literature [37]. We see more sensitivity in the normoxic and hypoxic tumour cell populations to a change in the initial vasculature with this new term and do not see biologically unrealistic changes for varying initial vasculatures. We therefore will use the nutrient-based vascular efficiency term preferentially over the original.

As we have previously mentioned, there is a difference in the speed of the outward growth in our 1D simulations with a change in the initial vasculature for both the original and nutrient-based vascular efficiency terms. Tumours in simulations with higher initial vasculatures grow more slowly than their counterparts with lower initial vasculatures. We were interested to see why this was, whether it was a hypoxia mediated effect, a more direct effect of the vasculature, or something else. We therefore found an analytical expression to predict the minimum wavespeed for the PIHNA model and to see which parameters played a role in this rate of tumour growth. We present the derivation of this analytical expression in the next section, and go on to show under which conditions this wavespeed is achieved through numerical simulations in Section 4.3.3.

4.3.2 *Travelling Wave Analysis*

In a similar fashion to the well-established minimum wavespeed of Fisher's Equation [43] that has been used for the Proliferation Invasion tumour growth model, we wanted to find an analytical expression for the tumour wavespeed in the PIHNA model. We start by linearising the model around the leading edge of the wave, that has the initial condition of $(c, h, n, v, a) = (0, 0, 0, v_0, 0)$

$$(c, h, n, v, a) = (0, 0, 0, v_0, 0) + (\tilde{c}, \tilde{h}, \tilde{n}, \tilde{v}, \tilde{a}). \tag{156}$$

Note that $|\tilde{c}| \ll 1$, $|\tilde{h}| \ll 1$, $|\tilde{n}| \ll 1$, $|\tilde{v}| \ll 1$ and $|\tilde{a}| \ll 1$.

Substituting in Equation (156) into the PIHNA model (Equations (136) – (140)) and discarding non-linear terms leads to the following equations:

$$\frac{\partial \tilde{c}}{\partial t} = \nabla \cdot \left(D_c \left(1 - \frac{v_0}{K}\right) \nabla \tilde{c} \right) + \rho \tilde{c} \left(1 - \frac{v_0}{K}\right) + \gamma \tilde{h} V(0,0,v_0) - \beta \tilde{c}(1 - V(0,0,v_0)) \tag{157}$$

$$\frac{\partial \tilde{h}}{\partial t} = \nabla \cdot \left(D_h \left(1 - \frac{v_0}{K}\right) \nabla \tilde{h} \right) - \gamma \tilde{h} V(v_0,0,0) + (\beta \tilde{c} - \alpha_h \tilde{h})(1 - V(0,0,v_0)) \tag{158}$$

$$\frac{\partial \tilde{n}}{\partial t} = \alpha_h \tilde{h}(1 - V(0,0,v_0)) + \alpha_n \tilde{n} \frac{v_0}{K} \tag{159}$$

$$\frac{\partial \tilde{v}}{\partial t} = \nabla \cdot \left(D_v \left(1 - \frac{v_0}{K}\right) \nabla \tilde{v} \right) + \mu \frac{v_0}{K_m} \left(1 - \frac{v_0}{K}\right) \tilde{a} - \alpha_n \frac{v_0}{K} \tilde{n} \tag{160}$$

$$\frac{\partial \tilde{a}}{\partial t} = \nabla \cdot (D_a \nabla \tilde{a}) + \delta_c \tilde{c} + \delta_h \tilde{h} - q\mu \frac{v_0}{K_m} \left(1 - \frac{v_0}{K}\right) \tilde{a} - \omega v_0 \tilde{a} - \lambda \tilde{a}. \tag{161}$$

The equations for $\tilde{c}$, $\tilde{h}$ and $\tilde{n}$ decouple from the system. We will analyse these three equations to look for travelling wave solutions of the form

$$(\tilde{c}, \tilde{h}, \tilde{n}) = (\bar{c}, \bar{h}, \bar{n}) \exp(\lambda(x - st)), \tag{162}$$

where s is the wavespeed. Substituting Equation (162) into Equations (157) - (159) gives rise to the following set of equations

$$-s\lambda \bar{c} = D_c \left(1 - \frac{v_0}{K}\right) \lambda^2 \bar{c} + \rho \left(1 - \frac{v_0}{K}\right) \bar{c} - \beta(1 - V(0,0,v_0))\bar{c} + \gamma V(0,0,v_0)\bar{h} \tag{163}$$

$$-s\lambda \bar{h} = D_h \left(1 - \frac{v_0}{K}\right) \lambda^2 \bar{h} + \beta(1 - V(0,0,v_0))\bar{c} - \gamma V(0,0,v_0)\bar{h} - \alpha_h(1 - V(0,0,v_0))\bar{h} \tag{164}$$

$$-s\lambda \bar{n} = \alpha_h(1 - V(0,0,v_0))\bar{h} + \alpha_n \frac{v_0}{K} \bar{n}. \tag{165}$$

Rearranging the equations into the matrix form of

$$A \begin{bmatrix} \bar{c} \\ \bar{h} \\ \bar{n} \end{bmatrix} = \mathbf{0}, \tag{166}$$

gives A as

$$\begin{bmatrix} a_{11} \\ a_{21} \\ a_{31} \end{bmatrix} = \begin{bmatrix} s\lambda + D_c \left(1 - \frac{v_0}{K}\right) \lambda^2 + \rho \left(1 - \frac{v_0}{K}\right) - \beta(1 - V(0,0,v_0)) \\ \beta(1 - V(0,0,v_0)) \\ 0 \end{bmatrix}$$

$$\begin{bmatrix} a_{12} \\ a_{22} \\ a_{32} \end{bmatrix} = \begin{bmatrix} \gamma V(0,0,v_0) \\ s\lambda + D_h\left(1-\frac{v_0}{K}\right)\lambda^2 - \gamma V(0,0,v_0) - \alpha_h(1-V(0,0,v_0)) \\ \alpha_h(1-V(0,0,v_0)) \end{bmatrix}$$

$$\begin{bmatrix} a_{13} \\ a_{23} \\ a_{33} \end{bmatrix} = \begin{bmatrix} 0 \\ 0 \\ s\lambda + \alpha_n \frac{v_0}{K} \end{bmatrix}.$$

The determinant of A needs to be 0 in order to give non-trivial solutions to the set of equations. The determinant of A is given by

$$\begin{aligned}\det(A) = \left(s\lambda + \alpha_n\frac{v_0}{K}\right)\Bigg[&\left(s\lambda + D_c\left(1-\frac{v_0}{K}\right)\lambda^2 + \rho\left(1-\frac{v_0}{K}\right) - \beta(1-V(0,0,v_0))\right)\times \\ &\left(s\lambda + D_h\left(1-\frac{v_0}{K}\right)\lambda^2 - \gamma V(0,0,v_0) - \alpha_h(1-V(0,0,v_0))\right) - \\ &\beta(1-V(0,0,v_0))\gamma V(0,0,v_0)\Bigg].\end{aligned}$$

Setting $\det(A) = 0$ leads to either

$$\lambda_1 = -\frac{\alpha_n v_0}{sK} \tag{167}$$

or

$$\begin{aligned}&\left(s\lambda + D_c\left(1-\frac{v_0}{K}\right)\lambda^2 + \rho\left(1-\frac{v_0}{K}\right) - \beta(1-V(0,0,v_0))\right)\times \\ &\left(s\lambda + D_h\left(1-\frac{v_0}{K}\right)\lambda^2 - \gamma V(0,0,v_0) - \alpha_h(1-V(0,0,v_0))\right) \\ &= \beta(1-V(0,0,v_0))\gamma V(0,0,v_0).\end{aligned} \tag{168}$$

With the original vascular efficiency term, Equation (143), we have

$$V(0,0,v_0) = \frac{v_0}{v_0+0} = 1. \tag{169}$$

The same holds for the nutrient-based vascular efficiency term (Equation (144))

$$V(0,0,v_0) = \frac{v_0}{v_0 + \frac{0\times\eta_c + 0\times\eta_h}{ps}} = 1. \tag{170}$$

So for both cases, we have cancellation in Equation (168); this becomes

$$\left(s\lambda + D_c\left(1-\frac{v_0}{K}\right)\lambda^2 + \rho\left(1-\frac{v_0}{K}\right)\right)\left(s\lambda + D_h\left(1-\frac{v_0}{K}\right)\lambda^2 - \gamma\right) = 0, \tag{171}$$

which we can find the eigenvalues for as functions of the wavespeed, s. We have four more values of λ, given by

$$\lambda_{2,3} = \frac{-s \pm \sqrt{s^2 - 4D_c\rho\left(1-\frac{v_0}{K}\right)^2}}{2D_c\left(1-\frac{v_0}{K}\right)} \text{ and } \lambda_{4,5} = \frac{-s \pm \sqrt{s^2 + 4D_h\gamma\left(1-\frac{v_0}{K}\right)}}{2D_h\left(1-\frac{v_0}{K}\right)}.$$

The first set of quadratic λ solutions are both negative as $s > 0$ by assumption. Due to positive restrictions on the state space (negative populations do not make any biological sense), a spiral approach around the point $(0, 0, 0, v_0, 0)$ cannot occur. Therefore, we need the discriminant of the set of quadratic $\lambda_{2,3}$ solutions to be greater than or equal to 0. In other words,

$$s^2 - 4D_c\rho\left(1 - \frac{v_0}{K}\right)^2 \geq 0. \tag{172}$$

Therefore, we have a minimum wave speed of

$$s_{min} = 2\sqrt{D_c\rho}\left(1 - \frac{v_0}{K}\right). \tag{173}$$

The model will follow this minimum wavespeed if the eigenvalue λ_2 at this minimum gives the smallest possible negative eigenvalue of $\lambda_{2,3,4,5}$. If there is another value of s that will produce smaller negative values from another eigenvalue, we will see a solution emerging with a larger wavespeed. The first eigenvalue, λ_1, does not affect the wavespeed of our simulations, as there is no proliferation or migration associated with the necrosis that can drive the tumour growth. A natural next step is to see if our simulations follow this minimum wave speed; we run this analysis in the next section.

4.3.3 *Wavespeed Verification*

To calculate the wavespeed in numerical simulations, we focused on the average growth rate per 0.5cm radial growth visible on a simulated T2 MR sequence (thresholded at $T = 0.16$) to look at the overall wavespeed values of each simulated tumour as it grows. We chose this over the simulated T1Gd MRI as the lower cell densities converge to the wavespeed earlier in simulations than the higher densities. We are particularly interested in the effect on the wavespeed of hypoxic cells, especially the change in their migration rate compared with normoxic cells (D_h/D_c), which we have added to the PIHNA model for the first time.

Running simulations with $D_h \leq D_c$, we see convergence of the tumour wavespeed towards the predicted value, see Figure 45. However, if we compute the wavespeed for simulations where $D_h > D_c$, we see that the wavespeed can be faster, and continues to increase for larger D_h/D_c values; this can be seen in Figure 45. From these observations, we can deduce that if the hypoxic cell migration is much faster than the normoxic cell migration, the hypoxic cell population drives the outward growth of the tumour in

the PIHNA model. This behaviour intuitively agrees with the biological cell movement patterns that the model is trying to capture; cells moving faster dominate the growth outwards as they search for nutrients.

The mathematical reasoning behind the switch from the predicted minimum wavespeed to the faster wavespeed can be seen from the eigenvalues and their corresponding eigenvectors. As previously mentioned, the least negative eigenvalues correspond to the wavespeed behaviour of the simulated tumours. The least negative eigenvalues of the diffusing tumour cells are given by

$$\lambda_2 = \frac{-s + \sqrt{s^2 - 4D_c\rho\left(1 - \frac{v_0}{K}\right)^2}}{2D_c\left(1 - \frac{v_0}{K}\right)} \text{ and } \lambda_5 = \frac{-s - \sqrt{s^2 + 4D_h\gamma\left(1 - \frac{v_0}{K}\right)}}{2D_h\left(1 - \frac{v_0}{K}\right)},$$

with the smallest negative eigenvalue for the minimum wavespeed given by

$$\lambda_{min} = -\frac{s_{min}}{2D_c\left(1 - \frac{v_0}{K}\right)}. \tag{174}$$

In simulations, we see that λ_5 can become even smaller than λ_{min} for large enough D_h/D_c and we see a corresponding switch in the wavespeed of tumour growth at the point when the magnitudes of λ_5 and λ_{min} switch, see Figure 45 for an example. We have also computed the corresponding eigenvectors for all of our eigenvalues, which we shall denote V_i for each λ_i. These are given by the the following expressions, up to a proportional constant:

$$V_1 = \begin{bmatrix} 0 \\ 0 \\ 1 \end{bmatrix}, V_{2,3} = \begin{bmatrix} 1 \\ 0 \\ 0 \end{bmatrix} \text{ and } V_{4,5} = \begin{bmatrix} -\gamma \\ s\lambda_{4,5} + \left(D_c\lambda_{4,5}^2 + \rho\right)\left(1 - \frac{v_0}{K}\right) \\ 0 \end{bmatrix}. \tag{175}$$

The eigenvector V_1 does not contribute to the wavespeed dynamics as the normoxic population cannot approach along this line (as there is no normoxic or even hypoxic component). Focusing on the eigenvectors corresponding to the least negative eigenvectors, V_2 and V_5, we see that they influence the dynamics of the model. By plotting the normoxic cell density across space against the hypoxic cell density across space for a fixed time point where each simulation has converged to a stable wavespeed, alongside V_2 and V_5, we can see which eigenvector is influencing the dynamics of the model. We present two simulations with their corresponding V_2 and V_5 eigenvectors in Figure 46, one for $D_h/D_c = 10^{-1}$ and another for $D_h/D_c = 10^1$. For $D_h/D_c = 10^{-1}$, where the wavespeed follows the predicted minimum value, we see that the model follows $(c, h) = (0, 0)$ along the eigenvector V_2, whereas for

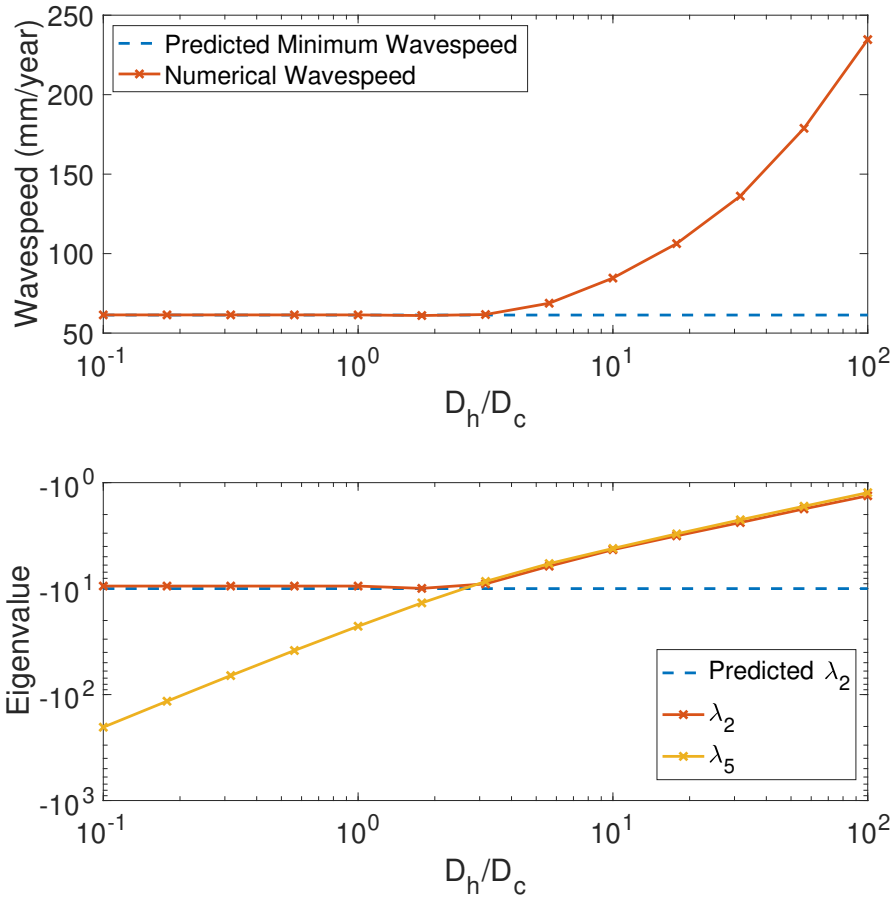


Figure 45: As D_h/D_c is increased for this example with $D_c = 10^{1.5}\text{mm}^2/\text{year}$ and $\rho = 10^{1.5}/\text{year}$, we see an increase in the converged numerical wavespeed at the same point that λ_5 becomes less negative than λ_{min}. At which point λ_3 diverges to follow the same trend as λ_5. Wavespeeds taken as the average speed between 8.5 and 9cm of growth on simulated T2 MRI (16% total cell density threshold).

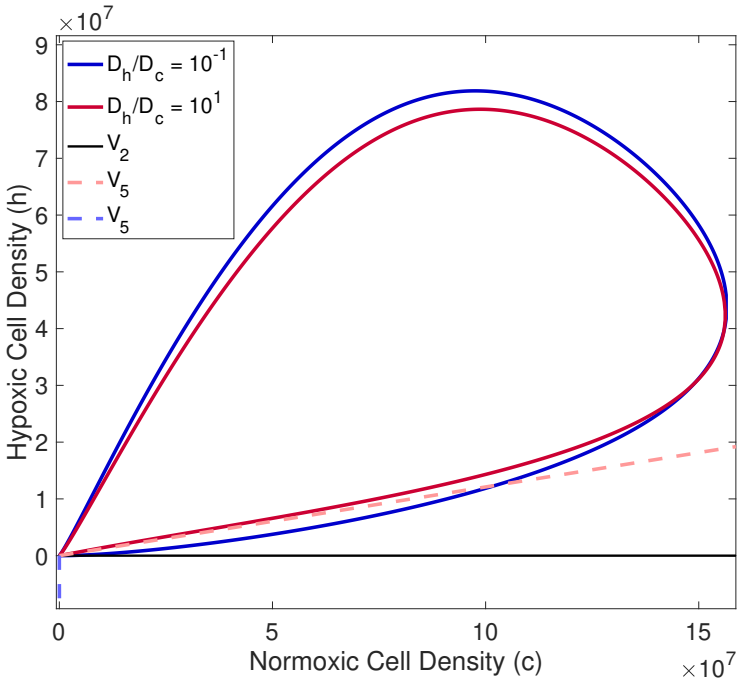


Figure 46: For $D_h/D_c = 10^{-1}$, we see the dynamics follow V_2 (black) near $(c,h) = (0,0)$, which corresponds to the predicted minimum wavespeed, s_{min}. For $D_h/D_c = 10^1$, the dynamics shift towards V_5 (pink), corresponding with the faster numerical wavespeed we have observed. Notice also that V_5 differs between the simulations whereas V_2 remains fixed. Here $D_c = 10^{1.5}\text{mm}^2/\text{year}$, $\rho = 10^{1.5}/\text{year}$. Eigenvectors shown correspond to the eigenvalues of Figure 45 at very large T2 sizes to ensure convergence (29.5 - 30cm of growth).

$D_h/D_c = 10^{-1}$, the approach is along V_5. We also see that V_5 differs between simulations. As D_h/D_c is increased, the gradient of V_5 becomes positive and thus enters the biologically realistic quadrant, where it affects the dynamics.

As we discussed in the introduction to this chapter, we are interested in simulating perioperative ischemia, a reduction in bloody supply that can occur as a surgical complication, as this has been shown clinically to lead to distant and diffuse recurrences. We hope to gain further insight into these dynamics through our adapted PIHNA model. To gain a more realistic understanding of the PIHNA model, we ran these simulations in 2D on a realistic brain geometry. We present the 2D model as well as simulations of tumour resection, subsequent ischemia and tumour recurrence patterns in the next section and suggest how the tumour wavespeed calculated in this section might tie into this behaviour.

4.4 THE PIHNA MODEL IN TWO SPATIAL DIMENSIONS

The two dimensional simulations of PIHNA follows the group of Equations (136) – (140) with the nutrient vascular efficiency term, which as a reminder is given by

$$V(c,h,v) = \frac{f}{f_{blood}} = \frac{v}{v + \frac{\eta_c(D_c,\rho)c + \eta_h(D_h)h}{ps}}. \tag{176}$$

The model equations are run on a two-dimensional slice of a realistic brain geometry from the Brainweb Database [28, 29, 74, 75], which spatially differentiates physiological structures such as white matter, grey matter, cerebrospinal fluid (CSF) and anatomical boundaries of the brain. This geometry is an average of multiple MR scans on a single patient to create a brain geometry with 1mm accuracy on and between MR slices. We have run our simulations on the white and grey matter, not allowing for any growth of the tumour into the CSF or past the boundaries of the brain.

Analogous to the 1D PIHNA model, we initiate the simulation with a small exponentially decreasing normoxic cell population from a point with coordinates (x_0, y_0)

$$c(\mathbf{x}, 0) = 1000e^{-100R^2}, \tag{177}$$

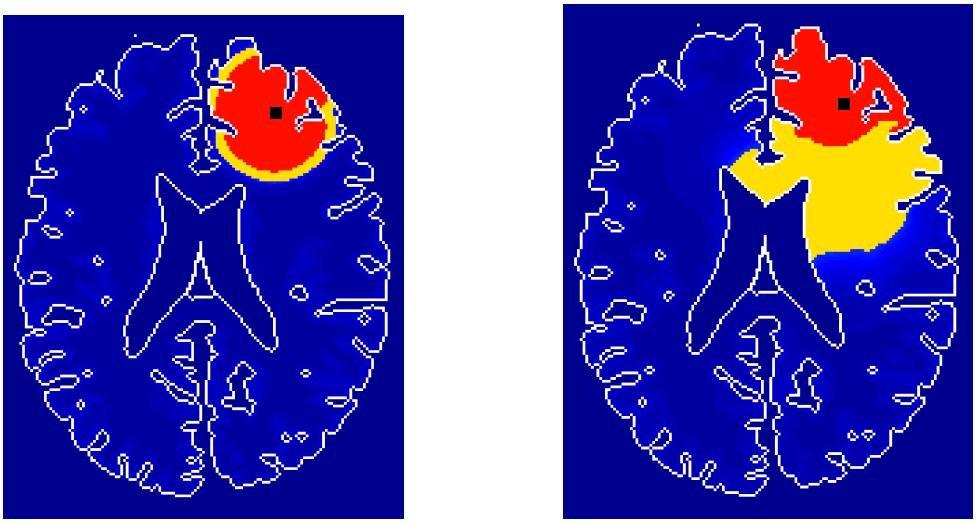
where $R^2 = (x - x_0)^2 + (y - y_0)^2$. Across simulations seen here, all tumours are seeded in a fixed location seen in Figure 47.

The initial vascular cell densities are heterogeneous between white and grey matter and are set to 3% and 5% of the carrying capacity, K; these values fall within the values for cerebral blood volume found from the literature [155].

$$v(x,0) = \begin{cases} 0.03K & \text{if } x \in \text{white matter} \\ 0.05K & \text{if } x \in \text{grey matter.} \end{cases} \tag{178}$$

All other spatio-temporal variables are initially set to zero. There are no-flux boundary conditions on the outer boundary of the brain for all variables as well as on the CSF.

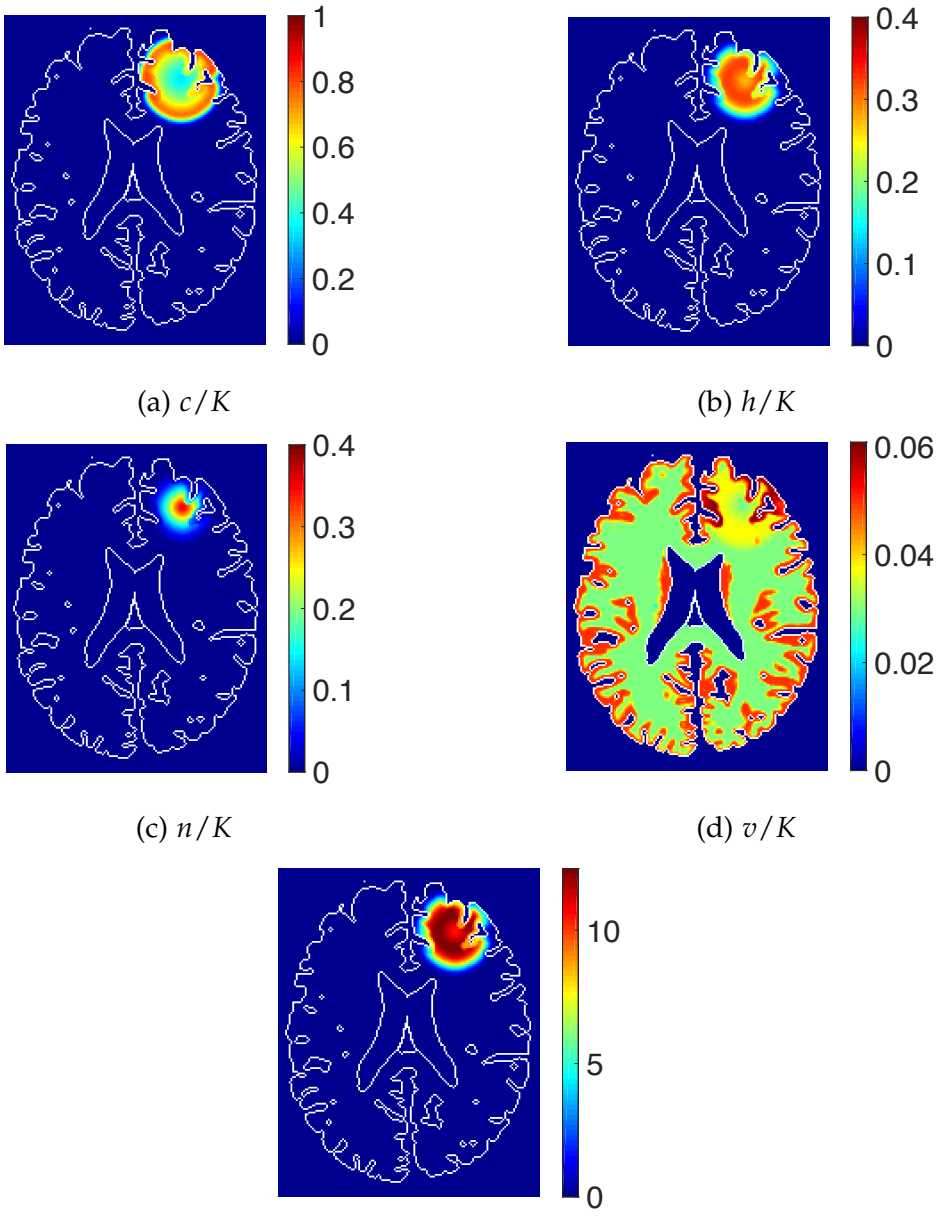
We present the total cell densities that are visible on simulated T1Gd and T2 in Figure 47 for two example simulations: one for high D_c and low ρ which is considered a diffuse tumour, and the other for low D_c and high ρ which is nodular. We also present the breakdown of these total cell densities for the nodular case in Figure 48. The dynamics of the growth are similar to the one-dimensional PIHNA simulations, in that the normoxic cell density is located on the periphery of the tumour, followed by the hypoxic cell density



(a) High ρ and low D_c - nodular tumour. (b) Low ρ and high D_c - diffuse tumour.

Figure 47: Simulated T1Gd area of $2\pi\text{cm}^2$ shown in red with T2 in yellow. T2 is relatively much larger than T1Gd for a diffuse tumour than a nodular tumour. The black square is the tumour seeding location for all 2D simulations seen in this chapter (position $(x(100), y(150))$ on brain slice number 85 on the Brainweb Atlas). The individual densities and angiogenic factor concentration are shown in Figures 48 and 49 at the same time point.

and necrotic cell densities as you travel towards the centre of the tumour. The angiogenic factors are concentrated mostly near the hypoxic cells, as is the increase in vasculature. We present the individual cell densities and angiogenic factor concentrations in Figures 48 and 49. The nodular tumour in Figure 48 has a clear necrotic core at this point of growth on simulated T1Gd, whereas the diffuse tumour in Figure 49 does not develop as much necrosis or hypoxia. Both simulations show a high level of normoxia spreading ahead of the other cell densities.



(a) c/K

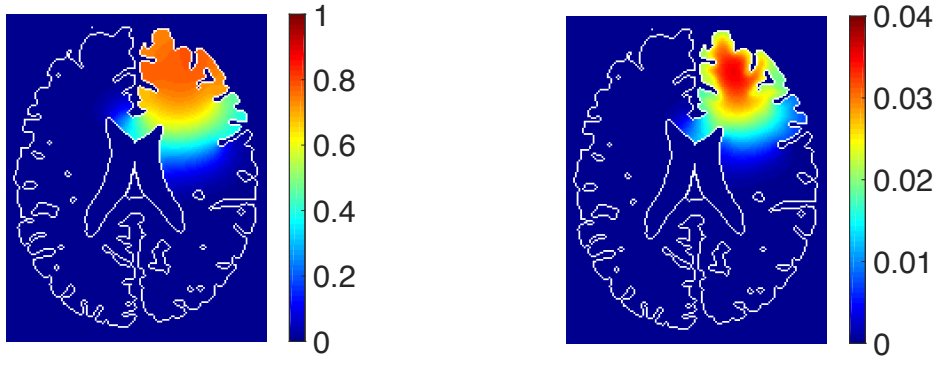
(b) h/K

(c) n/K

(d) v/K

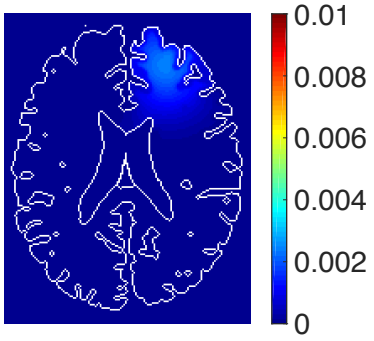
(e) a/K_M

Figure 48: Here we show the various densities as fractions of K and the angiogenic factor concentration (divided by K_M) of a nodular 2D PIHNA simulation ($D_c = 10\text{mm}^2/\text{year}$, $\rho = 100/\text{year}$, $D_h = 10D_c$, $\beta = 0.1\rho$). The normoxic cell density leads the outward growth, followed by the lower hypoxic and necrotic cell densities. The vascular cell density increases slightly above the initial condition and decreases towards the centre of the tumour. The angiogenic factors are most concentrated around the hypoxic cell population. Brain outline shown in white.

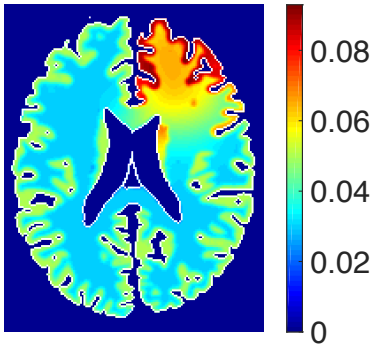


(a) c/K

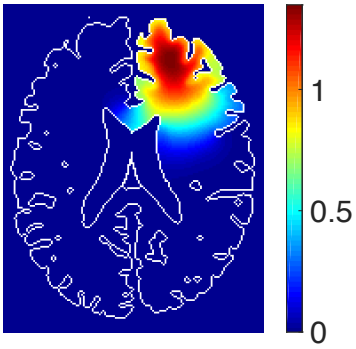
(b) h/K



(c) n/K



(d) v/K



(e) a/K_M

Figure 49: This is an example of a diffuse tumour ($D_c = 100\text{mm}^2/\text{year}$, $\rho = 10/\text{year}$, $D_h = 10D_c$, $\beta = 0.1\rho$). As in the one dimensional PIHNA simulations, the normoxic cell density leads the outward growth, followed by the much smaller hypoxic and necrotic cell densities. The vascular cell density increases in the tumour location The angiogenic factors are most concentrated around the hypoxic cell population. Brain outline shown in white.

Using the PIHNA model, we have simulated a resection that occurs once the tumour has grown to an area of πcm^2 on simulated T1Gd imaging. Post resection, zero-flux boundary conditions are added to the created cavity wall

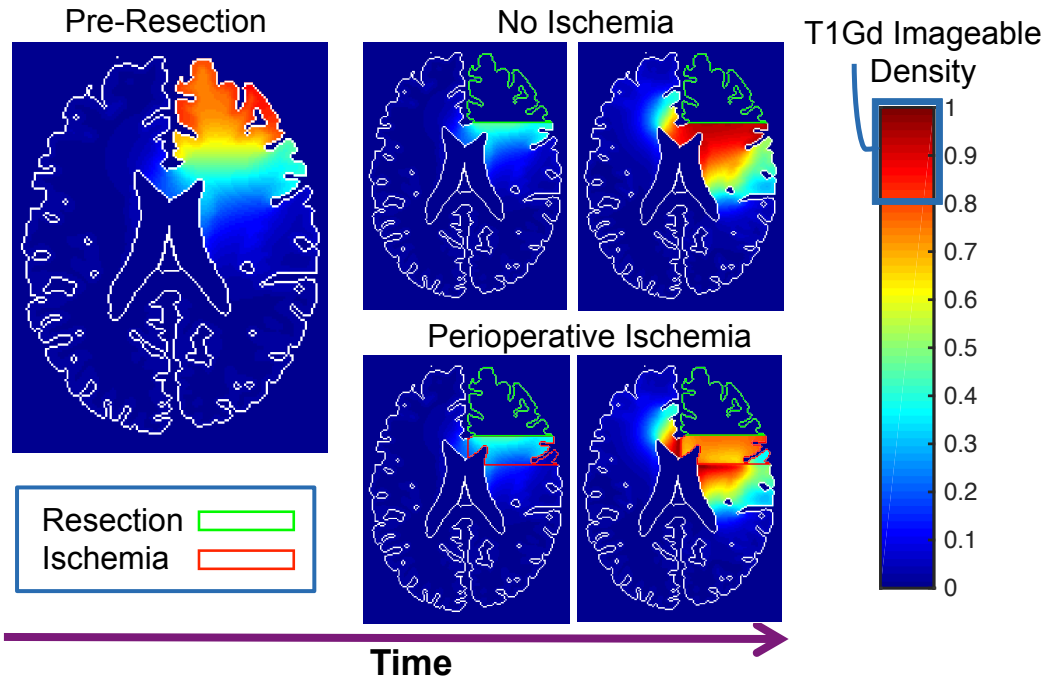


Figure 50: The tumour undergoes resection that removes the T1Gd imageable tumour cell density (assumed at 80% of the maximum cell density) as well as the surrounding tissue. In this illustrative example, the tumour without ischemia reestablishes to a T1Gd imageable density ($T > 0.8$) next to the resection cavity wall, a local recurrence. The tumour with ischemia instead establishes outside of the ischemic region and would appear as a distant recurrence.

so that regrowth into the resection cavity is not possible. Every resection is the same, in that the same region of brain geometry is removed. The resection geometry removes all T1Gd imageable tumour for every simulation. We add subsequent ischemia through a transient reduction in the vasculature term, v, to a region adjacent to the resection cavity wall. We have modelled ischemia as a reduction only at the time point of resection, the vessels then continue to follow the model equations. In the simulations seen here the reduction in vasculature is either 90% or 99%.

We run many simulations for different values of D_c ($1 - 1000\text{mm}^2/\text{year}$) and ρ ($10 - 100/\text{year}$), as well as β ($0.1\rho - -0.5\rho$), which is the switching rate from the normoxic cell density towards hypoxic cell density.

Recurrence location of a tumour is classified as the reappearance of the tumour on T1Gd MR scans as is done clinically [158]. We do not however implement a distance requirement away from the primary focal point of the tumour for a recurrence on simulated T1Gd MRI to be classified as distant. In-

stead, if a tumour initially reappears outside of the simulated ischemic region above a certain thresholded size (4πmm^2 simulated T1Gd area) before appearing anywhere else, it is classified as distant. Whereas if it appears within the ischemic region along the cavity wall above the same threshold before anywhere else, it is classed as a local recurrence. We define a mixed recurrence when the tumour appears on simulated T1Gd MRI both inside and outside the ischemic region before the size threshold within either region is reached.

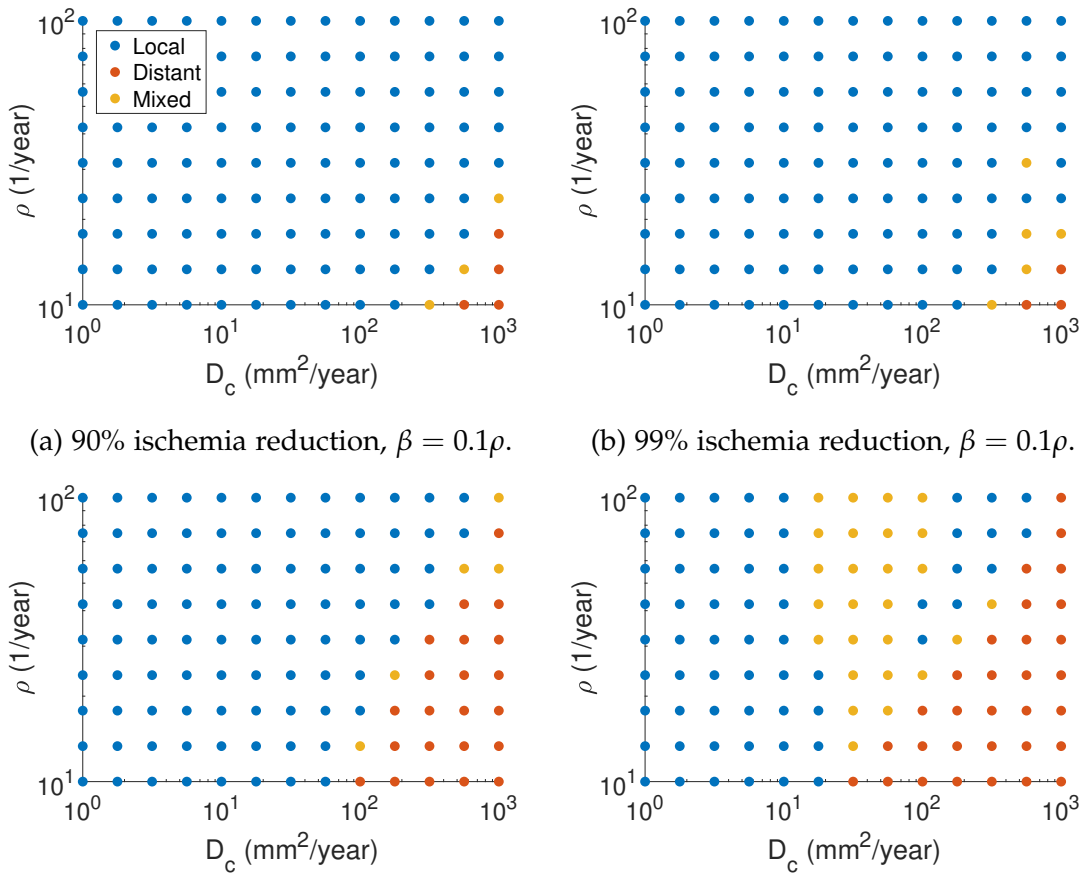
4.4.1 *Individual tumour kinetics affect recurrence location following perioperative ischemia*

Extending on the paper by Thiepold *et al.*, that suggests distant recurrence can occur through ischemia and subsequent hypoxia [143], the PIHNA model suggests that tumour kinetics also play a role. By varying individual tumour kinetics (D_c and ρ with $D_h = 10D_c$) and the maximal rate at which tumour cells become hypoxic and in turn necrotic (β), with a fixed vascular ischemia post resection, we are able to show differing tumour recurrence locations, see Figure 51. Recurrence location is classified as the first reappearance of a tumour on T1Gd MR imaging as described in the previous section.

PIHNA simulations suggest that following resection and a subsequent proximal ischemic event, tumours with higher diffusion rates and lower proliferation rates are more likely to recur distantly. In general, the more diffuse a tumour is, the more likely it is to recur distantly in this simulated setting. We present the recurrence locations in Figure 51. Such tumours remain in lower cell densities within the ischemic region and appear outside on simulated T1Gd imaging as they continue to increase their cell density outside of the ischemic region. We see this behaviour across different levels of ischemia and it becomes more apparent as the severity of the ischemia is increased, as well as the maximal switching rate from normoxia to hypoxia, β.

Higher tumour cell diffusion rates give distant recurrences. However, as expected, there are more local recurrences in the parameter space overall with the lesser of the two simulated levels of ischemia. This is because more of the simulated tumours are able to proliferate to a T1Gd imageable density within the ischemic region before they do outside, as the ischemia of a 90% reduction is slightly more favourable than the 99% ischemic reduction.

An increase in β leads to more sensitivity in the tumours to ischemia, which causes them to become less proliferative in the ischemic region. They are



(a) 90% ischemia reduction, $\beta = 0.1\rho$.

(b) 99% ischemia reduction, $\beta = 0.1\rho$.

(c) 90% ischemia reduction, $\beta = 0.5\rho$.

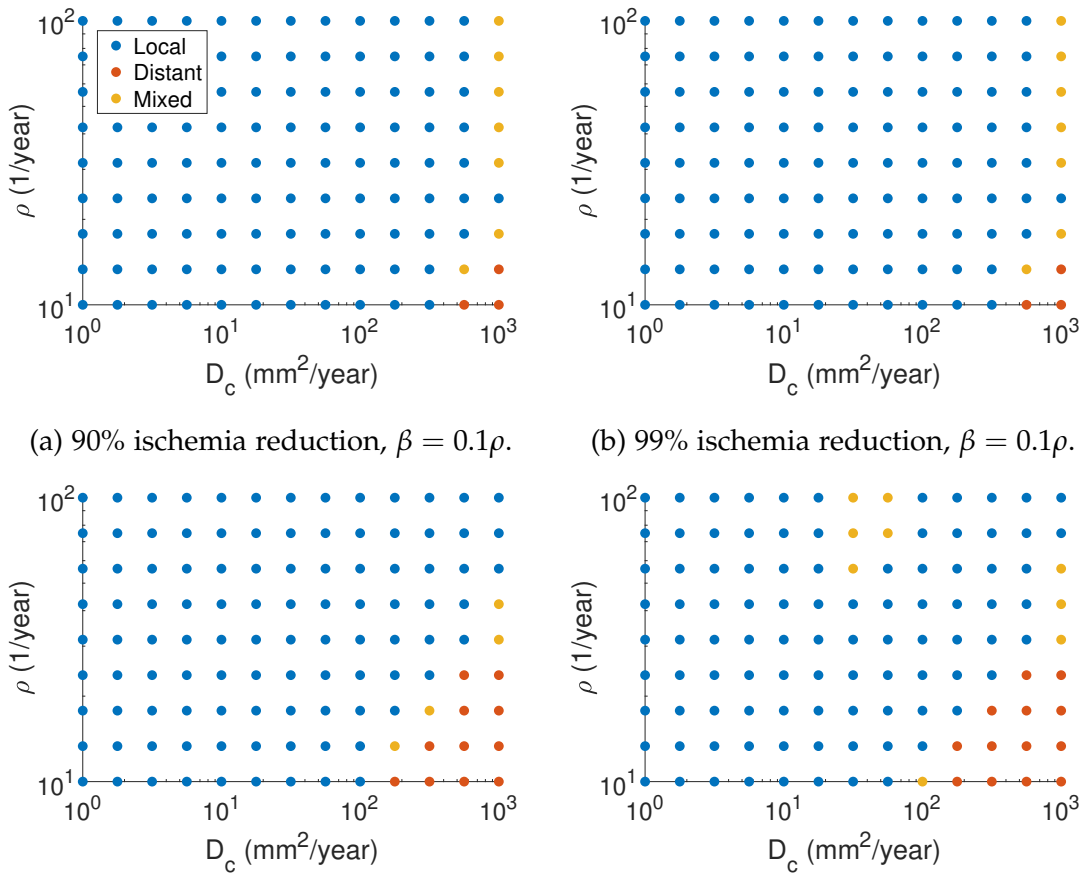
(d) 99% ischemia reduction, $\beta = 0.5\rho$.

Figure 51: Recurrence location classified for various D_c, ρ, β and levels of ischemia for $D_h = 10D_c$. We see that the higher level of ischemia and higher values of β lead to a larger proportion of distant recurrences in D_c and ρ parameter space. Higher migration rates, D_c, and lower proliferation rates, ρ, lead to more distantly recurring simulated tumours.

therefore more likely to become denser, and therefore imageable on simulated T1Gd MRI, outside of the ischemic region and be seen as a distant recurrence.

4.4.2 *Faster Hypoxic Diffusion Rates Promote Distant Recurrence*

Following this initial analysis, we also varied the hypoxic diffusion rate relative to the normoxic counterpart, D_h/D_c. Along with the simulations where $D_h = 10D_c$ described in the previous section, we have set $D_h/D_c = 1$ (see Figure 52) and $D_h/D_c = 100$ (see Figure 53). We see that the higher the D_h/D_c value, the more distantly recurring tumours occur for a fixed ischemia level



(a) 90% ischemia reduction, $\beta = 0.1\rho$.

(b) 99% ischemia reduction, $\beta = 0.1\rho$.

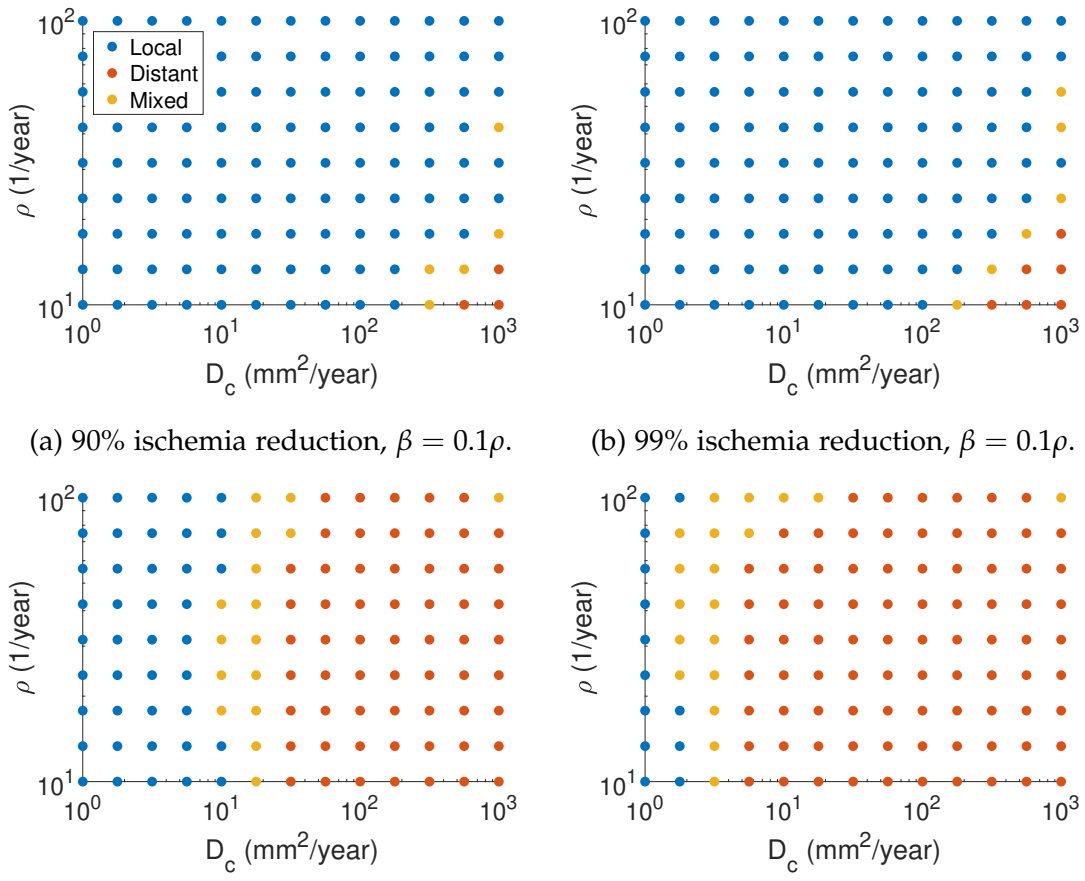
(c) 90% ischemia reduction, $\beta = 0.5\rho$.

(d) 99% ischemia reduction, $\beta = 0.5\rho$.

Figure 52: Recurrence location classified for various D_c, ρ, β and levels of ischemia for $D_h = D_c$. We see that the higher level of ischemia and higher values of β lead to a larger proportion of distant recurrences in D_c and ρ parameter space. Higher migration rates, D_c, and lower proliferation rates, ρ, lead to more distantly recurring simulated tumours.

and value of β. The effect of an increase in D_h/D_c is more pronounced for $\beta = 0.5\rho$ than $\beta = 0.1\rho$. In fact, we see that almost the entire D_c, ρ parameter space consists of distantly recurring tumours for $D_h = 100D_c$ and $\beta = 0.5\rho$.

In other words, the faster hypoxic cell migration rate (relative to the normoxic cell migration rate) promotes distantly recurring tumours *in silico*. We saw in the one-dimensional PIHNA model that the numerical wavespeed of simulated tumours increases as D_h/D_c is increased (Section 4.3.3), and we propose that this wavespeed increase caused by the hypoxic cells plays a role in the higher proportion of distantly recurring GBMs that we observe in our two-dimensional simulations for higher D_h/D_c values.



(a) 90% ischemia reduction, $\beta = 0.1\rho$.

(b) 99% ischemia reduction, $\beta = 0.1\rho$.

(c) 90% ischemia reduction, $\beta = 0.5\rho$.

(d) 99% ischemia reduction, $\beta = 0.5\rho$.

Figure 53: Recurrence location classified for various D_c, ρ, β and levels of ischemia for $D_h = 100D_c$. We see that the higher level of ischemia and higher values of β lead to a larger proportion of distant recurrences in D_c and ρ parameter space. Higher migration rates, D_c, and lower proliferation rates, ρ, lead to more distantly recurring simulated tumours.

4.5 DISCUSSION AND FUTURE WORK

In this chapter, we wanted to extend the PIHNA model and use it to suggest key drivers of both outward tumour growth and distally recurring tumours following ischemia. We have found and implemented a new nutrient-based vascular efficiency term for the PIHNA model calibrated with FDG PET data.

We have found an analytical minimum wave speed for the PIHNA model and shown numerically that this predicted wave speed is attained when normoxic cell diffusion is greater than or equal to the diffusion of hypoxic cells. However, due to the evidence indicating that hypoxia mediates migration [68, 156], we have varied the migration rate of hypoxic cells compared with

normoxic cells in our iteration of the PIHNA model. In the case that the hypoxic cells diffuse reasonably faster than the normoxic cells, we see that the outward growth of the tumour is faster than the predicted minimum value.

Mathematically, the increase in simulated wave-speed corresponds to a switch in the least negative eigenvalue as D_h/D_c is increased, which causes a different eigenvector to dominate the behaviour of the PIHNA model. Biologically, this suggests that the faster migration of hypoxic cells can drive the growth of the whole tumour, as they migrate towards nutrient-rich environments and convert back to normoxic cells. The model does not predict that the wavespeed is affected by the proportions of hypoxic and normoxic cells. However, a reduction in vasculature ahead of the wave does increase the wavespeed of the tumour due to spatial effects present in the minimum predicted wavespeed, which is a limitation of the model. It would be interesting to see the effect of healthy tissue on the wavespeed of a simulated PIHNA tumour, as in reality that is what the tumour is growing into.

Through mathematical modelling, we have found a possible mechanism for distant GBM recurrence. If ischemia levels are high enough and the tumour has an invasive phenotype, it can remain unimageable on simulated T1Gd MRI as it travels through the ischemic region (using our assumed threshold of 80% total cell density). Once it reaches healthy intact vasculature, it will return to a normoxic phenotype and proliferate to an imageable density outside of the ischemic region before it does so next to the cavity wall. From an imaging standpoint, this would be a distant recurrence. We found that the recurrence location is sensitive to the severity of the ischemia. Some tumours that recurred distantly for a simulated 99% reduction in vasculature are local for a 90% reduction. Tumours had to have very high diffusion coefficients to recur distantly for a 90% vasculature reduction. We also see that the switching rate from normoxic cells to hypoxic cells plays a role in this behaviour, increasing this rate leads to more distantly recurring tumours within the parameter range of D_c and ρ that we have used.

We have also varied the proportional constant between the hypoxic and normoxic cell diffusion, D_h/D_c, and looked at its effect on the recurrence patterns observed in simulations. The larger this proportional constant, the more distantly recurring tumours were found in the same D_c and ρ parameter space. It is curious that we see the D_h/D_c value drive distant recurrences as well as the tumour wavespeed, and falls to future work to study this relationship further.

The geometry that we have used here for the resection and subsequent ischemia is fairly simple, we used it to see whether or not we could see local and distant recurrence patterns in the PIHNA model. Now that we have seen distant recurrences in the model, and the dependence of this behaviour on D_c, ρ, β and ischemia reduction, we have a platform for further exploration. For example, we have not altered the switching rate from hypoxia to normoxia, γ. In future work we could vary this parameter also, to determine its effect on the recurrence location of the tumour as well as the wave-speed effects for varying D_h/D_c. We have also not introduced various tumour seeding locations and different regions of ischemia and resection.

The PIHNA model has yet to explain why a diffuse recurrence might occur, which has also been seen clinically to be promoted by ischemia. However, we do see in simulations that the ischemic region selects for hypoxic cells that lead to a less proliferative tumour within this region. This causes an increase in the T2/T1Gd ratio with ischemic events compared to the same simulation without ischemia, because the region that would have been visible on T1Gd has been reduced to below this threshold. If the tumour were to remain hypoxic following an ischemic event, it could remain more diffuse, in a clinical sense of a large T2 volume relative to T1Gd. It falls to future work to run the analogous set of simulations without ischemia, and to compare their T2 to T1Gd area ratio with the 2D ischemia simulations presented here. There are other mechanisms that might also explain diffuse recurrences: an evolutionary bottleneck caused through a low-nutrient selection pressure, a post-ischemia delay for the cells to return to normoxia or a switching off from hypoxia back to normoxia.

5

CONCLUSION

In this thesis, we have looked at the applications of several mathematical models to the growth and proposed treatment of glioblastoma multiforme (GBM), a deadly primary brain tumour. We have developed a mathematical model to characterise the diffusion dynamics of PLGA/PEG, a polymer in development as a local drug delivery material for the treatment of GBM. To calibrate the model and to analyse these drug diffusion dynamics, we designed and implemented *in vitro* experiments at the Children's Brain Tumour Research Centre (CBTRC). We were trained by the CBTRC in how to collect and analyse the data, such that we could run experiments without their assistance. We also investigated these dynamics further using homogenisation theory; this work was the product of collaboration with the Hounsfield Facility. Our results show that there are significantly lower median values and significantly different distributions between the direction in which the polymers were pushed into their moulds, and the other directions; this is a potential concern for the clinical application of the polymer as the drug diffusion would be inhibited in the direction of the tumour cells in a patient. We have seen that the PLGA/PEG constructs swell in water, and that the macro-scale mathematical model analogous to the *in vitro* concentration experiments fit the data best when diffusion through the PLGA/PEG is inhibited over time. We have also seen that there are micro-scale channels of fluid through the PLGA/PEG that facilitate drug diffusion before swelling has taken place. In the future we would like to gather data on swollen PLGA/PEG microstructures, to see the effect of swelling on these fluid channels. We suspect that these fluid channels close during the swelling process, and act as the mechanism that inhibits drug release over time.

In collaboration with the Precision Neurotherapeutics Innovation Progam, we have modelled GBM growth and spread using the previously published Proliferation Invasion Hypoxia Necrosis Angiogenesis (PIHNA) model. Fol-

lowing some adaptations to the PIHNA model, we have found an expression for the wavespeed of the tumour that is reached for large times and shown that an hypoxic cell density that is reasonably more migratory than its normoxic counterpart can drive the outward growth of simulated tumours above the minimum wavespeed expression. This wavespeed can be explained by studying the eigenvalues and eigenvectors of the linearised system, as the relevant parameters are varied. A clinical observation that perioperative ischemia leads to significantly higher rates of distal recurrence patterns within a cohort of GBM patients led us to apply the PIHNA model to perioperative ischemia, and suggested parameters that drive clinically-analogous recurrence patterns that follow this surgical complication. We found that simulated tumours with high migration and low proliferation rates led to distant recurrence, and this was promoted further by an increase in the ratio between hypoxic cell migration and normoxic cell migration as well as an increase in the switching rate between cell densities.

Ultimately, we aim to bring together the two threads of this thesis with a model incorporating a tissue-scale PDE model of GBM growth such as PIHNA, with a local drug delivery treatment such as PLGA/PEG constructs to investigate the PLGA/PEG treatment efficacy *in silico*. Such a model would have to incorporate the time dynamics of the PLGA/PEG swelling and inhibition of drug diffusion. We plan to adapt the PIHNA model presented in this work, including the same numerical scheme, to include a subdomain of PLGA/PEG as well as another variable of drug concentration. This concentration would diffuse out of the polymer, kill tumour cells that it came into contact with once they tried to proliferate, and be cleared out of the brain with some rate. Once the model was created, we would use it to vary the PLGA/PEG shape, initial drug concentration, and the tumour kinetics to analyse efficacy of the polymer treatment for various *in silico* patients. We would expect that the polymer treatment would be most effective for those with nodular tumours, as the released drug (that likely would penetrate only a few millimeters into the tissue) would be able to access and kill the majority of the tumour cells in these cases.

Appendices

A

MODELLING DRUG DIFFUSION THROUGH PLGA/PEG POLYMER CONSTRUCTS

A.1 PLGA/PEG SWELLING MASS DATA

To calculate the PLGA/PEG volume fraction and subsequent water volume fractions used in the model, we made use of the swelling volume data presented in the main body of this thesis. We also used swelling mass data at the same time points that we collected volume data for, this was not presented and we present it here. We did not fit an equation to this data as we did not need to use it directly in the model. See Figure 54 for the mean data and range of the replicates.

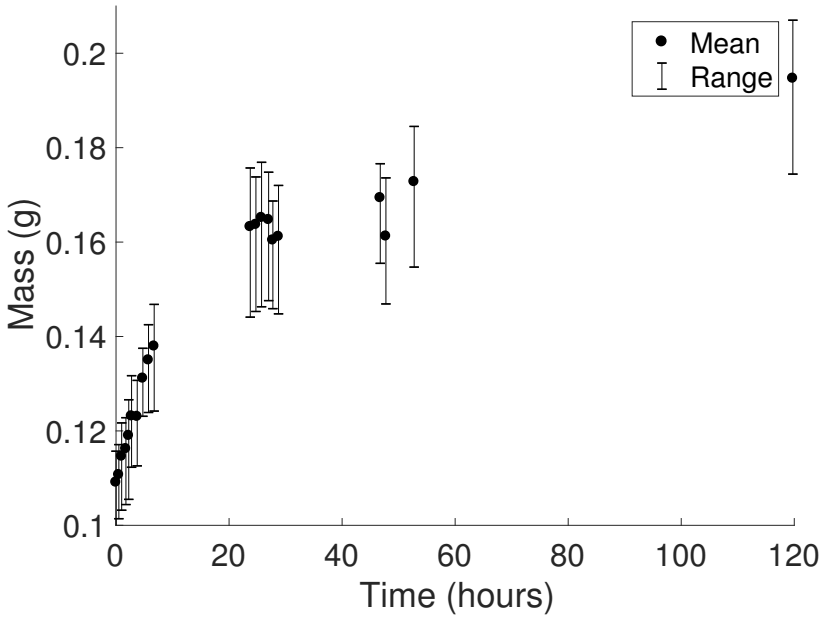

Mean
Range
0.2
0.18
0.16
0.14
0.12
0.1
Mass (g)
0
20
40
60
80
100
120
Time (hours)

Figure 54

B

HOMOGENISATION OF DIFFUSION APPLIED TO PLGA/PEG POLYMER CONSTRUCTS

B.1 SAMPLE CUBES FOR REPLICATES

Here we show the histograms for the sample of 300 $100 \times 100 \times 100$ cubes taken from the total number of 2197 cubes for each replicate of our microCT data.

B.2 WILCOXON SIGNED RANK TEST SIGNIFICANCE VALUES

In the main body of this thesis, we presented effective diffusion values for cubes of PLGA/PEG microCT data. Each cube provides a unique effective diffusion value in x, y and z directions. We ran Wilcoxon Signed Rank (WSR) Tests on pairs of directions across all cubes to look for significance between their medians. However, to provide clear figures to see the significant relationships that we saw, we did not present the p values of these tests and only presented whether the relationship was significant or not (with a p value less than 0.05). For the preliminary dataset, we saw some significance between medians of the effective diffusion values (x, y) and (x, z) but not for (x, y). The full set of p values, analogous to Figure 32 is given by

For the three replicates of microCT PLGA/PEG data, we saw significance between the medians of (x, z) and (y, z) across all replicates. The p values resulting from the WSR tests can be seen below.

B.3 KOLMOGOROV-SMIRNOV TEST SIGNIFICANCE VALUES

As also presented in the main body of this thesis were the significant and non-significant results of the Kolmogorov-Smirnoff (KS) Test. We again did

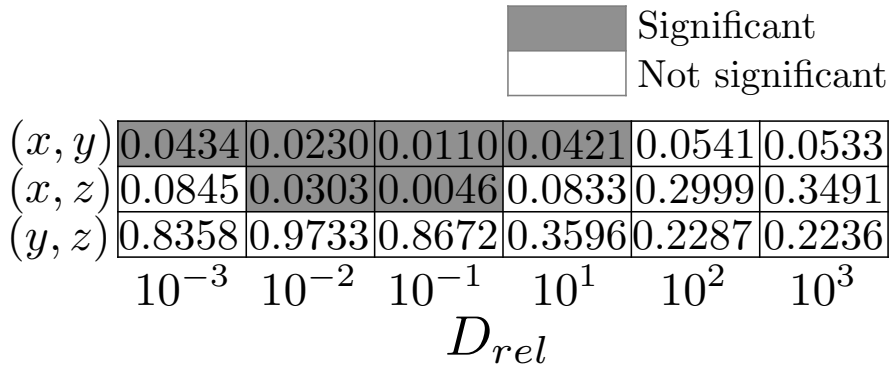


Figure 55: Results of the WSR Test on the significance between the differences in medians of pairs of effective diffusion values for various values of D_{rel}. The medians can be seen in Figure 34. We see some significance emerging between medians of both (x, y) and (x, z), but not (y, z).

not present the p values themselves and do so here. For the preliminary data-set, we did not see any significant values, see Figure 56. For the three replicates, we saw consistent significance between the (x, z) and (y, z) pairs within two replicates, see Figure 58.

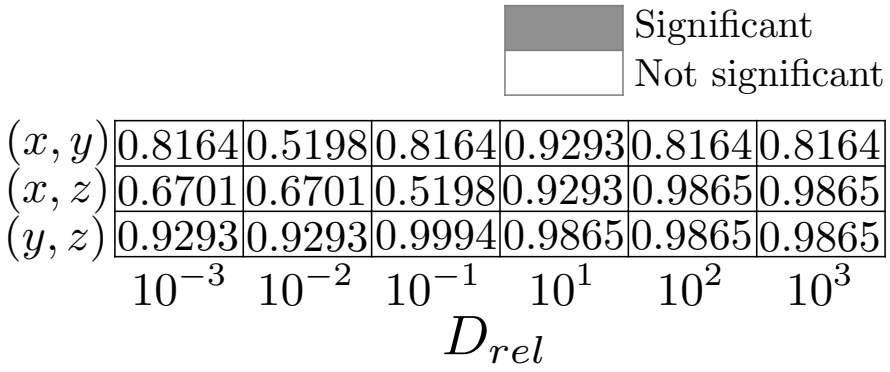


Figure 56: Results of the KS Test on the significance between the differences in cumulative distributions of pairs of effective diffusion values for various values of D_{rel} for the preliminary dataset. We see no significant pairs.

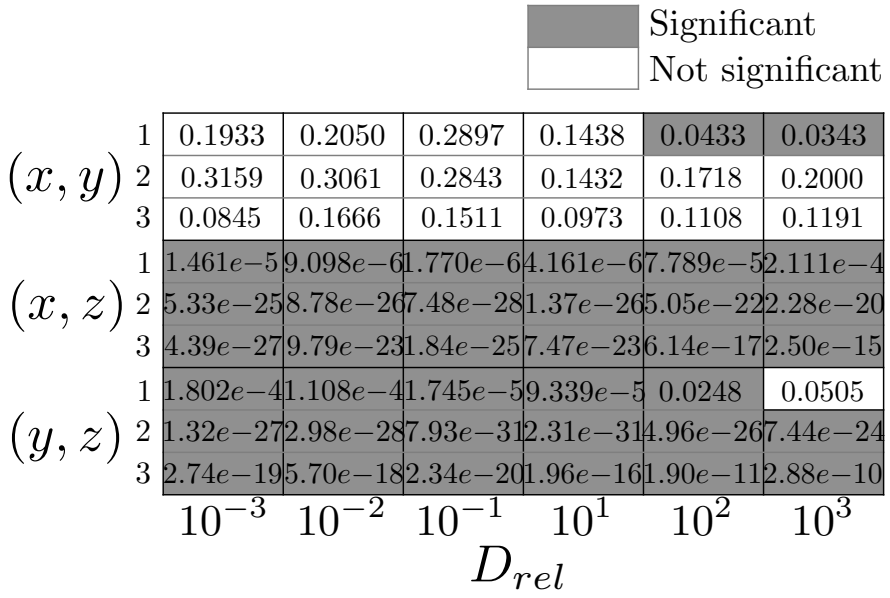


Figure 57: Results of the WSR Test on the significance between the differences in medians of pairs of effective diffusion values for various values of D_{rel}. The medians can be seen in Figure 34. We see some significance emerging between medians of both (x, y) and (x, z), but not (y, z).

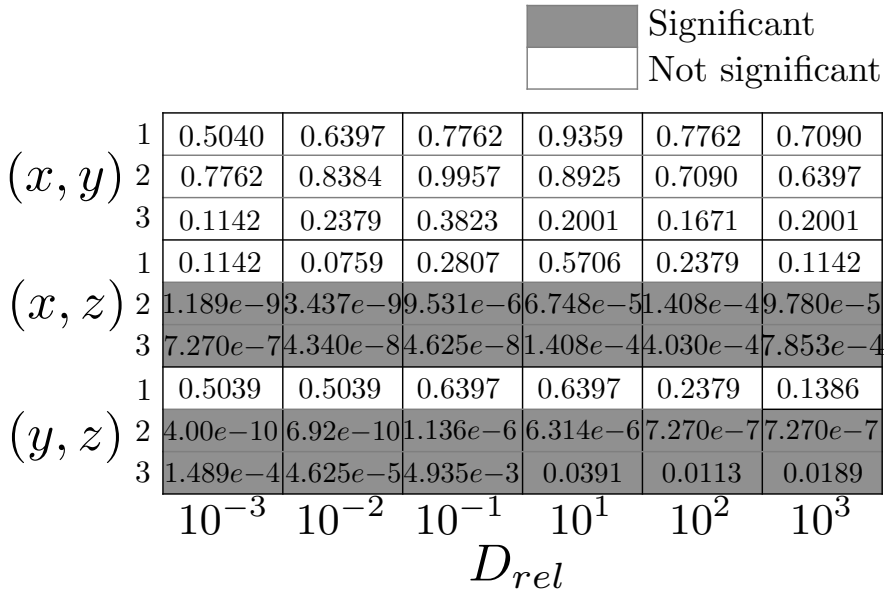


Figure 58: Results of the KS Test on the significance between the differences in medians of pairs of effective diffusion values for various values of D_{rel}. The medians can be seen in Figure 34. We see some significance emerging between medians of both (x, y) and (x, z), but not (y, z).

C

A MATHEMATICAL MODEL FOR BRAIN TUMOUR GROWTH APPLIED TO VASCULAR ISCHEMIA

C.1 PIHNA NON-DIMENSIONALISATION

In our case, it is useful to non-dimensionalise our equations so that when we change parameters/scales, we have a robust solver that is independent of the changes. We will denote each non-dimensionalised parameter with a hat. The variables are transformed to

$$\begin{aligned} \hat{c} &= c/K \\ \hat{h} &= h/K \\ \hat{n} &= n/K \\ \hat{v} &= v/K \\ \hat{a} &= a/K_m. \end{aligned} \tag{179}$$

The time, t, and space, x, are transformed to

$$\hat{t} = t * \rho \text{ and } \hat{x} = x * \sqrt{\frac{\rho}{D_c}}. \tag{180}$$

The diffusion coefficients are divided through by the diffusion of the normoxic cells

$$\begin{aligned} \hat{D}_c &= D_c/D_c \\ \hat{D}_h &= D_h/D_c \\ \hat{D}_v &= D_v/D_c \\ \hat{D}_a &= D_a/D_c. \end{aligned} \tag{181}$$

Many terms are divided through by the proliferation rate, ρ. These parameters are

$$\begin{aligned}
\hat{\rho} &= \rho/\rho \\
\hat{\beta} &= \beta/\rho \\
\hat{\gamma} &= \gamma/\rho \\
\hat{\alpha}_h &= \alpha_h/\rho \\
\hat{\lambda} &= \lambda_a/\rho \\
\hat{\mu} &= \mu/\rho \\
\hat{\alpha}_n &= \alpha_n/\rho.
\end{aligned} \tag{182}$$

The last of the parameters are transformed to

$$\hat{\delta}_c = \delta_c \frac{K}{K_m + \rho} \tag{183}$$

$$\hat{\delta}_h = \delta_h \frac{K}{K_m + \rho} \tag{184}$$

$$\hat{q} = q \frac{K}{K_m} \tag{185}$$

$$\hat{K} = K/K \tag{186}$$

$$\hat{K}_m = K_m/K_m. \tag{187}$$

C.2 PIHNA 2D NUMERICAL SCHEME

All PIHNA simulations in one spatial dimension are solved using the inbuilt Matlab partial differential equation solver, *pdepe.m*. The two-dimensional simulations on the brain slice seen in this chapter are solved using another scheme that we will describe here.

The PIHNA model is a set of reaction diffusion equations. We solve this by splitting up the reaction and diffusion operators and solving them separately using Godunov operator splitting; this involves fractional time stepping. The model is solved on an MRI slice of 1mm accuracy in both x and y.

Godunov Operator Splitting

The 2D PIHNA simulations are solved using Godunov Operator Splitting. We have a set of equations of the form

$$\mathbf{u}_t = A(\mathbf{u}) + B(\mathbf{u}) \tag{188}$$

where A and B are the diffusion and reaction operators, respectively. The vector $\mathbf{u}$ is shorthand for the collection of populations in the model. We have

$$\mathbf{u} = \begin{bmatrix} c \\ h \\ n \\ v \\ a \end{bmatrix} \text{ and } \mathbf{u}_t = \begin{bmatrix} c_t \\ h_t \\ n_t \\ v_t \\ a_t \end{bmatrix}. \tag{189}$$

Say we have two separate numerical schemes for solving each individual operator from time step n to $n+1$, given by

$$\mathbf{u}_A^{n+1} = \mathbf{u}^n + \Delta t A(\mathbf{u}^n) \text{ and } \mathbf{u}_B^{n+1} = \mathbf{u}^n + \Delta t B(\mathbf{u}^n), \tag{190}$$

then the Godunov splitting method says to apply the first scheme to an intermediary time point, $\mathbf{u}^{n+\star}$, and then apply the second to get to the next time point. Using the above generic schemes, this Godunov splitting gives

$$\mathbf{u}_A^{n+\star} = \mathbf{u}^n + \Delta t A(\mathbf{u}^n) \text{ and subsequently } \mathbf{u}_{A+B}^{n+1} = \mathbf{u}^{n+\star} + \Delta t B(\mathbf{u}^{n+\star}). \tag{191}$$

This process is then repeated until the desired end time point is achieved. We use this principle to solve our PIHNA model but with more complicated schemes that we will now explain.

Solving Diffusion Terms

To solve the diffusion terms for the normoxic and hypoxic cells, the vasculature and the angiogenic factors, we have used the Crank-Nicholson method alongside a Locally One Dimensional (LOD) Method. The LOD method was used to reduce computation time. The diffusion operator is given by

$$A(\mathbf{u}) = \begin{bmatrix} \nabla \cdot (D_c(1-T)\nabla c) \\ \nabla \cdot (D_h(1-T)\nabla h) \\ 0 \\ \nabla \cdot (D_v(1-T)\nabla v) \\ \nabla \cdot (D_a \nabla a) \end{bmatrix}. \tag{192}$$

The Crank-Nicholson method is given by

$$\mathbf{u}^{n+\star} = \mathbf{u}^n + \frac{\Delta t}{2}\left[\Delta F(\mathbf{u}^{n+\star}) + \Delta F(\mathbf{u}^n)\right], \tag{193}$$

where F is the net flux. We can re-express Equation (193) using

$$\mathbf{u}^{n+\star} = \mathbf{u}^n + \Delta \mathbf{u} \tag{194}$$

to give

$$\mathbf{u} = \frac{\Delta t}{2}\left[F(\Delta\mathbf{u}) + 2F(\mathbf{u}^n)\right], \tag{195}$$

where we have used that

$$F(\mathbf{u}^{n+\star}) = F(\Delta\mathbf{u}) + F(\mathbf{u}^n). \tag{196}$$

Now we have an implicit method for $\Delta\mathbf{u}$ given by Equation (195). We can solve this by computing the net flux, F, which is done with the LOD technique. We first remove the boundaries and consider the fluxes between the non-boundary interfaces. For our spatial discretisation $x = 0 \dots M$ and $y = 0 \dots N$, we use the LOD technique to split up the (M, N) matrices into a $(1, MN)$ vector. Information is not lost as we still keep track of neighbouring cells in each dimension.

The net flux is then computed along the interfaces between voxels for each population individually. Voxels are classified into origins and terminuses, and incoming and outgoing fluxes are computed; a voxel can be both an origin and a terminus. Discrepancies along interfaces between neighbouring voxels with different $T = (c + h + n + v)/K$ values is remedied using an average, $\hat{T}$. The net flux on each interface is given by

$$F = \mathbf{D}\left(1 - \hat{T}\right)\frac{\mathbf{u}^{\text{origin}} - \mathbf{u}^{\text{terminus}}}{\Delta x^2}, \tag{197}$$

where

$$\mathbf{D} = \begin{bmatrix} D_c \\ D_h \\ 0 \\ D_v \end{bmatrix}. \tag{198}$$

and D_a is solved using

$$F = \mathbf{D}\frac{\mathbf{u}^{\text{origin}} - \mathbf{u}^{\text{terminus}}}{\Delta x^2}, \tag{199}$$

as the diffusion of the angiogenic factors is not multiplied by $(1 - T)$ as the other diffusion coefficients are in the model. The vector $\mathbf{D}$ is also taken as the average of the voxels adjacent to each interface, but as we do not have any inherent diffusivity differences between voxels, as other formulations of PIHNA have done [140, 59], the average is just the same as each neighbouring cell. Note that there are no necrotic terms here. They are also excluded from $\mathbf{u}$ in this section as the necrotic cells do not diffuse.

We then input this flux into an inbuilt conjugate gradients solver in Matlab (pcg.m) that iterates the equation

$$\Delta\mathbf{u} - \frac{1}{2}\Delta t F(\Delta\mathbf{u}) = \Delta t F(\mathbf{u}^n) \tag{200}$$

until it converges to find $\Delta\mathbf{u}$. We then simply update to the intermediary time step

$$\mathbf{u}^\star = \mathbf{u}^n + \Delta\mathbf{u} \tag{201}$$

Reaction Terms

Once the diffusion terms have been computed to time point $n+\star$, we then use $\mathbf{u}^{n+\star}$ in another solver that computes the reaction terms to get to $\mathbf{u}^{n+1}$. To solve these reaction terms, we use the Runge-Kutta TR-BDF2 method. The TR-BDF2 method uses the trapezoidal rule (TR), followed by the backward differentiation formula of order 2 (BDF2). It further splits up the time step, so now we will go from $\mathbf{u}^{n+\star}$ to $\mathbf{u}^{n+(1+\star)/2}$ and finally to $\mathbf{u}^{n+1}$. The reaction operator is given by

$$B(\mathbf{u}) = \begin{bmatrix} \rho c(1-T) + \gamma hV - \beta c(1-V) - \alpha_n \frac{nc}{K} \\ -\gamma hV + \beta c(1-V) - \alpha_h h(1-V) - \alpha_n \frac{nh}{K} \\ \alpha_h h(1-V) + \alpha_n \frac{n(c+h+v)}{K} \\ \mu \frac{a}{K_m+a} v(1-T) - \alpha_n \frac{nv}{K} \\ \delta_c c + \delta_h h - q\mu \frac{a}{K_m+a} v(1-T) - \omega a v - \lambda a \end{bmatrix}. \tag{202}$$

The TR-BDF2 method is given by

$$\mathbf{u}^{n+(1+\star)/2} = \mathbf{u}^{n+\star} + \frac{\Delta t}{4}\left(B\left(\mathbf{u}^{n+\star}\right) + B\left(\mathbf{u}^{n+(1+\star)/2}\right)\right) \tag{203}$$

$$\mathbf{u}^{n+1} = \frac{1}{3}\left(4\mathbf{u}^{n+(1+\star)/2} - \mathbf{u}^{n+\star} + \Delta t B(\mathbf{u}^{n+1})\right). \tag{204}$$

As we had for the diffusion terms, this is an implicit method and needs to be solved by a non-linear solver. We use the Newton Method to solve this. For the first part of the TR-BDF2 method, we rearrange Equation (203) and set it equal to a function, $G(\mathbf{u}^{n+\star}, \mathbf{u}^{n+(1+\star)/2})$. This gives

$$G\left(\mathbf{u}^{n+\star}, \mathbf{u}^{n+(1+\star)/2}\right) = \mathbf{u}^{n+\star} + \frac{\Delta t}{4}B\left(\mathbf{u}^{n+\star}\right) + \frac{\Delta t}{4}B\left(\mathbf{u}^{n+(1+\star)/2}\right) - \mathbf{u}^{n+(1+\star)/2} \tag{205}$$

The corresponding Jacobian, J_G, for this solver is given by

$$J_G = \frac{\Delta t}{4}J\left(\mathbf{u}^{n+(1+\star)/2}\right) - I, \tag{206}$$

where I is the identity vector and J is the Jacobian

$$J_{i,j}(\mathbf{u}) = \frac{\partial(A(\mathbf{u})_i)}{\partial u_j}. \tag{207}$$

Explicitly, the Jacobian J is

$$J_{i,1} = \begin{bmatrix} \rho(1-T) - \rho\frac{c}{K} - \beta(1-F) + \beta c F_c' + \gamma h F_c' - \alpha_n \frac{n}{K} \\ -\gamma h F_c' + \beta(1-F) - \beta c F_c' + \alpha_h h F_c' \\ -\alpha_h h F_c' + \alpha_n \frac{n}{K} \\ -\mu \frac{a}{a+K_m}\frac{v}{K} \\ \delta_c + q\mu \frac{a}{K_m+a}\frac{v}{K} \end{bmatrix}$$

$$J_{i,2} = \begin{bmatrix} -\rho\frac{c}{K} + \gamma(V + hF_h') + \beta c F_h' \\ -\gamma V - \gamma h F_h' - \beta c F_h' - \alpha_h(1-V) + \alpha_h h F_h' - \alpha_n \frac{n}{K} \\ \alpha_h(1-F) - \alpha_h h F_h' + \alpha_n \frac{n}{K} \\ -\mu \frac{a}{a+K_m}\frac{v}{K} \\ \delta_h + q\mu \frac{a}{K_m+a}\frac{v}{K} \end{bmatrix}$$

$$J_{i,3} = \begin{bmatrix} -\rho\frac{c}{K} - \alpha_n \frac{c}{K} \\ -\alpha_n \frac{h}{K} \\ -\alpha_n h F_n' + \alpha_n \frac{c+h+v}{K} \\ -\mu \frac{a}{a+K_m}\frac{v}{K} - \alpha_n \frac{v}{K} \\ q\mu \frac{a}{K_m+a}\frac{v}{K} \end{bmatrix}$$

$$J_{i,4} = \begin{bmatrix} -\rho\frac{c}{K} + \gamma h F_v' + \beta c F_v' \\ -\gamma h F_v' - \beta c F_v' + \alpha_h h F_v' \\ -\alpha_h h F_v' + \alpha_n \frac{n}{K} \\ \mu a \frac{1-T}{K_m+a} - \mu \frac{a}{K_m+a}\frac{v}{K} - \alpha_n \frac{n}{K} \\ -q\mu(1_T)\frac{a}{K_m+a} + q\mu \frac{a}{K_m+a}\frac{v}{K} - \omega a \end{bmatrix}$$

$$J_{i,5} = \begin{bmatrix} 0 \\ 0 \\ 0 \\ \mu v \frac{1-T}{K_m+a} - \mu a v \frac{1-T}{(K_m+a)^2} \\ -\lambda - q\mu v(1-T)\frac{1}{K_m+1} + q\mu a v \frac{1-T}{(K_m+a)^2} - \omega v \end{bmatrix}.$$

The Newton Method iterates the set of equations

$$J_G \delta^{n+\star} = -G\left(\mathbf{u}^{n+\star}, \mathbf{u}^{n+(1+\star)/2}\right) \tag{208}$$

for each variable until the difference between two $\delta^{n+\star}$ iterations is lower than a tolerance in that variable. Once the satisfactory $\delta^{n+\star}$ is found across all variables, it is used to update the solutions to

$$\mathbf{u}^{n+(1+\star)/2} = \mathbf{u}^{n+\star} + \delta^{n+\star} \tag{209}$$

and we move on to the second step of the TR-BDF2 scheme.

The second part of the scheme follows the same procedure as the first. A Newton solver is also used and the corresponding equations are given by

$$G\left(\mathbf{u}^{n+1}, \mathbf{u}^{n+(1+\star)/2}, \mathbf{u}^{n+1}\right) = \frac{1}{3}\left(4\mathbf{u}^{n+(1+\star)/2} - \mathbf{u}^{n+\star} + \Delta t B(\mathbf{u}^{n+1})\right) - \mathbf{u}^{n+1} \tag{210}$$

and

$$J_G = \frac{\Delta t}{3} J(B(\mathbf{u}^{n+1})) - I. \tag{211}$$

Once the appropriate $\delta^{n+1+\star/2}$ has been found, it is used to update the solution to the next time step

$$\mathbf{u}^{n+1} = \mathbf{u}^{n+(1+\star)/2} + \delta^{n+(1+\star)/2}. \tag{212}$$

This whole process of the diffusion and reaction steps is repeated for each time step until the desired end point of the simulation.

BIBLIOGRAPHY

[1] N Ormiston-Smith A S Ahmad and P D Sasieni. Trends in the lifetime risk of developing cancer in great britain: comparison of risk for those born from 1930 to 1960. *British Journal of Cancer*, 2015.

[2] T. Alarcón, H.M. Byrne, and P.K. Maini. A cellular automaton model for tumour growth in inhomogeneous environment. *Journal of theoretical biology*, 225(2):257–274, 2003.

[3] T. Alarcón, M.R. Owen, H.M. Byrne, and P.K. Maini. Multiscale modelling of tumour growth and therapy: the influence of vessel normalisation on chemotherapy. *Computational and Mathematical Methods in Medicine*, 7(2-3):85–119, 2006.

[4] G. Alfred and J.R. Knudson. Mutation and cancer: Statistical study of retinoblastoma. *Proceedings of the National Academy of Sciences*, 68(4):820–823, April 1971.

[5] G. Allaire. Lecture 3 - numerical methods of homogenisation. http://www.cmap.polytechnique.fr/~allaire/homog/lect3.pdf, 2010.

[6] M.S. Alnaes, J. Blechta, J. Hake, A. Johansson, B. Kehlet, A. Logg, C. Richardson, J. Ring, M.E. Rognes, and G.N. Wells. The fenics project version 1.5. *Archive of Numerical Software*, 2015.

[7] A.R. Anderson and M.A. Chaplain. Continuous and discrete mathematical models of tumor-induced angiogenesis. *Bulletin of Mathematical Biology*, 60(5):857–99, Sep 1998.

[8] P. Armitage and R. Doll. The age distribution of cancer and a multistage theory of carcinogenesis. *British Journal of Cancer*, 8(1):1–12, March 1954.

[9] P. Armitage and R. Doll. A two-stage theory of carcinogenesis in relation to the age distribution of human cancer. *British Journal of Cancer*, 11(2):161–169, 1957.

[10] D. Balding and D.L. McElwain. A mathematical model of tumour-induced capillary growth. *Journal of Theoretical Biology*, 114(1):53–73, May 1985.

[11] R.F. Beerenwinkel, N. nd Schwarz, M. Gerstung, and F. Markowetz. Cancer evolution: mathematical models and computational inference. *Systematic Biology*, 64(1):e1–e25, 2014.

[12] N. Bellomo and M. Delitala. From the mathematical kinetic, and stochastic game theory to modelling mutations, onset, progression and immune competition of cancer cells. *Phsyics of Life Reviews*, pages 183–206, 2008.

[13] N. Bellomo and G. Forni. Dynamics of tumor interaction with the host immune system. *Mathematical and Computer Modelling*, 20(1):107–122, 1994.

[14] A. Belloquid, E. De Angelis, and D. Knopoff. From the modeling of the immune hallmarks of cancer to a black swan in biology. *Mathematical Models and Methods in Applied Sciences*, 23(5):949–978, 2012.

[15] Ahmed Boujelben, Michael Watson, Steven McDougall, Yi-Fen Yen, Elizabeth R Gerstner, Ciprian Catana, Thomas Deisboeck, Tracy T Batchelor, David Boas, Bruce Rosen, et al. Multimodality imaging and mathematical modelling of drug delivery to glioblastomas. *Interface focus*, 6(5):20160039, 2016.

[16] J. Bourgat. Numerical experiments of the homogenization method. 1979.

[17] L. Brannon-Peppas and N.A. Peppas. Dynamic and equilibrium swelling behaviour of ph-sensitive hydrogels containing 2-hydroxyethyl methacrylate. *Biomaterials*, 11(9):635–644, 1990.

[18] D.J. Brat, A.A. Castellano-Sanchez, S.B. Hunter, M. Pecot, C. Cohen, E.H. Hammond, S.N Devi, B. Kaur, and E.G. Van Meir. Pseudopalisades in glioblastoma are hypoxic, express extracellular matrix proteases, and are formed by an actively migrating cell population. *Cancer Research*, 64(3):920–927, 2004.

[19] Joseph D Bronzino. *Biomedical engineering handbook*, volume 2. CRC press, 1999.

[20] P.K. Burgess, P.M. Kulesa, J.D. Murray, and E.C Alvord Jr. The interaction of growth rates and diffusion coefficients in a three-dimensional mathematical model of gliomas. *Journal of Neuropathology & Experimental Neurology*, 56(6):704–713, 1997.

[21] R. Burridge and J.B. Keller. Poroelasticity equations derived from microstructure. *The Journal of the Acoustical Society of America*, 70(4):1140–1146, 1981.

[22] H.M. Byrne. Dissecting cancer through mathematics: from the cell to the animal model. *Nature Reviews Cancer*, 10:221–230, March 2010.

[23] D. Cahill and S. Turcan. Origin of gliomas. In *Seminars In Neurology*, volume 38, pages 005–010. Thieme Medical Publishers, 2018.

[24] F. Cavallo, C. De Giovanni, P. Nanni, G. Forni, and P. Lollini. 2011: the immune hallmarks of cancer. *Cancer Immunology, Immunotherapy*, 60(3):319–26, Mar 2011.

[25] M.C Chamberlain. Radiographic patterns of relapse in glioblastoma. *Journal of Neuro-oncology*, 101(2):319–323, 2011.

[26] M.A. Chaplain and A.M. Stuart. A model mechanism for the chemotactic response of endothelial cells to tumour angiogenesis factor. *IMA J Math Appl Med Biol*, 10(3):149–68, 1993.

[27] O. Clatz, M. Sermesant, P. Bondiau, H. Delingette, S.K. Warfield, G. Malandain, and N. Ayache. Realistic simulation of the 3-d growth of brain tumors in mr images coupling diffusion with biomechanical deformation. *IEEE transactions on medical imaging*, 24(10):1334–1346, 2005.

[28] Chris A Cocosco, Vasken Kollokian, Remi K-S Kwan, G Bruce Pike, and Alan C Evans. Brainweb: Online interface to a 3d mri simulated brain database. In *NeuroImage*. Citeseer, 1997.

[29] D Louis Collins, Alex P Zijdenbos, Vasken Kollokian, John G Sled, Noor J Kabani, Colin J Holmes, and Alan C Evans. Design and construction of a realistic digital brain phantom. *IEEE transactions on medical imaging*, 17(3):463–468, 1998.

[30] J. Collis, D.L. Brown, M.E. Hubbard, and R.D. O'Dea. Effective equations governing an active poroelastic medium. *Proceedings of*

the Royal Society A: Mathematical, Physical and Engineering Sciences, 473(2198):20160755, 2017.

[31] V. Cristini, J. Lowengrub, and Q. Nie. Nonlinear simulation of tumor growth. *Journal of Mathematical Biology*, 46(3):191–224, Mar 2003.

[32] S.J. Dalrymple, J.E. Parisi, P.C. Roche, S.C. Ziesmer, B.W. Scheithauer, and P.J. Kelly. Changes in proliferating cell nuclear antigen expression in glioblastoma multiforme cells along a stereotactic biopsy trajectory. *Neurosurgery*, 35(6):1036–1045, 1994.

[33] K.R. Daly, S.J. Mooney, M.J. Bennett, N.M.J. Crout, T. Roose, and S.R. Tracy. Assessing the influence of the rhizosphere on soil hydraulic properties using x-ray computed tomography and numerical modelling. *Journal of Experimental Botany*, 66(8):2305–2314, 2015.

[34] A. Dance. Cancer immunotherapy comes of age. *Science*, 355(6330):1220–1222, 2017.

[35] A.S. Deakin. Model for the growth of a solid in vitro tumor. *Growth*, 39(1):159–65, Mar 1975.

[36] T.S. Deisboeck, Z. Wang, P. Macklin, and V. Cristini. Multiscale cancer modeling. *The Annual Review of Biomedical Engineering*, 13:127–155, April 2011.

[37] D. Delbeke, C. Meyerowitz, R.L. Lapidus, R.J. Maciunas, M.T. Jennings, P.L. Moots, and R.M. Kessler. Optimal cutoff levels of f-18 fluorodeoxyglucose uptake in the differentiation of low-grade from high-grade brain tumors with pet. *Radiology*, 195(1):47–52, 1995.

[38] C. DeLisi and A. Rescigno. Immune surveillance and neoplasia: a minimal mathematical model. *Bulletin of Mathematical Biology*, 39(2):201–221, 1977.

[39] A. Dewanji, J. Jeon, R. Meza, and E.G. Luebeck. Number and size distribution of colorectal adenomas under the multistage clonal expansion model of cancer. *PLoS Computational Biology*, 7(10):e1002213, 2011.

[40] L. Edelstein, Y. Hadar, I. Chet, Y. Henis, and L.A. Segel. A model for fungal colony growth applied to scleotium rolfsii. *Journal of General Microbiology*, 129(6):1873–1881, 1983.

[41] A. Eladdadi, A.E. Radunskaya, et al. Modeling cancer-immune responses to therapy. *Journal of Pharmacokinetics and Pharmacodynamics*, 41(5):461–478, 2014.

[42] C. Engwer, T. Hillen, M. Knappitsch, and C. Surulescu. Glioma follow white matter tracts: a multiscale dti-based model. *Journal of Mathematical Biology*, pages 1–32, 2014.

[43] R.A. Fisher. The wave of advance of advantageous genes. *Annals of Eugenics*, 7(4):355–369, 1937.

[44] A.B. Fleming and M.W. Saltzman. Pharmacokinetics of the carmustine implant. *Clinical Pharmacokinetics*, 41(6):403–419, 2002.

[45] Office for National Statistics. Deaths registered in england and wales: 2015, 2015.

[46] A. Gandalovičová, D. Rosel, M. Fernandes, P. Veselỳ, P. Heneberg, V. Čermák, L. Petruželka, S. Kumar, V. Sanz-Moreno, and J. Brábek. Migrastatics anti-metastatic and anti-invasion drugs: promises and challenges. *Trends in Cancer*, 3(6):391–406, 2017.

[47] P. Gerlee and A.R.A. Anderson. An evolutionary hybrid cellular automaton model of solid tumour growth. *Journal of Theoretical Biology*, 246(4):583–603, 2007.

[48] A. Giese, R. Bjerkvig, M.E. Berens, and M. Westphal. Cost of migration: invasion of malignant gliomas and implications for treatment. *Journal of Clinical Oncology*, 21(8):1624–1636, 2003.

[49] P. Goel, J. Sneyd, and A. Friedman. Homogenization of the cell cytoplasm: the calcium bidomain equations. *Multiscale Modeling & Simulation*, 5(4):1045–1062, 2006.

[50] J.D. Gordan and M.C. Simon. Hypoxia-inducible factors: central regulators of the tumor phenotype. *Current Opinion in Genetics & Development*, 17(1):71–77, 2007.

[51] M. Grassi, I. Colombo, and R. Lapasin. Experimental determination of the theophylline diffusion coefficient in swollen sodium-alginate membranes. *Journal of Controlled Release*, 76(1-2):93–105, 2001.

[52] H.P. Greenspan. Models for the growth of a solid tumour by diffusion. *Studies in Applied Mathematics*, 51(4):317–340, 1972.

[53] H.P. Greenspan. On the growth and stability of cell cultures and solid tumors. *Journal of Theoretical Biology*, 56(1):229–42, Jan 1976.

[54] S. Gu, G. Chakraborty, K. Champley, A.M. Alessio, J. Claridge, R. Rockne, M. Muzi, K.A. Krohn, A.M. Spence, E.C. Alvord, et al. Applying a patient-specific bio-mathematical model of glioma growth to develop virtual [18f]-fmiso-pet images. *Mathematical Medicine and Biology*, 29(1):31–48, 2012.

[55] P. Hahnfeldt, D. Panigrahy, J. Folkman, and L. Hlatky. Tumor development under angiogenic signaling: a dynamical theory of tumor growth, treatment response, and postvascular dormancy. *Cancer Research*, 59(19):4770–5, Oct 1999.

[56] D. Hanahan and R.A. Weinberg. The hallmarks of cancer. *Cell*, 100(1):57–70, Jan 2000.

[57] D. Hanahan and R.A. Weinberg. Hallmarks of cancer: the next generation. *Cell*, 144(5):646–74, Mar 2011.

[58] H.L.P. Harpold, E.C. Alvord, and K.R. Swanson. The evolution of mathematical modeling of glioma proliferation and invasion. *Journal of Neuropathology & Experimental Neurology*, 66(1):1–9, 2007.

[59] A. Hawkins-Daarud, R.C. Rockne, A.R.A. Anderson, and K.R. Swanson. Modeling tumor-associated edema in gliomas during anti-angiogenic therapy and its impact on imageable tumor. *Frontiers in Oncology*, 3:66, 2013.

[60] C. Hogea, C. Davatzikos, and G. Biros. Modeling glioma growth and mass effect in 3d mr images of the brain. In *International Conference on Medical Image Computing and Computer-Assisted Intervention*, pages 642–650. Springer, 2007.

[61] Elizabeth C Holden, Joseph Collis, Bindi S Brook, and Reuben D O'DEA. A multiphase multiscale model for nutrient limited tissue growth. *The ANZIAM Journal*, 59(4):499–532, 2018.

[62] E.C. Holland. Glioblastoma multiforme: the terminator. *Proceedings of the National Academy of Sciences*, 97(12):6242–6244, 2000.

[63] S.J. Hollister and N. Kikuchi. Homogenization theory and digital imaging: a basis for studying the mechanics and design principles of bone tissue. *Biotechnology and Bioengineering*, 43(7):586–596, 1994.

[64] H. Hurwitz, L. Fehrenbacher, W. Novotny, T. Cartwright, J. Hainsworth, W. Heim, J. Berlin, A. Baron, S. Griffing, E. Holmgren, et al. Bevacizumab plus irinotecan, fluorouracil, and leucovorin for metastatic colorectal cancer. *New England Journal of Medicine*, 350(23):2335–2342, 2004.

[65] J. Jeon, Vito Q., and Peter T. C. An off-lattice hybrid discrete-continuum model of tumor growth and invasion. *Biophysical Journal*, 98(1):37–47, 2010.

[66] A.R. Kansal, S. Torquato, G.R. Harsh, E.A. Chiocca, and T.S. Deisboeck. Simulated brain tumor growth dynamics using a three-dimensional cellular automaton. *Journal of Theoretical Biology*, 203(4):367–382, 2000.

[67] J.P. Keener and A.V. Panfilov. A biophysical model for defibrillation of cardiac tissue. *Biophysical Journal*, 71(3):1335–1345, 1996.

[68] M. Keunen, O.and Johansson, A. Oudin, M. Sanzey, S.A.A. Rahim, F. Fack, F. Thorsen, T. Taxt, M. Bartos, R. Jirik, et al. Anti-vegf treatment reduces blood supply and increases tumor cell invasion in glioblastoma. *Proceedings of the National Academy of Sciences*, 108(9):3749–3754, 2011.

[69] D. Kirschner and J.C. Panetta. Modeling immunotherapy of the tumor–immune interaction. *Journal of Mathematical Biology*, 37(3):235–252, 1998.

[70] P. Korkolopoulou, E. Patsouris, A.E. Konstantinidou, P.M. Pavlopoulos, N. Kavantzas, E. Boviatsis, I. Thymara, M. Perdiki, E. Thomas-Tsagli, D. Angelidakis, et al. Hypoxia-inducible factor 1α/vascular endothelial growth factor axis in astrocytomas. associations with microvessel morphometry, proliferation and prognosis. *Neuropathology and Applied Neurobiology*, 30(3):267–278, 2004.

[71] H. Krug and G. Taubert. Practical application of logistic function to the growth of experimental tumors. *Archiv fur Geschwulstforschung*, 55(4):235–244, 1985.

[72] V.A. Kuznetsov, I.A. Makalkin, M.A. Taylor, and A.S. Perelson. Nonlinear dynamics of immunogenic tumors: parameter estimation and global bifurcation analysis. *Bulletin of Mathematical Biology*, 56(2):295–321, 1994.

[73] V.A. Kuznetsov, V.P. Zhivoglyadov, and L.A. Stepanova. Kinetic approach and estimation of the parameters of cellular interaction between the immunity system and a tumor. *Archivum Immunologiae et Therapiae Experimentalis*, 41(1):21–31, 1993.

[74] Remi K-S Kwan, Alan C Evans, and G Bruce Pike. An extensible mri simulator for post-processing evaluation. In *Visualization in biomedical computing*, pages 135–140. Springer, 1996.

[75] RK-S Kwan, Alan C Evans, and G Bruce Pike. Mri simulation-based evaluation of image-processing and classification methods. *IEEE transactions on medical imaging*, 18(11):1085–1097, 1999.

[76] A.K. Laird. Dynamics of tumour growth. *British Journal of Cancer*, 18(3):490, 1964.

[77] Mats G Larson and Fredrik Bengzon. *The finite element method: theory, implementation, and applications*, volume 10. Springer Science & Business Media, 2013.

[78] Z. Lidar, Y. Mardor, T. Jonas, R. Pfeffer, M. Faibel, D. Nass, M. Hadani, and Z. Ram. Convection-enhanced delivery of paclitaxel for the treatment of recurrent malignant glioma: a phase i/ii clinical study. *Journal of Neurosurgery*, 100(3):472–479, 2004.

[79] A.A. Linninger, M.R. Somayaji, M. Mekarski, and L. Zhang. Prediction of convection-enhanced drug delivery to the human brain. *Journal of Theoretical Biology*, 250(1):125–138, 2008.

[80] L.A. Liotta, G.M. Saidel, and J. Kleinerman. Stochastic model of metastases formation. *Biometrics*, pages 535–550, 1976.

[81] A. Logg, K.A. Mardal, and G.N. Wells, editors. *DOLFIN: a C++/Python Finite Element Library*, chapter 10. Springer, 2012.

[82] A. Logg and G.N. Wells. Dolfin: Automated finite element computing. *ACM Transaction on Mathematical Software*, 2010.

[83] D. Louis, H. Ohgaki, O. Wiestler, and W. Cavenee. *WHO Classification of Tumours of the Central Nervous System, Revised. Fourth Edition*. International Agency for Research on Cancer, 2016.

[84] A.N. Lowan, N. Davids, and A. Levenson. Table of the zeros of the legendre polynomials of order 1-16 and the weight coefficients for gauss' mechanical quadrature formula. *Bulletin of the American Mathematical Society*, 48(10):739–743, 1942.

[85] P. Macklin, S. McDougall, A.R.A. Anderson, M.A.J. Chaplain, V. Cristini, and J. Lowengrub. Multiscale modelling and nonlinear simulation of vascular tumour growth. *Journal of Mathematical Biology*, 58(4-5):765–98, Apr 2009.

[86] Paul Macklin, Steven McDougall, Alexander RA Anderson, Mark AJ Chaplain, Vittorio Cristini, and John Lowengrub. Multiscale modelling and nonlinear simulation of vascular tumour growth. *Journal of mathematical biology*, 58(4-5):765–798, 2009.

[87] Anna Marciniak-Czochra and Mariya Ptashnyk. Derivation of a macroscopic receptor-based model using homogenization techniques. *SIAM Journal on Mathematical Analysis*, 40(1):215–237, 2008.

[88] A. Martínez-González, G.F. Calvo, L.A.P. Romasanta, and V.M. Pérez-García. Hypoxic cell waves around necrotic cores in glioblastoma: a biomathematical model and its therapeutic implications. *Bulletin of Mathematical Biology*, 74(12):2875–2896, 2012.

[89] S.C. Massey, M.C. Assanah, K.A. Lopez, P. Canoll, and K.R. Swanson. Glial progenitor cell recruitment drives aggressive glioma growth: mathematical and experimental modelling. *Journal of The Royal Society Interface*, page rsif20120030, 2012.

[90] A. Matzavinos, M.A.J. Chaplain, and V.A. Kuznetsov. Mathematical modelling of the spatio-temporal response of cytotoxic t-lymphocytes to a solid tumour. *Mathematical Medicine and Biology*, 21(1):1–34, 2004.

[91] S.R. McDougall, A.R.A. Anderson, M.A.J. Chaplain, and J.A. Sherratt. Mathematical modelling of flow through vascular networks: implications for tumour-induced angiogenesis and chemotherapy strategies. *Bulletin of Mathematical Biology*, 64(4):673–702, Jul 2002.

[92] Steven R McDougall, Alexander RA Anderson, and Mark AJ Chaplain. Mathematical modelling of dynamic adaptive tumour-induced angiogenesis: clinical implications and therapeutic targeting strategies. *Journal of theoretical biology*, 241(3):564–589, 2006.

[93] D.L.S McElwain and L.E. Morris. Apoptosis as a volume loss mechanism in mathematical models of solid tumor growth. *Mathematical Biosciences*, 39(1):147–157, 1978.

[94] D.L.S McElwain and P.J. Ponzo. A model for the growth of a solid tumor with non-uniform oxygen consumption. *Mathematical Biosciences*, 35(3):267–279, 1977.

[95] A. Mohamed and C. Davatzikos. Finite element modeling of brain tumor mass-effect from 3d medical images. In *International Conference on Medical Image Computing and Computer-Assisted Intervention*, pages 400–408. Springer, 2005.

[96] JD Murray. *Mathematical Biology*. Springer, 1989.

[97] V.R. Muthukkaruppan, L. Kubai, and R. Auerbach. Tumor-induced neovascularization in the mouse eye. *Journal of the National Cancer Institute*, 69(3):699–708, Sep 1982.

[98] M.L. Neal, A.D. Trister, S. Ahn, A. Baldock, C. A Bridge, L. Guyman, J. Lange, R. Sodt, T. Cloke, A. Lai, et al. Response classification based on a minimal model of glioblastoma growth is prognostic for clinical outcomes and distinguishes progression from pseudoprogression. *Cancer Research*, 73(10):2976–2986, 2013.

[99] J.C. Neu and W. Krassowska. Homogenization of syncytial tissues. *Critical Reviews in Biomedical Engineering*, 21(2):137–199, 1993.

[100] P.K. Newton, J. Mason, K. Bethel, L.A. Bazhenova, J. Nieva, and P. Kuhn. A stochastic markov chain model to describe lung cancer growth and metastasis. *PloS ONE*, 7(4):e34637, 2012.

[101] F. Nilenius, F. Larsson, K. Lundgren, and K. Runesson. Computational homogenization of diffusion in three-phase mesoscale concrete. *Computational Mechanics*, 54(2):461–472, 2014.

[102] C.O. Nordling. A new theory of the cancer-inducing mechanism. *British Journal of Cancer*, 7:68–72, 1953.

[103] H. Nygren and S. Eksborg. Stability of temozolomide in solutions aimed for oral treatment prepared from a commercially available powder for infusion. *Pharmaceutical Methods*, 3(1):1–3, Jan 2012.

[104] M.S. O'Reilly, L. Holmgren, Y. Shing, C. Chen, R.A. Rosenthal, M. Moses, W.S. Lane, Y. Cao, E.H. Sage, and J. Folkman. Angiostatin: a novel angiogenesis inhibitor that mediates the suppression of metastases by a lewis lung carcinoma. *Cell*, 79(2):315–328, 1994.

[105] M.R. Owen, T. Alarcón, P.K. Maini, and H.M. Byrne. Angiogenesis and vascular remodelling in normal and cancerous tissues. *Journal of Mathematical Biology*, 58(4-5):689–721, Apr 2009.

[106] M.R. Owen, H.M. Byrne, and C.E. Lewis. Mathematical modelling of the use of macrophages as vehicles for drug delivery to hypoxic tumour sites. *Journal of Theoretical Biology*, 226(4):377–391, 2004.

[107] M.R. Owen and J.A. Sherratt. Mathematical modelling of macrophage dynamics in tumours. *Mathematical Models and Methods in Applied Sciences*, 9(04):513–539, 1999.

[108] W.M. Pardridge. The blood-brain barrier: bottleneck in brain drug development. *NeuroRx*, 2(1):3–14, 2005.

[109] W.M. Pardridge. Drug transport across the blood–brain barrier. *Journal of Cerebral Blood Flow & Metabolism*, 32(11):1959–1972, 2012.

[110] Grigoris Pavliotis and Andrew Stuart. *Multiscale methods: averaging and homogenization*. Springer Science & Business Media, 2008.

[111] H. Perfahl, B.D. Hughes, T. Alarcón, P.K. Maini, M.C. Lloyd, M. Reuss, and H.M. Byrne. 3d hybrid modelling of vascular network formation. *Journal of Theoretical Biology*, 414:254–268, 2017.

[112] Michael Clinton Perry. *The chemotherapy source book*. Lippincott Williams & Wilkins, 2008.

[113] R. Platt. Clonal ageing and cancer. *The Lancet*, 265(6869):867, 1955.

[114] R.T. Prehn. Two competing influences that may explain concomitant tumor resistance. *Cancer Research*, 53(14):3266–3269, 1993.

[115] C.V. Rahman, S.J. Smith, P.S. Morgan, K.A. Langmack, P.A. Clarke, A.A. Ritchie, D.C. Macarthur, F.R. Rose, K.M. Shakesheff, R.G. Grundy, et al. Adjuvant chemotherapy for brain tumors delivered via a novel intracavity moldable polymer matrix. *PloS ONE*, 8(10):e77435, 2013.

[116] G.A. Rodríguez, A.R. Holguín, F. Martínez, M. Khoubnasabjafari, and A. Jouyban. Volumetric properties of (peg 400+ water) and (peg 400+ ethanol) mixtures at several temperatures and correlation with the jouyban-acree model. *Revista Colombiana de Ciencias Químico-Farmacéuticas*, 41(2):187–202, 2012.

[117] A. Roniotis, V. Sakkalis, E. Tzamali, G. Tzedakis, M. Zervakis, and K. Marias. Solving the pihna model while accounting for radiotherapy. In *Advanced Research Workshop on In Silico Oncology and Cancer Investigation-The TUMOR Project Workshop (IARWISOCI), 2012 5th International*, pages 1–4. IEEE, 2012.

[118] G.M. Saidel, L.A. Liotta, and J. Kleinerman. System dynamics of a metastatic process from an implanted tumor. *Journal of Theoretical Biology*, 56(2):417–434, 1976.

[119] W Mark Saltzman. *Drug delivery: engineering principles for drug therapy*. Oxford University Press, 2001.

[120] W.M. Saltzman and M.L. Radomsky. Drugs released from polymers: diffusion and elimination in brain tissue. *Chemical Engineering Science*, 46(10):2429–2444, 1991.

[121] L.M. Sander and T.S. Deisboeck. Growth patterns of microscopic brain tumors. *Physical Review E*, 66(5):051901, 2002.

[122] J.G. Scott, D. Basanta, A.R.A. Anderson, and P. Gerlee. A mathematical model of tumour self-seeding reveals secondary metastatic deposits as drivers of primary tumour growth. *Journal of The Royal Society Interface*, 10(82):20130011, 2013.

[123] A. Shirinifard, J.S. Gens, B.L. Zaitlen, N.J. Popławski, M. Swat, and J.A. Glazier. 3d multi-cell simulation of tumor growth and angiogenesis. *PloS ONE*, 4(10):e7190, 2009.

[124] J. Siepmann, K. Elkharraz, F. Siepmann, and D. Klose. How autocatalysis accelerates drug release from plga-based microparticles: a quantitative treatment. *Biomacromolecules*, 6(4):2312–2319, 2005.

[125] J. Siepmann, N. Faisant, and J. Benoit. A new mathematical model quantifying drug release from bioerodible microparticles using monte carlo simulations. *Pharmaceutical Research*, 19(12):1885–1893, 2002.

[126] D.L. Silbergeld and M.R. Chicoine. Isolation and characterization of human malignant glioma cells from histologically normal brain. *Journal of Neurosurgery*, 86(3):525–531, 1997.

[127] D.L. Silbergeld, R.C. Rostomily, and E.C. Alvord Jr. The cause of death in patients with glioblastoma is multifactorial. *Journal of Neuro-oncology*, 10(2):179–185, 1991.

[128] L. Singh, V. Kumar, and B.D. Ratner. Generation of porous microcellular 85/15 poly (dl-lactide-co-glycolide) foams for biomedical applications. *Biomaterials*, 25(13):2611–2617, 2004.

[129] S.J. Smith, C.V. Rahman, P.A. Clarke, A.A. Ritchie, T.W. Gould, J.H. Ward, K.M. Shakesheff, R.G. Grundy, and R. Rahman. Surgical delivery of drug releasing poly (lactic-co-glycolic acid)/poly (ethylene glycol) paste with in vivo effects against glioblastoma. *The Annals of The Royal College of Surgeons of England*, 96(7):495–501, 2014.

[130] G.G. Steel. Cell loss from experimental tumours. *Cell Proliferation*, 1(3):193–207, 1968.

[131] C.L. Stokes and D.A. Lauffenburger. Analysis of the roles of microvessel endothelial cell random motility and chemotaxis in angiogenesis. *Journal of Theoretical Biology*, 152(3):377–403, Oct 1991.

[132] R. Stupp, M.E. Hegi, W.P. Mason, M.J. van den Bent, M.J.B. Taphoorn, R.C. Janzer, S.K. Ludwin, A. Allgeier, B. Fisher, K. Belanger, et al. Effects of radiotherapy with concomitant and adjuvant temozolomide versus radiotherapy alone on survival in glioblastoma in a randomised phase iii study: 5-year analysis of the eortc-ncic trial. *The Lancet Oncology*, 10(5):459–466, 2009.

[133] R. Stupp, W.P. Mason, M.J. Van Den Bent, M. Weller, B. Fisher, M.J.B. Taphoorn, K. Belanger, A.A. Brandes, C. Marosi, U. Bogdahn, et al. Radiotherapy plus concomitant and adjuvant temozolomide for glioblastoma. *New England Journal of Medicine*, 352(10):987–996, 2005.

[134] A. Swan, T. Hillen, J.C. Bowman, and A.D. Murtha. A patient-specific anisotropic diffusion model for brain tumour spread. *Bulletin of Mathematical Biology*, 80(5):1259–1291, 2018.

[135] K.R. Swanson. Mathematical modeling of the growth and control of tumors, 1999.

[136] K.R. Swanson, E.C. Alvord, Jr, and J.D. Murray. A quantitative model for differential motility of gliomas in grey and white matter. *Cell Prolif*, 33(5):317–29, Oct 2000.

[137] K.R. Swanson, C. Bridge, J.D. Murray, and E.C. Alvord. Virtual and real brain tumors: using mathematical modeling to quantify glioma growth and invasion. *Journal of the Neurological Sciences*, 216(1):1–10, 2003.

[138] K.R. Swanson, C. Bridge, J.D. Murray, and E.C. Alvord, Jr. Virtual and real brain tumors: using mathematical modeling to quantify glioma growth and invasion. *Journal of the Neurological Sciences*, 216(1):1–10, Dec 2003.

[139] K.R. Swanson, D. Corwin, and R. Rockne. We-e-17a-07: Patient-specific mathematical neuro-oncology: Biologically-informed radiation therapy and imaging physics. *Medical Physics*, 41(6):508–509, 2014.

[140] K.R. Swanson, R.C. Rockne, J. Claridge, M.A.J. Chaplain, E.C. Alvord, and A.R.A. Anderson. Quantifying the role of angiogenesis in malignant progression of gliomas: in silico modeling integrates imaging and histology. *Cancer Research*, 71(24):7366–7375, 2011.

[141] K.R. Swanson, R.C. Rostomily, and E.C. Alvord. A mathematical modelling tool for predicting survival of individual patients following resection of glioblastoma: a proof of principle. *British Journal of Cancer*, 98(1):113–119, 2008.

[142] M.H. Swat, G.L. Thomas, J.M. Belmonte, A. Shirinifard, D. Hmeljak, and J.A. Glazier. Multi-scale modeling of tissues using compucell3d. In *Methods in Cell Biology*, volume 110, pages 325–366. Elsevier, 2012.

[143] A. Thiepold, S. Luger, M. Wagner, N. Filmann, M.W. Ronellenfitsch, P.N. Harter, A.K. Braczynski, S. Dützmann, E. Hattingen, J.P. Steinbach, et al. Perioperative cerebral ischemia promote infiltrative recurrence in glioblastoma. *Oncotarget*, 6(16):14537, 2015.

[144] R.H. Thomlinson and L.H. Gray. The histological structure of some human lung cancers and the possible implications for radiotherapy. *British Journal of Cancer*, 9(4):539–549, 1955.

[145] C. Tomasetti and B. Vogelstein. Variation in cancer risk among tissues can be explained by the number of stem cell divisions. *Science*, 347(6217):78–81, 2015.

[146] P. Tracqui, G.C. Cruywagen, D.E. Woodward, G.T. Bartoo, J.D. Murray, and E.C. Alvord. A mathematical model of glioma growth: the effect of chemotherapy on spatio-temporal growth. *Cell Proliferation*, 28(1):17–31, 1995.

[147] A.N.F. Versypt, D.W. Pack, and R.D. Braatz. Mathematical modeling of drug delivery from autocatalytically degradable plga microspheresa review. *Journal of Controlled Release*, 165(1):29–37, 2013.

[148] J. Voges, R. Reszka, A. Gossmann, C. Dittmar, R. Richter, G. Garlip, L. Kracht, H.H. Coenen, V. Sturm, K. Wienhard, et al. Imaging-guided convection-enhanced delivery and gene therapy of glioblastoma. *Annals of Neurology*, 54(4):479–487, 2003.

[149] J. Wang, B.M. Wang, and S.P. Schwendeman. Characterization of the initial burst release of a model peptide from poly (d, l-lactide-co-glycolide) microspheres. *Journal of Controlled Release*, 82(2-3):289–307, 2002.

[150] J.P. Ward and J.R. King. Mathematical modelling of avascular-tumour growth. *Mathematical Medicine and Biology: A Journal of the IMA*, 14(1):39–69, 1997.

[151] J.P. Ward and J.R. King. Mathematical modelling of avascular-tumour growth ii: modelling growth saturation. *Mathematical Medicine and Biology: A Journal of the IMA*, 16(2):171–211, 1999.

[152] MG Watson, SR McDougall, MAJ Chaplain, AH Devlin, and CA Mitchell. Dynamics of angiogenesis during murine retinal development: a coupled in vivo and in silico study. *Journal of The Royal Society Interface*, 9(74):2351–2364, 2012.

[153] M. Westphal, D.C. Hilt, E. Bortey, P. Delavault, R. Olivares, P.C. Warnke, I.R. Whittle, J. Jääskeläinen, and Z. Ram. A phase 3 trial of local chemotherapy with biodegradable carmustine (bcnu) wafers (gliadel wafers) in patients with primary malignant glioma. *Neuro-oncology*, 5(2):79–88, 2003.

[154] D.E. Woodward, J. Cook, P. Tracqui, G.C. Cruywagen, J.D. Murray, and E.C. Alvord Jr. A mathematical model of glioma growth: the effect of extent of surgical resection. *Cell Proliferation*, 29(6):269–288, 1996.

[155] Tatsuo Yamaguchi, Iwao Kanno, Kazuo Uemura, Fumjo Shishido, A Inugami, Toshihide Ogawa, Matsutaro Murakami, and Kazuo Suzuki. Reduction in regional cerebral metabolic rate of oxygen during human aging. *Stroke*, 17(6):1220–1228, 1986.

[156] David Zagzag, Yevgeniy Lukyanov, Li Lan, M Aktar Ali, Mine Esencay, Olga Mendez, Herman Yee, Evelyn B Voura, and Elizabeth W Newcomb. Hypoxia-inducible factor 1 and vegf upregulate cxcr4 in glioblastoma: implications for angiogenesis and glioma cell invasion. *Laboratory Investigation*, 86(12):1221, 2006.

[157] David Zagzag, Hua Zhong, Joanne M Scalzitti, Erik Laughner, Jonathan W Simons, and Gregg L Semenza. Expression of hypoxia-inducible factor 1α in brain tumors. *Cancer*, 88(11):2606–2618, 2000.

[158] RM Zuniga, R Torcuator, R Jain, J Anderson, T Doyle, S Ellika, L Schultz, and T Mikkelsen. Efficacy, safety and patterns of response and recurrence in patients with recurrent high-grade gliomas treated with bevacizumab plus irinotecan. *Journal of Neuro-oncology*, 91(3):329, 2009.